LIGNOCELLULOSE VALORIZATION: FRACTIONATION, CONVERSION AND APPLICATIONS

EDITED BY: Xiaojun Shen, Jia-Long Wen, Chen Huang and Arthur Jonas Ragauskas

PUBLISHED IN: Frontiers in Energy Research

frontiers Research Topics

ISSN 1664-8714
ISBN 978-2-88976-831-8
DOI 10.3389/978-2-88976-831-8

About Frontiers

Frontiers is more than just an open-access publisher of scholarly articles: it is a pioneering approach to the world of academia, radically improving the way scholarly research is managed. The grand vision of Frontiers is a world where all people have an equal opportunity to seek, share and generate knowledge. Frontiers provides immediate and permanent online open access to all its publications, but this alone is not enough to realize our grand goals.

Frontiers Journal Series

The Frontiers Journal Series is a multi-tier and interdisciplinary set of open-access, online journals, promising a paradigm shift from the current review, selection and dissemination processes in academic publishing. All Frontiers journals are driven by researchers for researchers; therefore, they constitute a service to the scholarly community. At the same time, the Frontiers Journal Series operates on a revolutionary invention, the tiered publishing system, initially addressing specific communities of scholars, and gradually climbing up to broader public understanding, thus serving the interests of the lay society, too.

Dedication to Quality

Each Frontiers article is a landmark of the highest quality, thanks to genuinely collaborative interactions between authors and review editors, who include some of the world's best academicians. Research must be certified by peers before entering a stream of knowledge that may eventually reach the public - and shape society; therefore, Frontiers only applies the most rigorous and unbiased reviews.
Frontiers revolutionizes research publishing by freely delivering the most outstanding research, evaluated with no bias from both the academic and social point of view. By applying the most advanced information technologies, Frontiers is catapulting scholarly publishing into a new generation.

What are Frontiers Research Topics?

Frontiers Research Topics are very popular trademarks of the Frontiers Journals Series: they are collections of at least ten articles, all centered on a particular subject. With their unique mix of varied contributions from Original Research to Review Articles, Frontiers Research Topics unify the most influential researchers, the latest key findings and historical advances in a hot research area! Find out more on how to host your own Frontiers Research Topic or contribute to one as an author by contacting the Frontiers Editorial Office: frontiersin.org/about/contact

LIGNOCELLULOSE VALORIZATION: FRACTIONATION, CONVERSION AND APPLICATIONS

Topic Editors:
Xiaojun Shen, Dalian National Laboratory for Clean Energy, Dalian Institute of Chemical Physics, Chinese Academy of Sciences, China
Jia-Long Wen, Beijing Forestry University, China
Chen Huang, Institute of Forest Chemical Industry, Chinese Academy of Forestry, China
Arthur Jonas Ragauskas, The University of Tennessee, Knoxville, United States

Citation: Shen, X., Wen, J.-L., Huang, C., Ragauskas, A. J., eds. (2022). Lignocellulose Valorization: Fractionation, Conversion and Applications. Lausanne: Frontiers Media SA. doi: 10.3389/978-2-88976-831-8

Table of Contents

frontiers | Frontiers in Energy Research

TYPE Editorial
PUBLISHED 22 July 2022
DOI 10.3389/fenrg.2022.981134

OPEN ACCESS

EDITED AND REVIEWED BY
Uwe Schröder,
University of Greifswald, Germany

*CORRESPONDENCE
Jia-Long Wen,
wenjialong@bjfu.edu.cn

SPECIALTY SECTION
This article was submitted to Bioenergy and Biofuels,
a section of the journal
Frontiers in Energy Research

RECEIVED 29 June 2022
ACCEPTED 04 July 2022
PUBLISHED 22 July 2022

CITATION
Shen X, Wen J-L, Huang C and Ragauskas AJ (2022), Editorial: Lignocellulose valorization: Fractionation, conversion and applications.
Front. Energy Res. 10:981134.
doi: 10.3389/fenrg.2022.981134

Editorial: Lignocellulose valorization: Fractionation, conversion and applications

Xiaojun Shen[1], Jia-Long Wen[2]*, Chen Huang[3] and Arthur J. Ragauskas[4,5,6]

[1]State Key Laboratory of Catalysis, Dalian National Laboratory for Clean Energy, Dalian Institute of Chemical Physics, Chinese Academy of Sciences, Dalian, China, [2]Beijing Key Laboratory of Lignocellulosic Chemistry, Beijing Forestry University, Beijing, China, [3]Institute of Chemical Industry of Forest Products, Chinese Academy of Forestry, Jiangsu Province Key Laboratory of Biomass Energy and Materials, Nanjing, China, [4]Department of Chemical and Biomolecular Engineering, University of Tennessee Knoxville, Knoxville, TN, United States, [5]Department of Forestry Wildlife and Fisheries, Center for Renewable Carbon, The University of Tennessee Institute of Agriculture, Knoxville, TN, United States, [6]Joint Institute for Biological Science, Biosciences Division, Oak Ridge National Laboratory, Oak Ridge, TN, United States

KEYWORDS

lignocellulose, fractionation, structural characterization, conversion, value-added utilization

Editorial on the Research Topic
Lignocellulose valorization: Fractionation, conversion and applications

Introduction

Lignocellulosic biomass is the most abundant form of renewable feedstock on the Earth (Zhang et al., 2017). Chemicals, energies, and materials derived from lignocellulosic biomass are renewable and sustainable, and have the potential to replace fossil feedstocks (Shen et al., 2022). Biorefinery, a process to fractionate lignocellulose into the three major components, is considered the most pivotal step for bioenergy, biomaterials and biochemicals (Shen and Sun, 2021). However, due to the complex hierarchy and chemical structures, only limited lignocellulose is valorized into value-added products, and most of them are burnt or just discarded. Therefore, there is a need to investigate the heterogeneous structure of lignocellulose, improve its efficient fractionation into cellulose, hemicelluloses and lignin, and develop the technology that can convert the lignocellulose into high-value chemical products and high-performance functional materials in a sustainable and promising configuration (Ragauskas et al., 2006; Vermerris and Abril, 2015). In short, the ultimate goal of biomass utilization is that the production of biofuels and biomaterials in industrial applications must be cost-, and performance-competitive with petroleum-derived equivalents.

The topic "*Lignocellulose Valorization: Fractionation, Conversion and Applications*" covers the new applications of existing techniques and principles in interpreting the

heterogeneous structure of lignocellulose, novel and high-efficiency biomass fractionation methods for improving lignin and cellulose quality, new catalytic biomass/lignin valorization technologies. In addition, the developed lignin and carbohydrates-based materials can be applied as electrode and advanced materials. Here we sincerely appreciate the 87 authors for their nice work on this topic. Following are the highlights drawn from their contributions to this research topic.

New application of existing techniques and principles in interpreting the heterogeneous structure of lignocellulose

To enhance the yield of fermentable sugars from enzymatic hydrolysis of cellulose, the understanding of the cellulose supramolecular structure as well as the ability to modify it appropriately are essential. Agarwal proposed a novel Raman characterization method, which can further define aggregated/supramolecular structure of cellulose (Agarwal). In addition to crystallinity, several pieces of structure-related information can be obtained that overall provided a more comprehensive description of the cellulose aggregated state. Additionally, the information by Raman spectroscopy is more resolved because it comes from spectral features that represents both the aggregated and the molecular states of cellulose. To reveal the relationship between transport phenomena and deacetylation kinetics in alkaline pretreatment process, a first-principled, experimentally validated mesoscale modeling framework was developed by *Thornburg et al.* to capture and predict the fundamental reaction-diffusion phenomena that govern effective yields and productivities of corn stover deacetylation by sodium hydroxide (Thornburg et al.). Using this approach, they have demonstrated that the chemistry and physics of corn stover deacetylation compete on the similar time and length scales, with corn stover particles as short as 2.3 mm in length predicted to be entirely mass transfer-limited for acetate extraction processes.

Novel and high-efficiency biomass fractionation methods for improving lignin and cellulose quality

Tricin is a monomer of grass lignin with unique biological properties, which is beneficial to human health with the potential for various applications. The abundant grass lignin could be an alternative source for tricin if an effective separation method is available. *Xie et al.* prepared different lignin preparations, such as alkali lignin (AL), mild acidolysis lignin (MAL), cellulase enzymatic lignin (CEL), γ-valerolactone lignin (GVL), and organosolv lignin (OL) etc., to investigate the effect of different fractionation methods on the tricin content of the wheat straw lignin (Xie et al.). The tricin signal of different lignin fractions can be clearly identified by 2D heteronuclear singular quantum correlation (HSQC) spectra. It was found that γ-valerolactone lignin showed the highest tricin level among these lignin samples as the tricin content of GVL was accounted to be 8.6% by integrals.

The efficient preparation method of nanocellulose is the basis for its subsequent conversion and utilization. In this study, the production of CNC (cellulose nanocrystal) from *Pennisetum hydridum* fiber using ultrasound-assisted sulfuric acid hydrolysis was performed by *Yu and coauthors*. (Yu et al.) The highest yield of CNC was 43.6%. The fiber length of CNC was determined to be within 500 nm and the diameter was within 10 nm. This research showed that *Pennisetum hydridum* could be used as a raw material to prepare CNC, and provided a new way for the valorization of *Pennisetum hydridum* fertilized by municipal sewage sludge (MSS).

New catalytic biomass/lignin valorization technologies

The degradation of lignin is critical in the conversion of lignocellulose into second-generation biofuels which could facilitate the lignin valorization approaches. Effective ligninolytic *Bacillus sp.* strains were isolated from forest soils by Yang and coauthors (Yang et al.). Subsequently, they investigated the degradation capability of alkali lignin by the strains. Results showed that TR-03 displayed optimal 26.72% alkali lignin (2 g/L) degradation at 7 days and a 71.23% Azure-B (0.01%) decolorization at 36 h by cultivation at 37°C. These results also proved that *Bacillus sp.* strains were important microorganism in the depolymerization of lignin, and further study should focus on the degrading mechanism of lignin by *Bacillus sp*.

It is a promising strategy to break the interlinkages and remove oxygen by selective catalytic cracking of the C–O bond to further transform the main components of biomass into small molecular products. In a mini-review, *Jian et al.* discuss the significance of selectivity control of C–O bond cleavage with well-tailored catalytic systems/strategies for furnishing biofuels and value-added chemicals with high efficiency from lignocellulosic biomass (Jian et al.). The current challenges and future opportunities of converting lignocellulose biomass into high-value chemicals are also summarized and analyzed.

Catalytic hydrodeoxygenation (HDO) is one of the most important topics for upgrading and refining bio-oil or lignin degradation products. *Tong et al.* prepared the Nb_2O_5-supported bimetallic catalysts with the impregnation method applied for the *in-situ* hydrogenation of guaiacol (Tong et al.). Guaiacol can be effectively transformed into cyclohexanol over different bimetallic catalysts, using alcohol as a hydrogen donor.

The mercerization of fiber is an important method for the high-value utilization of cellulose. *Cao et al.* have investigated the mercerization of bagasse fiber by freeze–thaw-assisted alkali treatment (FT/AT) (Cao et al.). The effects of freezing temperature, freezing time, alkali concentration, and thawing temperature on cellulose and hemicellulose removal were studied. The effective alkali concentration (5.0%) in causing complete transformation of cellulose I to cellulose II was decreased by 66.67% compared with traditional alkaline mercerization (15.0%). It provides theoretical support for promoting the high-value utilization of lignocellulosic biomass.

The development of pretreatment processes to identify potential woody biomass feedstock for sustainable biorefinery and energy applications is highly needed. *Choudhary et al.* demonstrated and compared the feasibility of the IL pretreatment process for two woody biomasses, namely Maple and Aspen, using two distinct ILs, i.e., 1-ethyl-3-methylimidazolium acetate ([C2mim][OAc]) and cholinium lysinate ([Ch][Lys]) as the solvent (Choudhary et al.). Results showed that the two ionic liquids showed different pretreatment effects in terms of fractionation efficiency, enzymatic saccharification, cellulose transformation and lignin depolymerization.

Application of carbohydrates, lignin-based materials and other components in related fields

Valorization of side streams offers novel types of raw materials to complement or replace synthetic and food-based alternatives in materials and biological medicine science, increasing profitability and decreasing the environmental impacts. *Asikanius et al.* present how LCCs, derived from pulp mill effluent, can be turned into valuable biopolymers for industrial polymer film applications (Asikanius et al.).

The flexible and transparent film heaters (FTFHs) with the advantages of mechanical flexibility, portability, and excellent electrothermal performance, are key to the next generation portable, wearable heaters and thermal protection systems. In Cui et al.' work, the transparent regenerated cellulose fibers made from completely dissolving in NMMO solution followed by a regeneration process are presented to disperse and support carbon nanotubes (CNTs) by a vacuum-dewatering process (Liu et al., 2022). The FTFHs made with earth-abundant, cost-effective, and recyclable materials, have excellent potential in the areas of green flexible and transparent film heaters.

Establishing the processing-structure-property-performance relationships (PSPP) through an efficient activation method for preparing activated carbons from different lignin precursors with enhanced electrochemical properties is very important for industrial-scale manufacturing of activated carbons (ACs). In *Yu et al.'* work, the extracted lignins from two kinds of biomass were converted to carbon precursors for synthesizing porous activated carbon electrodes for high-energy-density supercapacitors (Yu et al.). This research detailed the impact of lignin composition on the derived porous structures and electrochemical properties of activated carbons. The inexpensive lignin-based porous electrodes synthesized in this work can be used for various electrochemical devices for improved performance, decreased cost, and enhanced durability.

Besides the applications of carbohydrates and lignin in numerous fields, the application of plant extracts in biological medicine can also increase the additional value of lignocellulosic biomass. The branches of *Ulmus davidiana var. japonica* (ULDA) have traditionally been used in Korea and other Asian countries. ULDA extracts are complex substances consisting of many components; a few of them have pharmaceutical applications in various diseases, such as inflammation and other chronic problems, and as antimicrobial agents. In this study, *Yun and coauthors* have investigated the effects of supercritical fluid-fractionated ULDA, including initial fractions of polyphenols, hydrophobic substances, and flavonoids, on innate immunity modulation and recovery of intestinal function in an *in vitro* model (Yun et al.). These results suggest that U. davidiana and catechin-glycoside may be useful for improving immune system function.

Author contributions

All authors listed have made a substantial, direct, and intellectual contribution to the work and the final version for publication.

Acknowledgments

We thank all authors, reviewers, topic editors, and editorial staff at Frontiers who contributed to this Research Topic.

Conflict of interest

The authors declare that the research was conducted in the absence of any commercial or financial relationships that could be construed as a potential conflict of interest.

Publisher's note

References

Liu, D., Cui, J., Li, Y., Xu, K., Li, Y., Shen, H., et al. (2022). The flexible and transparent film heaters based on regenerated cellulose and carbon nanotubes. *Front. Energy Res.* 10, 879257. doi:10.3389/fenrg.2022.879257

Ragauskas, A. J., Williams, C. K., Davison, B. H., Britovsek, G., Cairney, J., Eckert, C. A., et al. (2006). The path forward for biofuels and biomaterials. *Science* 311, 484–489. doi:10.1126/science.1114736

Shen, X., and Sun, R. (2021). Recent advances in lignocellulose prior-fractionation for biomaterials, biochemicals, and bioenergy. *Carbohydr. Polym.* 261, 117884. doi:10.1016/j.carbpol.2021.117884

Shen, X., Zhang, C., Han, B., and Wang, F. (2022). Catalytic self-transfer hydrogenolysis of lignin with endogenous hydrogen: Road to the carbon-neutral future. *Chem. Soc. Rev.* 51, 1608–1628. doi:10.1039/D1CS00908G

Thornburg, N., Ness, R., Crowley, M., Bu, L., Pecha, M., Usseglio-Viretta, F., et al. (2022). Mass transport limitations and kinetic consequences of corn stover deacetylation. *Front. Energy Res.* 10, 841169. doi:10.3389/fenrg.2022.841169

Tong, L., Cai, B., Zhang, R., Feng, J., and Pan, H. (2021). *In situ* hydrodeoxygenation of lignin-derived phenols with synergistic effect between the bimetal and Nb2O5 support. *Front. Energy Res.* 9, 746109. doi:10.3389/fenrg.2021.746109

Vermerris, W., and Abril, A. (2015). Enhancing cellulose utilization for fuels and chemicals by genetic modification of plant cell wall architecture. *Curr. Opin. Biotechnol.* 32, 104–112. doi:10.1016/j.copbio.2014.11.024

Xie, M., Chen, Z., Xia, Y., Lin, M., Li, J., Zhang, L., et al. (20222021). Influence of the lignin extraction methods on the content of tricin in grass lignins. *Front. Energy Res.* 9, 756285. doi:10.3389/fenrg.2021.756285

Yang, J., Zhao, J., Xu, H., Zhang, N., Xie, J. C., and Wei, M. (2021). Isolation and characterization of Bacillus sp. Capable of degradating alkali lignin. *Front. Energy Res.* 9, 807286. doi:10.3389/fenrg.2021.807286

Yu, L., Seabright, K., Bajaj, I., Keffer, D. J., Alonso, D. M., Hsieh, C. T., et al. (2022). Performance and economic analysis of organosolv softwood and herbaceous lignins to activated carbons as electrode materials in supercapacitors. *Front. Energy Res.* 10, 849949. doi:10.3389/fenrg.2022.849949

Yu, X., Jiang, Y., Wu, Q., Wei, Z., Lin, X., Chen, Y., et al. (2021). Preparation and characterization of cellulose nanocrystal extraction from Pennisetum hydridum fertilized by municipal sewage sludge via sulfuric acid hydrolysis. *Front. Energy Res.* 9, 774783. doi:10.3389/fenrg.2021.774783

Yun, J. H., Kim, H. O., Jeong, J. H., Min, Y., Park, K. H., Si, C. L., et al. (2022). Ulmus davidiana var. japonica extracts suppress lipopolysaccharide-induced apoptosis through intracellular calcium modulation in U937 macrophages. *Front. Energy Res.* 10, 820330. doi:10.3389/fenrg.2022.820330

Zhang, Z., Song, J., and Han, B. (2017). Catalytic transformation of lignocellulose into chemicals and fuel products in ionic liquids. *Chem. Rev.* 117, 6834–6880. doi:10.1021/acs.chemrev.6b00457

frontiers in Energy Research

ORIGINAL RESEARCH
published: 17 September 2021
doi: 10.3389/fenrg.2021.746109

In Situ Hydrodeoxygenation of Lignin-Derived Phenols With Synergistic Effect Between the Bimetal and Nb_2O_5 Support

Le Tong[1,2], *Bo Cai*[1,2], *Ronghua Zhang*[1], *Junfeng Feng*[1,2,3]* *and Hui Pan*[1,2]*

[1]*Jiangsu Co-Innovation Centre of Efficient Processing and Utilization of Forest Resources, Jiangsu Provincial Key Lab for the Chemistry and Utilization of Agro-Forest Biomass, College of Chemical Engineering, Nanjing Forestry University, Nanjing, China,* [2]*International Innovation Center for Forest Chemicals and Materials, Nanjing Forestry University, Nanjing, China,* [3]*Jiangsu Key Laboratory for Biomass Energy and Material Institute of Chemical Industry of Forest Products, Chinese Academy of Forestry, National Engineering Lab. for Biomass Chemical Utilization, Jiangsu Key Laboratory for Biomass Energy and Material, Nanjing, China*

OPEN ACCESS

Edited by:
Xiaojun Shen,
Dalian National Laboratory for Clean Energy, Dalian Institute of Chemical Physics (CAS), China

Reviewed by:
Riyang Shu,
Guangdong University of Technology, China
Yaxuan Jing,
East China University of Science and Technology, China
Yu Xin,
Institute of Chemistry (CAS), China

***Correspondence:**
Junfeng Feng
2018149@njfu.edu.cn
Hui Pan
hpan@njfu.edu.cn

Specialty section:
This article was submitted to Bioenergy and Biofuels, a section of the journal Frontiers in Energy Research

Received: *23 July 2021*
Accepted: *18 August 2021*
Published: *17 September 2021*

Citation:
Tong L, Cai B, Zhang R, Feng J and Pan H (2021) In Situ *Hydrodeoxygenation of Lignin-Derived Phenols With Synergistic Effect Between the Bimetal and Nb_2O_5 Support. Front. Energy Res. 9:746109. doi: 10.3389/fenrg.2021.746109*

Nb_2O_5-supported bimetallic catalysts were prepared by the impregnation method applied for the *in situ* hydrogenation of guaiacol. Guaiacol can be effectively transformed into cyclohexanol over different bimetallic catalysts using alcohol as the hydrogen donor. Meanwhile, the effects of different hydrogen donors such as isopropanol, sec-pentanol, and ethylene glycol on *in situ* hydrogenation of guaiacol were investigated in detail, and the results showed that isopropanol is the best hydrogen supply solvent. Then, the dependence of Ni–Mn/Nb_2O_5 properties on metal loading, reaction time, reaction temperature, and reaction pressure was studied for the *in situ* hydrogenation of guaiacol by using isopropanol as the hydrogen donor. Guaiacol can be completely converted, and the yield of cyclohexanol reached 71.8% over Ni–Mn/Nb_2O_5 with isopropanol as the hydrogen donor at 200°C for 5 h. The structures and characteristics of better catalytic properties of the Ni–Mn/Nb_2O_5 catalyst were determined by BET, NH_3-TPD, XRD, XPS, SEM, and TEM, and the results indicated the particle size of the metal was small (approximately 10 nm) and the metal particles are finely dispersed in the whole support. Therefore, a large number of medium acid sites were generated on the 10Ni-10Mn/Nb_2O_5 with a large specific surface area, which could increase the interface between the metal and the support and may be beneficial to the hydrodeoxygenation of guaiacol.

Keywords: *in situ* hydrodeoxygenation, phenol compounds, bimetallic and bifunctional catalyst, cyclohexanol, Nb_2O_5

INTRODUCTION

Lignocellulosic biomass is the largest renewable resource in nature and an ideal substitute for fossil energy (Mushtaq et al., 2015). It can be converted into transportation fuel (bio-oil) or fine chemicals and can also overcome the environmental challenges in using fossil energy. However, due to the complex components of bio-oil, there are shortcomings such as thermal instability, low calorific value, and high viscosity and cannot be widely used. These shortcomings are mainly caused by the large number of oxygen-containing compounds contained in the bio-oil, including aldehydes, acids,

and phenol. Among them, phenolic compounds derived from lignin (Ragauskas et al., 2014) are the main components of bio-oil. Therefore, to expand the wide application of bio-oil, it needs to be upgraded by reducing the oxygen content.

At present, the more commonly used methods for upgrading and refining bio-oil or lignin degradation products in domestic and foreign research include catalytic reforming, catalytic cracking, and catalytic hydrodeoxygenation. Catalytic hydrodeoxygenation (HDO) is one of the more important ones. Under the action of a specific catalyst, the bio-oil can be catalytically hydrogenated by pressurized external hydrogen supply or hydrogen generated by solvent (*in situ* hydrogenation), and the phenolic compounds in the bio-oil are refined into liquid fuels such as alkanes. The HDO operation of bio-oil can remove the oxygen in bio-oil by water or alcohol, increase the effective hydrogen–carbon ratio, reduce oxygen content, and improve the quality of bio-oil.

In previous studies, many catalysts applied to the hydrodeoxygenation process with excellent performance have been reported. Among them, precious metals [Pt (Zhu et al., 2011; Saidi et al., 2014; He et al., 2018; Funkenbusch et al., 2019), Pd (Rahzani et al., 2017), Rh (Wang et al., 2008; Chen et al., 2016), Au (Ferentz et al., 2015; Qin et al., 2019), Ag (Liu et al., 2019), Ru (Newman et al., 2014; Ma et al., 2019)] have attracted much attention in the HDO research of phenolic compounds because of their remarkable catalytic hydrogenolysis and catalytic hydrogenation capabilities. For example, Funkenbusch et al. (2019) studied the catalytic performance of Pt/Al_2O_3 using phenolic model compounds (anisole, phenol, and m-cresol) as reactants. And, the results showed that the Pt/Al_2O_3 catalyst exhibited good ring saturation, demethylation, and enhanced deoxygenation. Wang et al. (2008) prepared the Rh/CNF catalyst with an average particle size of 2-3 nm, and the metal was highly dispersed on the CNF support by using the incipient wetness impregnation method. The results of the Rh/CNF catalyst applied in the hydrogenation reaction of phenols suggested that the aromatic ring in phenols was hydrogenated and the yield of the target product cyclohexanone could reach 60%. Chen et al. (2015) used the impregnation method to prepare a supported Ru/CNT catalyst and then used for the deoxygenation of phenolic compounds. Under the conditions of a reaction temperature of 220°C and a hydrogen pressure of 5 MPa, the conversion of eugenol can reach 100% with Ru/CNT and the selectivity of HDO product (4-propylcyclohexane) was as high as 94%. Under mild conditions, noble metal catalysts have excellent adsorption capacity for reactants and active hydrogen generated in the hydrogenation process, so they have better catalytic performance and high activity for deoxygenated products than other catalysts. However, noble metal catalysts are too expensive and prone to inactivate (Ohta et al., 2014). The upgrading of bio-oils with large-scale production using noble metal catalysts requires high economic costs, thus limiting their commercial applications. Nonprecious metal catalysts are more cost-effective than precious metal catalysts and show acceptable catalytic performance in HDO of phenolic compounds. Among these nonprecious metal catalysts (Co (Han et al., 2019), Mo (Yang et al., 2019), Ni, etc.), nickel-based (Qiu et al., 2016; Zhang et al., 2018; Lu et al., 2019; Resende et al., 2019; Li et al., 2020; Shafaghat et al., 2020; Song et al., 2020) catalysts have been extensively studied for the hydrodeoxygenation of different bio-oil model compounds. Therefore, nonprecious metal catalysts represented by nickel-based catalysts have attracted much attention because of their high hydrogenation activity and low cost. It can effectively convert hydrogen into active hydrogen and then apply it to the hydrogenation of phenolic compounds. It exhibits high hydrogenation activity in the hydrogenation process of phenolic compounds with good stability. Loading nickel metal on a carrier (metal oxides, molecular sieves, carbon materials, etc.) with special functions can better exert the catalytic hydrogenation effect of nickel metal (Mortensen et al., 2016; Bjelić et al., 2019; Li et al., 2020). And, in supported catalysts, the support materials are also a key factor in determining catalytic performance, as the metal is the hydrogenation active center and the carrier provides acid sites for the HDO reaction. Metal oxides (Al_2O_3 (Zhao et al., 2011), SiO_2 (Li et al., 2015), TiO_2 (Shu et al., 2019), Nb_2O_5 (Kon et al., 2014; Jin et al., 2017; Song et al., 2020), etc.) are selected as catalyst supports due to their excellent performance. For example, Al_2O_3 was widely used as a catalyst carrier for HDO catalysts due to its low price, excellent texture, and moderate acidity. Besides, SiO_2 was also used as a catalyst support due to its large specific surface area. In the study of hydrodeoxygenation of bio-oil phenolic compounds, the kinds of main products and the selectivity of the product varied with different catalysts with distinguishing metals and carriers. Furthermore, bimetallic catalysts offered the possibility of improving catalyst performance and adjusting the selectivity of specific products compared with monometallic catalysts. In the bimetallic catalyst, the interaction between the bimetal and the support can improve the catalytic activity of the catalyst, which is beneficial to promote the HDO reaction of phenolic compounds. For example, Ohta et al. (2014) selected ZrO_2 as the carrier and prepared a Pt–Re/ZrO_2 catalyst by the impregnation method. Under the reaction conditions of 300°C and 2 MPa hydrogen, the catalytic performance was studied in the HDO reaction of the lignin model compound 4-propylphenol. The results show that compared with Pt/ZrO_2, the incorporation of Re metal in Re/ZrO_2 or Re–Pt/ZrO_2 is beneficial to improve the catalyst stability and can increase the yield and selectivity of the deoxygenated product. The reaction path followed the benzene ring hydrogenation-dehydration-dehydrogenation step in 4-propylphenol converting to 4-propylbenzene. Moreover, the selectivity of target products such as propyl benzene is as high as 80%, and Re metal can inhibit Pt from sintering at high temperature (300°C), which is beneficial to prevent and control catalyst deactivation. In general, the advantage of the bimetallic catalyst is that the interaction between the two metals can significantly improve the catalytic performance of the catalyst, which is beneficial to adjust the selectivity of the final product. In addition, the adjustment effect of the auxiliary metal on the oxygenphilic active site and the ability to improve the dispersion of the active phase are also the main advantages of the bimetallic catalyst.

On the other hand, many hydrogenation experiments of bio-oil or phenolic model compounds used the external hydrogen

sources. However, the traditional hydrogenation process conditions using external hydrogen are more difficult and will harm the reactor and the catalyst (causing reactor blockage and catalyst deactivation) (Shafaghat et al., 2020), limiting its industrial application. Therefore, some studies are devoted to finding a way to replace external hydrogen supply, which could produce the same hydrogen supply effect at relatively mild operating conditions. Among them, *in situ* hydrogenation is a very effective alternative method. *In situ* hydrogenation uses hydrogen-donating solvents such as lower alcohols to undergo reforming reaction with water to generate active hydrogen or hydrogen radicals, which can effectively provide a hydrogen source in the hydrodeoxygenation reactions of phenolic compounds. At present, there are many studies on *in situ* hydrogenation (Reddy Kannapu et al., 2015; Xu et al., 2015; Feng et al., 2017; Xu et al., 2017; Montañez Valencia et al., 2020; Shafaghat et al., 2020) of different model compounds of bio-oil. For instance, Shafaghat et al. (2020) reported that saturated cyclic compounds (cyclohexanol and cyclohexane) were produced in the *in situ* hydrogenation of phenol on Ni/CeO_2 (using 2-propanol and 2-butanol as hydrogen sources). Feng et al. (2017) used Raney nickel as a catalyst and methanol as a hydrogen donor to produce the cyclohexane and cyclohexanol derivatives in the hydrodeoxygenation reaction of guaiacol.

Because NbOx species had a strong ability to activate C-O bonds, niobium-based materials were often used as carriers in HOD. So, we choose niobium oxide as the carrier of the catalyst (Song et al., 2020). Therefore, this study prepared a series of bimetallic catalysts ($Ni–Mn/Nb_2O_5$, $Ni–Zr/Nb_2O_5$, $Ni–Cu/Nb_2O_5$, $Ni–Mo/Nb_2O_5$, and $Ni–Co/Nb_2O_5$) with Nb_2O_5 as the support and studied the hydrogenation process of lignin-derivative phenolic compounds by using a low-carbon alcohol and water composite solvent to *in situ* produce active hydrogen. The prepared Ni and Mn bimetallic catalysts supported on niobium oxide and isopropanol/water hydrogen supply system can efficiently convert guaiacol into cyclohexanol. By analyzing the structural characteristics of the catalyst, it is found that the better catalytic performance of the $Ni–Mn/Nb_2O_5$ catalyst is due to the structural characteristics of large pores and larger specific surface area. The catalyst can completely convert the lignin-derived phenolic compounds into cyclohexanol, cyclohexane, etc., and the selectivity and yield of the main product cyclohexanol were outstanding.

EXPERIMENTAL

Reagents and Materials

All reagents and solvents were of analytical grade, provided by commercial suppliers and used without further purification, unless otherwise noted. High-purity commercial niobium oxide was purchased from Aladdin Chemical Reagent. $Ni(NO_3)_2$ $6H_2O$ was purchased from Nanjing Chemical Reagent Co., Ltd. $Mn(CH_3COO)_2$ $4H_2O$ was purchased from Xilong Chemical Co., Ltd.

Catalyst Synthesis

A typical synthesis of bimetallic catalyst (Ni–Co/Cu/Mo/Zr/Mn) was the incipient wetness impregnation method. A certain amount of Nb_2O_5 and metal precursor were dispersed in deionized water (DI) for 1 h by ultrasonic and then magnetically stirred for 4 h to promote metal adsorption on the support. Subsequently, the solution was vacuum-dried using a rotary evaporator to a viscous state and further dried overnight at 120°C in an oven. After that, the prepared catalysts were finally calcinated in air at 500°C for 5 h with a heating rate of 5°C/min, then ground with a mortar and pestle, and reduced in 20 vol% H_2 in N_2 gas at 500°C for 5 h. The heating rate was 5°C/min.

Catalyst Characterization

The specific surface area, pore volume, and pore diameter of the catalyst sample are measured by the N_2 adsorption–desorption method at liquid nitrogen temperature at −196°C on a bedside instrument (3H-2000PS1). All data from the surface of the catalyst are calculated and determined by using Brunauer–Emmett–Teller (BET) equation and *t*-plot obtained from the isotherms. X-ray diffraction analysis (XRD) was implemented on the Ultima IV instrument equipped with Cu Kα radiation to observe the phase composition of the catalyst sample. The powder XRD spectrum test range of the catalyst sample is from 5° to 80° with a scan rate of 1°/min. Scanning electron microscope (SEM) measurement was performed on the Phenom LE instrument with an accelerating voltage of 15 kV to observe the surface morphology of the catalyst, and energy dispersive spectrometry (EDS) was carried out on a coupled AZtec, Oxford, to determine the elemental composition and weight proportion of metal on the surface of catalysts. The transmission electron microscope (TEM) measurement was carried out on the Jeol JEM 2100 F instrument with an accelerating voltage of 200 kV. XPS measurement was performed on the AXIS UltraDLD instrument equipped with an Al Ka X-ray anode source to determine the chemical state of the elements on the catalyst. The peaks of the XPS spectrum were corrected by the binding energy of C 1s (284.6 eV). NH_3-TPD by a Mike AutoChem II 2920 was implemented to measure the acidity of the catalyst. Using NH_3 as the probe molecule, the sample to be characterized is quantitatively adsorbed at room temperature, and then N_2 is used as the desorption medium to desorb NH_3 adsorbed on the sample under temperature-programmed conditions. Before TPD analysis, the sample was first reduced at 400°C for 60 min in Ar airflow with a gas flow velocity of 30 ml min^{-1}. Then, it was cooled to 100°C under Ar flow and exposed to 10% NH_3/90% Ar logistics of 30 ml min^{-1} at this temperature for 30 min. Finally, the sample was rinsed with Ar (90 min) to eliminate the physically adsorbed NH_3. Ammonia desorption was measured by increasing the sample temperature to 800°C (10°C min^{-1}) under Ar airflow (30 ml min^{-1}).

Catalyst Testing

The catalytic activity test was carried out in a 50 ml stainless steel autoclave equipped with magnetic stirring. The catalyst (0.5 g), solvent water (20 g), isopropanol (5 g), and guaiacol (1 g) were charged into the autoclave for each run. 1 MPa of nitrogen is

flushed to heat the reactor to the desired reaction temperature while stirring at 800 rpm. After the reaction was completed, the reaction kettle was cooled down to room temperature in air, and the liquid was collected for subsequent analysis. The solvent after the reaction was extracted with ethyl acetate to separate the organic phase. The organic phase was qualitatively analyzed using a gas chromatograph equipped with an HP-5 column and FID detector. Naphthalene was used as an internal standard for quantitative analysis of liquid products. The conversion of the reactants and the product composition and yield were defined by GC and GC-MS.

The conversion of the products and the yield of the products were calculated based on the following formula. For the repeatability test experiment of the catalyst, the used catalyst was separated by suction filtration, washed with water and ethanol for more than three times, dried at 105°C for 12 h, and then reused. Due to the partial weight loss of the catalyst during the operation, fresh unused catalyst was added to compensate before the next reaction.

$$\text{Conv.}\,(\text{mol\%}) = \frac{\textit{moles of substrate changed into product}}{\textit{initial moles of the substrate}} \times 100\%, \quad (1)$$

$$\text{product yield}\,(\text{mol\%}) = \frac{\textit{moles of product}\,(A)}{\textit{moles of the reacted substrate}} \times 100\%. \quad (2)$$

Product Analysis

By gas chromatography (Shimadzu GC-2010 with FID detector and DB-5 column) and GC-MS (Agilent 7890A-5975C with DB-FFAP capillary column), the liquid products obtained from the HDO of phenolic compounds were analyzed. The oven temperature program was increased from 50°C (hold for 1 min) to 260°C (hold for 10 min) at a rate of 10°C/min.

RESULTS AND DISCUSSION

As one of the most representative phenolic monomers derived from lignin, guaiacol containing phenolic hydroxyl and methoxy groups was selected as the phenolic model. During the *in situ* hydrogenation of guaiacol, the target product was cyclohexanol. The initial experiments were carried out to investigate the catalyst activities towards the HDO of guaiacol used in isopropanol/water as hydrogen supply solvent. Herein, the hydrodeoxygenation of guaiacol was carried out over 15Ni/Nb_2O_5 and Ni-based bimetallic catalyst with Nb_2O_5 as support. The conversion of guaiacol and yield of the target product cyclohexanol with various nickel-based bimetallic catalysts is presented in **Supplementary Table S1**. It could be clearly found that both the conversion of guaiacol and molar yield of main product were greatly affected by the change of active metal composition in catalyst. These results indicated that not all selected bimetals could promote the deoxygenation reaction of guaiacol. It was clearly shown that cyclohexanol was the main product in all nickel-based bimetallic catalysts under the same conditions. The addition of the second metal had a significant effect on the conversion of guaiacol. Initially, in entry 1–5, diversified nickel-based bimetallic catalysts were used to investigate the HDO of guaiacol in water/isopropanol-mixed solvents under the reaction conditions of reaction temperature 220°C kept for 5 h. As the results shown, all 15Ni-15Mn/Nb_2O_5, 15Ni-15Zr/Nb_2O_5, and 15Ni-15Co/Nb_2O_5 exhibited good catalytic performance in the HDO of guaiacol, the conversion was 100, 100, and 61.9%, respectively, and the yields of the main product cyclohexanol were 76.2 mol%, 61 mol%, and 60 mol%, respectively. However, 15Ni-15Cu/Nb_2O_5 and 15Ni-15Mo/Nb_2O_5 showed lower catalyst activity with the guaiacol conversion being 29 and 19%, and almost no target product cyclohexanol was detected in the product. Thus, it could be found that the addition of Cu or Mo to Ni suppressed the hydrogenation of guaiacol (entry 2 and 4).

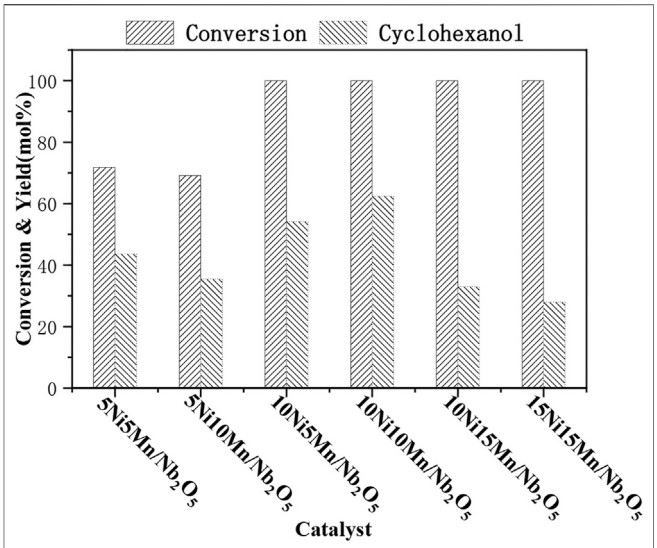

FIGURE 1 | Effect of ratio of metal loads on GUA conversion and the main product yield. Reaction conditions: 1 g GUA, 0.5 of Ni–Mn/Nb_2O_5, 1 MPa N_2, 200°C, 5 h, 5 g of isopropanol, and 20 g of water.

In addition, considering the influence of reaction conditions on the change of GUA selectivity to HDO, we tried to increase the temperature and reduce the relative content of the catalyst (reactant:catalyst = 2:1) to test the catalytic performance of these bimetallic catalysts (entry 6–10). The results shown that even though the 15Ni-15Mn/Nb_2O_5 catalyst still had good catalytic performance in the HDO of guaiacol, the yield of the main product cyclohexanol was significantly reduced, from 76.2 mol% (entry 3) to 53.32 mol% (entry 7). The same situation also appeared in 15Ni-15Zr/Nb_2O_5, and the yield of cyclohexanol decreased from 61 mol% (entry 1) to 24.4 mol% (entry 10). We speculated that this may be due to the relative reduction in the number of catalysts that caused the relative reduction of active sites, which reduced the hydrodeoxygenation efficiency of guaiacol. Besides, the increase in temperature would cause partial deactivation of the catalyst, which would reduce the catalytic performance of the catalyst.

TABLE 1 | Physicochemical structure properties of Nb_2O_5 and 10Ni-10Mn/Nb_2O_5 catalysts.

Catalyst	Surface area (m^2/g)	Micropore volume (m^3/g)	Total pore volume (cm^3/g)	Average pore size (nm)
Nb_2O_5	18.63	0.001	0.019	1.7
10Ni-10Mn/Nb_2O_5	42.77	0.003	0.056	1.9

Studies had pointed out that a short time of hydrogenation treatment led to repolymerization of the reactants in the hydrogenation process. In contrast, a longer reaction time can effectively promote the hydrogenation of the reactants (Li et al., 2014). Therefore, we tried to extend the reaction time to study the catalytic performance of the bimetallic catalyst (entry 11–15). The results showed that the conversion of guaiacol did not change much with the increase of reaction time. However, the yield of cyclohexanol increased slightly. Compared with 15Ni-15Cu/Nb_2O_5 and 15Ni-15Mo/Nb_2O_5 without catalytic activity, 15Ni-15Mn/Nb_2O_5, 15Ni-15Zr/Nb_2O_5, and 15Ni-15Co/Nb_2O_5 exhibited good catalytic performance in the HDO of guaiacol, and the yield of main product cyclohexanol was increased to 63.6 mol%, 57.8 mol%, and 61.2 mol%, respectively. In summary, the Ni–Mn/Nb_2O_5 catalyst exhibited better catalytic activity of guaiacol HDO. Therefore, we initially selected Ni–Mn/Nb_2O_5 as the research object.

It was reported that higher metal loading amount and better dispersity would lead to the improved catalytic activity (Zhou et al., 2017a). **Figure 1** showed a marked role played by the bimetal amount (5:5, 5:10, 10:5, 10:10, 10:15, and 15:15) of the catalyst's performance. It could be clearly seen from the results that the different proportions of the two metals could significantly affect the conversion process of guaiacol and the yield of the target product in the bimetallic catalyst. When the nickel loading 10% (10Ni-10Mn/Nb_2O_5), guaiacol could be completely converted, and the yield of cyclohexanol was highest (72 mol%).

When the nickel metal loading was 5 and 10%, the activity of the bimetallic catalyst increases with the increase of the loading, and the yield of the target product also increases from 35.5 mol% to 62.5 mol%. When the loading of nickel and manganese was both 10%, the conversion rate of guaiacol and the yield of cyclohexanol both reached the highest. At the same time, when the Ni metal loading was above 10%, the conversion rate of guaiacol could reach 100%, indicating that Ni metal contributed to the conversion of guaiacol. However, when the loading of Mn metal increased to 15% (10Ni-15Mn/Nb_2O_5 and 15Ni-15Mn/Nb_2O_5), the activity of the catalyst decreased, and the yield of the target product and the conversion rate of guaiacol was both decreased. We speculated that this may be due to (1) a part of the nickel metal phase may be covered by the manganese support; (2) when too much metal was loaded into Nb_2O_5, it would change the surface and pore distribution of the catalyst and then affect the hydrogenation activity of the catalyst. Finally, comprehensive research on the performance of guaiacol HDO with all different metal loading catalysts was carried out and selected 10Ni-10Mn/Nb_2O_5 catalyst as the research object. Following, we analyzed the specific structure of the catalyst to further analyze the reason.

Catalyst Characterization

Table 1 summarizes the textural properties of the Nb_2O_5 support and 10Ni-10Mn/Nb_2O_5. The specific surface area of Nb_2O_5 used in this work determined through the BET is 18.63 $m^2\ g^{-1}$. Compared with the Nb_2O_5 support, the Ni-based bimetallic catalyst 10Ni-10Mn/Nb_2O_5 exhibited a higher specific surface area of 42.77 $m^2\ g^{-1}$. The increasing of specific surface area may be due to the intrusion of metal playing a role in expanding the pores of the support. Moreover, the microspore volume and pore size of 10Ni-10Mn/Nb_2O_5 catalyst was better than the Nb_2O_5 support, which means the presence of metals could change structure and produce more pores of Nb_2O_5 during the preparation process. The 10Ni-10Mn/Nb_2O_5 catalyst displayed a better specific surface area and larger pore size, which may be beneficial to the hydrodeoxygenation of guaiacol.

The morphological features of the fresh catalyst were studied by scanning electron microscopy (SEM), while the chemical composition of the catalyst and the weight proportion of metal were proved by elemental spectra of the catalyst with energy dispersive X-ray analysis (EDS). The SEM images of the Nb_2O_5 support and 10Ni-10Mn/Nb_2O_5 catalyst are presented in **Figures 2A,B**. As shown above, the shape of the Nb_2O_5 support was relatively neat, whereas a small amount of particle aggregation and accumulation had occurred. Besides, the composition (wt% and at%) of the elements Ni and Mn in 10Ni-10Mn/Nb_2O_5 catalyst is summarized in the table near **Figure 2C**. EDS showed that the weight ratio of Ni to Mn on the catalyst surface of 10Ni-10Mn/Nb_2O_5 was 1.02:0.98, which was close to the theoretical loading ratio of Ni to Mn (1:1) for catalyst. It clearly shown that the Ni and Mn metal particles were well impregnated on the surface of the Nb_2O_5 support. It should be noted that the surface of the Nb_2O_5 support was smooth and flat in **Figure 2A**, and it was difficult to observe the metal particles on the surface of 10Ni-10Mn/Nb_2O_5 catalyst in **Figure 2B**. However, EDS chemical component analysis could confirm that the metal particles were finely dispersed in the whole support, which were agreed with the result of the XRD spectrum analysis of catalyst.

The TEM images are shown in **Figure 3**, the image of the Nb_2O_5 support is shown in **Figures 3A,B**, and the image of the 10Ni-10Mn/Nb_2O_5 is displayed in **Figures 3C,D**. As can be seen from **Figure 3A**, light and dark images appear on the surface of the support because the particle size of the support was too large for electrons to penetrate completely. There was no obvious particle agglomeration on the surface of Nb_2O_5 support in **Figure 3C**, which indicated that the Ni and Mn metal nanoparticles were well dispersed in the whole detection area. **Figure 3B** shows that the lattice fringe spacing of the Nb_2O_5 was 0.44 nm. The fringe distances (0.44 and 0.27 nm) shown in **Figure 3D** were consistent with the (001) and (111) planes of

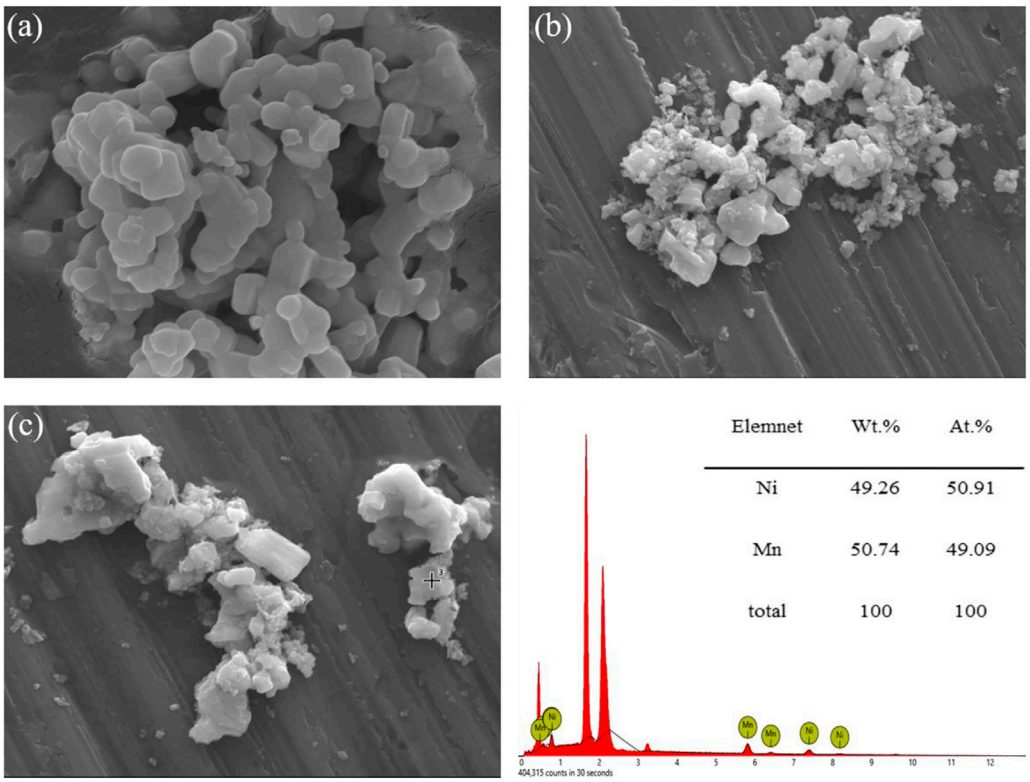

FIGURE 2 | SEM images of **(A)** 20000x Nb_2O_5, **(B)** 20000x and **(C)** 30000x 10Ni-10Mn/Nb_2O_5 samples.

Nb_2O_5 and metallic Ni, respectively. In addition, the microstructure information of MnO_2 was not observed in the TEM image, which may be due to the smaller particle size of MnO_2. Meanwhile, the particle size of metal was small and approximately 10 nm. This result was consistent with the analysis results of XRD and SEM.

Acidity was an important factor for the hydrodeoxygenation of phenolic compounds by affecting the dehydration process of the intermediate product cyclohexanol in the hydrogenated process. NH_3-TPD was an effective method to determine the acidity of catalyst through the difference of desorption temperature, in which the desorption temperature determines the acidity distribution. According to the difference of desorption temperature, acidity could be divided into the following three types: weak acid, medium strong acid, and strong acid. In order to conduct quantitative analysis on the acidity of the catalyst, standard NH_3-TPD analysis was carried out to measure the surface acidity of Nb_2O_5 and 10Ni-10Mn/Nb_2O_5 catalyst. The area of the desorption peak represented the strength of the catalyst acidity. In general, the desorption peak below 200°C corresponds to the weak acid position, the temperature range between 200 and 350°C relates to the moderate strong acid position, and the temperature above 350°C corresponds to the strong acid position. As a result, the results of NH_3-TPD are shown in **Supplementary Figure S1**. In Nb_2O_5 support, the desorption peak was observed at 366.5°C, which was ascribed to strong acid sites. In the 10Ni-10Mn/Nb_2O_5 catalyst, two desorption peaks appeared at 295.2 and 493.7°C corresponding to medium and strong acid sites, respectively. Moreover, the acid amounts of Nb_2O_5 and 10Ni-10Mn/Nb_2O_5 are summarized in **Table 2**, and the total acid sites of Nb_2O_5 and 10Ni-10Mn/Nb_2O_5 were measured to be 0.811 and 1.854 mmolNH_3/g-cat, respectively. It was worth noting that the introduction of metal species led to the increasing of acid strength and amount. In the process of preparing the catalyst, the metal was impregnated into the pores of the Nb_2O_5 support. As a result, the 10Ni-10Mn/Nb_2O_5 catalyst contained a larger specific surface area (this result was also consistent with the result of **Table 1**). Therefore, a large number of medium acid sites could be generated with 10Ni-10Mn/Nb_2O_5 having a relatively large specific surface area and good dispersibility, which could increase the interface between the metal and the support.

The X-ray powder diffraction (XRD) spectrum of the Nb_2O_5 support and metal-loading support catalyst 10Ni-10Mn/Nb_2O_5 is presented in **Figure 4**. Compared with Nb_2O_5, it could be clearly seen that 10Ni-10Mn/Nb_2O_5 had several new diffraction peaks (detected at 52.1° and 60.9°). The diffraction peaks located at 52.1° and 60.9° were ascribed to the reflections of metallic Ni. This showed that the reduction process during the preparation of the catalyst could convert the high valence state of Ni into metallic Ni. Meanwhile, the peaks of 35.2° and 38.8° belong to the reflections of MnO_2, which suggested that the high-valence Mn was not completely reduced to metallic Mn during the preparation of the catalyst. A sharp diffraction peak with higher peak intensity was

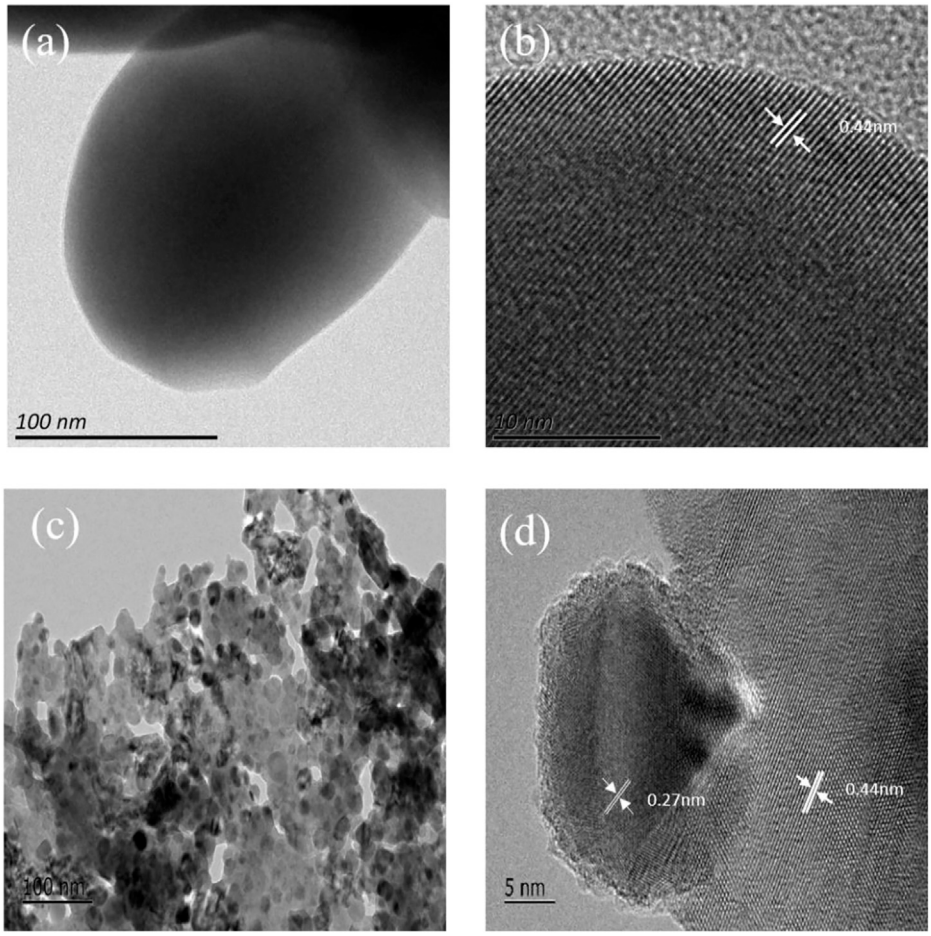

FIGURE 3 | TEM images of **(A,B)** Nb_2O_5 and **(C,D)** 10Ni-10Mn/Nb_2O_5 catalysts.

TABLE 2 | Acidity amount of the catalysts determined by NH_3-TPD.

Sample	Acidity (mmolg^{-1})		
	Total	Medium	Strong
Nb_2O_5	0.811	0	0.811
10Ni-10Mn/Nb_2O_5	1.854	0.823	1.031

observed at the position of 29.9°, which may be ascribed to the reflection of $NiMnO_3$ which need further confirmation by later characterization methods (Vivekanandan et al., 2020). In addition, no obvious diffraction peaks of metallic manganese were observed in the 10Ni-10Mn/Nb_2O_5 catalyst, which was attributed to the low crystallinity or small-size of metallic species. Besides, compared with the crystal diffraction intensity of the Nb_2O_5 support, the peak intensity of 10Ni-10Mn/Nb_2O_5 was relatively weakened, which may be attributed to the decrease of the crystallinity of the carrier as the addition of metal.

XPS analysis was used to confirm the chemical state of the metal elements on the catalyst surface. The spectrum of **Figure 5** recorded the respective valence states of these three elements Ni, Mn, and Nb. It should be clearly seen that there are five binding energy corresponding peaks in the XPS spectrum of Ni (**Figure 5**). Binding energies at 852.1 and 855.1 eV could be

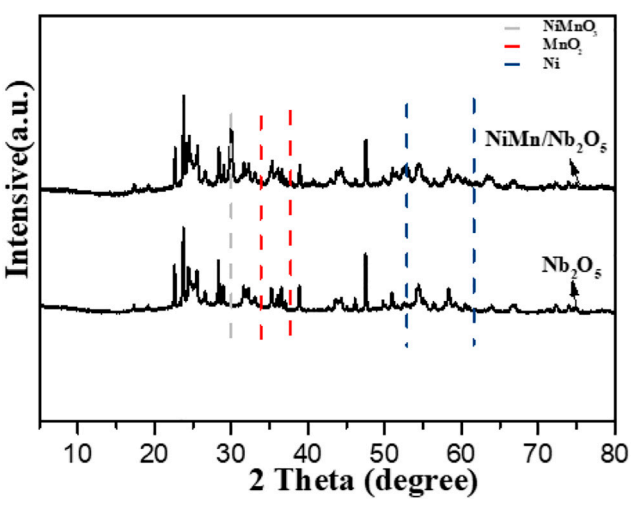

FIGURE 4 | X-ray diffraction pattern of catalysts.

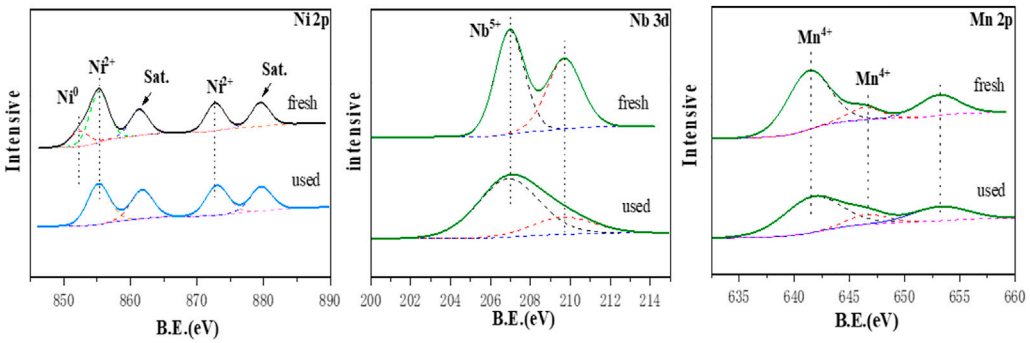

FIGURE 5 | XPS analysis of the reduced and used Ni–Mn/Nb_2O_5 catalysts.

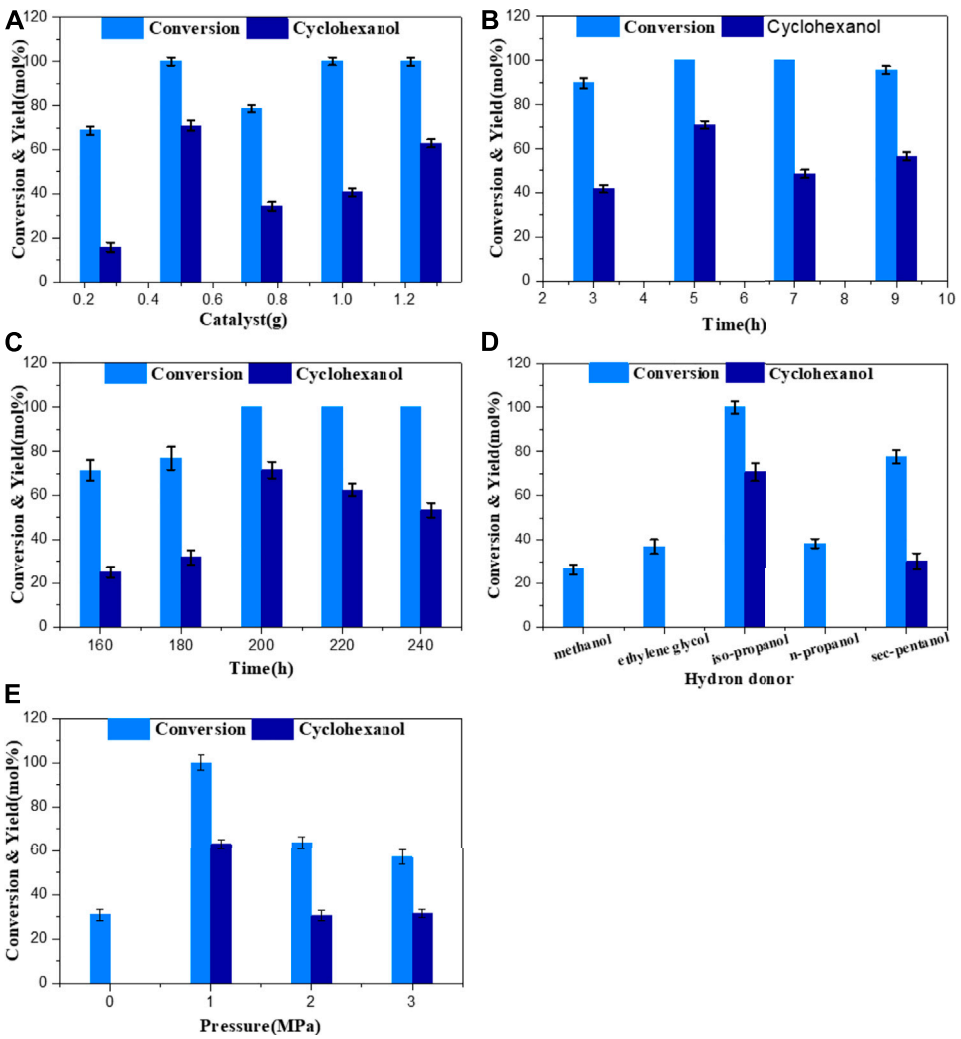

FIGURE 6 | Effect of **(A)** catalyst amount, **(B)** reaction time, **(C)** reaction temperature, **(D)** hydrogen sources, and **(E)** N_2 pressure on GUA conversion and main product yield. Reaction conditions: 1 g GUA and 0.5 g of 10Ni-10Mn/Nb_2O_5.

attributed to the main line of $Ni^0$and Ni^{2+}, suggesting the presence of both metallic Ni and NiO on the surface of Nb_2O_5. The binding energies at 873.1 eV attributed to Ni^{2+}. Simultaneously, two peaks at 861.4 and 879.7 eV corresponded to satellite peaks. And, the two different chemical states of Ni element detected were ascribed to the incomplete reduction of nickel oxide during the reduction process of the tube furnace. However, for the manganese element XPS spectrum, the main peaks at 641.3 and 646.3 eV were corresponding to the signal peaks of MnO_2 and its satellite peaks, and no related binding energy peaks of metallic manganese are observed, suggesting that MnO_2 was the present form of Mn element on the surface of the Nb_2O_5 support. The peaks centered at 206.9 eV, which was attributed to Nb in Nb_2O_5. In addition, no other Nb species appeared in spectrum indicating that the metal phase was only impregnated on the surface of the support and not interacted with the metal during the preparation of the catalyst. By comparing with the fresh catalyst in **Figure 5**, it could be found that there was no Ni^0 peak in the XPS spectrum of the spent catalyst, which indicates that the decrease in activity in the catalyst cycle experiment may be due to the absence of the metal active site Ni^0.

Catalytic Activity on the HDO of Guaiacol

To investigate the effect of catalyst usage on the HDO of guaiacol, the conversion of guaiacol and yield of target products cyclohexanol were studied in detail. The catalyst usage was varied from 0.25 to 1.25 g. **Figure 6A** depicts product evolution as a function of catalyst. The upsurge in the guaiacol conversion was consistent with the increase in catalyst usage from 0.25 to 1.25 g. The research shows that guaiacol was completely converted when the amount of catalyst exceeds 0.5 g and obtained the best cyclohexanol yield (70.8%).

Reaction time had a pronounced effect on the conversion of phenolic compounds and the distribution of products. As shown in **Figure 6B**, phenol conversion gradually increased when the reaction time increased from 3 to 5 h. When the reaction time was long enough (>5 h), guaiacol can be completely converted. But for the selectivity of the product, only the change in the yield of cyclohexanol could be clearly observed. When the reaction time was 5 h, the yield of cyclohexanol was the highest. With the further extension of the reaction time, the yield of cyclohexanol decreased that may be due to two reasons: (1) the product underwent a certain degree of polymerization, (2) the catalyst was covered by the polymer and led to partial deactivation. Therefore, using a moderated time 5 h was a prospect process for producing cyclohexanol from the hydrogenation of guaiacol.

The effect of reaction temperature on phenol conversion and product distribution was investigated. The hydrogenation reaction of guaiacol with 10Ni-10Mn/Nb_2O_5 catalyst was carried out at a range from 160°C to 240°C with the interval temperature of 20°C. As shown in **Figure 6C**, the conversion of guaiacol increased with the temperature increasing when the temperature was lower than 200°C. When the temperature reached 200°C, the complete conversion of guaiacol can be realized. However, further increase in temperature (such as 220°C and 240°C) would decrease the yield of the main product cyclohexanol and the possible reason was that the catalyst was partially deactivated at high temperature, or a relatively high temperature could cause the polymerization of products and could cover on the surface of the catalyst, thereby affecting the activity of the catalyst. Therefore, 200°C was the optimal reaction temperature for the conversion of guaiacol with the 10Ni-10Mn/Nb_2O_5 catalyst.

To examine the effects of different organic solvents on the HDO of guaiacol over 10Ni-10Mn/Nb_2O_5 in the solvent system composed of water and organic solvent, several organic solvents such as methanol (CH_3OH), ethylene glycol ($CH_2OH)_2$, isopropanol (C_3H_7OH), *n*-propanol (C_3H_7OH), and sec-pentanol ($C_5H_{11}OH$) were used for the HDO of guaiacol under the same conditions. The yield of cyclohexanol with the different organic solvents is shown in **Figure 6D**. It was worth noting that the catalytic activity and the product yield of 10Ni-10Mn/Nb_2O_5 for selective HDO of guaiacol varied greatly with a change in the different solvents. As the results shown that the HDO reaction of GUA using primary alcohols (ethylene glycol, methanol, and *n*-propanol) as hydrogen donors showed lower reactivity, the conversion of guaiacol was 37, 26.4, and 38.6%, respectively. And, the product of cyclohexanol was not detected. This was mainly because it was difficult to remove β-hydride from the primary alcohol during the reaction that limits its hydrogen supply performance, which was consistent with many previous reports (Kuwahara et al., 2014; Cai et al., 2017). For secondary alcohols, the yield of cyclohexanol was 70.8% in the reaction with isopropanol as the hydrogen donor, and the reaction with secondary amyl alcohol also provided 30.2 mol % of cyclohexanol yield. The system showed a good effect of *in situ* hydrogen production. Therefore, considering its reactivity and practicality, isopropanol was selected as the hydrogen donor for *in situ* hydrogenation to produce cyclohexanol in our system.

The reaction pressure also has a certain influence on the performance of the catalyst. Considering the influence of different reaction pressures on the HDO selectivity of guaiacol, the nitrogen pressure was optimized on the 10Ni-10Mn/Nb_2O_5 catalyst. **Figure 6E** showed the reaction product distribution and conversion of guaiacol. The conversion of guaiacol from 31 to 100% and cyclohexanol yield from 0 to 63% with the N_2 pressure from 0 to 1. However, higher pressure above 2 MPa decreased the guaiacol conversion and cyclohexanol yields. The phenomenon indicated that excessive pressure (above 2 MPa) had a negative effect on the hydrodeoxygenation of guaiacol. It may be desirable that too much pressure led to deactivation of the catalyst, thereby decreasing catalytic performance.

Catalyst Applicability of Different Phenolic Compounds

In order to investigate the applicability of the catalyst in *in situ* hydrogenation, other lignin-derived phenolic compounds were evaluated under 1 MPa N_2 at 200°C for 5 h. The 10Ni-10Mn/Nb_2O_5 catalyst was used for the *in situ* hydrogenation of m-cresol, phenol, ethyl-guaiacol, and 3-methoxyphenol (the common phenolic compounds of bio-oil) employing aqueous reforming reaction from water and isopropanol to produce hydrogen as a hydrogen donor. It could be seen from **Figure 7** that all phenolic compounds could be selectively converted into cyclohexanol compounds and phenolic compounds under the action of a catalyst, showing good hydrodeoxygenation performance. In the GC-MS images of

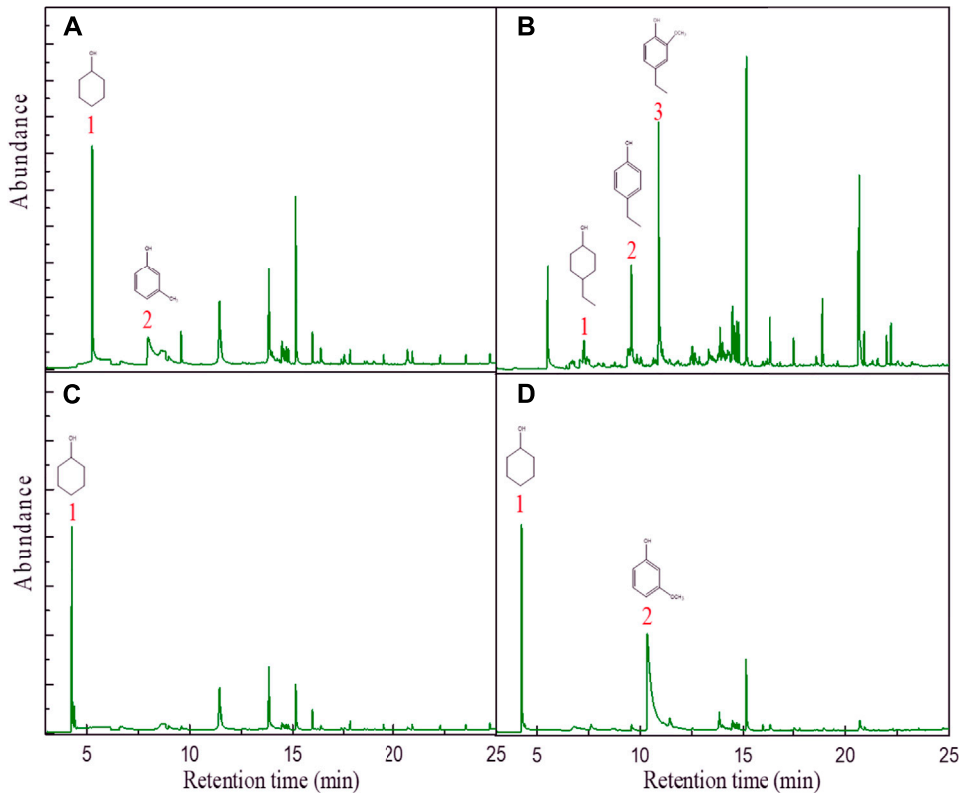

FIGURE 7 | The GC-MS data graph of **(A)** m-cresol, **(B)** ethyl-guaiacol, **(C)** phenol, and **(D)** 3-methoxyphenol. Reaction conditions: 0.5 g of 10Ni-10Mn/Nb_2O_5, 200°C, 5 h, and 1 MPa N_2.

m-cresol and 3-methoxyphenol, only cyclohexanol compounds were observed, and in the other compounds, in addition to cyclohexanol compounds, phenol was also observed. The results showed that, under the action of the catalyst, there was no complete hydrogenation, and the experimental conditions need to be further improved.

Possible Reaction Pathway of Guaiacol over Ni–Mn/Nb_2O_5 Catalyst

We deduced two possible pathways in guaiacol conversion based on the products detected by GC-MS in **Supplementary Figure S2**, with cyclohexanol as the main product. Under the optimal reaction conditions, we observed that the main byproducts of guaiacol hydrodeoxygenation on the catalyst are cyclohexanone and 1-methyl-1,2-cyclohexanediol, and only trace amount of phenol is produced.

As shown in **Supplementary Figure S2**, only trace amount of phenol is detected as phenol can be quickly hydrogenated to cyclohexanol, which was already confirmed. In addition, through the hydrodeoxygenation of phenol, the byproduct cyclohexanone was found. Therefore, we believe that there is a reaction path in which phenol is first hydrogenated to cyclohexanone and then further hydrogenated to cyclohexanol. In comparison with the amount of phenol, a relatively large amount of 1-methyl-1,2-cyclohexanediol is observed. According to reports in the literature (Zhou et al., 2017b) (Song et al., 2020), 1-methyl-1,2-cyclohexanediol can be used as an intermediate of cyclohexanol, so another reaction pathway to produce cyclohexanol is obtained. The proposed reaction pathway of guaiacol is demonstrated in **Figure 8**.

Applicability of the Recycled Catalyst

To examine the reusability of 10Ni-10Mn/Nb_2O_5 in the *in situ* hydrogenation of guaiacol, the stability of the catalyst was important for its practical usage. Therefore, the 10Ni-10Mn/Nb_2O_5 catalyst was subjected to stability testing by recycling the same catalyst for four consecutive cycles for guaiacol HDO reaction. At the end of each cycle, the catalyst was recovered from the reactor by filtration and dried overnight at 60°C. Due to the loss of part of the catalyst in the process of recovering the catalyst, this catalyst loss was compensated by adding a fresh catalyst. The results of stability test are shown in **Figure 9**. The catalyst was reused three times, and the conversion of guaiacol remained at 100%. However, the yield of the main product cyclohexanol gradually decreased, and the yield of cyclohexanol was reduced from 59.2 to 44.5% after repeated use. It may be because in the process of reuse, some metal sites on the catalyst lose their activity in the reaction, which leads to a decrease in the product yield. In addition, a regeneration experiment was carried out on the catalyst. After

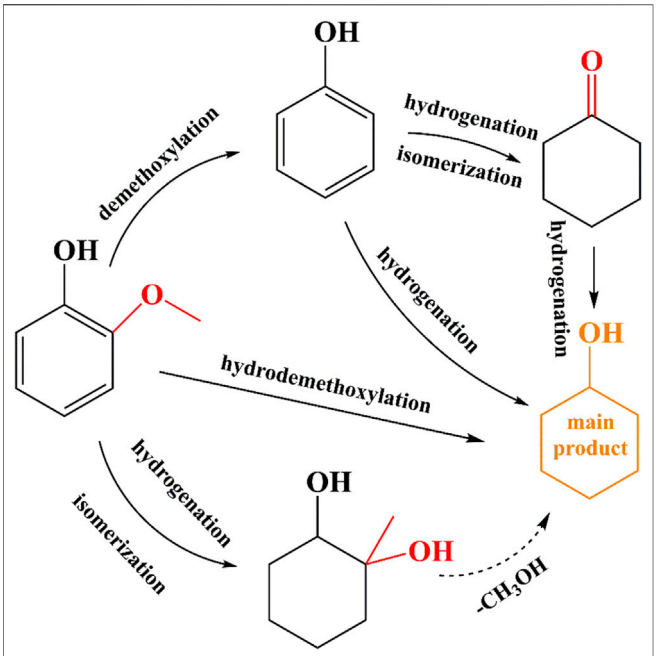

FIGURE 8 | Possible reaction pathway for the conversion of guaiacol over Ni–Mn/Nb_2O_5.

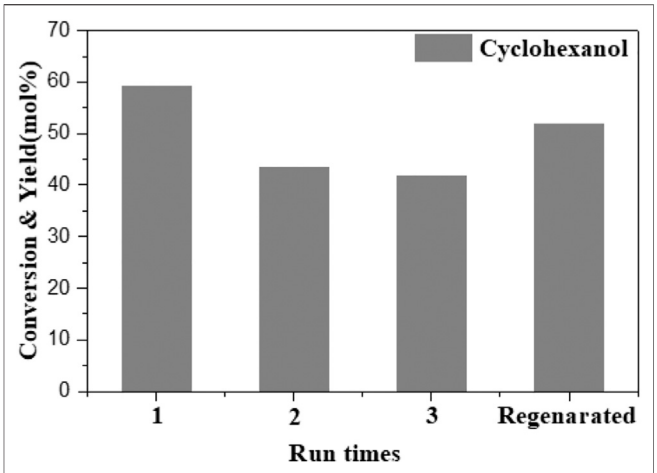

FIGURE 9 | The reusability test of the 10Ni-10Mn/Nb_2O_5 catalyst.

calcination in a muffle furnace at 500°C for 3 h in air and reduction with hydrogen in a tube furnace at 500°C for 3 h, the catalyst activity almost recovered to its original activity. It could be seen from the results that the stability of the catalyst is relatively good.

CONCLUSION

In this work, the *in situ* hydrogenation of guaiacol (a typical model compound of bio-oil), using isopropanol as the hydrogen donor, was conducted to measure the catalytic performance of 10Ni-10Mn/Nb_2O_5. The result showed that guaiacol can be efficiently converted into cyclohexanol under mild conditions (200°C, 1 MPa N_2), and the yield of target product cyclohexanol was up to 71.8%, which suggested the catalyst has remarkable hydrogenation performance. The results of hydrogenation of guaiacol with different hydrogen donors indicated isopropanol as the hydrogen donor had better activity. The catalyst had the characteristics of high metal dispersibility and large pore size from SEM, TEM, and BET, which may be helpful for the *in situ* hydrogen production of the hydrogen supply solvent and the hydrogenation process of phenolic chemicals. In addition, the stability of the catalyst was measured by the cyclic properties of guaiacol, and the yield of the target product cyclohexanol slightly decreases with each cycle. It suggested that 10Ni-10Mn/Nb_2O_5 may be partially deactivated during the reaction which the reason will be further proven. Hydroreforming reaction which avoids the need for molecular hydrogen to carry out hydrogenation reactions has some shortcomings and provides an effective reaction way for catalytic hydrogenation of different phenolic compounds.

DATA AVAILABILITY STATEMENT

The original contributions presented in the study are included in the article/**Supplementary Material**. Further inquiries can be directed to the corresponding authors.

AUTHOR CONTRIBUTIONS

LT contributed to data curation, conceptualized the study, and prepared the original draft. BC investigated and validated the study. RZ was responsible for methodology and provided software. JF visualized and supervised the study. HP reviewed and edited the article.

ACKNOWLEDGMENTS

The authors gratefully acknowledge the financial support provided by the Natural Science Fund for Colleges and Universities in Jiangsu Province (20KJB220010) for this investigation. The authors also thank the Research Grant of Jiangsu Province Biomass Energy and Materials Laboratory (JSBEM201903) for this investigation.

SUPPLEMENTARY MATERIAL

The Supplementary Material for this article can be found online at: https://www.frontiersin.org/articles/10.3389/fenrg.2021.746109/full#supplementary-material

REFERENCES

Bjelić, A., Grilc, M., Huš, M., and Likozar, B. (2019). Hydrogenation and Hydrodeoxygenation of Aromatic Lignin Monomers over Cu/C, Ni/C, Pd/C, Pt/C, Rh/C and Ru/C Catalysts: Mechanisms, Reaction Micro-kinetic Modelling and Quantitative Structure-Activity Relationships. *Chem. Eng. J.* 359, 305–320. doi:10.1016/j.cej.2018.11.107

Cai, B., Zhou, X.-C., Miao, Y.-C., Luo, J.-Y., Pan, H., and Huang, Y.-B. (2017). Enhanced Catalytic Transfer Hydrogenation of Ethyl Levulinate to γ-Valerolactone over a Robust Cu-Ni Bimetallic Catalyst. *ACS Sustain. Chem. Eng.* 5, 1322–1331. doi:10.1021/acssuschemeng.6b01677

Chen, L., Xin, J., Ni, L., Dong, H., Yan, D., Lu, X., et al. (2016). Conversion of Lignin Model Compounds under Mild Conditions in Pseudo-homogeneous Systems. *Green. Chem.* 18, 2341–2352. doi:10.1039/c5gc03121d

Chen, M.-Y., Huang, Y.-B., Pang, H., Liu, X.-X., and Fu, Y. (2015). Hydrodeoxygenation of Lignin-Derived Phenols into Alkanes over Carbon Nanotube Supported Ru Catalysts in Biphasic Systems. *Green. Chem.* 17, 1710–1717. doi:10.1039/c4gc01992j

Feng, J., Yang, Z., Hse, C.-y., Su, Q., Wang, K., Jiang, J., et al. (2017). *In Situ* catalytic Hydrogenation of Model Compounds and Biomass-Derived Phenolic Compounds for Bio-Oil Upgrading. *Renew. Energ.* 105, 140–148. doi:10.1016/j.renene.2016.12.054

Ferentz, M., Landau, M. V., Vidruk, R., and Herskowitz, M. (2015). Fixed-bed Catalytic Wet Peroxide Oxidation of Phenol with Titania and Au/titania Catalysts in Dark. *Catal. Today* 241, 63–72. doi:10.1016/j.cattod.2014.05.013

Funkenbusch, L. T., Mullins, M. E., Salam, M. A., Creaser, D., and Olsson, L. (2019). Catalytic Hydrotreatment of Pyrolysis Oil Phenolic Compounds over Pt/Al2O3 and Pd/C. *Fuel* 243, 441–448. doi:10.1016/j.fuel.2019.01.139

Han, G.-H., Lee, M. W., Park, S., Kim, H. J., Ahn, J.-P., Seo, M.-g., et al. (2019). Revealing the Factors Determining the Selectivity of Guaiacol HDO Reaction Pathways Using ZrP-Supported Co and Ni Catalysts. *J. Catal.* 377, 343–357. doi:10.1016/j.jcat.2019.07.034

He, Z., Hu, M., and Wang, X. (2018). Highly Effective Hydrodeoxygenation of Guaiacol on Pt/TiO2: Promoter Effects. *Catal. Today* 302, 136–145. doi:10.1016/j.cattod.2017.02.034

Jin, S., Guan, W., Tsang, C.-W., Yan, D. Y. S., Chan, C.-Y., and Liang, C. (2017). Enhanced Hydroconversion of Lignin-Derived Oxygen-Containing Compounds over Bulk Nickel Catalysts Though Nb2O5 Modification. *Catal. Lett.* 147, 2215–2224. doi:10.1007/s10562-017-2085-6

Kon, K., Onodera, W., Takakusagi, S., and Shimizu, K.-i. (2014). Hydrodeoxygenation of Fatty Acids and Triglycerides by Pt-Loaded Nb2O5 Catalysts. *Catal. Sci. Technol.* 4, 3705–3712. doi:10.1039/c4cy00757c

Kuwahara, Y., Kaburagi, W., and Fujitani, T. (2014). Catalytic Transfer Hydrogenation of Levulinate Esters to γ-valerolactone over Supported Ruthenium Hydroxide Catalysts. *RSC Adv.* 4, 45848–45855. doi:10.1039/c4ra08074b

Li, W., Wang, H., Wu, X., Betancourt, L. E., Tu, C., Liao, M., et al. (2020). Ni/hierarchical ZSM-5 Zeolites as Promising Systems for Phenolic Bio-Oil Upgrading: Guaiacol Hydrodeoxygenation. *Fuel* 274, 117859. doi:10.1016/j.fuel.2020.117859

Li, X., Gunawan, R., Wang, Y., Chaiwat, W., Hu, X., Gholizadeh, M., et al. (2014). Upgrading of Bio-Oil into Advanced Biofuels and Chemicals. Part III. Changes in Aromatic Structure and Coke Forming Propensity during the Catalytic Hydrotreatment of a Fast Pyrolysis Bio-Oil with Pd/C Catalyst. *Fuel* 116, 642–649. doi:10.1016/j.fuel.2013.08.046

Li, Y., Yang, X., Zhu, L., Zhang, H., and Chen, B. (2015). Hydrodeoxygenation of Phenol as a Bio-Oil Model Compound over Intimate Contact noble Metal-Ni2P/SiO2 Catalysts. *RSC Adv.* 5, 80388–80396. doi:10.1039/c5ra11203f

Liu, K., Yan, P., Jiang, H., Xia, Z., Xu, Z., Bai, S., et al. (2019). Silver Initiated Hydrogen Spillover on Anatase TiO2 Creates Active Sites for Selective Hydrodeoxygenation of Guaiacol. *J. Catal.* 369, 396–404. doi:10.1016/j.jcat.2018.11.033

Lu, M., Sun, Y., Zhang, P., Zhu, J., Li, M., Shan, Y., et al. (2019). Hydrodeoxygenation of Guaiacol Catalyzed by High-Loading Ni Catalysts Supported on SiO2-TiO2 Binary Oxides. *Ind. Eng. Chem. Res.* 58, 1513–1524. doi:10.1021/acs.iecr.8b04517

Ma, D., Lu, S., Liu, X., Guo, Y., and Wang, Y. (2019). Depolymerization and Hydrodeoxygenation of Lignin to Aromatic Hydrocarbons with a Ru Catalyst on a Variety of Nb-Based Supports. *Chin. J. Catal.* 40, 609–617. doi:10.1016/s1872-2067(19)63317-6

Montañez Valencia, M. K., Padró, C. L., and Sad, M. E. (2020). Gas Phase Acylation of Guaiacol with Acetic Acid on Acid Catalysts. *Appl. Catal. B Environ.* 278, 119317. doi:10.1016/j.apcatb.2020.119317

Mortensen, P. M., Grunwaldt, J.-D., Jensen, P. A., and Jensen, A. D. (2016). Influence on Nickel Particle Size on the Hydrodeoxygenation of Phenol over Ni/SiO 2. *Catal. Today* 259, 277–284. doi:10.1016/j.cattod.2015.08.022

Mushtaq, F., Abdullah, T. A. T., Mat, R., and Ani, F. N. (2015). Optimization and Characterization of Bio-Oil Produced by Microwave Assisted Pyrolysis of Oil palm Shell Waste Biomass with Microwave Absorber. *Bioresour. Techn.* 190, 442–450. doi:10.1016/j.biortech.2015.02.055

Newman, C., Zhou, X., Goundie, B., Ghampson, I. T., Pollock, R. A., Ross, Z., et al. (2014). Effects of Support Identity and Metal Dispersion in Supported Ruthenium Hydrodeoxygenation Catalysts. *Appl. Catal. A: Gen.* 477, 64–74. doi:10.1016/j.apcata.2014.02.030

Ohta, H., Feng, B., Kobayashi, H., Hara, K., and Fukuoka, A. (2014). Selective Hydrodeoxygenation of Lignin-Related 4-propylphenol into N-Propylbenzene in Water by Pt-Re/ZrO2 Catalysts. *Catal. Today* 234, 139–144. doi:10.1016/j.cattod.2014.01.022

Qin, L., Yi, H., Zeng, G., Lai, C., Huang, D., Xu, P., et al. (2019). Hierarchical Porous Carbon Material Restricted Au Catalyst for Highly Catalytic Reduction of Nitroaromatics. *J. Hazard. Mater.* 380, 120864. doi:10.1016/j.jhazmat.2019.120864

Qiu, S., Xu, Y., Weng, Y., Ma, L., and Wang, T. (2016). Efficient Hydrogenolysis of Guaiacol over Highly Dispersed Ni/MCM-41 Catalyst Combined with HZSM-5. *Catalysts* 6, 9–13. doi:10.3390/catal6090134

Ragauskas, A. J., Beckham, G. T., Biddy, M. J., Chandra, R., Chen, F., Davis, M. F., et al. (2014). Lignin Valorization: Improving Lignin Processing in the Biorefinery. *Science* 344, 1246843. doi:10.1126/science.1246843

Rahzani, B., Saidi, M., Rahimpour, H. R., Gates, B. C., and Rahimpour, M. R. (2017). Experimental Investigation of Upgrading of Lignin-Derived Bio-Oil Component Anisole Catalyzed by Carbon Nanotube-Supported Molybdenum. *RSC Adv.* 7, 10545–10556. doi:10.1039/c6ra26121c

Reddy Kannapu, H. P., Mullen, C. A., Elkasabi, Y., and Boateng, A. A. (2015). Catalytic Transfer Hydrogenation for Stabilization of Bio-Oil Oxygenates: Reduction of P-Cresol and Furfural over Bimetallic Ni-Cu Catalysts Using Isopropanol. *Fuel Process. Techn.* 137, 220–228. doi:10.1016/j.fuproc.2015.04.023

Resende, K. A., Braga, A. H., Noronha, F. B., and Hori, C. E. (2019). Hydrodeoxygenation of Phenol over Ni/Ce1-xNbxO2 Catalysts. *Appl. Catal. B Environ.* 245, 100–113. doi:10.1016/j.apcatb.2018.12.040

Saidi, M., Samimi, F., Karimipourfard, D., Nimmanwudipong, T., Gates, B. C., and Rahimpour, M. R. (2014). Upgrading of Lignin-Derived Bio-Oils by Catalytic Hydrodeoxygenation. *Energy Environ. Sci.* 7, 103–129. doi:10.1039/c3ee43081b

Shafaghat, H., Tsang, Y. F., Jeon, J.-K., Kim, J. M., Kim, Y., Kim, S., et al. (2020). *In-situ* Hydrogenation of Bio-Oil/bio-Oil Phenolic Compounds with Secondary Alcohols over a Synthesized Mesoporous Ni/CeO2 Catalyst. *Chem. Eng. J.* 382, 122912. doi:10.1016/j.cej.2019.122912

Shu, R., Lin, B., Zhang, J., Wang, C., Yang, Z., and Chen, Y. (2019). Efficient Catalytic Hydrodeoxygenation of Phenolic Compounds and Bio-Oil over Highly Dispersed Ru/TiO2. *Fuel Process. Techn.* 184, 12–18. doi:10.1016/j.fuproc.2018.11.004

Song, W., He, Y., Lai, S., Lai, W., Yi, X., Yang, W., et al. (2020). Selective Hydrodeoxygenation of Lignin Phenols to Alcohols in the Aqueous Phase over a Hierarchical Nb2O5-Supported Ni Catalyst. *Green. Chem.* 22, 1662–1670. doi:10.1039/c9gc03842f

Vivekanandan, A. K., Subash, V., Chen, S.-m., and Chen, S.-H. (2020). Sonochemical Synthesis of Nickel-Manganous Oxide Nanocrumbs Decorated Partially Reduced Graphene Oxide for Efficient Electrochemical Reduction of Metronidazole. *Ultrason. Sonochem.* 68, 105176. doi:10.1016/j.ultsonch.2020.105176

Wang, H., Zhao, F., Fujita, S.-i., and Arai, M. (2008). Hydrogenation of Phenol in scCO2 over Carbon Nanofiber Supported Rh Catalyst. *Catal. Commun.* 9, 362–368. doi:10.1016/j.catcom.2007.07.002

Xu, Y., Li, Y., Wang, C., Wang, C., Ma, L., Wang, T., et al. (2017). *In-situ* Hydrogenation of Model Compounds and Raw Bio-Oil over Ni/CMK-3

Catalyst. *Fuel Process. Techn.* 161, 226–231. doi:10.1016/j.fuproc.2016.08.018

Xu, Y., Long, J., Liu, Q., Li, Y., Wang, C., Zhang, Q., et al. (2015). *In Situ* hydrogenation of Model Compounds and Raw Bio-Oil over Raney Ni Catalyst. *Energ. Convers. Manag.* 89, 188–196. doi:10.1016/j.enconman.2014.09.017

Yang, F., Libretto, N. J., Komarneni, M. R., Zhou, W., Miller, J. T., Zhu, X., et al. (2019). Enhancement of M-Cresol Hydrodeoxygenation Selectivity on Ni Catalysts by Surface Decoration of MoOx Species. *ACS Catal.* 9, 7791–7800. doi:10.1021/acscatal.9b01285

Zhang, X., Tang, W., Zhang, Q., Wang, T., and Ma, L. (2018). Hydrodeoxygenation of Lignin-Derived Phenoic Compounds to Hydrocarbon Fuel over Supported Ni-Based Catalysts. *Appl. Energ.* 227, 73–79. doi:10.1016/j.apenergy.2017.08.078

Zhao, H. Y., Li, D., Bui, P., and Oyama, S. T. (2011). Hydrodeoxygenation of Guaiacol as Model Compound for Pyrolysis Oil on Transition Metal Phosphide Hydroprocessing Catalysts. *Appl. Catal. A: Gen.* 391, 305–310. doi:10.1016/j.apcata.2010.07.039

Zhou, M., Ye, J., Liu, P., Xu, J., and Jiang, J. (2017). Water-Assisted Selective Hydrodeoxygenation of Guaiacol to Cyclohexanol over Supported Ni and Co Bimetallic Catalysts. *ACS Sustain. Chem. Eng.* 5, 8824–8835. doi:10.1021/acssuschemeng.7b01615

Zhou, M., Ye, J., Liu, P., Xu, J., and Jiang, J. (2017). Water-Assisted Selective Hydrodeoxygenation of Guaiacol to Cyclohexanol over Supported Ni and Co Bimetallic Catalysts. *ACS Sustain. Chem. Eng.* 5, 8824–8835. doi:10.1021/acssuschemeng.7b01615

Zhu, X., Lobban, L. L., Mallinson, R. G., and Resasco, D. E. (2011). Bifunctional Transalkylation and Hydrodeoxygenation of Anisole over a Pt/HBeta Catalyst. *J. Catal.* 281, 21–29. doi:10.1016/j.jcat.2011.03.030

Conflict of Interest: The authors declare that the research was conducted in the absence of any commercial or financial relationships that could be construed as a potential conflict of interest.

Publisher's Note: All claims expressed in this article are solely those of the authors and do not necessarily represent those of their affiliated organizations, or those of the publisher, the editors, and the reviewers. Any product that may be evaluated in this article, or claim that may be made by its manufacturer, is not guaranteed or endorsed by the publisher.

frontiers in Energy Research

ORIGINAL RESEARCH
published: 15 October 2021
doi: 10.3389/fenrg.2021.756285

Influence of the Lignin Extraction Methods on the Content of Tricin in Grass Lignins

Minting Xie[1], Zhendong Chen[1], Yue Xia[1], Minsheng Lin[1], Jiaqi Li[1], Wu Lan[1], Liming Zhang[2] and Fengxia Yue[1,2]**

[1]State Key Laboratory of Pulp and Paper Engineering, School of Light Industry and Engineering, South China University of Technology, Guangzhou, China, [2]Guangxi Key Laboratory of Clean Pulp and Papermaking and Pollution Control, College of Light Industry and Food Engineering, Guangxi University, Nanning, China

Tricin as a monomer of grass lignin with unique biological properties is beneficial to human health with the potential for various applications. The abundant grass lignin could be an alternative source for tricin if an effective separation method is available. In this study, we used different lignin preparations, including alkali lignin (AL), mild acidolysis lignin (MAL), cellulase enzymatic lignin (CEL), γ-valerolactone lignin (GVL), and organosolv lignin (OL), to investigate the effect of different fractionation methods on the tricin content of the wheat straw lignin. The tricin signal of different lignins can be clearly identified by 2D heteronuclear singular quantum correlation (HSQC) spectra. GVL showed the highest tricin level among these lignin samples as the tricin content of GVL was accounted to be 8.6% by integrals. The tricin content was carefully determined using thioacidolysis combined with high-performance liquid chromatography-mass spectrometric (HPLC-MS), and the quantitative results of tricin by HPLC-MS were basically consistent with that of 2D HSQC integrals. Both methods have proved that the tricin contents of lignins isolated under acid conditions were significantly higher than that of AL. In addition, the determination of the sun protection factors (SPF) of lignin-based sunscreen and antioxidant activity of lignin preparations indicated that reserving more tricin was beneficial to the UV resistance of lignin samples. Therefore, this study not only provides new insights for the extraction methods of lignin with high tricin content but also is beneficial to the future study on the application of tricin and tricin-lignin.

Keywords: tricin, lignin, antioxidation, SPF, HSQC, HPLC-MS

OPEN ACCESS

Edited by:
Xiaojun Shen,
Dalian Institute of Chemical Physics (CAS), China

Reviewed by:
Caoxing Huang,
Nanjing Forestry University, China
Chenhuan Lai,
Nanjing Forestry University, China

****Correspondence:***
Wu Lan
lanwu@scut.edu.cn
Fengxia Yue
yuefx@scut.edu.cn

Specialty section:
This article was submitted to Bioenergy and Biofuels, a section of the journal Frontiers in Energy Research

Received: *10 August 2021*
Accepted: *06 September 2021*
Published: *15 October 2021*

Citation:
Xie M, Chen Z, Xia Y, Lin M, Li J, Lan W, Zhang L and Yue F (2021) Influence of the Lignin Extraction Methods on the Content of Tricin in Grass Lignins. Front. Energy Res. 9:756285. doi: 10.3389/fenrg.2021.756285

INTRODUCTION

Lignin, a natural and renewable aromatic polymer with complex structures, is primarily distributed in the secondary plant cell walls. The content of lignin in timber plants is 20–40%, whereas it is generally lower in Gramineae, about 15–25%. Conventional lignin is composed of guaiacyl (G), syringyl (S), and *p*-hydroxyphenyl (H) units, which are, respectively, derived from coniferyl alcohol, sinapyl alcohol, and *p*-coumaryl alcohol and differed by the methoxylation degree on the aromatic ring (Boerjan et al., 2003; Ralph, 2009). Recent studies revealed that, in addition to these three monolignols, lignin also contained many other unconventional monomers, such as tricin, piceatannol, feruloyltyramine, and caffeyl alcohol (Chen et al., 2021; del Río et al., 2020; Vanholme et al., 2019).

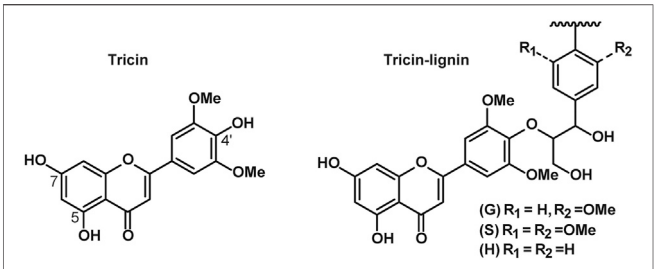

FIGURE 1 | Chemical structures of tricin and linkages between tricin and other lignin units.

Among these newly discovered monomers, tricin is one of the most interesting ones because it is the first phenolic from outside the monolignol biosynthetic pathway which is found to be integrated into the lignin polymer (Lan et al., 2015). Tricin has long been known as a secondary metabolite in monocots, which is extractable by organic solvents. In recent years, it was first disclosed to be present in the lignin preparation from wheat straw (del Rio et al., 2012) and was later authenticated as a monomer in grass lignin (Lan et al., 2015). Structural characterization of biomimetic radical coupling reaction proved that tricin linked with other monolignols exclusively through β–O–4 interlinkage and therefore only occurred at the starting point, i.e., serving as a nucleation site, of lignin chain. Chemical structures of tricin and linkages between tricin and other lignin units are provided by **Figure 1** (Lan et al., 2016). Compared with other compounds with similar structure, the potential application of tricin is distinctly higher in the aspect of agricultural, nutraceutical, and medicinal activities (Zhou and Ibrahim, 2009), considering its biological activities including antioxidant, antiviral, anticancer, antiaging, and hepatoprotective activities (Ogo et al., 2013; Oyama et al., 2009; Solyanik et al., 2021). Structure-activity relationship study demonstrates that the phenolic hydroxyl, ketone, and carboxyl group display a strong absorption of ultraviolet (Cao et al., 1997; Heim et al., 2002). As for tricin, the long resonance structure formed by two aromatic rings and the C=C and carbonyl in between, as well as the intramolecular hydrogen bonds, further enhances the UV absorption ability, antioxidation, and antibacterial properties, making it a natural UV protector and antioxidant with great potential for use in daily protective products (del Río et al., 2020; Lan et al., 2016; Oyama et al., 2009). On the other hand, natural tricin is featured by premium pricing because of the low content in the extractives from plants and difficulty in purification (Li et al., 2016). Therefore, the abundant grass lignin could be an alternative source for tricin if an effective separation method is available.

At present, certain straws of crops are underutilized as many agricultural residues are treated as wastes. Some of them were even burned and therefore cause serious pollution in the rural area (Kim and Dale, 2004; Sarkar et al., 2012). Therefore, more efforts should be made to take full advantage of the agricultural residues considering environmental and economic aspects. Wheat is one of the most important cereal crops. The annual production of wheat is about 134 million tons and resulting in close to 175 million tons of wheat straw per year calculated by the Food and Agriculture Organization (FAO) standards in 2020 in China according to data provided by the Ministry of Agriculture of the PRC. The previous study showed that wheat straw contains the highest amount of tricin compared with other plants which could be a promising source for natural tricin (Lan et al., 2016).

Although tricin has been confirmed in the lignin from Gramineae plants and the amount has been measured by thioacidolysis followed by HPLC-MS (Lan et al., 2016), its stability under different conditions is still unclear. For example, tricin would be depleted with increasing acid concentration or pretreatment temperature after reaching a critical condition, whereas most could be preserved under mild diluted acid treatment conditions (Jensen et al., 2017; Lin W. et al., 2021). At a low-temperature alkali pretreatment (70°C, 18 h), the content of tricin in lignin isolated from wheat straw was much lower than that in the untreated samples (Zikeli et al., 2016). On the contrary, tricin can be retained well under some mild conditions such as mild acid γ-valerolactone lignin (GVL) pretreatment (Luterbacher et al., 2014). Furthermore, tricin in the waste liquor of conventional pulping mostly disappeared (Jiang et al., 2018; Lauwaert et al., 2019). To take the best advantage of tricin for the subsequent application, it is important to develop a lignin fractionation method that can mostly reserve tricin in isolated lignin.

In this study, we explore the effect of different fractionation methods on the tricin content of the lignin components, including alkali lignin (AL) (from both ball-milled and nonball-milled samples), mild acidolysis lignin (MAL), cellulase enzymatic lignin (CEL), GVL, and organosolv lignin (OL). 2D heteronuclear singular quantum correlation (HSQC) spectra were used to characterize the lignin structure and HPLC-MS was applied to quantify tricin in the lignin preparations. The sun protection factors (SPF) of lignin-based sunscreen and antioxidation property of lignin preparations were also determined to evaluate the correlation between tricin content and the abilities of anti-UV radiation and antioxidation.

EXPERIMENTAL

Materials

The following reagents were used: L-cysteine (99%), NaOH (97%), 1,4-dioxane (98%), cellulase (hydrolyzing activity is >1000 U/g), viscozyme L (a cellulase with enzymatic activity value of 100 FBG/g), γ-valerolactone (98%), methanol (≥99.9%, HPLC level), and acetonitrile (≥99.9%, HPLC level). All chemicals used in this study were purchased from Macklin except the cellulase was from Sigma and viscozyme L from Novozymes.

The wheat straw collected in Jiaxiang county, Shandong province, was physically cut, crushed, and sieved to obtain the 40–60 mesh fraction. The crushed wheat straw was dewaxed in 80% ethanol (v/v) at 80°C for 8 h. This step was repeated twice and then followed by extraction in dichloromethane at 40°C for 8 h (Li et al., 2019). The final dewaxed sample was air-dried in the fume hood and then stored in a desiccator for later use.

Measurement of Lignin Content

The lignin content of wheat straw was determined by the L-cysteine assisted dissolution method as reported previously (Lu et al., 2021). A 0.1 g/mL L-cysteine stock solution was prepared by dissolving 1.0 g of L-cysteine in 10 ml 72% H_2SO_4. 0.3 g of the absolutely dried lignocellulosic sample was added to 10 ml of L-cysteine solution at 60°C in a sand bath with continuous stirring for 30 min to dissolve lignin. 105 ml of deionized water was subsequently added to the reaction to dilute the solution. The content of lignin was calculated using Bill's **formula (1)**:

$$SL(\%) = \frac{Abs' \times V_f \times \delta}{\varepsilon \times m_s \times P} \times 100\% \quad (1)$$

where Abs' is the UV absorption values at 283 nm; V_f (ml) is the volume after dilution, V_f = 115 ml; ε (L/gcm) is the UV absorptivity, ε = 15.0; m_s (mg) is the mass of absolutely dried lignin; p (cm) is the optical path length, p = 1 cm; δ is the absolute dryness, δ = 1.

The lignin content of wheat straw was 16.46% ± 0.31 according to our determination.

Lignin Extraction

Alkali lignin (AL)

5 g of the dewaxed wheat straw was mixed uniformly with 1 M NaOH solution in a solid-to-liquid ratio of 1:10 (g/ml) at 30°C. After 4 h, the liquor was collected by filtration, and the pH was adjusted to 3.0 by 1.0 M HCl solution. The neutralized liquor was placed in a fridge at 4°C for more than 12 h to let the lignin precipitate. The AL was separated by centrifugation and then freeze-dried to give a light brown powder. A control experiment was performed with ball-milled at 10 h wheat straw sample under the same reaction condition at 30°C.

Mild acidolysis lignin (MAL)

20 g of dewaxed wheat straw was added in a 1,4-dioxane/H_2O (9: 1, v/v) solution with 0.2 M HCl at a solid-to-liquid ratio of 1:12 (g/ml). The reaction mixture was refluxed in a 120°C sand bath with magnetic stirring (400 rpm) for 30 min. After cooling to room temperature, the liquor was collected by filtration and the pH value was adjusted to about 3.0 by saturated $NaHCO_3$ solution. The liquor was then concentrated to about 50 ml under reduced pressure at 45°C. The concentrated liquor was poured into 500 ml of deionized ice water to precipitate the lignin. The raw MAL was obtained by centrifugation and lyophilization.

Cellulase enzymatic lignin (CEL)

Enzymatic hydrolysis lignin of wheat straw was extracted according to previous literature (Chang et al., 1975). Briefly, the dewaxed wheat straw was ball-milled for 20 h in a plenary ball mill machine. 14.0 g of wheat straw powder, along with 525 mg of cellulase and 700 mg of viscozyme L, was added to a 175 ml of sodium acetate/acetic acid buffer (pH ≈ 5.0). The mixture was placed in a thermostatic incubator at 35°C for 72 h with 250 rpm vibration. After the reaction, the supernatant was removed by centrifugation and the solid residue was washed with buffer twice. After enzymatic hydrolysis for another excess 3 days, the solid sediment separated from being centrifuged and washed with deionized water three times to get the crude CEL.

γ-valerolactone lignin (GVL)

The preparation of GVL was based on the previous reference (Li et al., 2020). 3 g of wheat straw was placed in a 100 ml hydrothermal reactor with PTFE liner containing 36 ml GVL, 9 ml deionized water, and 24.6 μL 98% H_2SO_4 (the solid-to-liquid ratio was 3:40 and the acid concentration was 0.0113 M) and then soaked and stirred for 30 min. The reactor was heated at 170°C for 1 h. The reaction mixture was separated by filtration and the filtrate was collected, which was then added to 1,600 ml distilled ice water. The precipitated lignin was collected by centrifugation, then washed twice with deionized water, and freeze-dried.

Organosolv lignin (OL)

5 g of wheat straw was added to a 50 ml of acetic acid/formic acid/water (55:30:15, v/v/v) solution at a solid-to-liquid ratio of 1:10 (g/ml) reacted hermetically at 105°C for 3.5 h. Then, after being filtered and collected, the liquid was concentrated to about 3 ml by rotary evaporation and titrated back to 200 ml of deionized water. During the titration process, the sediment was continuously stirred, stood for 12 h for centrifugation, and freeze-dried to obtain a solid. Finally, the rough organic acid lignin was extracted and purified with a 1,4-dioxane/water (96/4, v/v) solution.

Lignin Purification

The above-extracted lignin samples were purified by the following method. 150 mg of the crude lignin was added to 15 ml 96% (v/v) 1,4-dioxane/water mixture and stirred at room temperature for 4 h, repeated three times. For the AL, the extraction liquid was evaporated to obtain pure lignin after centrifugation. As for the acid lignins, the 1,4-dioxane solutions were concentrated to ~3 ml, transferred into a centrifuge tube filled with 40 ml cold deionized water by drops, then centrifuged to remove the supernatant, and lyophilized to get the purified lignins.

Analytical Methods

High-Performance Liquid Chromatography-Mass Spectrometric (HPLC-MS) Analysis

Tricin was quantified by thioacidolysis followed by HPLC-MS according to an established method (Lan et al., 2016). The specific operations of analytical thioacidolysis are as follows: 2.5 ml ethanethiol (EtSH), 0.625 ml boron trifluoride diethyl etherate, and enough freshly distilled dioxane were added to a 25 ml volumetric flask to prepare the thioacidolysis reagent. Then, 4 ml of the newly preparative thioacidolysis reagent and 20 mg of biomass material were put into a 10 ml reaction flask to react at 100°C for 4 h. After natural cooling to room temperature, the reaction mixture was transferred to a 60 ml separating funnel, adding 0.4 M $NaHCO_3$ to pH ≈ 7.0 and 1 M HCl to pH ≈ 3.0. The degradation products were extracted with EtOAc, dehydrated with saturated NH_4Cl and anhydrous $MgSO_4$, and distilled under reduced pressure at 45°C, and the residue was dissolved in ethanol for HPLC-MS determination.

HPLC-MS analysis was performed based on the literature (Lan et al., 2019) using LC-electrospray ionization (ESI)/atmospheric

pressure ionization- (API-) MS (LCMS-8050, Shimadzu). A Kinetex C18 (2.1 × 100 mm, 1.9 μm) column was used in the LC system and eluted with water (solvent A) and acetonitrile (solvent B), using a constant method (80% B from 0 to 12.5 min) with 1 μL of the injection volume and column temperature at 40°C and 0.5 ml min^{-1} of flow rate. And ionization was performed under dual ionization (ESI and API) using a dual ion source, with the nebulizing gas at 2.5 L min^{-1} and drying gas at 10 L min^{-1}. The fragmented ions were measured by MS in positive mode and the quantitation of tricin was based on the peak area of the precursor ions in m/z 330.10.

A standard curve of tricin in HPLC-MS was established (**Supplementary Figure S1**). The content of wheat flavone in the original sample was calculated according to the following **formula (2)**:

$$TS(\%) = \frac{CT \times DM}{SM} \times 100\% \quad (2)$$

where TS (%) is the content of tricin in sample, CT (mg/ml) is the concentration of tricin, DM is diluted multiples, and SM is sample mass.

HSQC Characterization

50–100 mg of lignin sample was completely dissolved in 0.5 ml of deuterium dimethyl sulfoxide DMSO-d_6 and then transferred to an NMR tube. A 500 MHz superconducting nuclear magnetic resonance spectroscopy (NMR, Avance Neo 500M, Bruker) was used to record the 2D HSQC spectrum. The spectra were processed using Bruker Topspin 4.1.3 (Windows version). The content of tricin was calculated by the integrals of the corresponding contours.

Determination of SPF

The sample to be tested was ground and sifted to pass 300 meshes for collection. It was accurately weighed at 20.0 mg mixing with 980.0 mg moisturizing cream and the mixture was stirred at 500 rpm for more than 24 h under dark conditions (Qian et al., 2015; Lin M. et al., 2021).

Then, 25 mg of the sunscreen sample prepared above, after being evenly spread on a glass sheet of 1 mm thickness with 3 M adhesive tape and dried in the dark for 20 min, was taken seven different points to test the transmittance of the sample at 290–400 nm to calculate the SPF value (Sohn et al., 2016). The calculation **formula (3)** was as follows (ISO 24443: 2012 and 24,444: 2010):

$$SPF = \frac{\sum_{290}^{400} S_{er}(\lambda) S_s(\lambda)}{\sum_{290}^{400} S_{er}(\lambda) S_s(\lambda) T(\lambda)} \quad (3)$$

where Ser(λ) is the spectral weight of the action of erythema, Ss(λ) is the spectral irradiance of the ultraviolet source, and T(λ) is the transmittance of the sample.

Determination of Radical Scavenging Activity

DPPH (2,2′-diphenyl-1-picrylhydrazyl) radical scavenging activities of tricin and lignin samples were measured to evaluate the antioxidation activity according to the reported method (Jia et al., 2018). First, different concentration (0–0.025 mg/ml) of DPPH in methanol solution was prepared to obtain a standard curve between DPPH concentration and absorbance value by measuring their absorbance at λ = 517 nm. Then mixtures made by 0.1 ml methanol solution of different concentrations of each sample with 3.9 ml 0.025 mg/ml DPPH/methanol solution were evenly mixed and stored at room temperature for 60 min in dark to measure the absorbance of them at λ = 517 nm. The percentage of remaining DPPH radical was calculated as follows:

$$\%DPPH_R = \frac{(DPPH)_T}{(DPPH)_{T=0}} \times 100 \quad (4)$$

where the $(DPPH)_T$ is the concentration of the remaining DPPH free radical at 60 min and $(DPPH)_{T=0}$ is the concentration of the remaining DPPH free radical at 0 min. The oxidation resistance of the tested samples is expressed as EC_{50}, which refers to the sample concentration when the DPPH radical scavenging activity was 50%.

RESULTS AND DISCUSSION

Lignin Extraction Using Different Method

Wheat straw contains 15.9 mg tricin per g of dry matter biomass according to our determination, which is higher than many other plant species. Wheat, as one of the most common staple cereals, is widespread in Asia, especially in China. Accordingly, wheat straw lignin could be a potential source of natural tricin with high value for human health. In this study, we investigated the influence of fractionation methods on the tricin content of the lignin from wheat straw under different conditions, including those performed under acid, alkaline, and neutral conditions. For instance, we used alkaline extraction, mild acidolysis, cellulosic enzymatic hydrolysis, GVL pretreatment, and organosolv pretreatment to extract the wheat straw lignin and six different lignin samples were obtained (**Table 1**). As report previously, tricin was almost completely depleted under the alkaline condition at high temperature (Zikeli et al., 2016). Aiming to reserve the tricin component, we, therefore, performed the alkaline extraction under low temperature and obtained 13.1% crude AL on the base of wheat straw. The crude lignin was purified by dissolving in dioxane/H_2O solution and gave 8.9% yield, accounting for 54.2% of the lignin in wheat straw. A controlled experiment using ball-milled wheat straw samples was also performed hoping to improve the lignin yield. The crude lignin yield increased to 21.2%. But the increment turned out to be from the carbohydrate fraction, which was eliminated during purification and leading to a similar purified lignin yield (55.1%). The mild acidolysis, organic acid, and cellulase enzymatic hydrolysis methods all produced about 50% lignin. But the GVL pretreatment yielded only 22.5% lignin, which might be because of the incomplete precipitation of lignin from the GVL solution.

HSQC Characterization of the Lignin Sample

The extracted lignin samples were characterized by HSQC NMR spectra to determine their structure (**Figure 2** and **Table 2**). In

TABLE 1 | The yield of lignin by different extraction methods.

Sample	Rough lignin (%)[a]	Purified lignin (%)[a]	Purified lignin (%)[b]
AL	13.1	8.9	54.2
AL (ball-milled)	21.2	9.1	55.1
MAL	11.8	9.8	59.5
CEL	17.6	8.3	50.5
GVL	5.3	3.7	22.5
OL	11.9	9.7	58.7

[a]*The yield was calculated on the base of dry wheat straw.*

[b]*The yield was calculated on the basis of lignin content (using L-cysteine assisted measurement).*

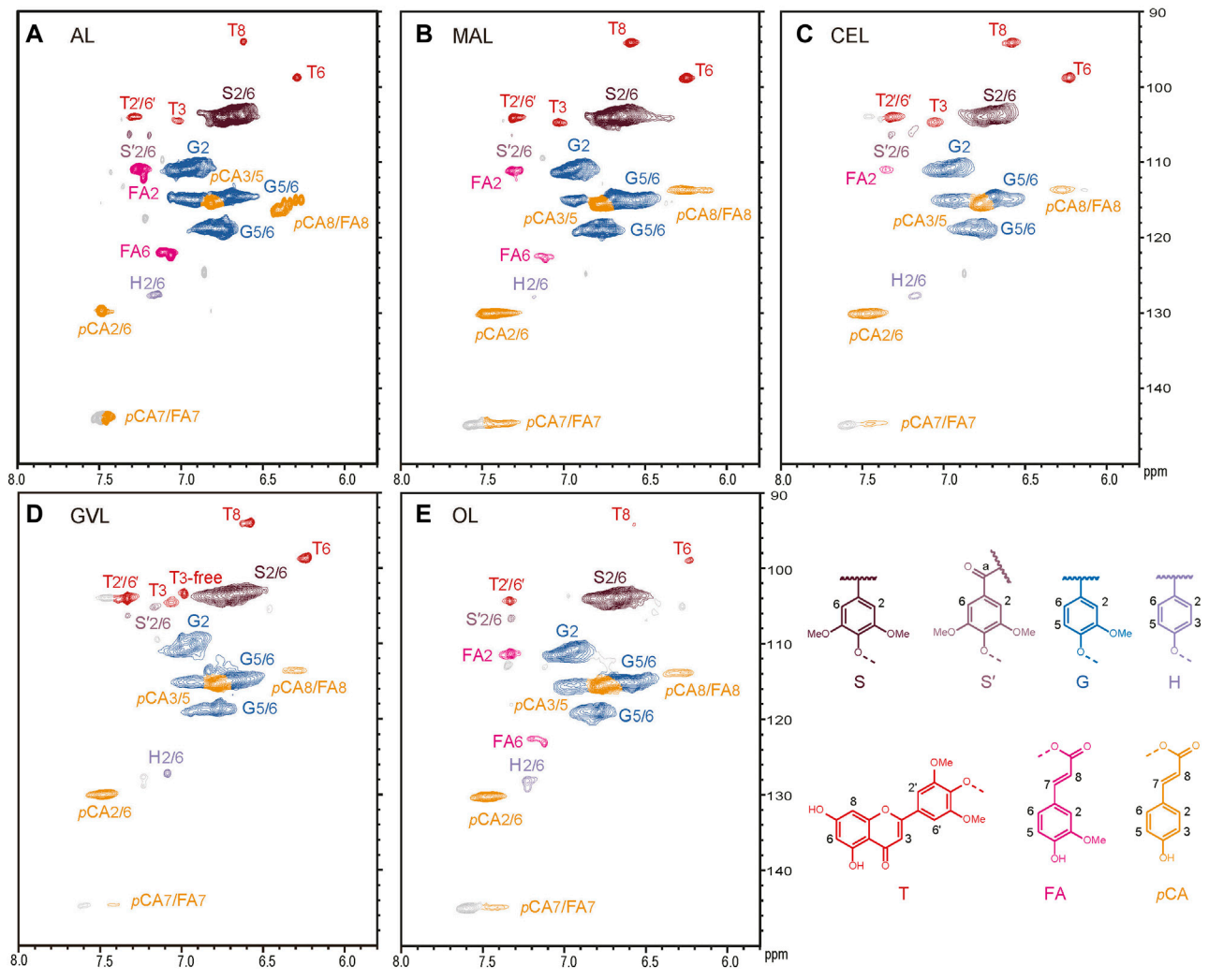

FIGURE 2 | Aromatic region of the 2D HSQC spectra of **(A)** alkali lignin (AL), **(B)** mild acidolysis lignin (MAL), **(C)** cellulase enzymatic lignin (CEL), **(D)** γ-valerolactone lignin (GVL), and **(E)** organosolv lignin (OL).

general, all the methods applied in this study were able to extract the lignin from the wheat straw without serious alternation. The characteristic signals of guaiacyl, syringyl, and *p*-hydroxyphenyl units were clearly identified on the HSQC spectra, as well as the peaks of tricin and *p*-coumarate (Zheng et al., 2021). Unlike most of the AL in other studies (Lan et al., 2019; Zikeli et al., 2016), a certain amount of *p*-coumarate remained on the lignin after alkaline treatment in this study, which should be due to the mild condition (30°C) that we applied. The relative content of tricin was calculated by integrals of the corresponding peaks. The

TABLE 2 | Assignments of $^{1}H/^{13}C$ correlation signals in the 2D HSQC spectra of the lignin in DMSO-d_6.

Label	δ_C/δ_H (ppm)	Assignment
T_8	94.0/6.56	C_8/H_8 in tricin units (**T**)
T_6	98.7/6.22	C_6/H_6 in tricin units (**T**)
$S_{2,6}$	103.8/6.69	C_2/H_2 and C_6/H_6 in etherified syringyl units (**S**)
$T_{2',6'}$	103.9/7.30	$C_{2'}/H_{2'}$ and $C_{6'}/H_{6'}$ in tricin units (**T**)
T_3	104.5/7.03	C_3/H_3 in tricin units (**T**)
$S'_{2,6}$	106.1/7.32 and 106.4/7.19	C_2/H_2 and C_6/H_6 in α-oxidized syringyl units (**S′**)
G_2	110.9/7.00	C_2/H_2 in guaiacyl units (**G**)
$H_{3,5}$	114.5/6.62	C_3/H_3 and C_5/H_5 in *p*-hydroxyphenyl units (**H**)
G_5/G_6	114.9/6.72 and 6.94 118.7/6.77	C_5/H_5 and C_6/H_6 in guaiacyl units (**G**)
$H_{2,6}$	128.0/7.23	C_2/H_2 and C_6/H_6 in *p*-hydroxyphenyl units (**H**)

TABLE 3 | The content of tricin in different lignin samples.

Sample	Absolute content by HPLC-MS	Relative content by 2D HSQC
	Content[a] (mg/g)	(%)[b]
Wheat straw	15.9 ± 0.3	—
AL	28.2 ± 5.9	1.7
AL (ball-milled)	44.6 ± 4.0	-
MAL	54.0 ± 1.8	6.3
CEL	67.3 ± 6.0	6.7
GVL	89.3 ± 5.4	8.6
OL	35.7 ± 1.2	1.1

[a]*The tricin content was defined as the mass of tricin over the mass of the sample to be tested.*
[b]*The relative content of tricin from HSQC was defined as the number of tricin per 100 S and G units.*

TABLE 4 | Sun protection factors (SPF) and DPPH free radical scavenging ability of different lignin.

Sample types	SPF	EC_{50}
Blank	2.04 ± 0.04	—
Tricin	5.65 ± 0.25	(0.00079[a])0.26[b]
AL	4.30 ± 0.48	1.63[b]
CEL	4.25 ± 0.45	1.80[b]
GVL	5.99 ± 0.19	1.02[b]

[a]*mmol/ml.*
[b]*mg/ml.*

percentages of tricin in GVL-pretreated lignin, CEL, and MAL were 8.6, 6.7, and 6.3, respectively, higher than that in AL and organic acid lignin, which was about 1.1–1.7 (**Table 3**). A close inspection on the spectrum of the GVL lignin revealed that a certain amount of free tricin was presented in this sample, as indicated by the characteristic peak of C_3/H_3 in free tricin at δ_C/δ_H 103/7.0. The ratio of linked tricin to free tricin was about 6:4 according to the contour area of the corresponding signals. This result suggests that the dilute H_2SO_4 treatment can selectively cleave the β–O–4-tricin ether bonds in GVL at high temperature.

Thioacidolysis for Tricin Quantitation

In order to determine the absolute content of tricin in the lignin samples, we applied the thioacidolysis degradation method followed by measurement using HPLC-MS under multiple reaction monitoring mode (MRM), as reported previously (Lan et al., 2016; Chen et al., 2021). The GVL lignin contained 89.3 mg/g of tricin. This was the highest tricin level among the six lignin samples, even higher than the tricin content in CEL (67.3 mg/g). The previous study also showed that the tricin level in the GVL lignin sample was higher than that in the CEL sample, according to the HSQC characterization. One of the possible reasons is that some of the tricin-(β–O–4)-lignin linkages were cleaved during GVL lignin extraction and the clipped-off tricin was isolated along with lignin, leading to a bit higher tricin level in the GVL lignin sample. The OL contained only 35.7 mg/g lignin, which might imply that tricin was degrade under such high concentration of acid solution at high temperature. The AL displayed the lowest tricin content with only 23.1 mg/g, although a mild condition was applied for the extraction. These results are generally in accordance with the semiquantitative result from HSQC. We further evaluated the stability of tricin under similar conditions using a pure tricin compound. Results showed that more than 98% of tricin remained after 9 h reaction at 30°C in 1.0 M NaOH solution, indicating that the tricin moiety was stable under this condition. The reason for the poor yield of tricin under alkaline conditions is still unclear. Further study using the dimeric tricin-monolignol model compound would be required to figure out the underlying mechanism.

UV Protection and Radical Scavenging Ability of the Lignin

Tricin is beneficial to human beings because of its various biological activities. The flavonoid backbone structure containing phenyl, carbonyl, and C=C double bonds endows strong UV absorption and radical scavenging ability to tricin. To explore the potential application of tricin-lignin, we further evaluated the SPF value of lignin-based sunscreens and radical scavenging ability of the extracted lignin samples, **Table 4**, to figure out how does the tricin level affect these properties.

The SPF of tricin-based sunscreen was 5.65, which was significantly higher than that of other dimeric model compounds (β–O–4, β–β, β–1, and β–5) and their derivatives formed by conventional monolignol (Lin M. et al., 2021). The SPF

of AL was 4.30, similar to that of CEL, even though its tricin content was much lower than CEL. On the other hand, GVL lignin-based sunscreen displayed the highest SPF value, even slightly higher than that of pure tricin. The free radical scavenging activity showed a similar trend as the SPF value. The EC_{50} of the free radical towards tricin was 0.26 mg/ml (0.00079 mmol/ml). The AL and CEL presented a similar EC_{50} value (1.63 and 1.80 mg/ml), while the GVL lignin was the most active lignin towards radical with EC_{50} of 1.02 mg/ml. In our previous study, we revealed that the β–O–4 and β–β interlinkages were not favorable to UV absorption and radical scavenging. Moreover, the CEL showed lower SPF and radical scavenging ability compared with OL and kraft extracted from *Pinus kesiya* and *Eucalyptus*. This might explain why even the CEL contains a much higher tricin level but showed similar SPF and EC_{50} values with AL. The SPF value of tricin itself was remarkable, and the lignins containing tricin extracted from wheat straw displayed better SPF than those from softwood and hardwood without tricin. This suggests that retaining tricin is beneficial to the anti-UV property of the lignin samples. However, tricin does not impact the radical scavenging ability that much, as the kraft lignin of *eucalyptus* exhibited very low EC_{50} as well (Lin M. et al., 2021).

CONCLUSION

In this study, we applied alkaline pretreatment, organic solvent extraction, cellulase enzymatic hydrolysis, GVL pretreatment, and organic acid pretreatment to extract lignin from wheat straw. The tricin content varied significantly from the lignin samples extracted by different methods. Within these lignin preparations, although the GVL lignin contained a higher tricin level than other samples, the yield of tricin was not high due to the low lignin yield, and the CEL gave the highest tricin yield. The AL produced the lowest tricin content and yield, but the reason was still unclear. SPF testing of the lignin samples showed that tricin significantly improved the anti-UV radiation ability of the lignin. DPPH results demonstrated that tricin is a strong radical scavenger, but the lignin containing a higher tricin level was not necessary resulting in a lower EC_{50} value of DPPH radicals. Overall, our study provides fundamental understanding of the effect of the lignin extraction method on tricin content and the correlation between tricin content and anti-UV radiation/antioxidation ability, which is beneficial to the future study on the application of tricin.

DATA AVAILABILITY STATEMENT

The original contributions presented in the study are included in the article/**Supplementary Material**, and further inquiries can be directed to the corresponding authors.

AUTHOR CONTRIBUTIONS

MX performed the experiment and analysis and wrote the paper. WL and FY designed the project, supervised the experiments and analysis, and obtained funding supporting. ZC, YX, ML, and JL performed lignin separation and aided in the analysis. LZ aided in the analysis and obtained funding supporting. All authors were involved in the writing and revisions.

FUNDING

The authors are grateful to the financial support for this work by the National Natural Science Foundation of China (21908072; 22108088), Guangxi Key Laboratory of Clean Pulp and Papermaking and Pollution Control (KF201805-5), and State Key Laboratory of Pulp and Paper Engineering (202105).

ACKNOWLEDGMENTS

The authors also acknowledge the Climbing Plan of South China University of Technology (j2tw2021020007) and the National Undergraduate Innovation and Entrepreneurship Training Program (202010561100).

SUPPLEMENTARY MATERIAL

The Supplementary Material for this article can be found online at: https://www.frontiersin.org/articles/10.3389/fenrg.2021.756285/full#supplementary-material

REFERENCES

Boerjan, W., Ralph, J., and Baucher, M. (2003). Ligninbiosynthesis. *Annu. Rev. Plant Biol.* 54, 519–546. doi:10.1146/annurev.arplant.54.031902.134938

Cao, G., Sofic, E., and Prior, R. L. (1997). Antioxidant and Prooxidant Behavior of Flavonoids: Structure-Activity Relationships. *Free Radic. Biol. Med.* 22, 749–760. doi:10.1016/s0891-5849(96)00351-6

Chang, H., Cowling, E. B., Brown, W., Adler, E., and Miksche, G. (1975). Comparative Studies on Cellulolytic Enzyme Lignin and Milled Wood Lignin of Sweetgum and spruce. *Holzforschung* 29, 153–159. doi:10.1515/hfsg.1975.29.5.153

Chen, F., Zhuo, C., Xiao, X., Pendergast, T. H., and Devos, K. M. (2021). A Rapid Thioacidolysis Method for Biomass Lignin Composition and Tricin Analysis. *Biotechnol. Biofuels* 14, 18. doi:10.1186/s13068-020-01865-y

del Río, J. C., Rencoret, J., Gutiérrez, A., Elder, T., Kim, H., and Ralph, J. (2020). Lignin Monomers from beyond the Canonical Monolignol Biosynthetic Pathway: Another brick in the wall. *ACS Sustain. Chem. Eng.* 8, 4997–5012. doi:10.1021/acssuschemeng.0c01109

del Río, J. C., Rencoret, J., Prinsen, P., Martínez, Á. T., Ralph, J., and Gutiérrez, A. (2012). Structural Characterization of Wheat Straw Lignin as Revealed by Analytical Pyrolysis, 2D-NMR, and Reductive Cleavage Methods. *J. Agric. Food Chem.* 60, 5922–5935. doi:10.1021/jf301002n

Heim, K. E., Tagliaferro, A. R., and Bobilya, D. J. (2002). Flavonoid Antioxidants: Chemistry, Metabolism and Structure-Activity Relationships. *J. Nutr. Biochem.* 13, 572–584. doi:10.1016/s0955-2863(02)00208-5

Jensen, A., Cabrera, Y., Hsieh, C.-W., Nielsen, J., Ralph, J., and Felby, C. (2017). 2D NMR Characterization of Wheat Straw Residual Lignin after Dilute Acid Pretreatment with Different Severities. *Holzforschung* 71, 461–469. doi:10.1515/hf-2016-0112

Jia, Y., He, Y., and Lu, F. (2018). The Structure-Antioxidant Activity Relationship of Dehydrodiferulates. *Food Chem.* 269, 480–485. doi:10.1016/j.foodchem.2018.07.038

Jiang, B., Zhang, Y., Gu, L., Wu, W., Zhao, H., and Jin, Y. (2018). Structural Elucidation and Antioxidant Activity of Lignin Isolated from Rice Straw and Alkali-oxygen Black Liquor. *Int. J. Biol. Macromol.* 116, 513–519. doi:10.1016/j.ijbiomac.2018.05.063

Kim, S., and Dale, B. E. (2004). Global Potential Bioethanol Production from Wasted Crops and Crop Residues. *Biomass Bioenergy* 26, 361–375. doi:10.1016/j.biombioe.2003.08.002

Lan, W., Lu, F., Regner, M., Zhu, Y., Rencoret, J., Ralph, S. A., et al. (2015). Tricin, a Flavonoid Monomer in Monocot Lignification. *Plant Physiol.* 167, 1284–1295. doi:10.1104/pp.114.253757

Lan, W., Rencoret, J., Lu, F., Karlen, S. D., Smith, B. G., Harris, P. J., et al. (2016). Tricin-lignins: Occurrence and Quantitation of Tricin in Relation to Phylogeny. *Plant J.* 88, 1046–1057. doi:10.1111/tpj.13315

Lan, W., Rencoret, J., Del Rio, J. C., and Ralph, J. (2019). "Tricin in Grass Lignin: Biosynthesis, Characterization, and Quantitation," in *Chapter in Lignin, Biosynthesis, Functions and Economic Significance*. New York: Nova science publishers.

Lauwaert, J., Stals, I., Lancefield, C. S., Deschaumes, W., Depuydt, D., Vanlerberghe, B., et al. (2019). Pilot Scale Recovery of Lignin from Black Liquor and Advanced Characterization of the Final Product. *Separat. Purif. Techn.* 221, 226–235. doi:10.1016/j.seppur.2019.03.081

Li, M., Pu, Y., Yoo, C. G., and Ragauskas, A. J. (2016). The Occurrence of Tricin and its Derivatives in Plants. *Green. Chem.* 18, 1439–1454. doi:10.1039/c5gc03062e

Li, J., Feng, P., Xiu, H., Li, J., Yang, X., Ma, F., et al. (2019). Morphological Changes of Lignin during Separation of Wheat Straw Components by the Hydrothermal-Ethanol Method. *Bioresour. Techn.* 294, 122157. doi:10.1016/j.biortech.2019.122157

Li, S., Zhao, C., Yue, F., and Lu, F. (2020). Revealing Structural Modifications of Lignin in Acidic γ-Valerolactone-H2O Pretreatment. *Polymers* 12, 116. doi:10.3390/polym12010116

Lin, M., Yang, L., Zhang, H., Xia, Y., He, Y., Lan, W., et al. (2021a). Revealing the Structure-Activity Relationship between Lignin and Anti-UV Radiation. *Ind. Crops Prod.*

Lin, W., Yang, J., Zheng, Y., Huang, C., and Yong, Q. (2021b). Understanding the Effects of Different Residual Lignin Fractions in Acid-Pretreated Bamboo Residues on its Enzymatic Digestibility. *Biotechnol. Biofuels* 14, 143. doi:10.1186/s13068-021-01994-y

Lu, F., Wang, C., Chen, M., Yue, F., and Ralph, J. (2021). A Facile Spectroscopic Method for Measuring Lignin Content in Lignocellulosic Biomass. *Green. Chem.* 23, 5106–5112. doi:10.1039/d1gc01507a

Luterbacher, J. S., Rand, J. M., Alonso, D. M., Han, J., Youngquist, J. T., Maravelias, C. T., et al. (2014). Nonenzymatic Sugar Production from Biomass Using Biomass-Derived -Valerolactone. *Science* 343, 277–280. doi:10.1126/science.1246748

Ogo, Y., Ozawa, K., Ishimaru, T., Murayama, T., and Takaiwa, F. (2013). Transgenic rice Seed Synthesizing Diverse Flavonoids at High Levels: a New Platform for Flavonoid Production with Associated Health Benefits. *Plant Biotechnol. J.* 11, 734–746. doi:10.1111/pbi.12064

Oyama, T., Yasui, Y., Sugie, S., Koketsu, M., Watanabe, K., and Tanaka, T. (2009). Dietary Tricin Suppresses Inflammation-Related colon Carcinogenesis in Male Crj: CD-1 Mice. *Cancer Prev. Res.* 2, 1031–1038. doi:10.1158/1940-6207.CAPR-09-0061

Qian, Y., Qiu, X., and Zhu, S. (2015). Lignin: a Nature-Inspired Sun Blocker for Broad-Spectrum Sunscreens. *Green. Chem.* 17, 320–324. doi:10.1039/c4gc01333f

Ralph, J. (2009). Hydroxycinnamates in Lignification. *Phytochem. Rev.* 9, 65–83. doi:10.1007/s11101-009-9141-9

Sarkar, N., Ghosh, S. K., Bannerjee, S., and Aikat, K. (2012). Bioethanol Production from Agricultural Wastes: An Overview. *Renew. Energ.* 37, 19–27. doi:10.1016/j.renene.2011.06.045

Sohn, M., Herzog, B., Osterwalder, U., and Imanidis, G. (2016). Calculation of the Sun protection Factor of Sunscreens with Different Vehicles Using Measured Film Thickness Distribution - Comparison with the SPF *In Vitro*. *J. Photochem. Photobiol. B: Biol.* 159, 74–81. doi:10.1016/j.jphotobiol.2016.02.038

Solyanik, G. I., Zulphigarov, O. S., Prokhorova, I. V., Pyaskovskaya, O. N., Kolesnik, D. L., and Atamanyuk, V. P. (2021). A Comparative Study on Pharmacokinetics of Tricin, a Flavone from Gramineous Plants with Antiviral Activity. *Jbm* 09, 76–91. doi:10.4236/jbm.2021.92008

Vanholme, R., De Meester, B., Ralph, J., and Boerjan, W. (2019). Lignin Biosynthesis and its Integration into Metabolism. *Curr. Opin. Biotechnol.* 56, 230–239. doi:10.1016/j.copbio.2019.02.018

Zheng, L., Yu, P., Zhang, Y., Wang, P., Yan, W., Guo, B., et al. (2021). Evaluating the Bio-Application of Biomacromolecule of Lignin-Carbohydrate Complexes (LCC) from Wheat Straw in Bone Metabolism via ROS Scavenging. *Int. J. Biol. Macromol.* 176, 13–25. doi:10.1016/j.ijbiomac.2021.01.103

Zhou, J.-M., and Ibrahim, R. K. (2009). Tricin-a Potential Multifunctional Nutraceutical. *Phytochem. Rev.* 9, 413–424. doi:10.1007/s11101-009-9161-5

Zikeli, F., Ters, T., Fackler, K., Srebotnik, E., and Li, J. (2016). Wheat Straw Lignin Fractionation and Characterization as Lignin-Carbohydrate Complexes. *Ind. Crops Prod.* 85, 309–317. doi:10.1016/j.indcrop.2016.03.012

Conflict of Interest: The authors declare that the research was conducted in the absence of any commercial or financial relationships that could be construed as a potential conflict of interest.

Publisher's Note: All claims expressed in this article are solely those of the authors and do not necessarily represent those of their affiliated organizations or those of the publisher, the editors, and the reviewers. Any product that may be evaluated in this article or claim that may be made by its manufacturer is not guaranteed or endorsed by the publisher.

frontiers in Energy Research

ORIGINAL RESEARCH
published: 08 November 2021
doi: 10.3389/fenrg.2021.774783

Preparation and Characterization of Cellulose Nanocrystal Extraction From *Pennisetum hydridum* Fertilized by Municipal Sewage Sludge via Sulfuric Acid Hydrolysis

Xiaoshan Yu[1], *Yu Jiang*[1], *Qitang Wu*[1,2], *Zebin Wei*[1,2], *Xianke Lin*[1] *and Yangmei Chen*[1,2]*

[1]College of Natural Resources and Environment, South China Agricultural University, Guangzhou, China, [2]Guangdong Provincial Key Laboratory of Agricultural & Rural Pollution Abatement and Environmental Safety, South China Agricultural University, Guangzhou, China

This research focuses on the preparation of cellulose nanocrystals (CNCs) from *Pennisetum hydridum* fertilized by municipal sewage sludge (MSS) through sulfuric acid hydrolysis in different acid concentrations (40–65%), temperature (room temperature ~55°C), and reaction time (50–120 min). The results showed that the obtained CNC possessed stable dispersion in water. The length of CNCs reached 272.5 nm under the condition of room temperature (RT), 65% acid concentration, and 120 min reaction time, and the diameter was within 10 nm. Furthermore, Fourier transform infrared (FTIR) showed that the CNC still kept the cellulose type I structure. The crystallinity of CNCs increased to the maximum by 18.34% compared with that of delignified *Pennisetum hydridum* fibers. Thermogravimetry (TG) illustrated the thermal stability of CNCs was lower than that of delignified *Pennisetum hydridum* fibers due to the introduction of sulfate groups in the cellulose. This study demonstrated that *Pennisetum hydridum* fertilized by MSS might be a suitable raw material for CNCs. This implies meaningful resource utilization of MSS and *Pennisetum hydridum*.

Keywords: ***Pennisetum hydridum*, cellulose nanocrystals, particle size, crystallinity, municipal sewage sludge**

OPEN ACCESS

Edited by:
Chen Huang,
Chinese Academy of Forestry, China

Reviewed by:
Chuan-Ling Si,
Tianjin University of Science and Technology, China
Zhouyang Xiang,
South China University of Technology, China

***Correspondence:**
Yangmei Chen
ymchen@scau.edu.cn

Specialty section:
This article was submitted to Bioenergy and Biofuels, a section of the journal Frontiers in Energy Research

Received: *13 September 2021*
Accepted: *28 September 2021*
Published: *08 November 2021*

Citation:
Yu X, Jiang Y, Wu Q, Wei Z, Lin X and Chen Y (2021) Preparation and Characterization of Cellulose Nanocrystal Extraction From Pennisetum hydridum *Fertilized by Municipal Sewage Sludge via Sulfuric Acid Hydrolysis. Front. Energy Res. 9:774783. doi: 10.3389/fenrg.2021.774783*

INTRODUCTION

Nanocellulose is defined as a fiber material with at least one dimension size of 1–100 nm, which can be dispersed in water to form a stable colloid. Nanocellulose is a new fiber material whose diameter in microfiber units is in the nanoscale (2–100 nm) (Ru et al., 2017), the source of which is relatively broad, coming from gramineous plants, wood, cotton, tunicate animals, and bacteria. Due to its excellent mechanical properties, high specific surface area, high Young's modulus, renewability, biodegradability, and other advantages (Mao et al., 2017), nanocellulose has been widely used in

Abbreviations: CNC, cellulose nanocrystal; MSS, municipal sewage sludge; RT, room temperature; FTIR, Fourier transform infrared; TG, thermogravimetry; CNF, cellulose nanofibril; BNC, bacterial nanocellulose; ECC, electrospun cellulose; SEM, scanning electron microscopy; GSED, gaseous secondary electron detector; TEM, transmission electron microscopy; XRD, X-ray diffraction; CrI, crystallinity

the fields of biomedical products, nanocomposites, textiles, and new energy (Phanthong, et al., 2018; Liu et al., 2021; Liu et al., 2020).

The structure of cellulose consists of amorphous and crystalline regions. Due to the disordered structure of amorphous cellulose, the principle of separation of nanocellulose extracted from natural cellulose under the effect of chemicals or mechanical forces is the degradation of the fiber molecule of the amorphous area before the reaction of the crystalline region. It reserves the crystalline region structure, obtaining a nanoscale fiber with a high degree of crystallinity (Habibi et al., 2010). According to different material sources, fiber morphology, and preparation methods, nanocelluloses can be divided into four categories: cellulose nanocrystals (CNCs), cellulose nanofibrils (CNFs), bacterial nanocelluloses (BNCs), and electrospun celluloses (ECCs) (Liu et al., 2021).

At present, the common preparation methods of nanocellulose include sulfuric acid, hydrochloric acid, nitric acid, and other strong acid hydrolysis, TEMPO oxidation, mechanical method, biological enzyme method, and steam explosion method. Among them, TEMPO reagent is expensive. The oxidant is difficult to recover, and a large amount of wastewater will be produced in the preparation process (Visanko et al., 2014). The mechanical and explosive methods require special equipment with high energy consumption and low purity (Gao, 2011). Although the biological method has low energy consumption and meets the requirements of green and sustainable development, it has low efficiency and strict requirements on reaction conditions, which limits its large-scale application (Chen et al., 2012). The acid hydrolysis method is simple and mature. As early as 1947, there were studies on the preparation of CNCs by hydrolyzing cellulose with sulfuric acid (Nickerson and Habrle, 1947). Its degraded sugar by-products could also be fermented into biofuel. The method is simple, and at the same time, the acid could be recovered. Therefore, acid hydrolysis is still the main method for the rapid preparation of nanocellulose (Tang et al., 2014).

The genus of *Pennisetum hydridum* (hybrid giant Napier) is *Pennisetum*. It is bred by crossbreeding between *Pennisetum americanum* and elephant grass (Lin et al., 2015). It has a strong tillering ability, strong adaptability, fast growth, high yield, and high fiber content. As a new type of energy crop with high efficiency and economy, it has attracted attention. It is often used in animal husbandry feed (Peng et al., 2010) and pulp or paper manufacturing (Jiang et al., 2019). In recent years, it has also been used in soil and water conservation, ecological environment degradation control, and other environmental control aspects (Zhao et al., 2015). There have been studies on the use of biochar prepared from *Pennisetum hydridum* to treat urban sewage (Zhao et al., 2017) and heavy metal sewage (Huang et al., 2016). The purpose of remediation of heavy metal–contaminated soil was obtained by planting *Pennisetum hydridum* to enrich heavy metals in the soil (Yi et al., 2014; Wang et al., 2015; Xie et al., 2016; He et al., 2017), and the red mud and saline soil were improved (Ma et al., 2012; Ma et al., 2013).

A lot of research has been done on the extraction of nanocellulose from natural plant resources, including sisal, kapok, pineapple leaves, coconut husks, rice husks, bamboo, hemp, and industrial denim waste (Dai 2011; Nurain et al., 2012; Wang 2013; Deepa et al., 2015; Culsum 2021). *Pennisetum hydridum* as large biomass of plant [90–105 t (air-dried)/hm^2] may be an ideal raw material for the preparation of nanocellulose (He et al., 2020). However, a lot of *Pennisetum hydridum* is discarded or burned directly, causing resource waste and environmental pollution (Huang et al., 2016). It is a new way of resource recycling used by the preparation of nanocellulose from *Pennisetum hydridum*.

Therefore, CNCs were firstly prepared from *Pennisetum hydridum* of the non-wood fiber raw material fertilized by MSS in this study. Many studies used two steps for the pretreatment of raw materials to obtain CNCs (Bano and Negi, 2017). One step is firstly used for the removal of lignin and the other step for the removal of hemicellulose. We used a one-step method to obtain CNCs in this study, i.e., the removal of lignin using sodium chlorite. Furthermore, the particle size, chemical structure, crystal structure, fiber morphology, and thermal degradation performance of CNCs were evaluated. This study could provide meaningful reference data for the research and application of CNCs obtained from *Pennisetum hydridum*.

MATERIALS AND METHODS

Materials

The method of cultivation of *Pennisetum hydridum* using municipal sludge sewage was the same as that in our previous work (Jiang et al., 2019). Stalks of *Pennisetum hydridum* were harvested after 6 months. The *Pennisetum hydridum* stalks were ground and sifted after equilibrium moisture was achieved. The powder of *Pennisetum hydridum* that passed a 40-mesh sieve but was retained on a 60-mesh sieve was collected and put into a storage jar to be kept at room temperature.

Pretreatment of Raw Material

Lignin of the powder of *Pennisetum hydridum* was removed by the traditional sodium chlorite method. The steps were as follows. An amount of 10 g *Pennisetum hydridum* powder was loaded into a 500 ml beaker, and 325 ml distilled water was added at a ratio of 1:32.5. The mixture was placed in a thermostat water bath at 75°C for 4 h, an amount of 3 g sodium chlorite was added every 1 h, and then glacial acetic acid was added to adjust the pH to 4.5. The above steps were repeated four times until the sample became white. The sample was placed in an extractor and cleaned with distilled water, repeatedly, until the filtrate pH was 7. The obtained delignified *Pennisetum hydridum* fiber was dried in an oven at 50°C.

Lignin and pentosane (hemicellulose) of the original *Pennisetum hydridum* and delignified sample were determined according to GB/T 2677.8-1994 and GB/T 2677.9-1994, respectively. The cellulose content was determined by the nitrate method.

Preparation of Cellulose Nanocrystals

An amount of 3 g delignified *Pennisetum hydridum* fiber was mixed with sulfuric acid (30 ml) with a certain mass fraction (40, 55, and 65% wt), and the reaction was carried out in a Thermostat Ultrasonic Cleaner (SB-5200 DTD, Xinzhi Biological Technology Co., Ltd., Ningbo, China) at 40°C, 55°C, 70°C, and room temperature (RT, 25°C) for a certain period (50 min, 120 min). The frequency and power of the ultrasound were 40 Hz and 50 kW. The reaction product was centrifuged using a centrifuge (LL5-2A, Beijing Medical Centrifuge Factory, China) for 15 min at 5,310 × g, and the supernatant was removed. The supernatant was repeatedly centrifuged several times until the pH of the solution was about 6, and the supernatant became turbid. A certain amount of dried solid samples were taken to obtain CNCs.

Particle Size and Zeta Potential Analysis

2 ml CNC sample solution was taken, diluted 100 times using deionized water, dispersed with ultrasonic treatment, and dropped into the sample pool. The particle size and zeta potential were measured using the Malvern laser particle analyzer (Nano ZS90, Malvern Instruments Co., Ltd., United Kingdom). The reported results were the average of two measurements.

The Yield of CNCs

The obtained CNC suspension was dried to a constant weight at 50°C for at least 8 h in an oven and weighed after drying. The yield of CNCs was calculated as follows:

$$Y = \frac{m_2}{m_1} \times 100\%, \quad (1)$$

where Y is the yield of CNCs, %; m_2 is the weight of CNCs after drying, g; and m_1 is the weight of the original *Pennisetum hydridum*, g.

Scanning Electron Microscopy Analysis of *Pennisetum hydridum* Fiber

The *Pennisetum hydridum* fiber was fixed on the observation table with copper adhesive conductive tape. A small amount of powder was sprinkled on the conductive adhesive and plated with gold. SEM imaging (XL-30-ESEM, FEI Corporation, Holland) was conducted using a gaseous secondary electron detector (GSED) at a temperature of about 23°C, accelerating voltage of 10–20 kV, and pressure of 800 Pa in the sample chamber. SEM images at different scales of 200, 100, and 10 μm were obtained, and their contrast and brightness were adjusted.

Transmission Electron Microscopy Analysis

The CNC solution was dispersed evenly by ultrasonic treatment (power 600 W, shaking time 2 s, interval time 1 s, and duration of shaking 10 min), 10 μL solution was absorbed and dipped onto a carbon film copper mesh (200 mesh), and the excess liquid was absorbed by a clean filter paper. After a few minutes, a 10 μL 3% phosphotungstate stain (pH 7) was adsorbed and dropped onto the copper net for negative staining for 5 min, the missing liquid was absorbed by a clean filter paper, and then the sample was dried naturally. The sample was observed using TEM under 80 kV acceleration voltage (Tecnai 12, FEI Corporation, Holland). 50 nanofibers were measured for the morphological analysis.

TABLE 1 | Components of *Pennisetum hydridum* before and after delignification.

Components	Cellulose (%)	Lignin (%)	Hemicellulose
Before delignification	40.8	20.4	23.5
After delignification	50.9	6.5	24.1

Fourier Transform Infrared Spectrometry Analysis

The amounts of 1 mg CNC powder and 100 mg KBr were mixed and ground, and the mixture was pressed into a high-transparency tablet with a diameter of 13 mm by the tablet pressing method and then tested by FTIR (Vertex 70, Bruker Corporation, Germany) in the range of 4,000–500 cm^{-1}, with an accumulation of 64 scans and a resolution of 4 cm^{-1}.

X-Ray Diffraction Analysis

The crystal structure of CNCs was analyzed by XRD (Ultima IV, Rigaku Corporation, Japan). The analyzing conditions were Cu-Kα source, 40 kV, and $\lambda = 0.154$. The scanning range was 5°–40°, with a scanning step width of 0.020° per scan. The crystallinity (CrI) was calculated by the Segal empirical formula (Chen et al., 2018) as

$$CrI, \% = \frac{I_{002} - I_{am}}{I_{002}} \times 100, \quad (2)$$

where I_{002} is the maximum diffraction intensity of the cellulose (002) crystal plane and I_{am} is the diffraction intensity of the non-crystalline zone between the 002 peak and the 101 peak.

Thermogravimetric Analysis

An amount of 10 mg sample was taken and tested by a thermogravimetric analyzer (STA449 F3, NETZSCH Corporation, Germany). The analysis conditions were nitrogen atmosphere, a room temperature of 600°C, and a heating rate of 10°C/min.

RESULTS AND DISCUSSION

Chemical Components of Materials

The basic chemical components of *Pennisetum hydridum* before and after delignification are shown in **Table 1**. The cellulose content of *Pennisetum hydridum* after delignification reached 50.9%, which showed *Pennisetum hydridum* could be a good material for the production of nanocellulose. The lignin content of *Pennisetum hydridum* after delignification became very low. The hemicellulose content of *Pennisetum hydridum* after delignification became 24.1%.

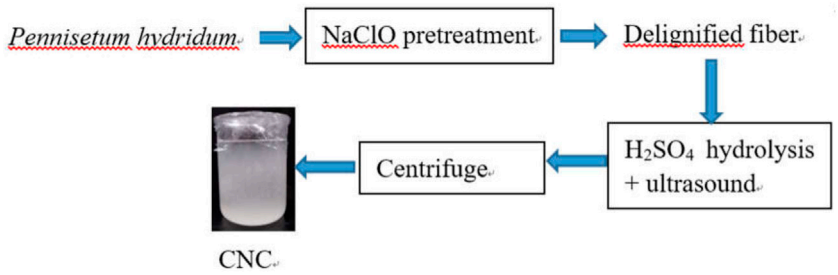

FIGURE 1 | Flowchart of CNC production.

TABLE 2 | Particle size, zeta potential, and yield of CNCs at 40°C.

H_2SO_4 (%)	Time (min)	Particle size (nm)	Zeta potential (mV)	Yield (%)
40	50	447.6	−22.9	31.0
	120	439.7	−17.8	34.3
55	50	438.4	−22.5	40.3
	120	422.2	−27.4	43.6
65	50	624.9	−28.4	35.6
	120	620.2	−32.6	34.8

TABLE 3 | Particle size, zeta potential, and yield of CNCs at 55°C.

H_2SO_4 (%)	Time (min)	Particle size (nm)	Zeta potential (mV)	Yield (%)
40	50	625.1	−15.3	41.4
	120	551.9	−20.8	42.2
55	50	722.1	−35.5	37.5
	120	467.6	−33.0	37.0
65	50	668.1	−29.7	26.4
	120	409.3	−27.0	23.2

TABLE 4 | Particle size, zeta potential, and yield of CNCs at RT.

H_2SO_4 (%)	Time (min)	Particle size (nm)	Zeta potential (mV)	Yield (%)
40	50	355.0	−23.1	32.5
	120	406.6	−28.8	35.6
55	50	459.2	−35.9	35.6
	120	278.0	−36.9	36.8
65	50	369.8	−34.2	35.3
	120	272.5	−34.9	38.2

Particle Size, Zeta Potential, and Yield of CNCs

The flowchart of the CNC production process used in this work is presented in **Figure 1**. The preparation method of nanocellulose is mainly to decompose large cellulose molecules into smaller nanocellulose molecules through physical crushing and chemical deconstruction (Du et al., 2018), which is known as the top-down approach (Nechyporchuk et al., 2016). Sulfuric acid hydrolysis is the earliest inorganic acid hydrolysis method of CNCs. Later, there have been studies to prepare CNCs by hydrolysis of hydrochloric acid, phosphoric acid, and other inorganic acids (Kontturi et al., 2016; Espinosa et al., 2013; Vanderfleet et al., 2018).

Three treatment variables (treatment temperature, sulfuric acid mass fraction, and treatment time) were set in this study. After sulfuric acid hydrolysis for a certain period, the amorphous structure of cellulose was decomposed to obtain cellulose with a smaller size (Liu et al., 2017). As shown in **Tables 2**, **3**, **4**, the acid-hydrolyzed products under all conditions reached the nanometer size, and the mean particle size of CNCs was the smallest under RT, 65% wt H_2SO_4, and 120 min (**Figure 2A**; **Table 4**). When the other treatment conditions were the same, the longer the acid

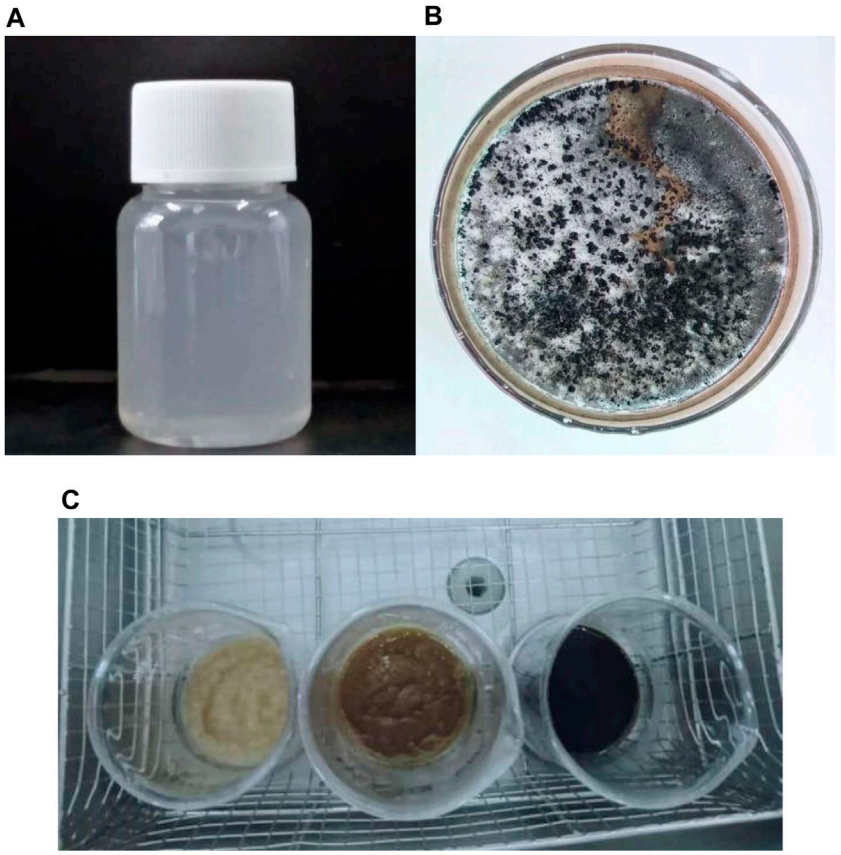

FIGURE 2 | CNC pictures at different treatment conditions: **(A)** CNC solution (RT); **(B)** carbonization (70°C); **(C)** color change of the CNC at 55°C under different H_2SO_4 mass fractions (from left to right: 40% wt, 55% wt, and 65% wt).

hydrolysis time, the smaller the particle size of the CNC. In general, the CNC prepared at room temperature had the smallest particle size compared to that at other temperatures when the other treatment conditions were the same. The particle size of the CNC was highest under 40°C and 65% H_2SO_4, as shown in **Table 2**. This may be caused by overreaction resulting in the partial flocculation of glucose generated by decomposition and carbonization of cellulose.

Different colors of production are shown due to the difference in the mass fraction of sulfuric acid (**Figure 2C**). When the temperature reaches 70°C and the mass fraction of sulfuric acid ≥ 55%, the product carbonizes and the color turns black (**Figure 2B**), so the measurement results of the product obtained at 70°C are not listed.

The zeta potential is used to measure the strength of repulsion or attraction between particles, which is an important parameter of the characterization of colloid system stability (Qin, 2018). Usually, the greater the zeta potential, the greater the stability of the colloid system. In most of the colloid systems, 30 mV is called the stability threshold. The zeta potential is higher than the threshold; strong electrostatic repulsion can prevent particles from getting close, thus increasing their stability (Qin, 2018). If the zeta potential is between −15 and 15 mV, the gel will condense. Due to the addition of sulfuric acid, the resulting nanocrystals have sulfuric acid ester groups on the surface, which is negatively charged (Xu et al., 2016). It can be seen from **Table 2** that the zeta potential of CNCs obtained under all conditions is negative, and the absolute value is above 15 mV, which indicates that the prepared CNCs have good stability.

As shown in **Table 4**, the CNC yield was higher when the mass fraction of sulfuric acid was 65%, and the CNC yield increased with the increase of treatment time under the same mass fraction of sulfuric acid. When the temperature rises to 40°C, the yield of CNCs increases first and then decreases with the increase of sulfuric acid mass fraction. When the temperature is 55°C, the yield of CNCs increases first and then decreases with the increase of sulfuric acid. This is because of the different results produced by the interaction of temperature, sulfuric acid mass fraction, and time (Tang et al., 2011).

Although CNCs can be prepared from various cellulose sources and hydrolysis conditions, the conditions are not ideal, the yield and charge content may be very low, or the agglomeration may be caused by large CNC particles (Vanderfleet et al., 2018). It is generally concluded from previous studies that, by increasing time, temperature, and acid concentration, hydrolysis would be more intense, CNCs with a higher sulfate content and smaller size would be produced, and the yield would be higher (Beck-candanedo et al., 2005).

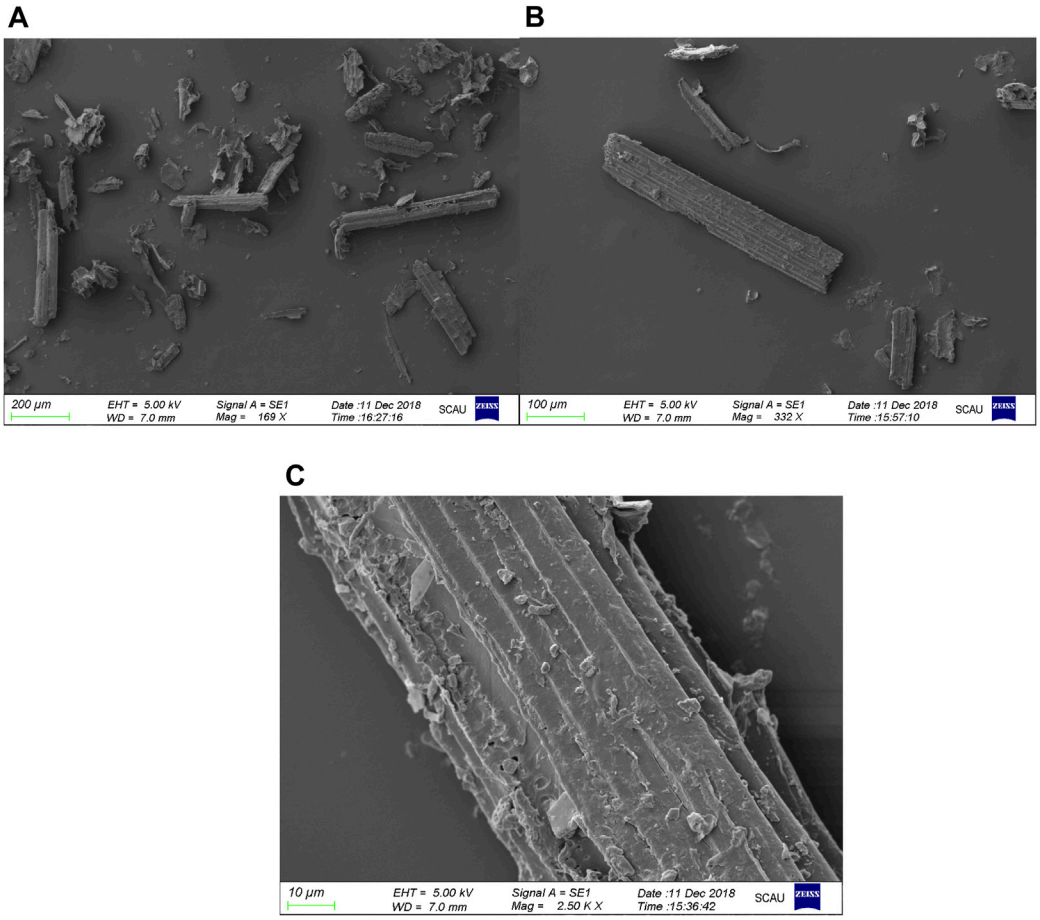

FIGURE 3 | SEM images of the *Pennisetum hydridum* fiber at different scales: **(A)** 200 µm; **(B)** 100 µm; **(C)** 10 µm.

However, if the intensity of hydrolysis exceeds a certain point, the crystallinity of CNC would be damaged, cellulose would be degraded into sugar, and furfural would be formed further (Wang, 2014), which would also lead to the decrease of CNC yield and the increase of by-products (Agarwal, 2015). In this study, CNCs were not obtained when hydrolyzed at 70°C with a higher concentration of sulfuric acid, which indicated that hydrolysis was too severe and the experimental conditions should be adjusted.

Electron Microscopy Analysis of CNCs

From images of SEM, it can be seen that the length and width of the *Pennisetum hydridum* fiber were within 100 µm and about 10 µm, respectively (**Figure 3**). The average particle size of CNCs was around 400 nm under different acid hydrolysis conditions (**Tables 2**, **3**, **4**), and the difference was not big. Therefore, a few samples were observed by TEM (**Figures 2A,B**: RT, 40% wt, and 120 min; **Figure 2C**: RT, 55% wt, and 120 min; **Figure 2C**: RT, 65% wt, and 120 min). From **Figure 4**, it can be seen that the fiber length of CNCs was within 500 nm and the diameter was within 10 nm. Under the conditions of sulfuric acid concentration of 40 and 55% wt, there were some fiber bundles formed between celluloses, and it was not easy to observe a single CNC. It can be seen that CNCs at the concentration of 65% wt sulfuric acid had the smallest length, were relatively uniform, and had the best dispersion. This might be due to the degradation of more amorphous cellulose of fiber as the acid concentration increases. Mukherjee (1953) was the first person to use TEM to obtain images of CNCs from sulfuric acid hydrolysis and observed rod-like particles of about 200 nm length and 10–20 nm diameter, which were consistent with the TEM images of CNCs prepared in this study (**Figure 4**).

FTIR Analyses of Chemical Structures of CNCs

The chemical structure analysis of the delignified/bleached *Pennisetum hydridum* fiber and CNCs prepared at different temperatures was carried out by FTIR (**Figure 5**). The absorption bands and the corresponding structure assignments from the infrared spectra are based on literature values (Chen et al., 2013). From **Figure 5**, it can be seen that there was a major peak near 3,390 cm^{-1} with the presence of -OH and C-H absorption peaks near 2,918 cm^{-1} and a C-O absorption peak near 1,060 cm^{-1}. These main characteristic peaks did not change

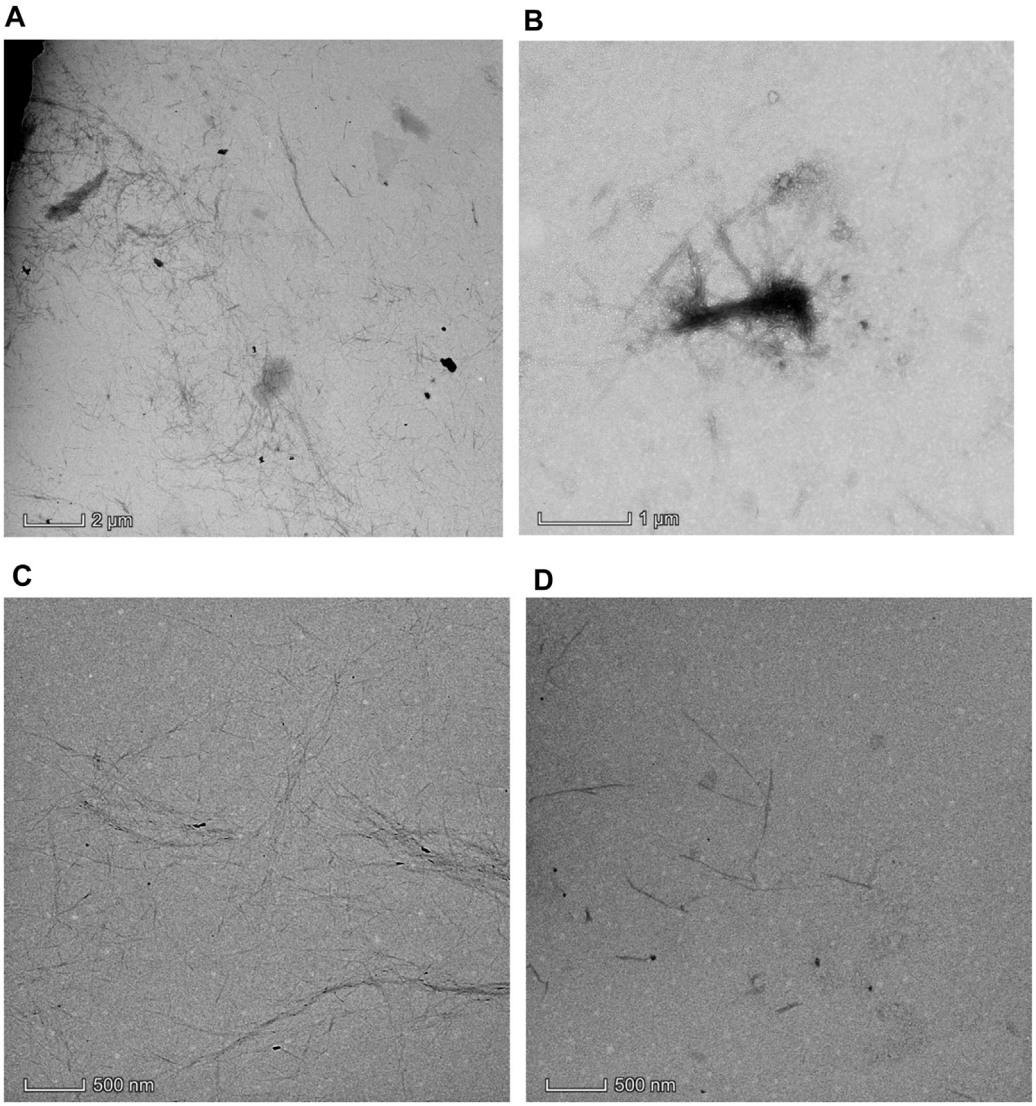

FIGURE 4 | TEM images of the CNC under different sulfuric acid concentrations: **(A)** RT, 40% wt, and 120 min; **(B)** RT, 40% wt, and 120 min; **(C)** RT, 55% wt, and 120 min; **(D)** RT, 65% wt, and 120 min.

significantly, indicating that the CNC still had the basic structure of cellulose after acid hydrolysis.

The appearance of the asymmetrical S=O vibration associated with the C-O-SO_3 group in the CNC samples was approximately 1,250 cm^{-1} and the appearance of the symmetrical C-O-SO_3 vibration was approximately 833 cm^{-1} (Gu et al., 2013). There were some bands between 750 and 1,000 cm^{-1} and other bands around 1,350 and 1,175 cm^{-1}, which indicated the presence of sulfonates in the CNC samples (Morais et al., 2013).

The main feature of the CNC samples was the appearance of the band at 1,730 cm^{-1} related to carbonyl groups (C=O) from hemicellulose or esterification of cellulose (Liu et al., 2017). The band of CNCs prepared at 55°C at 1,163 cm^{-1} assigned to C-O in lignin and xylan disappeared, which demonstrated that the lignin or hemicellulose was reduced during the acid hydrolysis procedure with the increasing reaction temperature.

The relative intensity of the band at 1,100 cm^{-1} related to crystalline cellulose was increased in the CNC samples; however, the relative intensity of the band at 900 cm^{-1} related to amorphous cellulose was decreased. It demonstrated that the ratio of crystalline to amorphous cellulose significantly increased after acid hydrolysis.

Crystal Structure of CNC Analysis

Cellulose is composed of the crystalline zone and amorphous zone. The percentage of the crystalline zone as a whole of cellulose is crystallinity. Above cellulose's microproperties, it is very important to study the crystallinity of CNCs. As shown in **Figure 6**, the 002 crystal plane diffraction peak of cellulose I appeared near 22°. The diffraction angle overlapped each other between 101 and 10$\bar{1}$ crystal planes of cellulose I forming the broad diffraction peak during 14.5–17°. It is not hard to find that

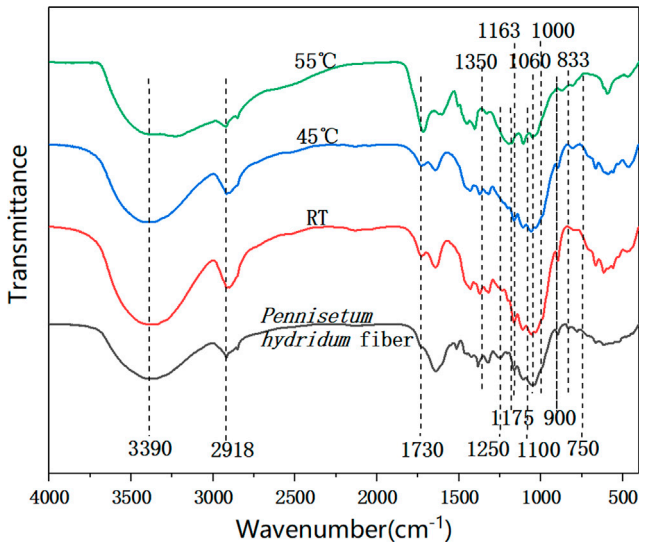

FIGURE 5 | FTIR spectra of the delignified *Pennisetum hydridum* fiber and CNC prepared at different temperatures: **(A)** *Pennisetum hydridum* fiber; **(B)** CNC prepared at RT, 65% wt, and 120 min; **(C)** CNC prepared at 40°C, 65% wt, and 120 min; **(D)** CNC prepared at 55°C, 65% wt, and 120 min.

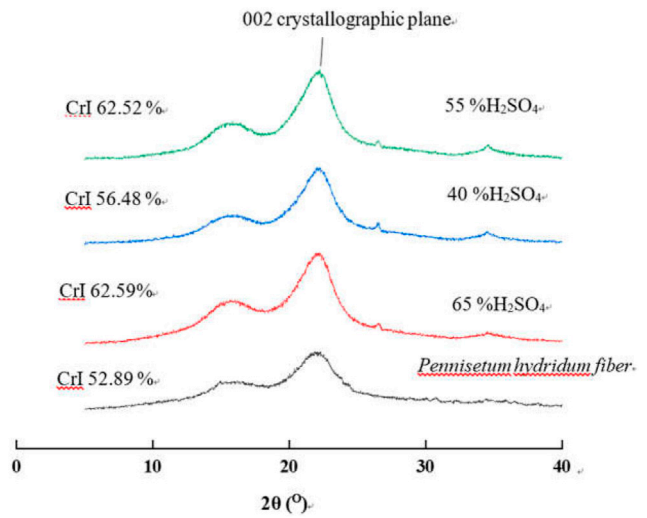

FIGURE 6 | XRD patterns of the CNC at different sulfuric acid concentrations (other conditions: RT, 120 min).

the peak patterns of the CNC and delignified *Pennisetum hydridum* fiber were the same after sulfuric acid hydrolysis. They retained the crystal structure of cellulose I and have been changed. This is because the amorphous region of cellulose is damaged during sulfuric acid hydrolysis, which is consistent with the results of FTIR. The CrI of CNCs increased with the increase of the mass fraction of sulfuric acid due to the hydrolysis of amorphous cellulose. Compared with that of the *Pennisetum hydridum* fiber, the crystallinity of the CNC prepared with the mass fraction of sulfuric acid of 40, 55, and 65% wt increased by

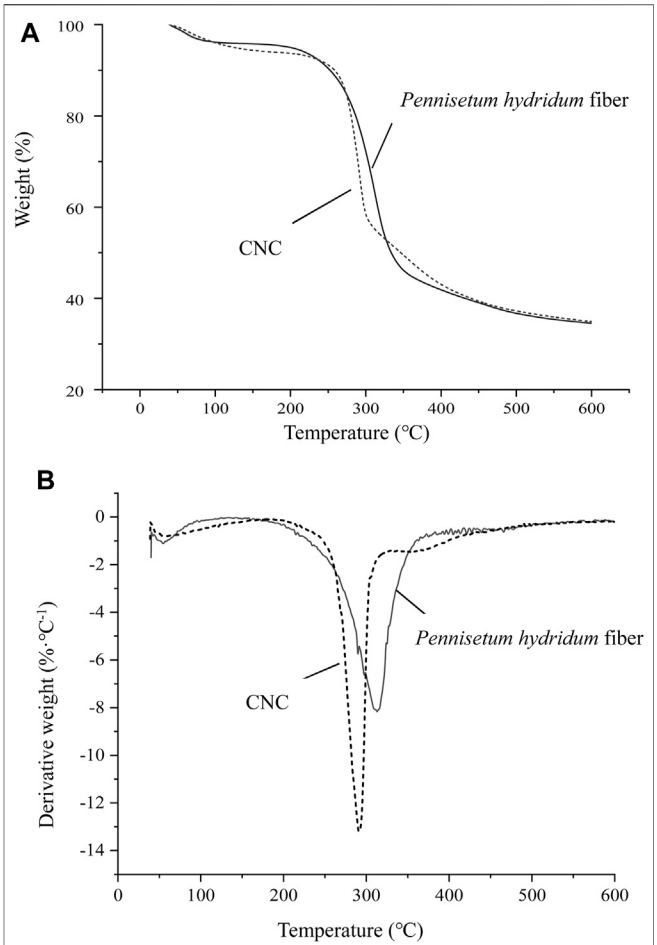

FIGURE 7 | TG **(A)** and DTG **(B)** curves of the CNC prepared at RT, 65% wt, and 120 min and delignified *Pennisetum hydridum* fiber.

6.79, 18.21, and 18.34%, respectively, and the maximum crystallinity reached 62.59% when H_2SO_4 was 65% wt.

Thermogravimetric Analysis of CNCs

During the heating process, the structure of cellulose will be changed and the crystalline zone will be destroyed and even carbonized, finally. The relationship between the sample quality and the temperature change was tested by a thermal analyzer. As shown in **Figure 7**, when the temperature was below 200°C, that stage was mainly the process of water evaporation. TG curves of the CNC and *Pennisetum hydridum* fiber showed a small weight loss ratio, but the CNC (−6.06%) had more weight loss than the *Pennisetum hydridum* fiber (−4.02%) because of its better absorption. The stage of 250–400°C was the process of mass weight loss, and the structure of cellulose was decomposed into various volatile substances. The CNC first exhibited a degradation peak (291.1°C); this is because the presence of sulfur ester groups accelerated the pyrolysis process. When the temperature increased above 400°C, the degradation of cellulose was finished, and the residual masses of the CNC and *Pennisetum hydridum* fiber were equal. The CNC exhibited lower thermal stability compared to the *Pennisetum hydridum* fiber. This is

consistent with the research results of Xu (2016), in which the thermal stability of nanocellulose obtained from palm sheath is significantly lower than that of raw materials. The main reason for this might be linked to disruption of its crystalline structure and the introduction of sulfate groups during sulfuric acid hydrolysis. Moreover, smaller fiber dimensions, leading to higher surface areas exposed to heat, also have negative effects on thermal stability (Widsten et al., 2014).

Thermal stability is also an important parameter that is often considered in applications of materials. Kargarzadeh (2012) studied the influence of hydrolysis conditions on the thermal stability of CNCs obtained from kenaf bast fibers using sulfuric acid. A continuous and progressive decrease in the thermal stability of the nanoparticles occurred as the hydrolysis time increased, probably because of the high sulfation rate demonstrated by the zeta potential measurements (Kargarzadeh et al., 2012). Although reducing the hydrolysis time could improve thermal stability, the size of CNCs produced was larger and the colloid stability was lower. The experimental results of this study also indicated that the size of the CNC was smaller when the hydrolysis time was longer because of degradation of the amorphous region.

CONCLUSION

In this study, the production of CNC-based *Pennisetum hydridum* fiber using ultrasound-assisted sulfuric acid hydrolysis was investigated. The highest yield of CNCs was 43.6%. The fiber length of CNCs was within 500 nm, and the diameter was within 10 nm. CNCs still had the basic structure of cellulose after acid hydrolysis. The significant difference of the CNC samples was the appearance of the band at 1730 cm^{-1} related to carbonyl groups (C=O) from hemicellulose or esterification of cellulose. CNCs exhibited lower thermal stability than the original fiber due to the disruption of crystalline structures and the introduction of sulfate groups in the cellulose. The crystallinity of CNCs increased due to the damage of the amorphous region of cellulose during acid hydrolysis. This research showed that *Pennisetum hydridum* could be used as a raw material to prepare CNCs and provided a new way for resource use of *Pennisetum hydridum* fertilized by MSS, although more studies regarding process optimization, the recovery rate of acid, and end uses for CNC products are needed. In future research, we will use CNCs obtained from *Pennisetum hydridum* as the adsorbent of heavy metals of wastewater or washing agent of heavy metal–contaminated soil.

DATA AVAILABILITY STATEMENT

The original contributions presented in the study are included in the article/supplementary material, and further inquiries can be directed to the corresponding author.

AUTHOR CONTRIBUTIONS

XY have carried out the CNC preparation experiments and YJ have carried out the detailed characterization of the products. QW, ZW and XL have corrected and edited manuscript. YC supported the project financially, reviewed and edited the manuscript.

FUNDING

This work was supported by the Science and Technology Planning Project of Guangdong Province, China (2018B030324003); Local Innovation and Entrepreneurship Team Project of Guangdong Special Support Program (2019BT02L218); Key Realm Research and Development Program of Guangdong Province (2020B0202080001); Pearl River S&T Nova Program of Guangzhou, China (201710010109); National Natural Science Foundation of China (21606092); and China Scholarship Council Fund (201907630001).

REFERENCES

Agarwal, U. (2015). Tailoring the Yield and Characteristics of wood Cellulose Nanocrystals (CNC) Using Concentrated Acid Hydrolysis. *Cellulose* 22 (3), 1753–1762. doi:10.1007/s10570-015-0615-1

Bano, S., and Negi, Y. S. (2017). Studies on Cellulose Nanocrystals Isolated from Groundnut Shells. *Carbohydr. Polym.* 157, 1041–1049. doi:10.1016/j.carbpol.2016.10.069

Beck-Candanedo, S., Roman, M., and Gray, D. G. (2005). Effect of Reaction Conditions on the Properties and Behavior of wood Cellulose Nanocrystal Suspensions. *Biomacromolecules* 6 (2), 1048–1054. doi:10.1021/bm049300p

Camarero Espinosa, S., Kuhnt, T., Foster, E. J., and Weder, C. (2013). Isolation of Thermally Stable Cellulose Nanocrystals by Phosphoric Acid Hydrolysis. *Biomacromolecules* 14 (4), 1223–1230. doi:10.1021/bm400219u

Chen, X., Deng, X., Shen, W., and Liang, J. (2012). Controlled Enzymolysis Preparation of Nanocrystalline Cellulose from Pretreated Cotton Fibers. *Bioresources* 7 (3), 4237–4248.

Chen, Y., Jiang, Y., Wan, J., Wu, Q., Wei, Z., and Ma, Y. (2018). Effects of Wet-Pressing Induced Fiber Hornification on Hydrogen Bonds of Cellulose and on Properties of eucalyptus Paper Sheets. *Holzforschung* 72 (10), 829–837. doi:10.1515/hf-2017-0214

Chen, Y., Wan, J., Dong, X., and Ma, Y. (2013). Fiber Properties of eucalyptus Kraft Pulp with Different Carboxyl Group Contents. *Cellulose* 20, 2839–2846. doi:10.1007/s10570-013-0055-8

Culsum, N. T. U., Melinda, C., Leman, I., Wibowo, A., and Budhi, Y. W. (2021). Isolation and Characterization of Cellulose Nanocrystals (CNCs) from Industrial Denim Waste Using Ammonium Persulfate. *Mater. Today Commun.* 26, 101817. doi:10.1016/j.mtcomm.2020.101817

Dai, S. (2011). *Fabrication, Characterization and Application of Nancellulose from Hemp Fibres.* Fuzhou, China: Dissertation, Fujian Agriculture and Forestry University.

Deepa, B., Abraham, E., Cordeiro, N., Mozetic, M., Mathew, A. P., Oksman, K., et al. (2015). Utilization of Various Lignocellulosic Biomass for the Production of Nanocellulose: a Comparative Study. *Cellulose* 22, 1075–1090. doi:10.1007/s10570-015-0554-x

Gao, B. B. (2011). Summarization of Nano-Cellulose. *Value Eng.* 30 (34), 272–273.

Gu, J., Catchmark, J. M., Kaiser, E. Q., and Archibald, D. D. (2013). Quantification of Cellulose Nanowhiskers Sulfate Esterification Levels. *Carbohydr. Polym.* 92 (2), 1809–1816. doi:10.1016/j.carbpol.2012.10.078

Habibi, Y., Lucia, L. A., and Rojas, O. J. (2010). Cellulose Nanocrystals: Chemistry, Self-Assembly, and Applications. *Chem. Rev.* 110, 3479–3500. doi:10.1021/cr900339w

He, H., Pan, J., Yu, P., Chen, G., and Li, H. (2017). Effects of Hybrid Giant Napier Biochar on Cadmium Migration in a Cabbage-Soil System Contaminated with

Cadmium and Butachlor. *Pol. J. Environ. Stud.* 26 (2), 619–625. doi:10.15244/pjoes/65362

He, L., Zhu, Q. L., Wang, Y. W., He, M. X., and Tan, F. R. (2020). Advances in Research on the Comprehensive Utilization of a Perennial Grass Pennisetum Hydridum. *Chin. J. Appl. Environ. Biol.* 26 (3), 705–712.

Huang, Z. J., Zhu, Z. A., Wu, X. S., Lai, X. L., Wang, P. Y., Hu, X. J., et al. (2016). Adsorption of Heavy Metals by Biochar Derived from *Pennisetum* Sinese Roxb. *Environ. Chem.* 35 (4), 766–772.

Jiang, Y., Wu, Q., Wei, Z., Wang, J., Fan, Z., Pang, Z., et al. (2019). Papermaking Potential of Pennisetum Hybridum Fiber after Fertilizing Treatment with Municipal Sewage Sludge. *J. Clean. Prod.* 208, 889–896. doi:10.1016/j.jclepro.2018.10.148

Kargarzadeh, H., Ahmad, I., Abdullah, I., Dufresne, A., Zainudin, S. Y., and Sheltami, R. M. (2012). Effects of Hydrolysis Conditions on the Morphology, Crystallinity, and thermal Stability of Cellulose Nanocrystals Extracted from Kenaf Bast Fibers. *Cellulose* 19 (3), 855–866. doi:10.1007/s10570-012-9684-6

Kontturi, E., Meriluoto, A., Penttilä, P. A., Baccile, N., Malho, J.-M., Potthast, A., et al. (2016). Degradation and Crystallization of Cellulose in Hydrogen Chloride Vapor for High-Yield Isolation of Cellulose Nanocrystals. *Angew. Chem. Int. Ed.* 55, 14455–14458. doi:10.1002/anie.201606626

Lin, X. Y., Wang, H., Wang, H., Chen, C., Wu, Q. T., Wei, Z. B., et al. (2015). Using Hybrid Giant Napier to Treat Municipal Sewage Sludge and Produce Plant Biomass. *Acta Ecol. Sin* 35 (12), 4324–4240. doi:10.5846/stxb201311042658

Liu, C., Du, H. S., Yu, G., Zhang, Y. D., Kong, Q. S., Li, B., et al. (2017). Simultaneous Extraction of Carboxylated Cellulose Nanocrystals and Nanofibrils via Citric Acid Hydrolysis—A Sustainable Route. *Pap. Biomater.* 2 (4), 19–26.

Liu, H., Du, H., Zheng, T., Liu, K., Ji, X., Xu, T., et al. (2021). Cellulose Based Composite Foams and Aerogels for Advanced Energy Storage Devices. *Chem. Eng. J.* 426, 130817. doi:10.1016/j.cej.2021.130817

Liu, K., Du, H., Zheng, T., Liu, H., Zhang, M., Zhang, R., et al. (2021). Recent Advances in Cellulose and its Derivatives for Oilfield Applications. *Carbohydr. Polym.* 259, 117740. doi:10.1016/j.carbpol.2021.117740

Liu, W., Du, H., Zhang, M., Liu, K., Liu, H., Xie, H., et al. (2020). Bacterial Cellulose-Based Composite Scaffolds for Biomedical Applications: a Review. *ACS Sustainable Chem. Eng.* 8, 7536–7562. doi:10.1021/acssuschemeng.0c00125

Ma, C. J., Ming, H., and Li, H. S. (2013). Study of Red Mud Improvement with the Mixing Method and the Impact of Pennisetum Hybridum Plantation on Red Mud Amendment. *Amr* 807-809, 392–401. doi:10.4028/www.scientific.net/amr.807-809.392

Ma, C., Naidu, R., Liu, F., Lin, C., and Ming, H. (2012). Influence of Hybrid Giant Napier Grass on Salt and Nutrient Distributions with Depth in a saline Soil. *Biodegradation* 23 (6), 907–916. doi:10.1007/s10532-012-9583-4

Mao, H. Q., Gong, Y. Y., Liu, Y. L., Wang, S. Q., and Du, L. L. (2017). Progress in Nanocellulose Preparation and Application. *Pap. Biomater.* 2 (4), 65–76.

Morais, J. P. S., Rosa, M. d. F., de Souza Filho, M. d. S. M., Nascimento, L. D., do Nascimento, D. M., and Cassales, A. R. (2013). Extraction and Characterization of Nanocellulose Structures from Raw Cotton Linter. *Carbohydr. Polym.* 91, 229–235. doi:10.1016/j.carbpol.2012.08.010

Mukherjee, S. M., and Woods, H. J. (1953). X-ray and Electron Microscope Studies of the Degradation of Cellulose by Sulphuric Acid. *Biochim. Biophys. Acta* 10, 499–511. doi:10.1016/0006-3002(53)90295-9

Nickerson, R. F., and Habrle, J. A. (1947). Cellulose Intercrystalline Structure. *Ind. Eng. Chem.* 39 (11), 1507–1512. doi:10.1021/ie50455a024

Nurain, J., Ishak, A., and Alain, D. (2012). Extraction, Preparation and Characterization of Cellulose Fibres and Nanocrystals from rice Husk. *Ind. Crop Prod.* 37 (1), 93–99. doi:10.1016/j.indcrop.2011.12.016

Peng, N. M., Chen, X. R., Zhang, R. X., and Zheng, M. J. (2010). The Cultivation and Comprehensive Utilization Technology of Hybrid Giant Napier. *Mod. Agric. Sci. Technol.* (8), 348–358.

Phanthong, P., Reubroycharoen, P., Hao, X., Xu, G., Abudula, A., and Guan, G. (2018). Nanocellulose: Extraction and Application. *Carbon Resour. Convers.* 1 (1), 32–43. doi:10.1016/j.crcon.2018.05.004

Qin, F. Y. (2018). *Study on Zeta Potential Measurement Based on Phase Analysis Light Scattering*. Zibo, China: Dissertation, Shandong University of Technology.

Ru, J., Geng, B. Y., Tong, C. C., Wang, H. Y., Wu, S. C., and Liu, H. Z. (2017). Nanocellulose-based Adsorption Materials. *Prog. Chem.* 29 (10), 1228–1251. doi:10.7536/PC170616

Tang, L. R., Ou, W., Lin, W. Y., Chen, Y. D., Chen, X. R., and Huang, B. (2011). Optimization of Acid Hydrolysis Processing of Nanocellulose crystal Using Response Surface Methodology. *Chem. Ind. Prod.* 31 (6), 61–65.

Tang, Y., Yang, S., Zhang, N., and Zhang, J. (2014). Preparation and Characterization of Nanocrystalline Cellulose via Low-Intensity Ultrasonic-Assisted Sulfuric Acid Hydrolysis. *Cellulose* 21 (1), 335–346. doi:10.1007/s10570-013-0158-2

Vanderfleet, O. M., Osorio, D. A., and Cranston, E. D. (2018). Optimization of Cellulose Nanocrystal Length and Surface Charge Density through Phosphoric Acid Hydrolysis. *Phil. Trans. R. Soc. A.* 376 (2112), 20170041. doi:10.1098/rsta.2017.0041

Visanko, M., Liimatainen, H., Sirviö, J. A., Heiskanen, J. P., Niinimäki, J., and Hormi, O. (2014). Amphiphilic Cellulose Nanocrystals from Acid-free Oxidative Treatment: Physicochemical Characteristics and Use as an Oil-Water Stabilizer. *Biomacromolecules* 15 (7), 2769–2775. doi:10.1021/bm500628g

Wang, H. K. (2013). Preparation, Characterization and Application of Nano Cellulose Fibrils from Bamboo. *Dissertation, Chinese Academy of Forestry, Beijing, China*.

Wang, Q., Zhao, X., and Zhu, J. Y. (2014). Kinetics of Strong Acid Hydrolysis of a Bleached Kraft Pulp for Producing Cellulose Nanocrystals (CNCs). *Ind. Eng. Chem. Res.* 53 (27), 11007–11014. doi:10.1021/ie501672m

Wang, X. N., Yi, Z. C., Zhang, Y. F., Wang, J. Q., Zhang, Y. J., and Li, H. S. (2015). Responses and Remediating Effects of *Pennisetum Hydridum* to Application of Heavy-Metals-Contaminated Chicken Manures and Sewage Sludges. *J. Agric. Resour. Environ.* 32 (5), 477–484. doi:10.13254/j.jare.2015.0064

Widsten, P., Dooley, N., Parr, R., Capricho, J., and Suckling, I. (2014). Citric Acid Crosslinking of Paper Products for Improved High-Humidity Performance. *Carbohydr. Polym.* 101, 998–1004. doi:10.1016/j.carbpol.2013.10.002

Xie, H., Zhao, X. M., Xie, Z., Wu, K. Q., Li, X. L., Yang, R. G., et al. (2016). Phytoremediation Efficiency of *Pennisetum Hydridum* for Acid- and Cadmium-Polluted Soil and its Safe Utilization. *J. Agric. Resour. Environ.* 35 (3), 478–484. doi:10.11654/jaes.2016.03.010

Xu, W. Y., Fu, S. Y., Peng, Y. Y., and Liu, H. (2016). Preparation of Nanocellulose from Three Typical Plants in the South Area. *J. Dalian Polytech Uni* 35 (5), 347–352.

Xu, W. Y. (2016). *The Research of Nanocellulose Fiber Raw Material Preparation*. Dissertation, South China University of Technology, Guangzhou, China.

Yi, Z. C., He, J. B., Cheng, H., Lu, S. M., He, H. Z., Zhang, W. Q., et al. (2014). Effects of Cd Polluted Soil on the Modular Growth and Physiological Characteristics of *Pennisetum Hydridum*. *J. Agric. Resour. Environ.* 33 (2), 276–282.

Zhao, T., Jiang, C. A., Qiu, J. R., Wang, X. J., Zeng, J. W., and Zhou, Z. H. (2017). Research on Adsorption Properties of Sulfonamides in Aqueous Solution by *Pennisetum Hydridum* Derived Biochar. *Technol. Water Treat.* 43 (4), 56–65. doi:10.16796/j.cnki.1000-3770.2017.04.013

Zhao, Y. H., Lun, Y. H., Chen, W., and Jiang, Q. (2015). Research on the Comprehensive Exploitation and Utilization of Hybrid Giant Napier. *J. Yichun Coll.* 37 (9), 89–91.

Conflict of Interest: The authors declare that the research was conducted in the absence of any commercial or financial relationships that could be construed as a potential conflict of interest.

Publisher's Note: All claims expressed in this article are solely those of the authors and do not necessarily represent those of their affiliated organizations, or those of the publisher, the editors, and the reviewers. Any product that may be evaluated in this article, or claim that may be made by its manufacturer, is not guaranteed or endorsed by the publisher.

frontiers in Energy Research

ORIGINAL RESEARCH
published: 25 November 2021
doi: 10.3389/fenrg.2021.782545

Durable Biopolymer Films From Lignin-Carbohydrate Complex Derived From a Pulp Mill Side Stream

Brita Asikanius[1,2], Anna-Stiina Jääskeläinen[2], Hanna Koivula[3], Petri Oinonen[4] and Monika Österberg[1]**

[1]Department of Bioproducts and Biosystems, Aalto University, Espoo, Finland, [2]Research and Development Center, Kemira Oyj, Espoo, Finland, [3]Department of Food and Nutrition and Helsinki Institute of Sustainability Science, University of Helsinki, Helsinki, Finland, [4]Ecohelix AB, Stockholm, Sweden

Valorization of side streams offers novel types of raw materials to complement or replace synthetic and food-based alternatives in materials science, increasing profitability and decreasing the environmental impacts of biorefineries. Lignocellulose biomass contains lignin and carbohydrates that are covalently linked into lignin-carbohydrate complexes (LCCs). In biomass fractionation processes, these complexes are conventionally considered as waste, which hinders the biomass fractionation process, and they may solubilize into aqueous effluents. This study presents how LCCs, derived from pulp mill effluent, can be turned into valuable biopolymers for industrial polymer film applications. Free-standing composite films containing hydroxyethyl cellulose (HEC) and LCCs with varying molar mass, charge density and lignin/hemicellulose ratio were prepared to study the effect of LCC amount on mechanical properties and oxygen permeability. Increasing the LCC content increased the yield point and Young's modulus of the films. Breaking strain measurements revealed a non-linear correlation with the LCC concentration for the samples with higher lignin than hemicellulose content. The addition of LCC enhanced oxygen barrier properties of HEC films significantly even at high relative humidity. The present research demonstrates how a currently underutilized fraction of the biorefinery side stream has the potential to be valorized as a biopolymer in industrial applications, for example as a barrier film for paper and board packaging.

Keywords: lignin-carbohydrate complex, LCC, biopolymer film, lignocellulose biomass, side stream valorization, mechanical properties, oxygen barrier

OPEN ACCESS

Edited by:
Chen Huang,
Chinese Academy of Forestry, China

Reviewed by:
Chunbao (Charles) Xu,
Western University, Canada
Caoxing Huang,
Nanjing Forestry University, China
Bailiang Xue,
Shaanxi University of Technology, China

****Correspondence:***
Brita Asikanius
brita.asikanius@aalto.fi
Monika Österberg
monika.osterberg@aalto.fi

Specialty section:
This article was submitted to Bioenergy and Biofuels, a section of the journal Frontiers in Energy Research

Received: *24 September 2021*
Accepted: *03 November 2021*
Published: *25 November 2021*

Citation:
Asikanius B, Jääskeläinen A-S, Koivula H, Oinonen P and Österberg M (2021) Durable Biopolymer Films From Lignin-Carbohydrate Complex Derived From a Pulp Mill Side Stream. Front. Energy Res. 9:782545. doi: 10.3389/fenrg.2021.782545

INTRODUCTION

Lignin-carbohydrate complexes (LCCs) are biopolymers consisting of covalently bound lignin and carbohydrate moieties. They are formed during the biosynthesis of plant cell walls, and their function in natural systems is to enhance the mechanical strength of plants (Zhang et al., 2020). It is estimated that all lignin fragments in softwood and 47–66% of the lignin in hardwood are bound with carbohydrate moieties, mostly hemicellulose (Lawoko et al., 2005; Henriksson et al., 2007). The chemical structures of LCCs vary depending on the wood source and type of the refinery process. Therefore, their chemical and physical properties are not well understood (Zhao et al., 2020). The covalent bonds between lignin and carbohydrate moieties have been studied by ^{1}H, ^{13}C and 2D NMR spectroscopies, and the main linkages identified are phenyl

glycoside, acetal, ester and benzyl ether bonds (Balakshin et al., 2011; Giummarella et al., 2019; Pei et al., 2020; Zhao et al., 2020).

In a biomass fractionation process, the aim is to separate cellulose, lignin and hemicellulose. However, the stable covalent bonds between lignin and carbohydrate moieties reduce the selective fractionation of the wood components and hinder the delignification processes, restricting the efficient use of biomass (Balakshin et al., 2011; Yuan et al., 2012; Giummarella et al., 2019; Carvalho et al., 2020; Zhao et al., 2020). The fraction containing LCCs is typically considered to have minor value and therefore ends up in the process side stream. The majority of biorefinery side streams are currently used in low-value applications, for example as combustible material, or treated as waste (Strassberger et al., 2014; Abbadessa et al., 2018; Giummarella et al., 2019). Some challenges hindering the efficient use of the biorefinery side streams are, for example, the low technology readiness level for efficient recovery, the varying chemical structure of the components and the competition from cheaper fossil-based alternatives with well-known chemical characteristics in applications. Enabling the use of new types of raw materials derived from such side streams would require developing novel extraction technologies which in turn may lead to the need for investments to modify the host process.

Finding valuable uses for biorefinery side streams is a significant factor in optimizing the use of biomass. Valorizing the currently unexploited fraction in second-generation biorefineries is expected to increase the process profitability and to have a positive impact on the carbon footprint of the process plants (Steinmentz et al., 2019; Wu et al., 2020). Aiming for zero-waste production is an ambitious goal for biorefineries seeking to develop a more sustainable bioeconomy. However, it is well aligned with the climate change targets of the United Nation's Sustainable Development Goals. Efficient valorization of process side streams could reduce the amount of waste produced at the mill. As an example, we have calculated that for a pulp mill with a 200 000-ton yearly production rate it is possible to reduce the amount of organic waste by 20 000-ton and turn that side stream into valuable biopolymers. To be able to valorize the process effluents, deeper insights into the chemical composition of the produced side streams are required and efficient approaches for their application in materials are needed.

While the structure of various LCCs has been extensively studied (Balakshin et al., 2011; Giummarella et al., 2019; Pei et al., 2020; Zhao et al., 2020), the potential of LCCs in applications is less explored. Dong et al. (2020) reported on the advantage of the oxygen scavenging ability of LCCs in biomedical applications, while (Rivière et al., 2020) suggested that the carbohydrate rich residue from biorefineries could be used in nanocomposites together with cellulose nanofibrils, but in that case the LCCs had a detrimental effect on both mechanical properties and oxygen permeability. The aim of this study is to show examples of how a currently underutilized LCC from a specific biorefinery side stream could be converted into a valuable biopolymer. The experiments were performed at laboratory scale, but the LCC production is aiming to reach technology readiness level 7 meaning that the production will be demonstrated at industrially relevant scale. The feedstock originates from a dissolving pulp mill with a sulphite cooking process using a prehydrolysis step to remove LCC and other impurities from the cellulose fraction. Some of the prehydrolysis liquor is circulated back into the process but most of it is treated as waste. The LCC was derived from this side stream and modified enzymatically by Ecohelix technology (Oinonen 2014). The polymer studied in this work is water soluble and anionically charged. The work demonstrates the potential of the LCC to be valorized in polymeric film applications.

As an example, composite films with LCC, hydroxyethyl cellulose and glycerol were produced. The effect of LCC amount, molecular weight and lignin/hemicelluose ratio on mechanical properties is shown and compared to the behavior of lignosulphonate. Increased LCC content is observed to enhance durability. The oxygen barrier was selected as an example application for polymeric films in paper and packaging application. It is shown that LCC decreases the oxygen transmission rate significantly at various humidity levels.

MATERIALS AND METHODS

Materials

The LCC studied in this work was produced by Ecohelix technology (Oinonen et al., 2013; Oinonen et al., 2015) from the side stream of the Domsjö Fabriker dissolving pulp mill and polymerized by laccase treatment using Ecohelix technology (Henriksson et al., 2012). The Ecohelix process (**Figure 1**) is based on membrane filtration and enzymatic treatment working in unison. The first membrane filtration unit was used to concentrate the desired molecules in the pre-hydrolysis liquor and to return cooking liquors and undesired organic molecules back to the host process. The consecutive enzymatic treatment phase utilized a redox enzyme laccase for the chain extension of molecules containing reactive phenolic moieties, such as non-condensed guaiacyl units in the LCC. The last phase of the process utilized another membrane filtration process to refine and control the molecular weight of the polymeric product and to separate the sugar fraction that contained the unreacted molecules. The produced lignin-carbohydrate complex consisted of alternating lignin and polysaccharide segments, providing an amphiphilic structure. It was negatively charged due to the sulfonic acid groups on the lignin, and carboxyl groups on the polysaccharide moieties.

The specific LCC used here, LCC 80/20, was an aqueous solution with approximately 20 w-% solids content. LCC 80/20 was compared to three other polymers: LCC 80/20 high molecular weight (HMW), LCC 40/60, and lignosulphonate. LCC 80/20 HMW was derived from the same feedstock as LCC 80/20 but polymerized for longer time to reach a higher degree of polymerization. LCC 40/60 was derived from a thermomechanical pulping process (TMP) and had a larger hemicellulose fraction compared to LCC 80/20. The final reference was lignosulphonate from Domsjö Fabriker AB. All samples were provided by Ecohelix AB. Free-standing films were formed as composites with hydroxyethyl cellulose (HEC) having

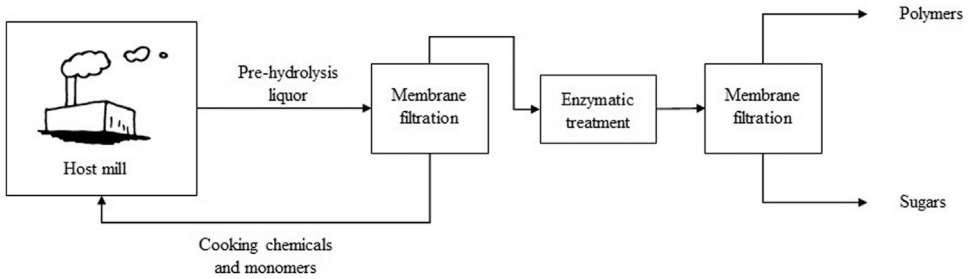

FIGURE 1 | Schematic description of the Ecohelix process for LCC production.

a viscosity based molar mass of 90 kDa on average. Glycerol was used as a plasticizer. HEC and glycerol were purchased from Sigma Aldrich, United States.

Lignin and Carbohydrate Content

The lignin content of LCC 80/20 was quantified by UV spectroscopy at 280 nm wavelength using absorptivity of 11.9 g^{-1} cm^{-1}, reported previously for lignosulphonate (Lin 1992). The carbohydrate content was analyzed after acid methanolysis and silylation by gas chromatography equipped with a flame ionization detector (GC FID) (Sundberg et al., 2007; Wang et al., 2020).

Molar Mass

The weight average molar masses of LCC 80/20, LCC 80/20 HMW, LCC 40/60, and lignosulphonate were determined by size-exclusion chromatography (SEC) using Viscotek GPCmax TDA 302 SEC equipment with refractive index detection. The eluent was 0.1 M $NaNO_3$ in MilliQ-water with 2.5 v-% acetonitrile, and a flow rate of 0.8 ml/min in 35°C was used. The column set consisted of three columns (Waters Ultrahydrogel 2000, 500 and 120) and a guard column. The injection volume was 50 µL. The quantification was performed using pullulan calibration standards with molar masses between 342 and 708 000 Da purchased from Polymer Standard Service, Germany.

Charge Density

To quantify the charge densities, the polymers were titrated with cationic PDADMAC (polydiallyl dimethyl ammonium chloride) (BTG, Germany) having a specific charge of 1 meq/l and molar mass of 107 kDa. The specific charge of the samples was calculated by **Eq. 1**, where q is the specific charge (meq/g), c and V are the concentration (meq/l) and volume (l) of the titrant respectively, and m is the mass of the studied polyelectrolyte (g).

$$q = \frac{cV}{m} \tag{1}$$

Free Standing Films

In preliminary film formation trials, it was observed that the pure LCC 80/20 produced too fragile films to be handled in the tensile and oxygen transmission tests. Therefore, preparation of composite films with another film forming biopolymer and plasticizer was required. Free-standing films were prepared to an average grammage of 100 g/m^2. Dry composite films contained 5 w-% glycerol as a plasticizer, 0–50 w-% LCC or lignosulphonate at 10 w-% intervals, and 95–45 w-% HEC. Films were prepared by mixing the components as 2 w-% water solutions for at least 30 min prior to solvent evaporation. Prior to mixing the components, HEC was dissolved by magnetic stirring, heating the solution to 80°C, and filtering with 75 and 20 µm sieves before use. LCC 80/20, LCC 80/20 HMW, LCC 40/60, lignosulphonate and glycerol were diluted using magnetic stirring at room temperature and filtered using a 20 µm sieve. The films were cast on plastic petri dishes with a 9 cm diameter, and water was evaporated in a 50°C heating chamber for 1 day. The thickness of the films was measured with a Lorentzen and Wettre SE 250 D micrometer by placing the films between two transparencies to avoid mechanical damage to the films.

Mechanical Properties

Mechanical properties of the composite films containing LCC 80/20, LCC 80/20 HMW, LCC 40/60, and lignosulphonate were evaluated by measuring stress-strain curves with a tensile and compression testing machine, MTS 400 (MTS Systems Norden AB, Sweden). The films were cut into slices with 15 mm width, and three parallel samples were measured. A load cell of 50 N was used with a pulling rate of 5 mm/min. Measurements were performed in a climate-controlled laboratory with 50% humidity and 23°C temperature after 2–6 h climatization before the measurement. The average values of the three samples were used to quantify Young's modulus and breaking strain.

Oxygen Transmission Rate

The oxygen transmission rate (OTR) for the composite films containing varying amounts of LCC 80/20 was quantified at two different humidity levels, according to the standard test method for oxygen gas transmission rate through plastic film and sheeting using a coulometric sensor (ASTM D 3985-05). The films were measured using a 5 cm^2 area and a pressure gradient of 1 atm. The first set of samples was measured with a Systech Oxygen Permeation Analyzer 8001 at 23°C and 50% relative humidity (RH), analyzing four parallel

TABLE 1 | Lignin/hemicellulose ratio, charge density at pH 6 and apparent molar mass for LCC 80/20, LCC 80/20 HMW, LCC 40/60 and lignosulphonate.

Sample	Lignin (L) + Hemicellulose (H)	Charge density (pH 6)	Apparent M_w (PDI)
LCC 80/20	790 mg/g L + 180 mg/g H	−2.2 meq/g	50 kDa (3.8)
LCC 80/20 HMW	800 mg/g L + 190 mg/g H	−2.9 meq/g	200 kDa (5.9)
LCC 40/60	430 mg/g L + 570 mg/g H	−0.3 meq/g	50 kDa (4.2)
Lignosulphonate	1,000 mg/g L	−1.3 meq/g	10 kDa (5.8)

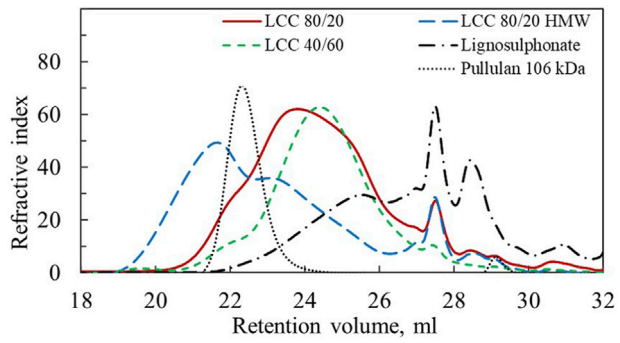

FIGURE 2 | SEC chromatograms for LCC 80/20, LCC 80/20 HMW, LCC 40/60, lignosulphonate and pullulan calibration standard with M_w 106 kDa.

samples of each film containing 0, 10, 20, 30 and 40 w-% LCC 80/20. Prior to the analysis, the films were stabilized overnight in a climate-controlled room with constant 50% humidity and 23°C temperature.

The oxygen transmission rate test for the second set of samples was performed with another Systech Oxygen Permeation Analyzer 8001 having the capability to raise the humidity level. This time the experiments were performed at 23°C and 80% RH, again analyzing four parallel samples of each concentration. Prior to the test, the samples were stored for at least 24 h at 50% RH and 23°C. To ensure that the films were at the desired humidity, they were measured under these conditions at least one day. Before recording the result, the variation in oxygen transmission had to be less than 5% during the last 20% of the measuring time.

Oxygen permeability (OP) in $(cm^3\ mm)/(m^2\ day\ atm)$ was calculated from the OTR result in $(cm^3)/(m^2\ day)$ using **Eq. 2** where l is thickness (mm) of the films and ΔP (atm) is the pressure gradient.

$$OP = OTR\left(\frac{l}{\Delta P}\right) \quad (2)$$

RESULTS AND DISCUSSION

LCC Characterization

The lignin/hemicellulose ratio, charge density and weight average molar mass (M_w) of LCC 80/20, LCC 80/20 HMW, LCC 40/60, and lignosulphonate are shown in **Table 1**. The polydispersity index (PDI) describes the heterogeneity of the size distribution and is reported with the molar mass values. Pullulan was used for the molar mass calibration because standards made of LCCs were not commercially available and pullulan has been used for the molar mass determination of similar water soluble LCC previously (Abbadessa et al., 2018). It should be noted that the chemical composition of pullulan differs significantly from the studied LCC, and hence the measured molar mass values are only estimates used for qualitative comparison of the size of the different polymers studied in this work and should not be taken as exact values. SEC chromatograms presented in **Figure 2** visualize the molar mass distribution for the different samples and the pullulan standard with 106 kDa M_w.

The apparent M_w of LCC 80/20 HMW is four times higher than for LCC 80/20 (**Table 1**). In the SEC chromatogram (**Figure 2**) it is observed that although the LCC 80/20 HMW peak has a bimodal shape indicating large polydispersity, the peak maximum has moved to a smaller retention volume. Thus, it can be concluded that the HMW sample was notably larger in size compared to the LCC 80/20, and these two samples could be used to study the effect of molecular weight on performance.

Comparing LCC 80/20 and LCC 40/60 in **Figure 2**, their peak maxima and shapes are both similar, indicating that their molar masses are close. These samples had different lignin/hemicellulose ratios and charge densities. LCC 80/20 had significantly higher lignin content, while for the LCC 40/60, the hemicellulose content was higher; the lignin/hemicellulose ratios were 80/20 and 40/60, respectively. The charge densities of LCC 80/20 and LCC 40/60 were −2.2 meq/g and −0.3 meq/g, respectively. The samples originated from different pulping processes and raw materials. LCC 80/20 was produced from the side stream of the Domsjö Fabriker mill that utilizes a mixture of Norway spruce and Scotch pine as the raw material, while LCC 40/60 was produced from a side stream of a Swedish pulp mill with only Norway spruce as the raw material. LCC 80/20 was derived from dissolving pulp production, which is a chemical pulping process utilizing sulfite and bisulfite ions to digest the wood chips. In the Domsjö Fabriker process, a pre-hydrolysis step was included, utilizing sulphur dioxide and sodium hydroxide to form sodium bisulfite in low chemical concentrations and at a higher pH (4) than in the main cooking process. This caused sulphonation of the lignin as well as its dissolution. Due to the higher pH, the hemicelluloses were not completely hydrolyzed and could be utilized. The sulphonate groups were the main contributors to the high negative charge of the polymer. LCC 40/60 was derived from the TMP process utilizing water and heat to soften the wood

TABLE 2 | Hemicellulose content of LCC 80/20 analyzed by GC-FID.

Substance	Amount (%)	Substance	Amount (%)	Substance	Amount (%)
Arabinose	0.6	Galactose	3.9	Galacturonic acid	0.4
Rhamnose	0.1	Glucose	2.4	Glucuronic acid	0.3
Xylose	1.6	Mannose	7.8	4-O-methylglucuronic acid	0.4

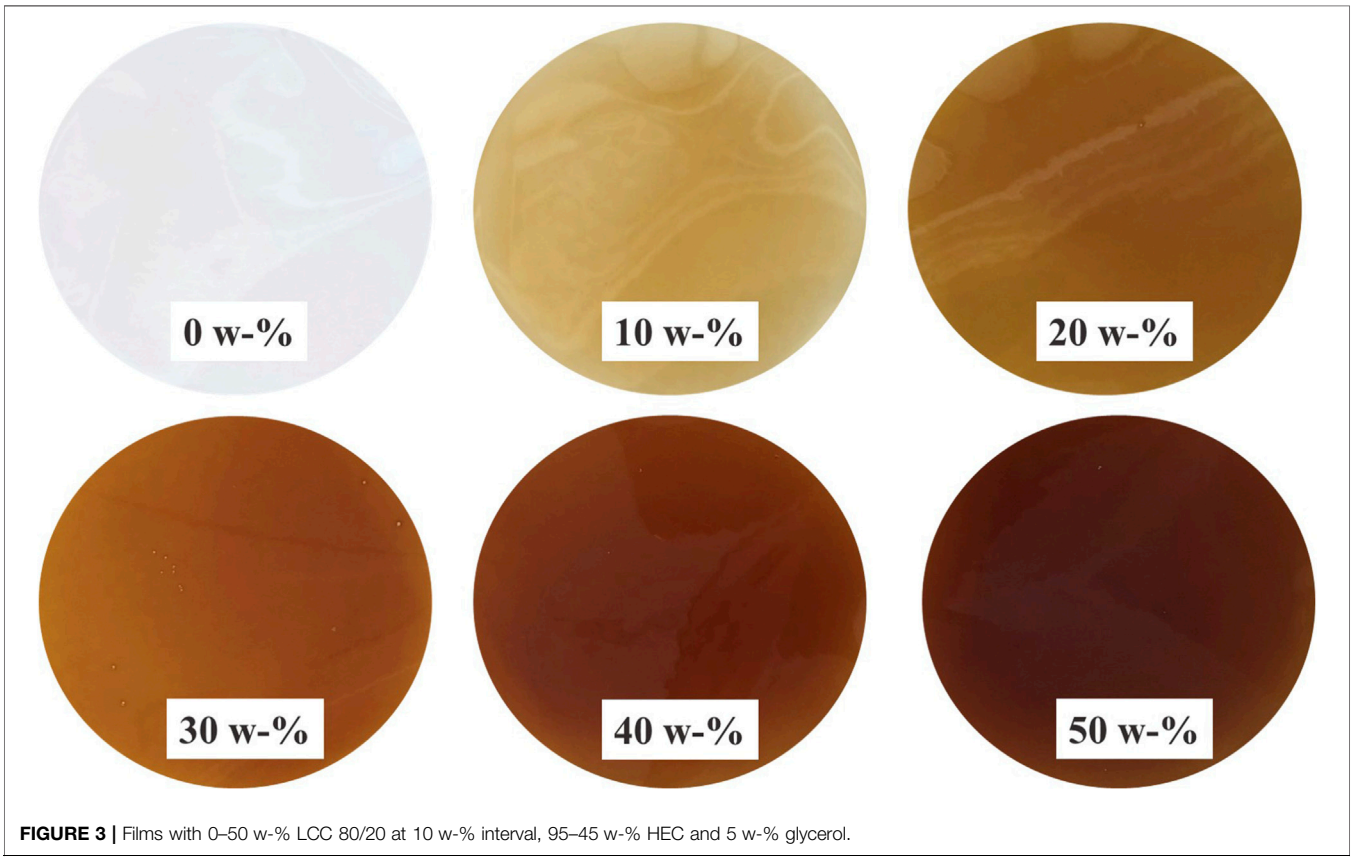

FIGURE 3 | Films with 0–50 w-% LCC 80/20 at 10 w-% interval, 95–45 w-% HEC and 5 w-% glycerol.

matrix and especially the lignin. The wood chips were then processed in mechanical refiners to separate the wood fibers into pulp. During this process, hemicelluloses and some bound and unbound lignin were dissolved in the side-stream liquors.

The lignosulphonate sample had substantially lower molecular weight than the LCC samples, although this sample also had a bimodal shape (**Figure 2**). Lignosulphonate contained no hemicellulose fraction, and its charge density (−1.1 meq/g) was in between the charge of LCC 80/20 and LCC40/60.

The hemicellulose fraction in LCC 80/20 consisted of varying sugar units (**Table 2**), mostly mannose, galactose, glucose and xylose. This result confirms the earlier observation (Oinonen 2014) that the LCC 80/20 possess predominantly galactoglucomannan as the hemicellulose moiety.

Visual Appearance of the Films

Free-standing films of LCC 80/20 are shown in **Figure 3**. The glycerol content was held constant at 5 w-%, the LCC content was varied between 0–50 w-% at 10 w-% intervals, and the remaining part (95-45 w-%) was completed with HEC. The brown color in the films originated from the lignin fraction of LCCs.

LCC 80/20 with HEC and glycerol formed very smooth films without any visible irregularities, and similar films were achieved with LCC80/20 HMW, LCC 40/60, and lignosulphonate. This is well in line with previous confocal reflectance microscopy images of thin films from pure LCC 80/20 films showing that the LCCs form very smooth films without any visible precipitates (Borrega et al., 2020).

Mechanical Properties of Composite Films

Mechanical properties of the free-standing films containing varying amounts of LCC 80/20, LCC 80/20 HMW, LCC 40/60, and lignosulphonate were characterized by measuring stress-strain curves (**Figure 4**). In the stress-strain experiment, the films are mechanically elongated until they break, which quantifies stress as a function of strain. During the measurement, the sample

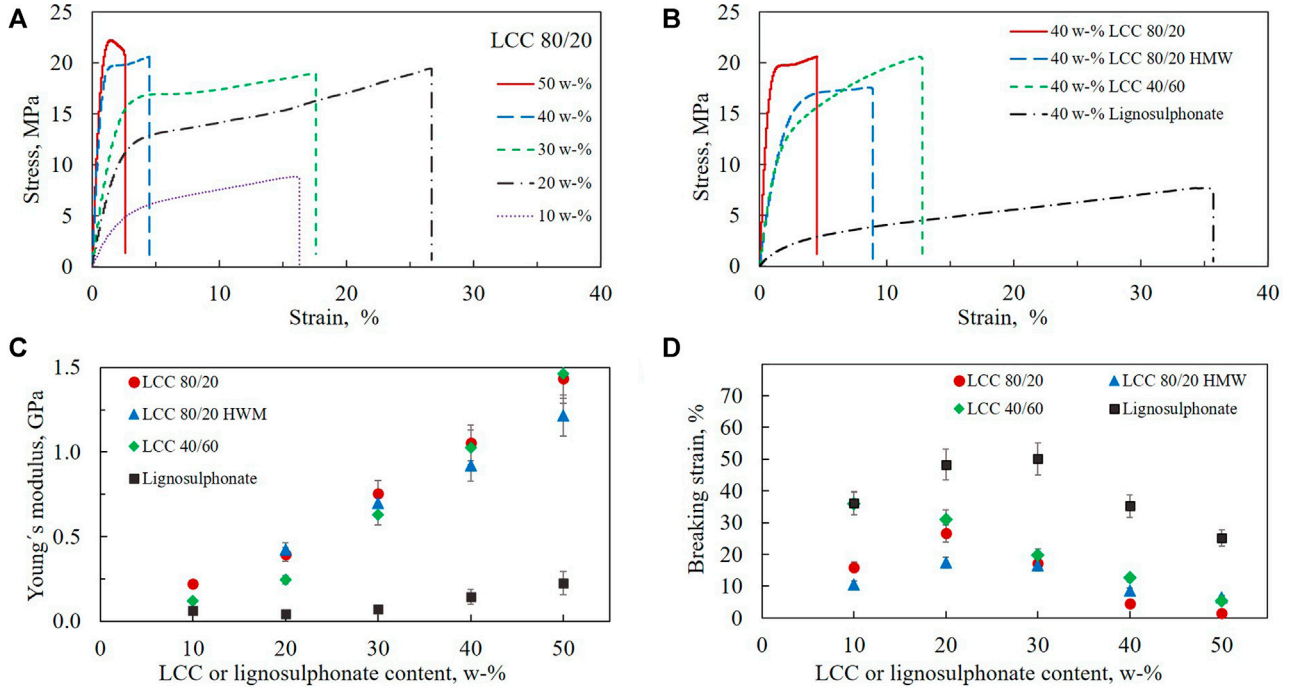

FIGURE 4 | Mechanical properties of free-standing HEC-based films containing LCCs or lignosulphonate. **(A)** Stress-strain curves for films containing 10–50 w-% LCC 80/20. **(B)** Stress-strain curves for films containing 40 w-% LCC or lignosulphonate. **(C)** Young´s modulus of films as a function of LCC or lignosulphonate content. **(D)** Breaking strain of films as a function of LCC or lignosulphonate content. All films contained 5 w-% glycerol and 85–45 w-% HEC depending on LCC content.

absorbs energy by viscoelastic deformation as the polymer chains start to flow past one another until the sample fractures. The Young's modulus is obtained from the initial slope in the linear region of the stress-strain curve. It is defined as the material's ability for reversible elastic deformation, stiffness of the films in this case. The steeper the slope in the stress-strain curve, the higher the stress needed to generate deformation of material. The magnitude depends on interatomic energies per unit volume. The end of the linear region is called the yield point, after which plastic and at least partly irreversible deformation occurs. Finally, a break point is observed when the stress drops to zero. (Sperling et al., 2005; Youssefian et al., 2015; Tanzi et al., 2017).

Figure 4A shows representative stress-strain curves with varying LCC 80/20 content as an example of the effect of LCC concentration. The curves demonstrate how the Young's modulus increases as a function of concentration, seen as a steeper slope of the curve. The breaking strain decreases with increased concentration except for the film with 10 w-% LCC 80/20. Comparing the films containing 40 w-% LCC 80/20 and LCC 40/60 (**Figure 4B**), it can be observed that the linear region at the beginning of the curves is higher for LCC 80/20, meaning that yield points are encountered at higher stress. This means that the maximum load the films withstood before irreversible deformation occurred was higher for LCC 80/20 compared to LCC 40/60. When comparing the region after the yield point, it seems that, for LCC 80/20, the elongation occurred at relatively constant stress, while for LCC 40/60, stress continued to increase with strain. A yield point followed by extensive elongation at almost constant stress is typical for tough plastic polymers. This type of elongation is called cold drawing which typically describes deformation where extensive chain orientation occurs (Sperling et al., 2005).

Comparing LCC 80/20, 80/20 HMW, and LCC 40/60 to lignosulphonate (**Figure 4B**), an even more pronounced difference is observed. The linear elastic region for lignosulphonate was significantly lower compared to the LCCs, and strain before breaking point was higher. This difference could be observed even during handling of the films. The films containing lignosulphonate appeared much softer with manual inspection.

Young's modulus was measured as a function of LCC and lignosulphonate content in the composite films (**Figure 4C**). All LCCs increased the Young's modulus of the composite films significantly, and the modulus increased with increasing LCC content. However, neither molar mass nor relative lignin/hemicellulose ratio had any significant effect on Young's modulus. At 50 w-% LCC content, the Young's modulus of LCC 80/20 HMW was even slightly lower compared to the two other LCC samples. As Young's modulus is higher for a material that is more resistant to being stretched (Sperling et al., 2005), it was expected that the LCC 80/20 HMW would have demonstrated more entangled polymer chains causing larger Young's modulus. One reason for not observing this kind of behavior could be that the LCC 80/20 HMW might be

more branched instead of having longer chains participating in the chain entanglement. However, since the three-dimensional structures of the LCCs are not known, this can only be hypothesized at this point. Comparing the results of the LCCs to lignosulphonate, it was observed that lignosulphonate did not increase the Young's modulus of the composite films significantly. This may be due to the smaller molar mass of the lignosulphonate polymer compared to the LCC samples or due to the lack of hemicelluloses in the lignosulphonate.

Youssefian and Rahbar (2015) have used atomistic simulations to study Young's modulus and energy densities of hydrogen bonds in hemicelluose, LCC and lignin in bamboo fibrils. The bamboo hemicellulose was xylan, and the lignin modelled in their work differs from the current study by being non-sulphonated. They found that, of the polymers studied, hemicellulose films had the highest Young's modulus due to having the highest energy density of hydrogen bonds. The second highest values were measured for LCC and lowest for lignin. Although the specific chemical structures of the materials studied in the present work differ from the former study, it can be assumed that the higher hemicellulose fraction in the LCC samples compared to the lignosulphonate increases the density of hydrogen bonds, contributing to higher Young's modulus values.

The ability of films to stretch before breaking is described by the breaking strain. An interesting finding was that increasing the concentration of LCC 80/20, LCC 80/20 HMW, and lignosulphonate from 10 to 20 w-% increased the breaking strain while increasing the concentration further to 30 w-% and above caused the strain to decrease (**Figure 4D**). For LCC 40/60, the strain constantly decreased as a function of increasing concentration from 10 to 50 w-%. As the increase in strain at 20 w-% was not observed for LCC 40/60, which contained a higher fraction of hemicellulose than lignin, it is assumed that the non-linear correlation between strain and LCC or lignosulphonate content can be attributed to a higher lignin fraction in the LCC 80/20, LCC 80/20 HMW, and lignosulphonate. Based on the results, it is concluded that viscoelastic properties of the composite films can be adjusted by optimizing the dosage of LCC. The ratio of lignin and hemicellulose in LCC seems to affect the strain properties of the films depending on polymer concentration. It is hypothesized that reason for the decrease in the breaking strain at 30% or higher dosage is the same for both LCC and lignosulphonate and would be due to more hydrogen bonding. Although the lignosulphonate is lacking the hemicellulose fraction, it is still able to form hydrogen bonds. Therefore, increasing the LCC or lignin concentration increased the number of attractive interactions in the films.

Breaking strain was clearly highest for the lignosulphonate sample (**Figure 4D**). This finding is consistent with previous findings by (Baumberger et al., 1996), who studied the effect of lignosulphonate concentration on starch composite films. The elongation at break was stated to increase owing to a plasticization effect of lignosulphonate. In the present work, the higher plasticizing effect of lignosulphonate compared to LCC samples is probably due to both the chemical structure and the lower molar mass of lignosulphonate.

Oxygen Permeability of LCC 80/20 Composite Films

As the LCC was found to enhance mechanical properties of polymeric films, it has the potential to be used in packaging applications. Renewable barrier films are an interesting area of research, and therefore, oxygen permeabilities of HEC-LCC composite films were studied. Since the molecular weight and lignin/hemicellulose ratio did not significantly affect Young's modulus of the films, and LCC 80/20 showed the best mechanical properties (**Figure 4B**), only this sample was further used to evaluate oxygen permeability. Due to the softness and water sensitivity of lignosulphonate, that sample could be assumed to not perform well in OTR measurements.

The OTR was analyzed for the composite films containing 0–40 w-% LCC 80/20, 95–55 w-% HEC and 5 w-% glycerol. Measurements were performed at 23°C, and 50 and 80% relative humidity (**Figures 5A,B**, respectively). The results demonstrate clearly that increasing the LCC 80/20 content decreased the oxygen transmission rate through the composite films at both the studied humidities.

There is a clear correlation between the OTR and Young's modulus of the films. The stiffer the film, the lower the oxygen transmission rate. Comparing the oxygen transmission rates of the films at 80% RH to the results at 50% RH, a clear difference can be observed. At higher humidity, the oxygen transmission through the films was much higher, and the standard deviation between the measurements was also quite high for other samples except those containing 10 and 40 w-% of LCC 80/20.

To enable comparison to the literature, OTR values were normalized with the mean thickness of the films to estimate the oxygen permeability of the samples (**Table 3**). The thickness of the films was calculated as an average of three measurements per film, combining the results of films containing 10–50 w-% LCCs. On average, the thickness of LCC 80/20 films was 70 ± 5 μm. There was a small variation in the results describing deviation in the film preparation method by casting on a petri dish.

The increased oxygen permeability at higher humidity is assumed to be mostly caused by the hygroscopicity of the hydroxyethyl cellulose used in the composite films as a film-forming polymer. The sample containing 0 w-% LCC 80/20 contained 95 w-% HEC and 5 w-% glycerol. For this film, the OP at 50% RH was 0.3 (cm^3 mm)/(m^2 day atm) and at 80% RH it was 38 (cm^3 mm)/(m^2 day atm). It can be concluded that HEC was not a suitable polymer to be used at high humidity in the composite films with LCC 80/20 to achieve low oxygen permeability. However, despite using HEC with poor oxygen barrier properties, the effect of LCC 80/20 lowering the oxygen permeability is evident. The films containing 40% of LCC 80/20 had 15 times lower OP at 50% RH and two times lower OP in 80% RH compared to pure HEC films.

Wang et al. (2018) have classified barrier properties based on OP at 23°C and 50% or 0% RH. High barrier quality is achieved when the OP is between 0.04–0.4, medium between 0.4-4, low between 4–40,

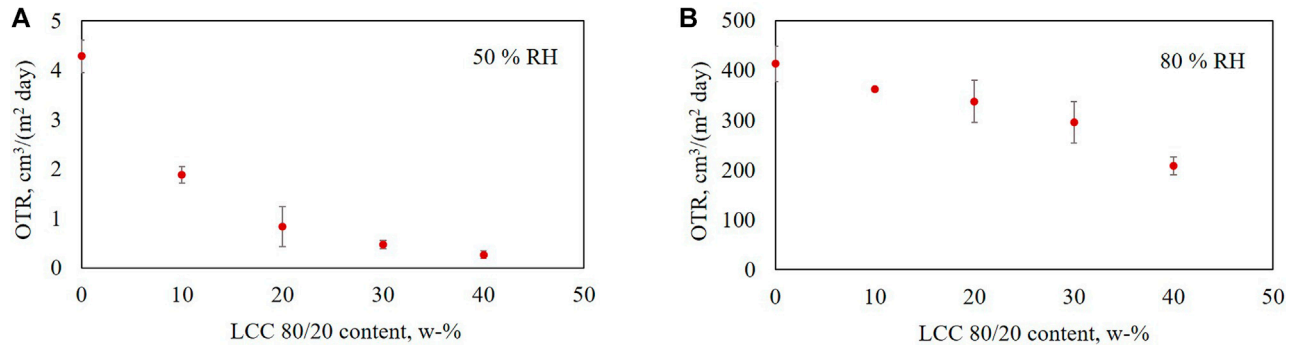

FIGURE 5 | Oxygen transmission rate for films containing 0–40 w-% LCC 80/20, 95–55 w-% HEC and 5 w-% glycerol at 23°C and **(A)** 50% and **(B)** 80% humidity.

TABLE 3 | Oxygen permeability for LCC 80/20 films at 23°C and 50 and 80% relative humidity.

LCC 80/20	OP at 50% RH, (cm^3 mm)/(m^2 day atm)	OP at 80% RH, (cm^3 mm)/(m^2 day atm)
0 w-%	0.30	38
10 w-%	0.13	35
20 w-%	0.06	30
30 w-%	0.03	27
40 w-%	0.02	19

and poor above 40 (cm^3 mm)/(m^2 day atm). Comparing the OP results of the LCC composite films at 50% RH (**Table 3**) to the values by Wang et al. (2018), two conclusions can be made: HEC film had a high oxygen barrier quality and increasing the LCC content in the composite films led to excellent performance as a function of LCC content. At 80% humidity, the barrier quality of all tested composite films was low. However, increasing the LCC content in the films significantly decreased oxygen permeability, even at 80% RH.

It is interesting to compare the results obtained herein with the oxygen permeability for various biopolymers and fossil-based alternatives reported previously (Lange et al., 2003; Aulin et al., 2010; Wang et al., 2018; Wu et al., 2021). However, there is a large variation between OP values for similar polymers depending on the raw material source and preparation of the films, which makes comparison challenging. For example, OP of nanocellulose films can vary between 0.02 (cm^3 mm)/(m^2 day atm) at 53% RH (Österberg et al., 2013) to 0.58 (cm^3 mm)/(m^2 day atm) at 50% RH (Rivière et al., 2021). For polypropylene, the variation might be 50–100 (cm^3 mm)/(m^2 day atm) at 0–90% RH and for ethylene vinyl alcohol 0.001–0.01 (cm^3 mm)/(m^2 day atm) at 0% RH (Wang et al., 2017). The best OP in the present work, 0.02 (cm^3 mm)/(m^2 day atm), was observed for the film containing 40 w-% LCC 80/20 at 50% humidity. Compared to the values of cellulose nanofibril films, the result is similar to what was found in the work of Österberg et al. (2013) and significantly better compared to the CNF films studied in the work of Rivière et al. (2021). If the fragile nature of LCC 80/20 films could be overcome by using alternative plasticizers, one could expect to achieve even better oxygen barrier properties with the LCC by increasing the concentration above 40 w-% in the free-standing films.

The effect of humidity has been studied also previously, and many researchers have found that increasing RH increases OP for hydrophilic polymers exponentially above a certain threshold. (Hong et al., 2005; Aulin et al., 2010; Österberg et al., 2013; Aguirre-Loredo et al., 2016; Blanchard et al., 2017; Wang et al., 2018; Wu et al., 2021; Zhu Rydberg et al., 2021) Plasticizing water molecules in the amorphous sections of the films are stated to reduce intermolecular interactions between polymer chains while increasing hydrogen bonding between polymer and water, reducing stiffness of the films. For example, Österberg et al. (2013) and Aulin et al. (2010) observed that oxygen transmission through fibrillated cellulose films increases sharply above 70% RH. Ethylene vinyl alcohol is reported to lose good oxygen barrier properties already above 60% RH (Wu et al., 2021).

Oxygen permeability depends on diffusion and solubility, and there are several explanations for the effect of relative humidity. At low RH, the intermolecular interactions, such as hydrogen bonding and Van der Waals attraction, enable compact packing and a high cohesive energy density of the polymeric films. This lowers free volume and mobility of the polymer chains, decreasing gas permeability. Increasing water content in the films induces higher oxygen solubility (Aulin et al., 2010; Blanchard et al., 2017; Wang et al., 2018). The LCC studied in the present work is a hydrophilic polymer able to form intra- and intermolecular hydrogen bonds, which is assumed to contribute to the superior barrier properties of the LCC films at 50% RH.

Increasing LCC content in the films was demonstrated not only to enhance mechanical properties but also to decrease oxygen permeability of the films as a function of concentration. These results support the potential use of LCCs, for example, in oxygen barrier applications in the packaging industry. Since HEC is very susceptible to losing gas barrier performance at elevated RH, alternative biopolymers will be studied in the composite films as a film forming polymer in the future.

CONCLUSION

In this paper, we present a study of free-standing composite films to demonstrate the feasibility of a specific lignin-carbohydrate complex (LCC) for polymeric film applications. LCC samples with varying molecular weight and lignin/hemicellulose ratio were compared to lignosulphonate analyzing mechanical properties of the films. We observed that increasing LCC content increased Young's modulus of the composite films while the pure lignosulphonate did not have a significant effect. The LCC with higher lignin content withstood higher load. The increased Young's modulus of LCC films was speculated to originate from the higher energy density of hydrogen bonds facilitated mainly by the hemicellulose fraction in the polymer. The breaking strain had a non-linear correlation with concentration for the samples with high content of sulphonated lignin. The highest breaking strain was found for the lignosulphonate polymer. Oxygen permeabilities were analyzed at 50 and 80% relative humidity for the LCC sample demonstrating the best mechanical properties. Oxygen permeability decreased significantly with increasing LCC content in both humidities.

For future studies, a more comprehensive examination of the interactions of LCC with other film-forming polymers and plasticizers is recommended to find the optimal composition for specific types of applications. The enhanced mechanical properties and ability to decrease oxygen permeability of the composite films presented in this work indicate that LCC has potential in applications where polymeric films are used, such as barrier films in paper and board packaging. Hence it would be interesting to study the interactions of LCC with cellulose fibers in more detail. The LCC polymers could be used to enhance properties of the final products while simultaneously enabling more holistic and sustainable use of biomass.

DATA AVAILABILITY STATEMENT

The original contributions presented in the study are included in the article/Supplementary Material. Raw data is available upon request from corresponding authors.

AUTHOR CONTRIBUTIONS

BA designed and conducted experiments and interpret the data with input from A-SJ and MÖ. HK designed, supervised and interpreted the OTR measurements at high humidity. PO wrote about the LCC production by demonstration scale unit and provided the samples. The manuscript was otherwise written by BA with contributions from all authors. All authors have given approval to the final version of the manuscript.

FUNDING

This document is part of a project that has received funding from the Bio Based Industries Joint Undertaking (JU) under the European Union's Horizon 2020 research and innovation programme under grant agreement No. 837866. The JU receives support from the European Union's Horizon 2020 research and innovation programme and the Bio Based Industries Consortium.

REFERENCES

Abbadessa, A., Oinonen, P., and Henriksson, G. (2018). Characterization of Two Novel Bio-Based Materials from Pulping Process Side Streams: Ecohelix and CleanFlow Black Lignin. *Bioresources* 13 (4), 7606–7627. doi:10.15376/biores.13.4.7606-7627

Aguirre-Loredo, R. Y., Rodríguez-Hernández, A. I., Morales-Sánchez, E., Gómez-Aldapa, C. A., and Velazquez, G. (2016). Effect of Equilibrium Moisture Content on Barrier, Mechanical and thermal Properties of Chitosan Films. *Food Chem.* 196, 560–566. doi:10.1016/j.foodchem.2015.09.065

ASTM D3985-05 (2005). *Standard Test Method for Oxygen Gas Transmission Rate through Plastic Film and Sheeting Using a Coulometric Sensor*. West Conshohocken, PA: ASTM International.

Aulin, C., Gällstedt, M., and Lindström, T. (2010). Oxygen and Oil Barrier Properties of Microfibrillated Cellulose Films and Coatings. *Cellulose* 17 (3), 559–574. doi:10.1007/s10570-009-9393-y

Balakshin, M., Capanema, E., Gracz, H., Chang, H.-m., and Jameel, H. (2011). Quantification of Lignin-Carbohydrate Linkages with High-Resolution NMR Spectroscopy. *Planta* 233 (6), 1097–1110. doi:10.1007/s00425-011-1359-2

Baumberger, S., Lapierre, C., Monties, B., Lourdin, D., and Colonna, P. (1997). Preparation and Properties of Thermally Moulded and Cast Lignosulfonates-Starch Blends. *Ind. Crops Prod.* 6 (3), 253–258. doi:10.1016/S0926-6690(97)00015-0

Blanchard, A., Gouanvé, F., and Espuche, E. (2017). Effect of Humidity on Mechanical, thermal and Barrier Properties of EVOH Films. *J. Membr. Sci.* 540, 1–9. doi:10.1016/j.memsci.2017.06.031

Borrega, M., Päärnilä, S., Greca, L. G., Jääskeläinen, A.-S., Ohra-aho, T., Rojas, O. J., et al. (2020). Morphological and Wettability Properties of Thin Coating Films Produced from Technical Lignins. *Langmuir* 36 (33), 9675–9684. doi:10.1021/acs.langmuir.0c00826

Carvalho, D. M. d., Lahtinen, M. H., Lawoko, M., and Mikkonen, K. S. (2020). Enrichment and Identification of Lignin-Carbohydrate Complexes in Softwood Extract. *ACS Sustainable Chem. Eng.* 8 (31), 11795–11804. doi:10.1021/acssuschemeng.0c03988

Dong, H., Zheng, L., Yu, P., Jiang, Q., Wu, Y., Huang, C., et al. (2020). Characterization and Application of Lignin-Carbohydrate Complexes from Lignocellulosic Materials as Antioxidants for Scavenging *In Vitro* and *In Vivo* Reactive Oxygen Species. *ACS Sustainable Chem. Eng.* 8 (1), 256–266. doi:10.1021/acssuschemeng.9b05290

Giummarella, N., Balakshin, M., Koutaniemi, S., Kärkönen, A., and Lawoko, M. (2019). Nativity of Lignin Carbohydrate Bonds Substantiated by Biomimetic Synthesis. *J. Exp. Bot.* 70 (20), 5591–5601. doi:10.1093/jxb/erz324

Giummarella, N., Pu, Y., Ragauskas, A. J., and Lawoko, M. (2019). A Critical Review on the Analysis of Lignin Carbohydrate Bonds. *Green. Chem.* 21 (7), 1573–1595. doi:10.1039/c8gc03606c

Henriksson, G., Areskogh, D., and Oinonen, P. A. (2012). Method to Increase the Molecular Weight of wood Mannans and Xylans Comprising Aromatic Moieties. European Patent Office, Patent WO 2012/071004 Al.

Henriksson, G., Lawoko, M., Martin, M. E. E., and Gellerstedt, G. (2007). Lignin-carbohydrate Network in wood and Pulps: A Determinant for Reactivity. *Holzforschung* 61 (6), 668–674. doi:10.1515/HF.2007.097

Hong, S.-I., and Krochta, J. M. (2006). Oxygen Barrier Performance of Whey-Protein-Coated Plastic Films as Affected by Temperature, Relative Humidity, Base Film and Protein Type. *J. Food Eng.* 77, 739–745. doi:10.1016/j.jfoodeng.2005.07.034

Lange, J., and Wyser, Y. (2003). Recent Innovations in Barrier Technologies for Plastic Packaging?a Review. *Packag. Technol. Sci.* 16 (4), 149–158. doi:10.1002/pts.621

Lawoko, M., Henriksson, G., and Gellerstedt, G. (2005). Structural Differences between the Lignin–Carbohydrate Complexes Present in Wood and in Chemical Pulps. *Biomacromolecules* 6 (6), 3467–3473. doi:10.1021/bm058014q

Lin, S. Y. (1992). "Ultraviolet Spectrophotometry," in *Methods in Lignin Chemistry*. Editors S. Y. Lin and C. W. Dence (Berlin, Heidelberg: Springer), 217–232. doi:10.1007/978-3-642-74065-7_15

Oinonen, P. (2014). *A Biomimicking Approach for Hemicellulose Processing. [Dissertation]*. Sweden: KTH Royal Institute of Technology.

Oinonen, P., Areskogh, D., and Henriksson, G. (2013). Enzyme Catalyzed Cross-Linking of spruce Galactoglucomannan Improves its Applicability in Barrier Films. *Carbohydr. Polym.* 95, 690–696. doi:10.1016/j.carbpol.2013.03.016

Oinonen, P., Zhang, L., Lawoko, M., and Henriksson, G. (2015). On the Formation of Lignin Polysaccharide Networks in Norway spruce. *Phytochemistry* 111, 177–184. doi:10.1016/j.phytochem.2014.10.027

Österberg, M., Vartiainen, J., Lucenius, J., Hippi, U., Seppälä, J., Serimaa, R., et al. (2013). A Fast Method to Produce strong NFC Films as a Platform for Barrier and Functional Materials. *ACS Appl. Mater. Inter.* 5 (11), 4640–4647. doi:10.1021/am401046x

Pei, W., Chen, Z. S., Chan, H. Y. E., Zheng, L., Liang, C., and Huang, C. (2020). Isolation and Identification of a Novel Anti-protein Aggregation Activity of Lignin-Carbohydrate Complex from Chionanthus Retusus Leaves. *Front. Bioeng. Biotechnol.* 8, 1112. doi:10.3389/fbioe.2020.573991

Rivière, G. N., Pion, F., Farooq, M., Sipponen, M. H., Koivula, H., Jayabalan, T., et al. (2021). Toward Waste Valorization by Converting Bioethanol Production Residues into Nanoparticles and Nanocomposite Films. *Sustainable Mater. Tech.* 28, e00269. doi:10.1016/j.susmat.2021.e00269

Sperling, L. (2005). *Introduction to Physical Polymer Science*. Incorporated, Hoboken: John Wiley & Sons.

Steinmetz, V., Villain-Gambier, M., Klem, A., Gambier, F., Dumarcay, S., and Trebouet, D. (2019). Unveiling TMP Process Water Potential as an Industrial Sourcing of Valuable Lignin-Carbohydrate Complexes toward Zero-Waste Biorefineries. *ACS Sustainable Chem. Eng.* 7 (6), 6390–6400. doi:10.1021/acssuschemeng.9b00181

Strassberger, Z., Tanase, S., and Rothenberg, G. (2014). The Pros and Cons of Lignin Valorisation in an Integrated Biorefinery. *RSC Adv.* 4 (48), 25310–25318. doi:10.1039/c4ra04747h

Sundheq, A., Sundherg, K., Lillandt, C., and Holmhom, B. (1996). Determination of Hemicelluloses and Pectins in wood and Pulp Fibres by Acid Methanolysis and Gas Chromatography. *Nordic Pulp Paper Res. J.* 11, 216–219. doi:10.3183/npprj-1996-11-04-p216-219

Tanzi, M., and Farè, S. (2017). *Characterization of Polymeric Biomaterials*. Cambridge: Elsevier Science & Technology.

Wang, J., Gardner, D. J., Stark, N. M., Bousfield, D. W., Tajvidi, M., and Cai, Z. (2018). Moisture and Oxygen Barrier Properties of Cellulose Nanomaterial-Based Films. *ACS Sustainable Chem. Eng.* 6 (1), 49–70. doi:10.1021/acssuschemeng.7b03523

Wang, L., Lagerquist, L., Zhang, Y., Koppolu, R., Tirri, T., Sulaeva, I., et al. (2020). Tailored Thermosetting Wood Adhesive Based on Well-Defined Hardwood Lignin Fractions. *ACS Sustainable Chem. Eng.* 8, 13517–13526. doi:10.1021/acssuschemeng.0c05408

Wu, F., Misra, M., and Mohanty, A. K. (2021). Challenges and New Opportunities on Barrier Performance of Biodegradable Polymers for Sustainable Packaging. *Prog. Polym. Sci.* 117, 101395. doi:10.1016/j.progpolymsci.2021.101395

Youssefian, S., and Rahbar, N. (2015). Molecular Origin of Strength and Stiffness in Bamboo Fibrils. *Sci. Rep.* 5, 11116. doi:10.1038/srep11116

Yuan, T.-Q., Xu, F., and Sun, R.-C. (2013). Role of Lignin in a Biorefinery: Separation Characterization and Valorization. *J. Chem. Technol. Biotechnol.* 88, 346–352. doi:10.1002/jctb.3996

Zhang, F., Lan, X., Peng, H., Hu, X., and Zhao, Q. (2020). A "Trojan Horse" Camouflage Strategy for High-Performance Cellulose Paper and Separators. *Adv. Funct. Mater.* 30 (32), 2002169. doi:10.1002/adfm.202002169

Zhao, Y., Shakeel, U., Saif Ur Rehman, M., Li, H., Xu, X., and Xu, J. (2020). Lignin-carbohydrate Complexes (LCCs) and its Role in Biorefinery. *J. Clean. Prod.* 253, 120076. doi:10.1016/j.jclepro.2020.120076

Zhu Ryberg, Y. Z., Albertsson, A.-C., and Albertsson, A. (2011). Conceptual Approach to Renewable Barrier Film Design Based on wood Hydrolysate. *Biomacromolecules* 12 (4), 1355–1362. doi:10.1021/bm200128s

Conflict of Interest: Authors BA and A-SJ were employed by the company Kemira Oyj. Author PO was employed by the company Ecohelix AB.

The remaining authors declare that the research was conducted in the absence of any commercial or financial relationships that could be construed as a potential conflict of interest.

Publisher's Note: All claims expressed in this article are solely those of the authors and do not necessarily represent those of their affiliated organizations, or those of the publisher, the editors and the reviewers. Any product that may be evaluated in this article, or claim that may be made by its manufacturer, is not guaranteed or endorsed by the publisher.

frontiers in Energy Research

ORIGINAL RESEARCH
published: 17 December 2021
doi: 10.3389/fenrg.2021.807286

Isolation and Characterization of *Bacillus* Sp. Capable of Degradating Alkali Lignin

Jing Yang[1,2,3,4,5], *Jian Zhao*[1,2,3,4,5], *Jianchun Jiang*[1,2,3,4,5]*, *Hao Xu*[1,2,3,4,5], *Ning Zhang*[1,2,3,4,5], *Jingcong Xie*[1,2,3,4,5]* and *Min Wei*[1,2,3,4,5]

[1]Institute of Chemical Industry of Forest Products, CAF, Nanjing, China, [2]National Engineering Laboratory for Biomass Chemical Utilization, Nanjing, China, [3]Key and Open Laboratory of Forest Chemical Engineering, SFA, Nanjing, China, [4]Key Laboratory of Biomass Energy and Material, Nanjing, China, [5]Co-Innovation Center of Efficient Processing and Utilization of Forest Resources, Nanjing Forestry University, Nanjing, China

Alkali lignin-degrading *Bacillus* were isolated from forest soils in China and were identified as *Bacillus subtilis* TR-03 and *Bacillus cereus* TR-25 by 16S rDNA sequence analysis. Wherein TR-03 displayed optimal 26.72% alkali lignin (2 g/L) degradation at 7 days and 71.23% of Azure-B (0.01%) decolorization at 36 h of cultivation at 37°C. Ligninolytic enzyme analysis revealed that TR-03 was capable of depolymerizing alkali lignin effectively by the producing of lignin peroxidase and laccase, wherein higher laccase activity was cell-associated. At last, the physical and chemical changes of lignin *via* SEM and FTIR analysis was further observed to prove the lignin degradation by *Bacillus subtilis* TR-03.

Keywords: *Bacillus* sp., alkali lignin, biodegradation, isolation, enzyme

OPEN ACCESS

Edited by:
Jia-Long Wen,
Beijing Forestry University, China

Reviewed by:
Quan Bu,
Jiangsu University, China
Wang Yunpu,
Nanchang University, China

***Correspondence:**
Jianchun Jiang
aeziox@163.com
Jingcong Xie
xiejingcong@icifp.cn

Specialty section:
This article was submitted to Bioenergy and Biofuels, a section of the journal Frontiers in Energy Research

Received: *02 November 2021*
Accepted: *15 November 2021*
Published: *17 December 2021*

Citation:
Yang J, Zhao J, Jiang J, Xu H, Zhang N, Xie J and Wei M (2021) Isolation and Characterization of Bacillus *Sp. Capable of Degradating Alkali Lignin. Front. Energy Res. 9:807286. doi: 10.3389/fenrg.2021.807286*

INTRODUCTION

Lignin is an aromatic heteropolymer and closely associated with hemicellulose and cellulose to form a complex compound. Owing to its irregular matrix structure and highly branched polymer network, lignin is extremely resistant to microbial breakdown (Muaaz-Us-Salam et al., 2020). The degradation of lignin is critical in the conversion of lignocellulose into second-generation biofuels as well as the lignin valorization strategies (Tonin et al., 2016). Lignin depolymerization by microorganism is one of the significant mechanisms due to its low energy consumption, no chemical addition and environmental friendliness (Niu et al., 2021).

So far, fungi are dominant in the efficiently degradation of lignin and the related enzymes including Manganese peroxidase (MnP), Lignin peroxidase (Lip) and Laccase (Lac) (Wong, 2009) have been extensively studied. LiP is a glycoprotein and could oxidize both non-phenolic and phenolic compounds. MnP is a glycosylated heme-protein and could convert lignin phenolic compounds to phenoxy-radicals. Lac is a multi-copper oxidase and could oxidize the phenolic hydroxyl of lignin to destroy the internal stability of the aromatic ring (Xu Z. et al., 2018; Weng et al., 2021). However, the lignin degradation by fungi failed to make a breakthrough due to the strict growth conditions, long pretreatment cycle, consumption of cellulose and hemicellulose, poor adaptability to the environment (Wang et al., 2013). In contrast, bacteria have been much less clarified as degraders of lignin, even though bacteria are identified as important participants in the lignin depolymerization (Mei et al., 2020). Compared with fungi, bacteria offer advantages for lignocellulosic application, such as rapid propagation, strong environmental adaptability, convenient molecular genetics and protein expression with a smaller genome, etc., (Tonin et al., 2016). Studies have confirmed that bacteria can also secrete enzymes required for lignin degradation, metabolize poplar dioxane lignin and break the lignin biphenyl structure (Navas et al., 2019).

So far, some lignin-degrading bacteria strains such as *Thodococcus jostii* (Henson et al., 2018), *Pseudomonas* (Xu R. et al., 2018), *Bacillus* Sp have been isolated from soil, sediments, animals, insect guts, etc. *Bacillus* Sp. is a kind of gram-positive bacteria, which can produce spores with special resistance to adverse conditions. Nowadays, *Bacillus* Sp is widely used in the production of enzymes, antibiotics and exogenous proteins, and has become an important biotechnology tool in the industrial production of medicine, feed and food (Zhu et al., 2020). *Bacillus* Sp. is known as lignin-degrading bacteria since a few years ago, and several stains, such as *Bacillus subtilis*, *Bacillus licheniformis, Bacillus ligniniphilus* have been isolated from compost, soil or other environment all around world (Yang et al., 2021; Lu et al., 2012; Zhu et al., 2017). *Bacillus* could effectively degrade lignin through the secretion of ligninolytic enzymes including Lip, Lac and MnP (Zhu et al., 2017; Chang et al., 2014). Compared with other lignin degrading bacteria, *Bacillus* Sp. is secure and can form dormant spores in adverse environment, which is feasible in the industrial application of lignin degradation.

Although some *Bacillus* strains have been proved to be capable of solubilizing lignin, their lignin-degrading mechanism was still unclear and the lignin-degrading rate was lower than that of fungi. Mei et al. (2020) found the maximum lignin degradation rate of *Bacillus amyloliquefaciens* SL-7 was 28.55%, which was close to that of 30–36% of fungi. However, the generally degradation rate of lignin in most *Bacillus* was only 15–18% (Chang et al., 2014; Mishra et al., 2017; Weng et al., 2021). Thus, more efficient ligninolytic *Bacillus* strains should be explored to expand the knowledge of lignin valorization by bacteria. This paper focuses on the isolation and characterization of *Bacillus* strains from forest soil samples and their degradation capability of alkali lignin. The isolates obtained are feasible in lignin degradation owing to their excellent growth rate as well as high activity of ligninolytic enzymes.

MATERIALS AND METHODS

Materials

Soil samples were collected from Zijin Mountain of Nanjing City, China. 2 g samples were suspended in 30 ml LB medium (peptone 10 g/L, yeast extract 5 g/L, NaCl 10 g/L) for enrichment culture at 37°C for 20 h, separately. 1 ml of the clear supernatant was added into 9 ml sterile water and incubated at 75–80°C for 15–20 min. After mixing all the samples, 1 ml of the solution was diluted using 0.9% normal saline and inoculated into the selective medium (alkali lignin medium: $MgSO_4$ $7H_2O$ 0.2 g, K_2HPO_4 1.0 g, KH_2PO_4 1.0 g, $(NH_4)_2SO_4$ 2.0 g, $CaCl_2$ 0.1 $FeSO_4$ $7H_2O$ 0.05 g, $MnSO_4$ H_2O 0.02 g, $CuSO_4$ $5H_2O$ 1.0 mg, $ZnSO_4$ $7H_2O$ 1.0 mg, alkali lignin 2.0 g; Azure-B medium: 0.01% azure-B was added in LB medium; 15 g agar was added in 1,000 ml distilled water). The plates were incubated at 29°C, and single colonies were isolated on LB plates.

Identification of Bacterial Isolates

Genomic DNA of the screened was extracted according to the DNA isolation Kit (Sangon Biotech, China). 16S rDNA gene was amplifed using universal primers (27 F: 5′-AGAGTTTGATCC TGGCTCAG-3′ and 1541 R:5′-AAGGAGGTGATCCAGCC-3′). PCR was performed with an initial denaturation step at 94°C for 5 min followed by 30 cycles of denaturation at 94°C for 30 s, annealing at 55°C for 30 s, extension at 72°C for 60 s and a final extension at 72°C for 10 min. Amplified product was run on 0.8% agarose gel, then recovered and sequenced by Sangon Biotech (Shanghai, China). The resulting sequences were compared using BLAST program and MEGA 7.0 software.

Dye Decolorization of Azure-B and Lignin Degradation

The fading rate of Azure-B in liquid medium by lignin-degrading isolates was determined. The isolates were maintained on LB slants at 4°C. Mature spores were harvested with physiological saline and incubated at 37°C and 150 rpm for about 12 h (about OD_{600} 1.0) to make seed culture. 1% seed volume was inoculated into Azure-B (0.01%)-LB fluid medium and cultured in dark at 180 rpm, 37°C. The Azure-B (0.01%)-LB medium with inactivated bacterium as the control. 1 ml fermentation liquor was taken at 6, 12, 18, 24 and 36 h and centrifuged at 1,000 rpm, 8 min. The supernatant was measured for absorbance at 590 nm Microplate reader (Multi-mode Reader, Gene Company Limited, China). The formula of decolorizing rate (Picart et al., 2016) was as follows:

$$V = \frac{\lambda^* - \lambda}{\lambda^*}$$

Where λ^* *is the* absorbance of the control sample, which is 0.775; λ is the absorbance of the test samples.

The decrease in absorbance at 280 nm was determined to characterize the lignin degradation (Kumar et al., 2015). 2 ml culture was harvested and centrifuged at 8,000 rpm for 10 min. The absorbance of the supernatant at 280 nm was measured, with uninoculated medium as the control. The degradation ratio of lignin was calculated according to the equation described by Xu Z. et al. (2018). All of the experiments was conducted in triplicates.

Ligninolytic Enzymes Assay

Fermentation was performed with 50 ml alkali lignin medium in a 250 ml shake flask, at 37°C and 150 rpm for 48 h, with 2% (v/v) inoculum. 2 ml cultured fluid was centrifuged at 8,000 rpm for 10 min and the supernatant was used for Lac, Lip and MnP activities measurement according to the procedures of Yang et al. (2011) using ABTS, veratryl and 2,6-dimethoxyphenol as substrates. One unit of laccase activity was defined as the amount of enzyme required to oxidize 1 μmol of substrate per min. All assays were performed in triplicate.

Intracellular Laccase Activity and Characteristics

The intracellular laccase activity was further determined according to the method described by Lu et al. (2012). The

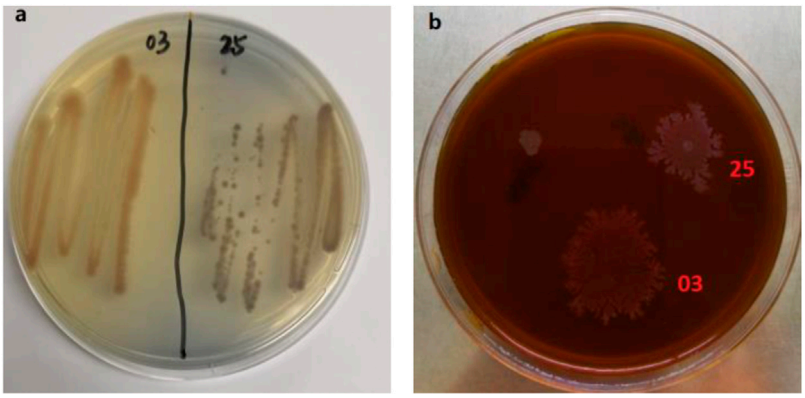

FIGURE 1 | Screened strains on the Azure-B and lignin plates.**(A)** Azure-B plates, with 0.01% azure-B added; **(B)** alkali lignin plates with alkali lignin as the sole carbon source (2 g/L).

bacterial pellets were obtained by the centrifugation at 8,000 rpm for 10 min at 4°C. The cells were broken by lysozyme (0.1 mg/ml) at 37°C for 10 min, washed by 1 M, 0.14 M NaCl and 0.1% (w/v) SDS containing 10 mM EDTA and 0.3 mg/ml PMSF, respectively, then heated at 80°C for 10 min, and washed with sterile deionized water for 3 times. The cell extract was suspended in sterile deionized water to make the crude intracellular enzyme.

The effect of pH on the spore laccase activity was measured under standard assay conditions at 30°C in citrate–phosphate buffer (0.1 M, pH 2.2–7.0) and Tris-HCl buffer (0.1 M, pH7.0–9.0). The intracellular activity was measured based on the oxidation of ABTS, syringaldazine (SGZ) and 2,6-dimethoxyphenol (2,6-DMP) at different pH.

The effect of temperature on the spore laccase activity was investigated under standard assay conditions at temperatures ranging from 20 to 100°C for 5 min. The residual laccase activity was measured periodically with ABTS as the substrate at pH 3.0. The maximum enzyme activity was considered as 100% to calculate the relative activity.

Scanning Electron Microscopy

SEM images were conducted to analyze the microstructural changes and surface characteristics of untreated and pretreated lignin. Control and inoculated samples (50 ml for each) were centrifuged at 8,000 rpm for 10 min. The cell-free supernatant was dried by a freeze drier (LGJ-10, Beijing Songyuanhuaxing Technology Develop Co., Ltd., China). The dried samples were mounted on a stub and sputter-coated with gold prior to imaging with a field emission scanning electron microscope (3400-N, Hitachi, Japan) using 2 kV accelerating voltage.

FTIR Spectroscopy

The structures of untreated and pretreated alkali lignin were analyzed by FTIR spectroscopy. 1 mg dried sample was uniformly mixed with 100 mg KBr and then pressed into a transparent thin film, with a thickness of 10–20 μm. Infrared spectra were conducted by a spectrometer (MAGNA-IR 550, Thermo Nicolet Corporation, United States). Sample spectra were recorded from 4,000 to 400 cm^{-1} with a spectral resolution of 2 cm^{-1} using an accumulation of 32 scans.

RESULTS

Screening of Lignin-Degrading *Bacillus* and Identification

Bacillus sp. strains were proved to be important microorganism in the depolymerization of lignin (Zhou et al., 2017). Several strains of *Bacillus* sp. have been screened worldwide and their lignin-degrading abilities have been studied. To enrich the diversity of lignin-decomposing bacteria, azure-B and lignin plates were used to screen the lignin-degrading *Bacillus*. Two strains were isolated from soil samples from Zijin Mountain and named as TR-03 and TR-25. Prominent pale yellow and light brown areas appeared around the colonies on the Azure-B plates (**Figure 1A**), which illustrates probably LiP, Lac or MnP production of the strains. Furthermore, the 2 strains can effectively grow on the selective medium with lignin as the sole carbon (**Figure 1**), which also confirms their preliminary lignin-degrading ability.

The sequence of 16S rDNA of isolate was determined and submitted to NCBI with accession number of OK559643 and OK559727, respectively. On the basis of 16 S rDNA gene sequencing and taxonomic analyses, TR-03 was closely matched to *Bacillus subtilis* NR 112116.2 and TR-25 was closely matched to *Bacillus cereus* NR 115714.1 (**Figure 2**). Thus, the isolates were identified and named as *Bacillus subtilis* TR-03 and *Bacillus cereus* TR-25.

Decolorizing of Azure-B and Lignin Degradation

TR-03 and TR-25 were preliminarily confirmed to decolorize the Azure-B during the plate screening. To quantitatively determine their decoloration ability, fluid medium supplemented with Azure-B was further prepared and the decolorizing rate was determined (**Figure 3**). The isolates both showed obvious decolorizing of Azure-B. Especially for TR-03, which showed

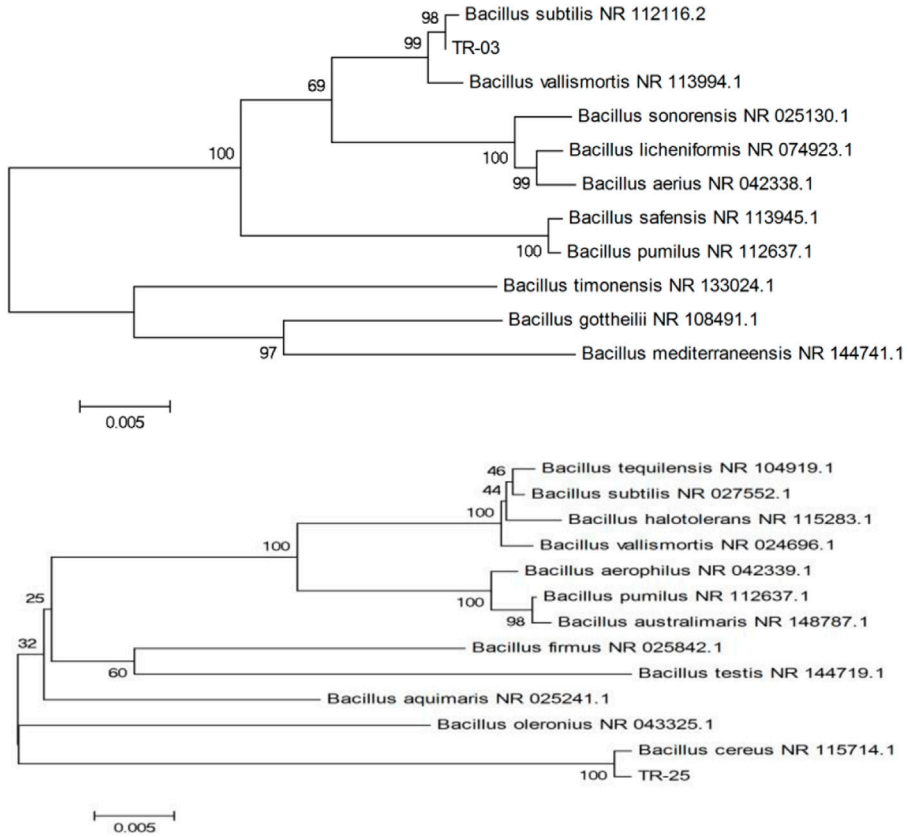

FIGURE 2 | Evolutionary relationships and phylogenetic trees based on 16S rDNA sequence of TR-03 and TR-25.

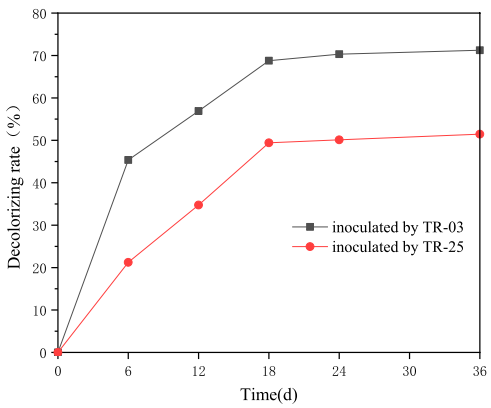

FIGURE 3 | Dye decoloration of Azure-B (0.01%) by TR-03 and TR-25 at 590 nm.

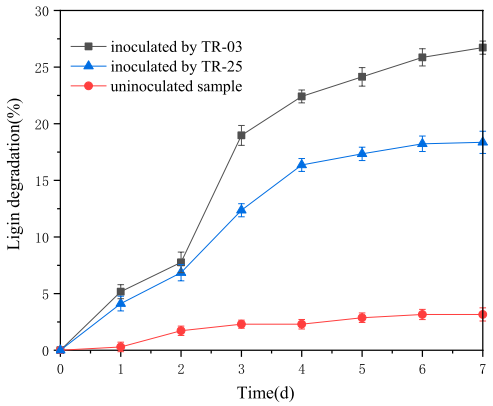

FIGURE 4 | Time course of alkali lignin degradation at A_{280} by TR-03 and TR-25. Initial concentration of alkali lignin was 2 g/L.

the highest rate of 71.23% Azure-B decolorization at 36 h of cultivation and over 94% of decolorization appeared at about 18 h of cultivation. TR-25 also presented excellent decolorization of Azure-B, with decolorizing rate over 50% at 36 h of cultivation. Azure-B belongs to triarylmethane dyes, with similar structure to that of lignin, and is usually used as the substrate to measure the enzyme activity of lignin-degradation (Bandounas et al., 2013). Tawaf et al. found that *Bacillus* tequilensis AN-1 only showed 67.6% decolorization of 2.5 mg/L Azure-B after 7 days (Tawaf et al., 2018). Thus, the rapid decolorization of Azure-B suggests the lignin-degrading potentiality of both the isolates.

The intense absorption of benzene ring at 280 nm was characterized to indicate the lignin degradation for the isolates (Chai et al., 2014), and the results are shown in **Figure 4**. The

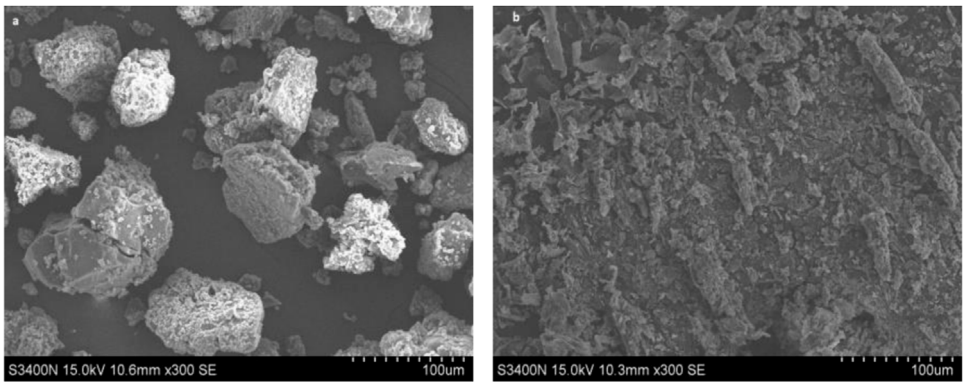

FIGURE 5 | SEM images on lignin treated with *Bacillus subtilis* TR-03. **(A)** untreated lignin; **(B)** lignin treated for 5 days with *Bacillus subtilis* TR-03.

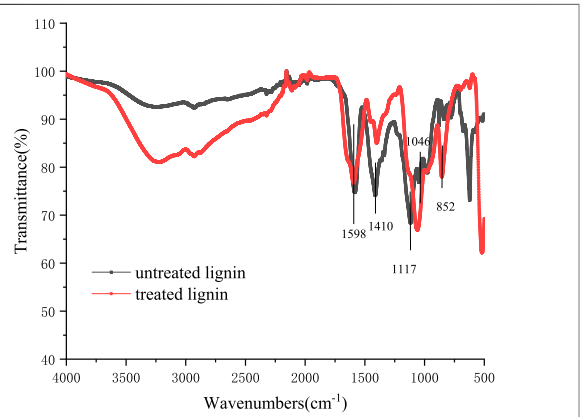

FIGURE 6 | FTIR spectrum of alkali lignin before and after biodegradation with *Bacillus subtilis* TR-03.

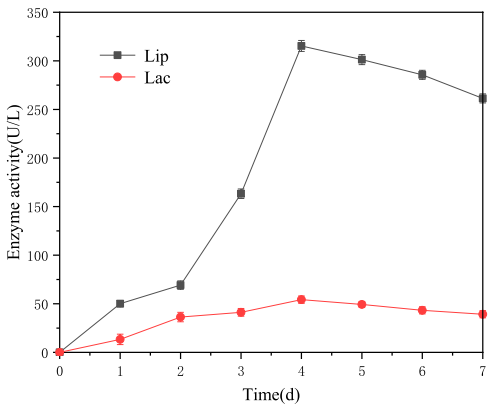

FIGURE 7 | Time course of lignin-degrading enzymes in the culture of strain TR-03. Initial concentration of alkali lignin was 2 g/L.

absorbance of A_{280} dropped from 0.348 to 0.255 and 0.268 during the 7 days of incubation for TR-03 and TR-25, respectively (data not shown), which means 26.72 and 23% of the lignin degradation. And most of the degradation occurred in the initial 4 days. It indicates that the isolates could break down lignin for their growth and metabolism when lignin is used as sole carbon source. At the same time, both the Azure-B decoloration and lignin degradation tests show more superior lignin-degrading activity for the *Bacillus subtilis* TR-03. Thus, TR-03 was further investigated for the characterization of lignin depolymerization.

Micro-morphology by SEM

The change in the morphology of the alkali lignin by *Bacillus subtilis* TR-03 was further observed by SEM and the images were presented in **Figure 5**. The figure showed that the untreated lignin maintained irregular spherical shapes with porous internal structure (**Figure 5A**). After microbial treatment, the structure of alkali lignin was severely damaged, and smaller-sized particles of lignin were produced instead of irregular spherical particles (**Figure 5B**).

FTIR Spectroscopy

FTIR could demonstrate a visualized and rapid indication of the changes in chemical bonds of lignin (Chen et al., 2015). The absorption peaks in FTIR spectra of alkali lignin samples treated by *Bacillus subtilis* TR-03 are presented in **Figure 6**. It can be seen that the FTIR spectra of alkali lignin showed obvious changes from 1,600 to 600 cm^{-1}. The bands representing the aromatic skeleton vibrations appeared at 1,598 cm^{-1} and 1,410 cm^{-1} (Chong et al., 2017; Sun et al., 2019). The weaker intensity of these two signals indicated the breakage or replacing of the aromatic ring chain reaction of lignin structure, which suggested that the lignin was degraded to a certain extent with the *Bacillus subtilis* TR-03 treatment. The band at 1,117 cm^{-1} was attributed to the C-O stretch of syringyl group and the band at 1,046 cm^{-1} may be assigned to the deformation of aromatic ring of guaiacyl group in the lignin (Wang et al., 2015). After degradation, the different intensities of 1,117 cm^{-1} and 1,046 cm^{-1} suggested the destroyed syringyl and guaiacyl group in the delignification process of lignin, and the degradation of guaiacyl group was faster than that of syringyl group.

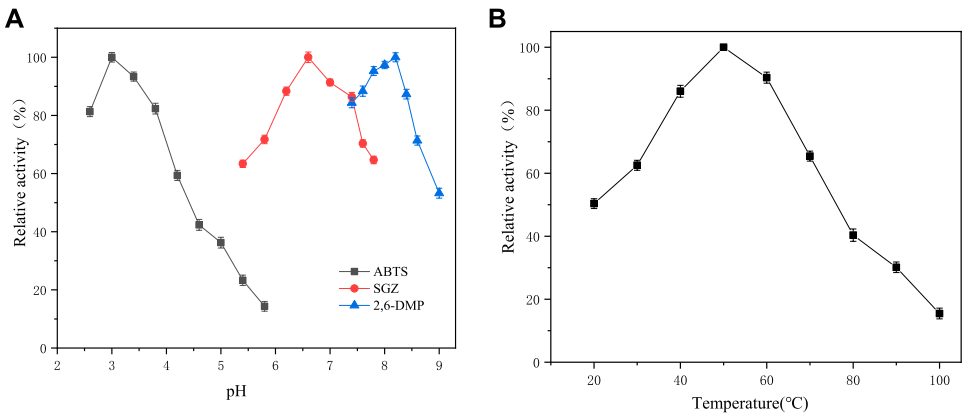

FIGURE 8 | Effect of pH and temperature on intracellular laccase activity of *Bacillus subtilis* TR-03. **(A)** pH, with ABTS, SGZ and 2,6-DMP as substrate at 30°C; **(B)** temperature, with ABTS as the substrate at pH 3.0.

Enzyme Activity Assay of *Bacillus subtilis* TR-03

There are three kinds of enzymes involved in lignin degradation, namely lignin peroxidase (Lip), laccase (Lac) and manganese peroxidase (MnP) (Xu et al., 2017). The enzymes activities determine the ability of bacteria to degrade lignin. Mei et al. (2020) found that *Bacillus amyloliquefaciens* SL-7 could produce MnP, Lip and Lac with the maximum level of 258.57, 422.68 and 55.95 U/L during 7 days, which could reduce the chemical oxygen demand by 69.35% in lignin. The above-mentioned results all exhibit the considerable lignin degradation by *Bacillus subtilis* TR-03. The degradation must be related to various lignin degrading enzymes. The activities of three enzymes were determined during 7 days incubation of TR-03. The results show that TR-03 showed considerable Lip and Lac activity, but with no MnP activity observed (**Figure 7**). The maximum Lip and Lac reached 315.34 U/L and 54.26 U/L on day 4 of incubation, and the Lac activity was lower than that of Lip on the whole level.

Intracellular laccase activity was 129.44 U/L at the end of the fermentation, which was extremely higher than that of extracellular Lac activity. The results are directly in line with that of Chang et al. (2014), which indicates that more local activity was cell-associated. Intracellular and extracellular Lac activities were found in several *Bacillus* sp. strains, such as *Bacillus atrophaeus* and *Bacillus pumilus*, which could successfully degrade kraft lignin (Huang et al., 2013). The intracellular laccase showed an extensive pH range for catalyzing different substrates with an optimum pH of 3.0, 6.6 and 8.2 for ABTS, SGZ and 2,6-DMP, respectively (**Figure 8A**). For temperature adaptability, the crude intracellular laccase showed relatively high activity between 40–70°C, with the maximal activity observed at 50°C (**Figure 8B**). Lac from *Bacillus* sp. is found to withstand high temperature (80–90°C) and alkaline conditions (pH 7–11) (Xu et al., 2019; Das et al., 2020). The extreme robustness in pH and temperature adaptability of intracellular laccase from TR-03 makes it available in the application of different industrial and environmental remediation processes, such as delignification, pulp bleaching and wastewater treatment.

CONCLUSION

Effective ligninolytic *Bacillus* sp. strains were isolated from forest soils and investigated their capability of alkali lignin. *Bacillus subtilis* TR-03 show fairly ligninolytic ability by producing enzymes of Lip and Lac. SEM and FTIR results show the physical and chemical changes in the lignin by smaller particle sizes and the breakage or replacing of the aromatic ring chain reaction of lignin structure. These results prove that *Bacillus* sp. strains were important microorganism in the depolymerization of lignin, and further study should be focus on the degrading mechanism of lignin by *Bacillus* sp.

DATA AVAILABILITY STATEMENT

The datasets presented in this study can be found in online repositories. The names of the repository/repositories and accession number(s) can be found below: https://www.ncbi.nlm.nih.gov/, OK559643 https://www.ncbi.nlm.nih.gov/, OK559727.

AUTHOR CONTRIBUTIONS

All authors read and approved the final manuscript. JY, JZ, HX, and NZ carried out the studies and drafted the manuscript, JJ, JX, and MW participated in the project design and manuscript preparation. The work undertaken is not owned by nor has it been conducted for any for-profit entity. The authors have no financial interest in this work.

FUNDING

This work was financially supported by the Key Lab. of Biomass Energy and Material, Jiangsu Province (JSBEM-S-202011), Natural Science Foundation of Jiangsu Province (BK20200162), National Natural Science Foundation of China (31770636), and Natural Science Foundation of Jiangsu Province (Grant No. K20180153).

REFERENCES

Bandounas, L., Pinkse, M., de Winde, J. H., and Ruijssenaars, H. J. (2013). Identification of a Quinone Dehydrogenase from a Bacillus Sp. Involved in the Decolourization of the Lignin-Model Dye, Azure B. *New Biotechnol.* 30 (2), 196–204. doi:10.1016/j.nbt.2012.04.003

Chai, L.-y., Chen, Y.-h., Tang, C.-j., Yang, Z.-h., Zheng, Y., and Shi, Y. (2014). Depolymerization and Decolorization of Kraft Lignin by Bacterium *Comamonas* Sp. B-9. *Appl. Microbiol. Biotechnol.* 98, 1907–1912. doi:10.1007/s00253-013-5166-5

Chang, Y.-C., Choi, D., Takamizawa, K., and Kikuchi, S. (2014). Isolation of *Bacillus* Sp. Strains Capable of Decomposing Alkali Lignin and Their Application in Combination with Lactic Acid Bacteria for Enhancing Cellulase Performance. *Bioresour. Techn.* 152 (1), 429–436. doi:10.1016/j.biortech.2013.11.032

Chen, Y., Huang, J., Li, Y., Zeng, G., Zhang, J., Huang, A., et al. (2015). Study of the Rice Straw Biodegradation in Mixed Culture of *Trichoderma Viride* and *Aspergillus niger* by GC-MS and FTIR. *Environ. Sci. Pollut. Res.* 22, 9807–9815. doi:10.1007/s11356-015-4149-8

Chong, G.-G., Huang, X.-J., Di, J.-H., Xu, D.-Z., He, Y.-C., Pei, Y.-N., et al. (2017). Biodegradation of Alkali Lignin by a Newly Isolated *Rhodococcus Pyridinivorans* Cczu-B16. *Bioproc. Biosyst. Eng.* 41, 501–510. doi:10.1007/s00449-017-1884-x

Das, R., Liang, Z., Li, G., and An, T. (2020). A Non-blue Laccase of Bacillus Sp. GZB Displays Manganese-Oxidase Activity: A Study of Laccase Characterization, Mn(II) Oxidation and Prediction of Mn(II) Oxidation Mechanism. *Chemosphere* 252, 126619. doi:10.1016/j.chemosphere.2020.126619

Henson, W. R., Hsu, F.-F., Dantas, G., Moon, T. S., and Foston, M. (2018). Lipid Metabolism of Phenol-Tolerant *Rhodococcus Opacus* Strains for Lignin Bioconversion. *Biotechnol. Biofuels* 11 (339), 1–15. doi:10.1186/s13068-018-1337-z

Huang, X.-F., Santhanam, N., Badri, D. V., Hunter, W. J., Manter, D. K., Decker, S. R., et al. (2013). Isolation and Characterization of Lignin-Degrading Bacteria from Rainforest Soils. *Biotechnol. Bioeng.* 110, 1616–1626. doi:10.1002/bit.24833

Kumar, M., Singh, J., Singh, M. K., Singhal, A., and Thakur, I. S. (2015). Investigating the Degradation Process of Kraft Lignin by β-proteobacterium, Pandoraea Sp. ISTKB. *Environ. Sci. Pollut. Res.* 22, 15690–15702. doi:10.1007/s11356-015-4771-5

Lu, L., Zhao, M., Wang, T.-N., Zhao, L.-Y., Du, M.-H., Li, T.-L., et al. (2012). Characterization and Dye Decolorization Ability of an Alkaline Resistant and Organic Solvents Tolerant Laccase from *Bacillus Licheniformis* Ls04. *Bioresour. Techn.* 115, 35–40. doi:10.1016/j.biortech.2011.07.111

Mei, J., Shen, X., Gang, L., Xu, H., Wu, F., and Sheng, L. (2020). A Novel Lignin Degradation Bacteria-*Bacillus Amyloliquefaciens* SL-7 Used to Degrade Straw Lignin Efficiently. *Bioresour. Techn.* 310, 123445. doi:10.1016/j.biortech.2020.123445

Mishra, V., Jana, A. K., Jana, M. M., and Gupta, A. (2017). Enhancement in Multiple Lignolytic Enzymes Production for Optimized Lignin Degradation and Selectivity in Fungal Pretreatment of Sweet Sorghum Bagasse. *Bioresour. Techn.* 236, 49–59. doi:10.1016/j.biortech.2017.03.148

Muaaz-Us-Salam, S., Cleall, P. J., and Harbottle, M. J. (2020). Application of Enzymatic and Bacterial Biodelignification Systems for Enhanced Breakdown of Model Lignocellulosic Wastes. *Sci. Total Environ.* 728, 138741. doi:10.1016/j.scitotenv.2020.138741

Navas, L. E., Martínez, F. D., Taverna, M. E., Fetherolf, M. M., Eltis, L. D., Nicolau, V., et al. (2019). A Thermostable Laccase from Thermus Sp. 2.9 and its Potential for Delignification of Eucalyptus Biomass. *AMB Expr.* 9, 24. doi:10.1186/s13568-019-0748-y

Niu, J., Li, X., Qi, X., and Ren, Y. (2021). Pathway Analysis of the Biodegradation of Lignin by *Brevibacillus Thermoruber*. *Bioresour. Techn.* 341, 125875. doi:10.1016/j.biortech.2021.125875

Picart, P., Wiermans, L., Pérez-Sánchez, M., Grande, P. M., Schallmey, A., and Domínguez de María, P. (2016). Assessing Lignin Types to Screen Novel Biomass-Degrading Microbial Strains: Synthetic Lignin as Useful Carbon Source. *ACS Sustain. Chem. Eng.* 4, 651–655. doi:10.1021/acssuschemeng.5b00961

Sun, Y.-C., Liu, X.-N., Wang, T.-T., Xue, B.-L., and Sun, R.-C. (2019). Green Process for Extraction of Lignin by the Microwave-Assisted Ionic Liquid Approach: Toward Biomass Biorefinery and Lignin Characterization. *ACS Sustain. Chem. Eng.* 7 (15), 13062–13072. doi:10.1021/acssuschemeng.9b02166

Shah, T. A., Ali, S., Afzal, A., and Tabassum, R. (2018). Simultaneous Pretreatment and Biohydrogen Production from Wheat Straw by Newly Isolated Ligninolytic *Bacillus* Sp. Strains with Two-Stage Batch Fermentation System. *Bioenerg. Res.* 11 (4), 835–849. doi:10.1007/s12155-018-9936-x

Tonin, F., Vignali, E., Pollegioni, L., D'Arrigo, P., and Rosini, E. (2017). A Novel, Simple Screening Method for Investigating the Properties of Lignin Oxidative Activity. *Enzyme Microb. Techn.* 96, 143–150. doi:10.1016/j.enzmictec.2016.10.013

Wang, Y., Liu, Q., Yan, L., Gao, Y., Wang, Y., and Wang, W. (2013). A Novel Lignin Degradation Bacterial Consortium for Efficient Pulping. *Bioresour. Techn.* 139, 113–119. doi:10.1016/j.biortech.2013.04.033

Wang, S., Ru, B., Lin, H., Sun, W., and Luo, Z. (2015). Pyrolysis Behaviors of Four Lignin Polymers Isolated from the Same Pine Wood. *Bioresour. Techn.* 182, 120–127. doi:10.1016/j.biortech.2015.01.127

Weng, C., Peng, X., and Han, Y. (2021). Depolymerization and Conversion of Lignin to Value-Added Bioproducts by Microbial and Enzymatic Catalysis. *Biotechnol. Biofuels* 14 (1), 84. doi:10.1186/s13068-021-01934-w

Wong, D. W. S. (2009). Structure and Action Mechanism of Ligninolytic Enzymes. *Appl. Biochem. Biotechnol.* 157, 174–209. doi:10.1007/s12010-008-8279-z

Xu, H., Guo, M.-Y., Gao, Y.-H., Bai, X.-H., and Zhou, X.-W. (2017). Expression and Characteristics of Manganese Peroxidase from *Ganoderma Lucidum* in *Pichia pastoris* and its Application in the Degradation of Four Dyes and Phenol. *BMC Biotechnol.* 17, 19. doi:10.1186/s12896-017-0338-5

Xu, Z., Qin, L., Cai, M., Hua, W., and Jin, M. (2018a). Biodegradation of Kraft Lignin by Newly Isolated *Klebsiella pneumoniae, Pseudomonas Putida*, and *Ochrobactrum Tritici* Strains. *Environ. Sci. Pollut. Res.* 25 (2), 14171–14181. doi:10.1007/s11356-018-1633-y

Xu, R., Zhang, K., Liu, P., Han, H., Zhao, S., Kakade, A., et al. (2018b). Lignin Depolymerization and Utilization by Bacteria. *Bioresour. Techn.* 269 (11), 557–566. doi:10.1016/j.biortech.2018.08.118

Xu, K.-Z., Wang, H.-R., Wang, Y.-J., Xia, J., Ma, H., Cai, Y.-J., et al. (2020). Enhancement in Catalytic Activity of Cota-Laccase from *bacillus Pumilus* W3 via Site-Directed Mutagenesis. *J. Biosci. Bioeng.* 129 (4), 405–411. doi:10.1016/j.jbiosc.2019.09.020

Yang, Y. S., Zhou, J. T., Lu, H., Yuan, Y. L., and Zhao, L. H. (2011). Isolation and Characterization of a Fungus *Aspergillus* Sp. Strain F-3 Capable of Degrading Alkali Lignin. *Biodegradation* 22, 1017–1027. doi:10.1007/s10532-011-9460-6

Yang, G., Yang, D., Wang, X., and Cao, W. (2021). A Novel Thermostable Cellulase-Producing Bacillus Licheniformis A5 Acts Synergistically with Bacillus Subtilis B2 to Improve Degradation of Chinese Distillers' Grains. *Bioresour. Techn.* 325, 9124729–9124810. doi:10.1016/j.biortech.2021.124729

Zhou, H., Guo, W., Xu, B., Teng, Z., Tao, D., Lou, Y., et al. (2017). Screening and Identification of Lignin-Degrading Bacteria in Termite Gut and the Construction of Lip-Expressing Recombinant *Lactococcus Lactis*. *Microb. Pathogenesis* 112, 63–69. doi:10.1016/j.micpath.2017.09.047

Zhu, D., Zhang, P., Xie, C., Zhang, W., Sun, J., Qian, W.-J., et al. (2017). Biodegradation of Alkaline Lignin by Bacillus Ligniniphilus L1. *Biotechnol. Biofuels* 10 (1), 1–14. doi:10.1186/s13068-017-0735-y

Zhu, D., Liang, N., Zhang, R., Ahmad, F., Zhang, W., Yang, B., et al. (2020). Insight into Depolymerization Mechanism of Bacterial Laccase for Lignin. *ACS Sustain. Chem. Eng.* 8 (34), 12920–12933. doi:10.1021/acssuschemeng.0c03457

Conflict of Interest: The authors declare that the research was conducted in the absence of any commercial or financial relationships that could be construed as a potential conflict of interest.

frontiers in Energy Research

MINI REVIEW
published: 13 January 2022
doi: 10.3389/fenrg.2021.827680

Selectivity Control of C-O Bond Cleavage for Catalytic Biomass Valorization

*Yumei Jian, Ye Meng and Hu Li**

State Key Laboratory Breeding Base of Green Pesticide and Agricultural Bioengineering, Key Laboratory of Green Pesticide and Agricultural Bioengineering, Ministry of Education, State-Local Joint Laboratory for Comprehensive Utilization of Biomass, Center for R&D of Fine Chemicals, Guizhou University, Guiyang, China

Increasing fossil fuels consumption and global warming have driven the global revolution towards renewable energy sources. Lignocellulosic biomass is the main source of renewable carbon-based fuels. The abundant intermolecular linkages and high oxygen content between cellulose, hemicellulose, and lignin limit the use of traditional fuels. Therefore, it is a promising strategy to break the above linkages and remove oxygen by selective catalytic cracking of C–O bond to further transform the main components of biomass into small molecular products. This mini-review discusses the significance of selectivity control in C–O bond cleavage with well-tailored catalytic systems or strategies for furnishing biofuels and value-added chemicals of high efficiency from lignocellulosic biomass. The current challenges and future opportunities of converting lignocellulose biomass into high-value chemicals are also summarized and analyzed.

Keywords: high-value chemicals, biofuels, C-O bond, selectivity control, lignocellulosic biomass

OPEN ACCESS

Edited by:
Xiaojun Shen,
Dalian Institute of Chemical Physics (CAS), China

Reviewed by:
Yaxuan JING,
East China University of Science and Technology, China
Qineng Xia,
Jiaxing University, China

****Correspondence:***
Hu Li
hli13@gzu.edu.cn

Specialty section:
This article was submitted to Bioenergy and Biofuels, a section of the journal Frontiers in Energy Research

Received: *02 December 2021*
Accepted: *20 December 2021*
Published: *13 January 2022*

Citation:
Jian Y, Meng Y and Li H (2022) Selectivity Control of C-O Bond Cleavage for Catalytic Biomass Valorization. Front. Energy Res. 9:827680. doi: 10.3389/fenrg.2021.827680

INTRODUCTION

With the over-exploitation and utilization of non-renewable fossil fuels in the conventional chemical industry, the concomitant issues like energy depletion and environmental contamination stimulate the human to explore and develop renewable sources (Li et al., 2017; Wu H. et al., 2020). Lignocellulosic biomass is the most abundant organic carbon source on earth, with great potential to reduce the global reliance on fossil fuels by catalytic upgrading to obtain renewable energy, high-value chemicals, and functional materials (Liu et al., 2019; Wang et al., 2020). However, the oxygen content of virgin biomass is quite high (ca. 40%), mainly existing in the form of cellulose (35–50%), hemicellulose (25–30%), lignin (15–30%), and other extractives (1–5%), which limits its use as traditional fuels (Schutyser et al., 2018). To make better use of lignocellulosic biomass as energy, it is necessary to reduce the oxygen content not only by using the existing infrastructure, but by maximizing energy return (Deng et al., 2015a; Shivhare et al., 2021). To achieve this goal, it is necessary to develop a strategy for selectively controlling the C–O bond scission in biomass to remove oxygen (Krishna et al., 2018). Therefore, exploring new and advanced catalytic systems for selective catalytic cleavage of C–O bonds from lignocellulose biomass under mild conditions has attracted great interest in various fields.

Cellulose is a macromolecular polymer of D-glucose, in which a single glucose unit is connected by β-1,4-glycosidic (C–O–C) bonds (Deng et al., 2015a). This connection causes the glucose units to be arranged side by side in a chain-like manner, resulting in a strong intramolecular hydrogen bond interaction between the hydroxyl groups near the sugar bond, which makes the crystal structure of cellulose very robust (Rinaldi and Schuth, 2009). Therefore, the glycosidic bond of cellulose is also

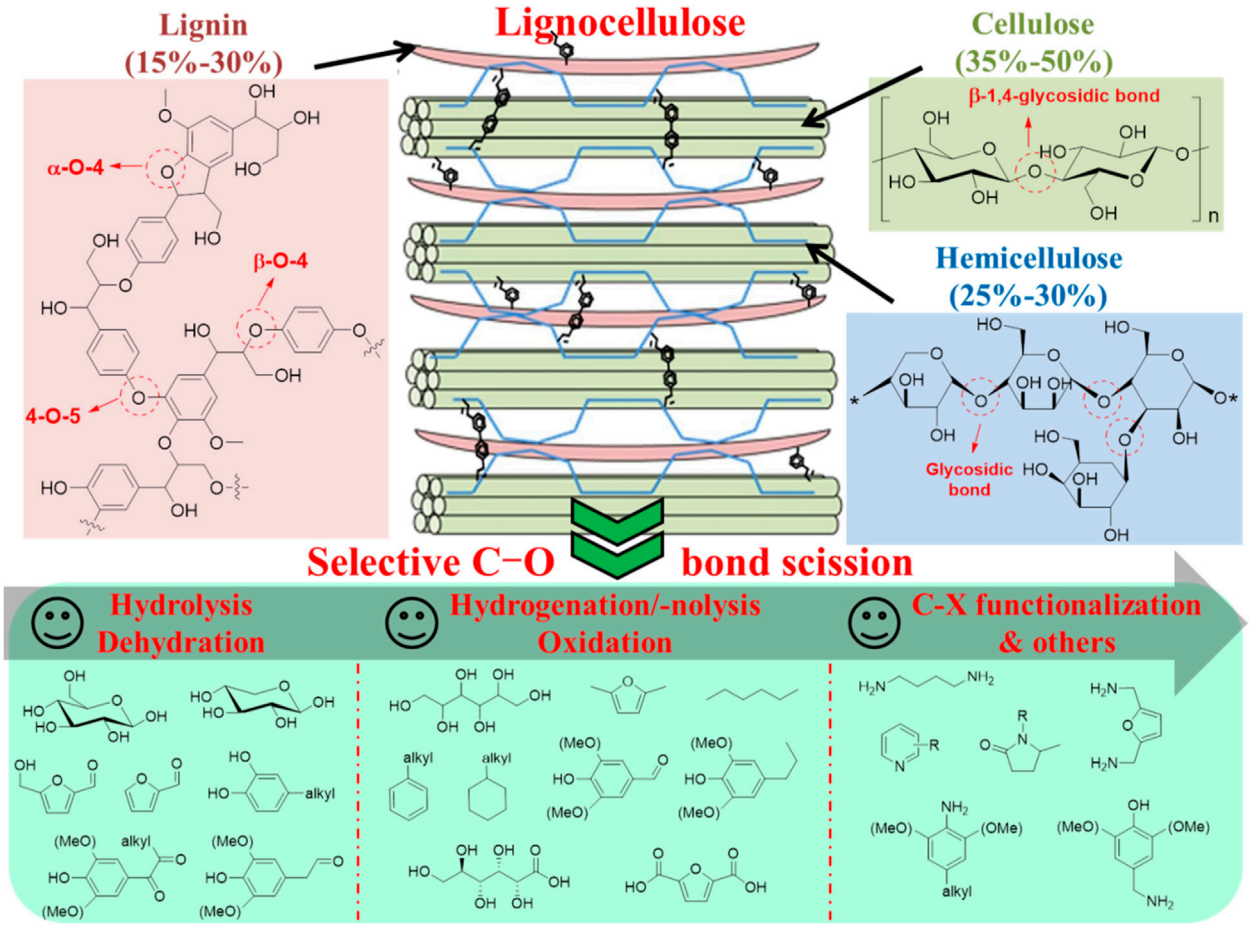

FIGURE 1 | The schematic of biomass valorization via selective C–O bond scission.

difficult to access by a catalytic site for C–O bond cleavage. Compared with cellulose, hemicellulose is a polysaccharide composed of different sugar units (e.g., glucose, xylose, arabinose, and galactose). Although these basic sugar units are also linked by glycosidic bonds, the overall heterogeneity of hemicellulose structure makes it a highly branched polymer, which makes the crystallinity of hemicellulose much lower than that of cellulose (Maki-Arvela et al., 2011). Lignin is a three-dimensional amorphous and complex aromatic polymer mainly composed of phenylpropanoids (Delgado-Aguilar et al., 2016). The three main monomers in lignin have been identified as *p*-coumaric acid, coniferous alcohol, and mustard alcohol (Jampa et al., 2019). Different monomers are connected by various C–O (e.g., *α*-O–4, *β*-O–4 and 4-O–5) and C–C bonds (**Figure 1**) (Wu et al., 2021). Among these bonds, the *β*-O–4 bond is dominant (Enright et al., 2019; Huang et al., 2020).

In view of the different composition and structure of cellulose, hemicellulose, and lignin, it is of great significance to develop an efficient catalytic strategy for selectively converting each component into value-added chemicals, and the cleavage of C–O bonds is a common and important step in the transformation process to release their potential and value-added components (Deng et al., 2015a; Iravani and Varma, 2020). Acid-catalyzed hydrolysis of cellulose is an effective strategy for decomposing its glycosidic (C–O) bond to produce glucose as a primary product, and the further cleavage of glycosidic bonds can be converted into alkyl glucoside, gluconic acid, or hexanol (Li et al., 2018). Compared with cellulose, the glycosidic bond catalytic cracking of hemicellulose is easier to generate monosaccharides (e.g., xylose and arabinose), which is due to the higher reactivity of polysaccharides (Zakzeski et al., 2010). Lignin can decompose its C–O bond by hydrolysis and hydrogenolysis to obtain phenols and a series of other aromatic compounds (Subbotina et al., 2021). However, the selective and efficient cleavage of C–O bonds in lignocellulose biomass is still a major challenge, and the realization of this transformation is crucial for the bio-renewable industry at present.

In the past few years, some excellent reviews have also discussed the selective control of C–O bond cleavage in lignocellulosic biomass from the aspects of different reaction types using various catalysts (Lohr et al., 2016; Yoo et al., 2020). This mini-review summarizes the various high-value biological products available through the highly selective control cleavage pathways of C–O bonds. In addition, different conversion methods of cellulose, hemicellulose, lignin, and their

model compounds controlled by solvents, catalysts, and temperature were discussed, and the challenges faced by selective C–O bond cleavage in biomass upgrading were also summarized.

THE C-O BOND SCISSION ROUTES TO HIGH-VALUE BIOPRODUCTS

The composition and structure of cellulose, hemicellulose, and lignin are different. The intermolecular linkages among these three components are complicated and strong, in which cellulose is covered by the lignin shell (biomass outer cell wall) while hemicellulose is located around cellulose (**Figure 1**) (Rinaldi and Schuth, 2009; Laurichesse and Avérous, 2014). Ether bond, the most abundant intermolecular C–O linkages, exists between side-chain C_α of lignin and C_6 of cellulose or C of hemicellulose (Grabber, 2005). Also, C_γ and C_β in the lignin side-chain can partially connect with cellulose via glycosidic bonding, while ester and acetal/hemiacetal bonds can be formed between the hydroxyl species in the lignin side-chain and–COOH in low quantity or free hydroxyl species of polysaccharides, respectively (Jiang et al., 2018). In addition, the three components interact with each other through hydrogen bonding (Zhang et al., 2015). In this respect, severe mass and heat transfer hindrance are unavoidable in the thermal or catalytic treatment of solid lignocellulosic materials, due to their integral and recalcitrant structure resulting from various C–O binding (e.g., ether bond, glycosidic bond, ester bond, and acetal/hemiacetal bond) and hydrogen bonding modes, as well as low miscibility with water and organic solvents (Grabber, 2005; Hosoya et al., 2007).

For the direct valorization of lignocellulosic biomass, gasification is able to produce syngas that can further undergo the Fischer-Tropsch synthesis to afford hydrocarbon fuels, while pyrolysis can be utilized to yield bio-oils in relatively low quality (Kamm, 2007; Deng et al., 2015a). Because of the relatively high temperature involved, the dominant shortages of these two thermal conversion processes are high energy consumption and low selectivity. It is thus desirable to develop mild and improved routes for the catalytic transformation of lignocellulose into terminal products in satisfactory selectivity. As a prerequisite process to undergo enhanced depolymerization of the three main components, the biomass intermolecular linkages need efficient cleavage to afford the corresponding fluids primarily via C–O bond scission (Zakzeski et al., 2010). The fractionation or pretreatment step coupled with downstream processes can further facilitate the breaking of the intramolecular linkages inside each component, and then simplify the starting materials for furnishing valuable chemicals with high selectivity (Wong et al., 2020).

Both water and organic solvents can destroy the intermolecular linkages among the biopolymeric mixtures under thermal conditions. Hydrothermal conversion of biomass under conventional, subcritical, and supercritical conditions is considered as one of the most economic and greenest processes, generally in need of relatively lower temperatures compared to pyrolysis and gasification (Xue et al., 2016; Jiang et al., 2018). There is an increase in the K_w value of H_2O in the hydrothermal system, giving more active H^+ and OH^- ions that show enhanced capability in biomass depolymerization and hydrolysis by disrupting the intermolecular linkages of hemicellulose-cellulose and hemicellulose-lignin (Luo et al., 2017). In the organosolv process, hemicellulose and lignin can be dissolved into liquid organic solvents, while solid cellulose is recovered in high purity. The presence of acid catalysts can remarkably decrease the reaction temperature, and Brønsted and Lewis acids mainly help to break intermolecular linkages and undergo hydrolysis to yield carbohydrates-based chemicals and lignin-derived oligomers (Constant et al., 2015; Jiang et al., 2018). Base can efficiently catalyze lignin depolymerization to produce monophenols. Moreover, metal metals are beneficial for breaking inter- and intramolecular linkages in carbohydrates or lignin by hydrogenolysis using H_2 or alcohols as hydrogen donor, affording polyols/alkanes or monophenols of high efficiency, respectively.

Cellulose is a crystalline macropolymer composed of glucose units linked by β-1,4-glycosidic (C-O-C) bonds, while hemicellulose in relatively lower crystallinity is a heteropolysaccharide consisting of C_6 and C_5 sugar units (e.g., glucose, mannose, xylose, arabinose and galactose) (Deng et al., 2015a; Deng et al., 2015b). Due to the formation of hydrogen bond network, glycosidic bonds are easier to be protonated and hydrolyzed to glucose in H_2O. Acid catalysts can significantly promote the scission of glycosidic (C-O-C) bonds in cellulose to yield glucose via hydrolysis, while alkyl glucosides can be obtained in an alcohol solvent instead of H_2O (**Figure 1**). These alkyl glycosides are more stable than glucose, which is an effective strategy to accelerate the selective activation of glycosidic bond (Almohalla et al., 2018). In addition, with breaking glycosidic bonds in combination with hydrogenation or oxidation, cellulose can be transformed into hexitols/alkanes or gluconic acid in high selectivity due to their relatively higher stability than glucose. In contrast, the glycosidic bonds of hemicellulose are more likely to cleave compared with cellulose due to the higher reactivity of the heteropolysaccharide, which can afford monosaccharides (e.g., xylose and arabinose) through dilute acid-catalyzed hydrolysis of hemicellulose (Deng et al., 2015a; Song et al., 2019). In both cases, to efficiently access the carbohydrates-derived chemicals such as furanic compounds, nitrogenous chemicals, organic acids, and polyols, well-tailored bifunctional catalysts are therefore required for realizing the occurrence of multiple reactions (Maki-Arvela et al., 2011).

Apart from sugar components, the C–O bonds (e.g., α-O-4, β-O-4 and 4-O-5 linkages) of lignin are often selectively disrupted by hydrolysis and hydrogenolysis, especially the β-O-4 bonds (representing 45–62% of the linkages in lignin), which can produce phenols via simultaneous extraction and conversion processes, but accompanying other aromatic compounds or low-molecular-mass products generated (Guo et al., 2016; Yoo et al., 2020). In addition to the one-step conversion approaches, the oxidative, reductive, and thermal depolymerization or chemical modification of lignin can initially afford platform

monomeric products in the form of a complex mixture of oxygenated hydrocarbons or solid polymers, which can further undergo downstream processes such as deoxygenation, dealkylation, transalkylation, oxidation and polymerization to provide high-value chemicals, biofuels, and polymeric materials (Wong et al., 2020). Three strategies are typically adopted for lignin valorization (**Figure 1**) (Gazi, 2019). 1) Lignin directly undergoes gasification to syngas or pyrolysis to small molecules mixture. 2) Extensive removal of functional groups in lignin monomers gives simple aromatic compounds (e.g., benzene, toluene, xylene, and phenol) (**Figure 1**), followed by using subsequent commercial technology to yield bulk and fine chemicals. 3) Oriented or targeted conversion of lignin and its derivatives furnishes specific functionalized aromatic or aliphatic compounds using highly selective catalysts. Furthermore, the introduction of heteroatom (X = N, Si, Li, etc.) elements rather than C, H, and O in the lignin depolymerization processes permit the formation of C-X and O-X bond in the aromatic ring skeleton, further expanding the scope of lignin products (Li et al., 2020).

All in all, it is still challenging to control the selectivity in cleavage of specific C–O linkages together with other bonds (especially C–C linkage) on lignocellulosic biomass, so as to exclusively afford the desired bioproducts. Developing more versatile and suitable techniques for biomass conversion that destroy the targeted C–O bonds while preserving the pivotal structure (e.g., carbon chain, furanic ring, and aromatic ring) may be one of the most essential objectives.

THE CHALLENGES ASSOCIATED WITH THE SELECTIVE C–O BOND CLEAVAGE FOR BIOMASS UPGRADING

Indeed, the oriented breakage of inter- and intramolecular C–O linkages along with C–C bonding in lignocellulosic biomass is crucial for the whole conversion process, which not only affects the distribution and selectivity of products obtained by downstream processing, but also determines the subsequent treatment parameters and reaction conditions (e.g., solvent, catalyst, and temperature with the heating method) (Hu et al., 2010; Wu X. et al., 2020). A variety of fractionation approaches have been explored to initially break the specific C–O linkages among the biopolymeric mixtures, followed by selective conversion of fractionated-derivatives to either terminal products or intermediates (Jiang et al., 2018). One or two component-first strategy has been adopted on the basis of the component contents and the bonding nature, while the product selectivity is still not satisfying over designed catalysts in optimal solvents, which is hence generally faced with high separation cost, and additional investigations on the fate of disrupting the involved inter- and intramolecular bonds to guide the design of appropriate solvent systems and renewed catalysts.

To selectively break inter- and intramolecular linkages of biomass in a simultaneous or consecutive manner, multifunctional or mixture catalysts able to modulate different reactions towards the desired direction can be envisioned but greatly challenging (Zheng et al., 2020). Instead, the initial production of building monomers (primarily monosaccharides and monophenols) in high purity using industrially available processes can significantly increase the flexibility of biomass being further converted to specific value-added products (Renders et al., 2017). However, the dominant challenge is to suppress the further degradation of the resulting small molecules, considering the difficulty in switching the catalyst reactivity. With a fortunate possibility, chemical funneling and functionalization of a mixture stream derived from biomass to a single product seems a promising strategy for improving the selectivity of the overall conversion process.

The focus of biorefinery in the early 21 century is predominantly on cellulose and hemicellulose. Substantial efforts have been devoted to hydrolytic cleavage of the polysaccharide glycosidic bonds catalyzed by an acid species, including intrinsic acid, and H_2O- or H_2-derived Brønsted acidic sites (Hilgert et al., 2013; Zhang et al., 2014; Zhou et al., 2015). A wide range of bioproducts like monosaccharides, polyols, alkanes, organic acids, 5-hydroxymethylfurfural/furfural, and their derivatives can be attained in the presence of acid and/or metal catalysts (Luo et al., 2016; Sweygers et al., 2020). However, the leaching issue of acidic or metallic species from the solid catalysts is significant and needs to solve properly.

For lignin valorization, inter- and intramolecular C–O linkages (α-O-4, β-O-4 and 4-O-5) can be efficiently destroyed by both hydrolysis with acid or base catalysts and hydrogenolysis with metal catalysts (e.g., Pt, Pd, Rh, Ru, and Ni) (Deng et al., 2015a). The recalcitrant lignin intramolecular linkages are required to be disrupted under more rigorous reaction conditions compared to those for the intermolecular linkages. High-pressure water or organic solvents (e.g., methanol, ethanol, and THF) are efficient for the degradation of lignin fragments, especially for breaking the ether linkages (Jasiukaityte-Grojzdek et al., 2020). Nevertheless, various cross-linking side reactions (predominantly Friedel-Crafts) take place to produce larger fragments, due to the high reactivity of phenolic intermediates and products at high temperatures (Zakzeski et al., 2010). Also, the appropriate design of metal catalysts with enhanced capability to destroy the C–O bonds by hydrogenolysis while inhibiting the hydrogenation of the aromatic rings is highly challenging and in need of solution (Wu et al., 2021). Developing novel strategies like pre-modification of active groups and stabilization of *in situ* formed active species to obstruct the repolymerization of lignin fragments and the occurrence of over-hydrogenation is essential for comprehensive utilization of lignocellulosic biomass.

As a simple and potentially low-cost strategy, simultaneous extraction and depolymerization of lignin directly from biomass to produce monophenols can be implemented over Ni or precious metal catalysts, which is attributed to the fact that nickel or precious metal catalysts can significantly increase the activation of phenoxy and reduce the reaction barrier (Jiang and Hu, 2016). However, the co-existent sugar-derived products markedly complicate the lignin conversion process, because the accompanying degradation of carbohydrates is easier to occur under thermal conditions (Luo et al., 2014; Jiang and Hu, 2016). In addition, the cleavage temperature for cellulose intermolecular

and hemicellulose intramolecular linkages is greatly overlapped, which should be thoroughly selected to impede unwanted reactions in a one-pot conversion process. Alternatively, stepwise routes are often employed for the three components in actual biomass, in which lignin or saccharides are first separated selectively, followed by catalytic degradation to produce targeted small molecules.

The development of efficient biomass conversion routes is highly correlated with the understanding of the unconverted components. Notably, a big difference in the conversion performance is generally observed between lignin model molecules and real lignin in biomass (Jiang and Hu, 2016). It is a pity that the catalytic mechanism for natural lignin depolymerization remains blurred due to its recalcitrant structure, and most current investigations focus on the catalytic materials and systems explored for upgrading of lignin-derived oligomers and model compounds that mimic the C–O linkages in lignin (Deng et al., 2015a). In connection to this, scission and functionalization of C–O bonds triggered by heteroatoms (e.g., N, S, and P) in atypical ways have been exploited as competitive routes to utilize lignocellulose despite of unsatisfactory outcome obtained in most real biopolymeric feedstocks, which needs much further improvement (Liu et al., 2018; Li et al., 2020). Moreover, it would be another economical process to prepare artificial polymeric materials from lignocellulose such as lignin and cellulose through either modification of inherent polymeric frameworks or bio-derived specific monomers. These achievements are closely to rely on the development of innovative strategies that can effectively control the cleavage of designated linkages, especially C–O bonds that are rich and ubiquitous in the connections of actual lignocellulosic biomass.

CONCLUSION AND PERSPECTIVES

In conclusion, it is crucial to develop efficient selective pyrolysis methods of C–O bonds in cellulose, hemicellulose, lignin, or their model compounds to convert them into value-added chemicals or fuels under mild conditions. This mini-review introduces the research progress of selective cleavage of C–O bonds in cellulose and its carbohydrate derivatives and hemicellulose, as well as lignin or its model compounds. In addition, it is still challenging to control the cleavage selectivity of specific C–O bonds and other bonds (especially C–C bonds) on lignocellulose biomass, which provides a reference for the development of more general and applicable biomass conversion technologies, the destruction of target C–O bonds and the retention of key structures (e.g., carbon-chain, furanic ring, and aromatic ring).

Hydrolytic cleavage of glycosidic bonds in cellulose leads to the formation of glucose or related oligomers. The acidic catalyst has high catalytic performance and can selectively hydrolyze glycosidic bonds to obtain glucose, which is attributed to the formation of hydrogen bonds between the functional groups of the acidic catalysts and cellulose. The hydrolysis of hemicellulose in the presence of acid catalyst can lead to the cleavage of glycosidic bonds. Xylose, arabinose and other monosaccharides can be obtained under mild conditions, but also can undergo further dehydration of monosaccharides to furfural and its derivatives. Apart from acid and alkali that can catalyze the hydrolysis of lignin and its model compounds, metal catalysts can also effectively hydrogenate C–O bonds in lignin to give corresponding aromatic compounds. In some cases, the cleavage of C–O bonds is accompanied by the hydrogenation of aromatic rings, thus providing a complex mixture of corresponding cyclohexane derivatives. Therefore, it is necessary to design efficient catalysts with enhanced hydrogenolysis ability but inhibiting hydrogenation ability to improve the selectivity in catalytic production of aromatic compounds.

To meet mankind's demand for chemical products and fuels, efficient catalytic strategies should be developed to convert lignocellulose biomass fractions from low-quality, low-cost wastes into high-quality, high-value feedstocks. This shift is crucial because lignocellulose biomass is the only viable alternative source on which society depends today. Last but not the least, talented and dedicated efforts along with insights and holistic analyses to depreciate the "cost-determining" conversion processes would shift biomass valorization from "proof-of-concept" to "proof-of-value" stage and perpetuate its research liveliness.

AUTHOR CONTRIBUTIONS

YJ organized and prepared all this manuscript; YM made preliminary revisions to the manuscript; HL contributed to writing and reviewing the part of the manuscript.

FUNDING

The study was funded by the National Natural Science Foundation of China (21908033), and Fok Ying-Tong Education Foundation (161030).

REFERENCES

Almohalla, M., Rodríguez-Ramos, I., Ribeiro, L. S., Órfão, J. J. M., Pereira, M. F. R., and Guerrero-Ruiz, A. (2018). Cooperative Action of Heteropolyacids and Carbon Supported Ru Catalysts for the Conversion of Cellulose. *Catal. Today* 301, 65–71. doi:10.1016/j.cattod.2017.05.023

Constant, S., Basset, C., Dumas, C., Di Renzo, F., Robitzer, M., Barakat, A., et al. (2015). Reactive Organosolv Lignin Extraction from Wheat Straw: Influence of Lewis Acid Catalysts on Structural and Chemical Properties of Lignins. *Ind. Crops Prod.* 65, 180–189. doi:10.1016/j.indcrop.2014.12.009

Delgado-Aguilar, M., González, I., Tarrés, Q., Pèlach, M. À., Alcalà, M., and Mutjé, P. (2016). The Key Role of Lignin in the Production of Low-Cost Lignocellulosic Nanofibres for Papermaking Applications. *Ind. Crops Prod.* 86, 295–300. doi:10.1016/j.indcrop.2016.04.010

Deng, W., Zhang, H., Xue, L., Zhang, Q., and Wang, Y. (2015a). Selective Activation of the C-O Bonds in Lignocellulosic Biomass for the Efficient Production of Chemicals. *Chin. J. Catal.* 36, 1440–1460. doi:10.1016/s1872-2067(15)60923-8

Deng, W., Zhang, Q., and Wang, Y. (2015b). Catalytic Transformation of Cellulose and its Derived Carbohydrates into Chemicals Involving C C Bond Cleavage. *J. Energ. Chem.* 24, 595–607. doi:10.1016/j.jechem.2015.08.016

Enright, M. J., Gilbert-Bass, K., Sarsito, H., and Cossairt, B. M. (2019). Photolytic C-O Bond Cleavage with Quantum Dots. *Chem. Mater.* 31, 2677–2682. doi:10.1021/acs.chemmater.9b00943

Gazi, S. (2019). Valorization of wood Biomass-Lignin via Selective Bond Scission: A Minireview. *Appl. Catal. B: Environ.* 257, 117936. doi:10.1016/j.apcatb.2019.117936

Grabber, J. H. (2005). How Do Lignin Composition, Structure, and Cross-Linking Affect Degradability? A Review of Cell Wall Model Studies. *Crop Sci.* 45, 820–831. doi:10.2135/cropsci2004.0191

Guo, H., Zhang, B., Li, C., Peng, C., Dai, T., Xie, H., et al. (2016). Tungsten Carbide: A Remarkably Efficient Catalyst for the Selective Cleavage of Lignin C–O Bonds. *ChemSusChem* 9, 3220–3229. doi:10.1002/cssc.201600901

Hilgert, J., Meine, N., Rinaldi, R., and Schüth, F. (2013). Mechanocatalytic Depolymerization of Cellulose Combined with Hydrogenolysis as a Highly Efficient Pathway to Sugar Alcohols. *Energy Environ. Sci.* 6, 92–96. doi:10.1039/c2ee23057g

Hosoya, T., Kawamoto, H., and Saka, S. (2007). Influence of Inorganic Matter on wood Pyrolysis at Gasification Temperature. *J. Wood Sci.* 53, 351–357. doi:10.1007/s10086-006-0854-8

Hu, R., Lin, L., Liu, T., and Liu, S. (2010). Dilute Sulfuric Acid Hydrolysis of Sugar maple wood Extract at Atmospheric Pressure. *Bioresour. Technol.* 101, 3586–3594. doi:10.1016/j.biortech.2010.01.005

Huang, D., Li, R., Xu, P., Li, T., Deng, R., Chen, S., et al. (2020). The Cornerstone of Realizing Lignin Value-Addition: Exploiting the Native Structure and Properties of Lignin by Extraction Methods. *Chem. Eng. J.* 402, 126237. doi:10.1016/j.cej.2020.126237

Iravani, S., and Varma, R. S. (2020). Greener Synthesis of Lignin Nanoparticles and Their Applications. *Green. Chem.* 22, 612–636. doi:10.1039/c9gc02835h

Jampa, S., Puente-Urbina, A., Ma, Z., Wongkasemjit, S., Luterbacher, J. S., and van Bokhoven, J. A. (2019). Optimization of Lignin Extraction from Pine Wood for Fast Pyrolysis by Using a γ-Valerolactone-Based Binary Solvent System. *ACS Sustain. Chem. Eng.* 7, 4058–4068. doi:10.1021/acssuschemeng.8b05498

Jasiukaitytė-Grojzdek, E., Huš, M., Grilc, M., and Likozar, B. (2020). Acid-catalysed α-O-4 Aryl-Ether Bond Cleavage in Methanol/(aqueous) Ethanol: Understanding Depolymerisation of a Lignin Model Compound during Organosolv Pretreatment. *Sci. Rep.* 10, 11037. doi:10.1038/s41598-020-67787-9

Jiang, Z., and Hu, C. (2016). Selective Extraction and Conversion of Lignin in Actual Biomass to Monophenols: A Review. *J. Energ. Chem.* 25, 947–956. doi:10.1016/j.jechem.2016.10.008

Jiang, Z., Zhao, P., and Hu, C. (2018). Controlling the Cleavage of the Inter- and Intra-molecular Linkages in Lignocellulosic Biomass for Further Biorefining: A Review. *Bioresour. Technol.* 256, 466–477. doi:10.1016/j.biortech.2018.02.061

Kamm, B. (2007). Production of Platform Chemicals and Synthesis Gas from Biomass. *Angew. Chem. Int. Ed.* 46, 5056–5058. doi:10.1002/anie.200604514

Krishna, S. H., Huang, K., Barnett, K. J., He, J., Maravelias, C. T., Dumesic, J. A., et al. (2018). Oxygenated Commodity Chemicals from Chemo-catalytic Conversion of Biomass Derived Heterocycles. *Aiche J.* 64, 1910–1922. doi:10.1002/aic.16172

Laurichesse, S., and Avérous, L. (2014). Chemical Modification of Lignins: Towards Biobased Polymers. *Prog. Polym. Sci.* 39, 1266–1290. doi:10.1016/j.progpolymsci.2013.11.004

Li, H., Bunrit, A., Li, N., and Wang, F. (2020). Heteroatom-participated Lignin Cleavage to Functionalized Aromatics. *Chem. Soc. Rev.* 49, 3748–3763. doi:10.1039/d0cs00078g

Li, H., Riisager, A., Saravanamurugan, S., Pandey, A., Sangwan, R. S., Yang, S., et al. (2017). Carbon-Increasing Catalytic Strategies for Upgrading Biomass into Energy-Intensive Fuels and Chemicals. *ACS Catal.* 8, 148–187. doi:10.1021/acscatal.7b02577

Li, S., Deng, W., Wang, S., Wang, P., An, D., Li, Y., et al. (2018). Catalytic Transformation of Cellulose and its Derivatives into Functionalized Organic Acids. *ChemSusChem* 11, 1995–2028. doi:10.1002/cssc.201800440

Liu, X., Zhang, H., Wu, C., Liu, Z., Chen, Y., Yu, B., et al. (2018). Copper-catalyzed Synthesis of Benzanilides from Lignin Model Substrates 2-phenoxyacetophenones under an Air Atmosphere. *New J. Chem.* 42, 1223–1227. doi:10.1039/c7nj02589k

Liu, Y., Nie, Y., Lu, X., Zhang, X., He, H., Pan, F., et al. (2019). Cascade Utilization of Lignocellulosic Biomass to High-Value Products. *Green. Chem.* 21, 3499–3535. doi:10.1039/c9gc00473d

Lohr, T. L., Li, Z., and Marks, T. J. (2016). Thermodynamic Strategies for C-O Bond Formation and Cleavage via Tandem Catalysis. *Acc. Chem. Res.* 49, 824–834. doi:10.1021/acs.accounts.6b00069

Luo, Y., Hu, L., Tong, D., and Hu, C. (2014). Selective Dissociation and Conversion of Hemicellulose in Phyllostachys Heterocycla Cv. Var. Pubescens to Value-Added Monomers via Solvent-thermal Methods Promoted by AlCl3. *RSC Adv.* 4, 24194–24206. doi:10.1039/c4ra02209b

Luo, Y., Li, Z., Zuo, Y., Su, Z., and Hu, C. (2017). A Simple Two-step Method for the Selective Conversion of Hemicellulose in Pubescens to Furfural. *ACS Sustain. Chem. Eng.* 5, 8137–8147. doi:10.1021/acssuschemeng.7b01766

Luo, Y., Yi, J., Tong, D., and Hu, C. (2016). Production of γ-valerolactone via Selective Catalytic Conversion of Hemicellulose in Pubescens without Addition of External Hydrogen. *Green. Chem.* 18, 848–857. doi:10.1039/c5gc01775k

Mäki-Arvela, P., Salmi, T., Holmbom, B., Willför, S., and Murzin, D. Y. (2011). Synthesis of Sugars by Hydrolysis of Hemicelluloses- A Review. *Chem. Rev.* 111, 5638–5666. doi:10.1021/cr2000042

Renders, T., Van den Bosch, S., Koelewijn, S.-F., Schutyser, W., and Sels, B. F. (2017). Lignin-first Biomass Fractionation: the Advent of Active Stabilisation Strategies. *Energ. Environ. Sci.* 10, 1551–1557. doi:10.1039/c7ee01298e

Rinaldi, R., and SchÃ¼th, F. (2009). Acid Hydrolysis of Cellulose as the Entry point into Biorefinery Schemes. *ChemSusChem* 2, 1096–1107. doi:10.1002/cssc.200900188

Schutyser, W., Renders, T., Van den Bosch, S., Koelewijn, S.-F., Beckham, G. T., and Sels, B. F. (2018). Chemicals from Lignin: an Interplay of Lignocellulose Fractionation, Depolymerisation, and Upgrading. *Chem. Soc. Rev.* 47, 852–908. doi:10.1039/c7cs00566k

Shivhare, A., Kumar, A., and Srivastava, R. (2021). Metal Phosphate Catalysts to Upgrade Lignocellulose Biomass into Value-Added Chemicals and Biofuels. *Green. Chem.* 23, 3818–3841. doi:10.1039/d1gc00376c

Song, H., Wang, P., Li, S., Deng, W., Li, Y., Zhang, Q., et al. (2019). Direct Conversion of Cellulose into Ethanol Catalysed by a Combination of Tungstic Acid and Zirconia-Supported Pt Nanoparticles. *Chem. Commun.* 55, 4303–4306. doi:10.1039/c9cc00619b

Subbotina, E., Rukkijakan, T., Marquez-Medina, M. D., Yu, X., Johnsson, M., and Samec, J. S. M. (2021). Oxidative Cleavage of C-C Bonds in Lignin. *Nat. Chem.* 13, 1118–1125. doi:10.1038/s41557-021-00783-2

Sweygers, N., Depuydt, D. E. C., Van Vuure, A. W., Degrève, J., Potters, G., Dewil, R., et al. (2020). Simultaneous Production of 5-hydroxymethylfurfural and Furfural from Bamboo (Phyllostachys Nigra "Boryana") in a Biphasic Reaction System. *Chem. Eng. J.* 386, 123957. doi:10.1016/j.cej.2019.123957

Wang, H., Yang, B., Zhang, Q., and Zhu, W. (2020). Catalytic Routes for the Conversion of Lignocellulosic Biomass to Aviation Fuel Range Hydrocarbons. *Renew. Sustain. Energ. Rev.* 120, 109612. doi:10.1016/j.rser.2019.109612

Wong, S. S., Shu, R., Zhang, J., Liu, H., and Yan, N. (2020). Downstream Processing of Lignin Derived Feedstock into End Products. *Chem. Soc. Rev.* 49, 5510–5560. doi:10.1039/d0cs00134a

Wu, D., Wang, Q., Safonova, O. V., Peron, D. V., Zhou, W., Yan, Z., et al. (2021). Lignin Compounds to Monoaromatics: Selective Cleavage of C–O Bonds over a Brominated Ruthenium Catalyst. *Angew. Chem. Int. Ed.* 60, 12513–12523. doi:10.1002/anie.202101325

Wu, H., Dai, W., Saravanamurugan, S., Li, H., and Yang, S. (2020a). Endogenous X-C✓O Species Enable Catalyst-free Formylation Prerequisite for CO2 Reductive Upgrading. *Green. Chem.* 22, 5822–5832. doi:10.1039/d0gc02142c

Wu, X., Luo, N., Xie, S., Zhang, H., Zhang, Q., Wang, F., et al. (2020b). Photocatalytic Transformations of Lignocellulosic Biomass into Chemicals. *Chem. Soc. Rev.* 49, 6198–6223. doi:10.1039/d0cs00314j

Xue, Y., Chen, H., Zhao, W., Yang, C., Ma, P., and Han, S. (2016). A Review on the Operating Conditions of Producing Bio-Oil from Hydrothermal Liquefaction of Biomass. *Int. J. Energ. Res.* 40, 865–877. doi:10.1002/er.347310.1002/er

Yoo, C. G., Meng, X., Pu, Y., and Ragauskas, A. J. (2020). The Critical Role of Lignin in Lignocellulosic Biomass Conversion and Recent Pretreatment Strategies: A Comprehensive Review. *Bioresour. Technol.* 301, 122784. doi:10.1016/j.biortech.2020.122784

Zakzeski, J., Bruijnincx, P. C. A., Jongerius, A. L., and Weckhuysen, B. M. (2010). The Catalytic Valorization of Lignin for the Production of Renewable Chemicals. *Chem. Rev.* 110, 3552–3599. doi:10.1021/cr900354u

Zhang, J., Choi, Y. S., Yoo, C. G., Kim, T. H., Brown, R. C., and Shanks, B. H. (2015). Cellulose-Hemicellulose and Cellulose-Lignin Interactions during Fast Pyrolysis. *ACS Sustain. Chem. Eng.* 3, 293–301. doi:10.1021/sc500664h

Zhang, J., Teo, J., Chen, X., Asakura, H., Tanaka, T., Teramura, K., et al. (2014). A Series of NiM (M = Ru, Rh, and Pd) Bimetallic Catalysts for Effective Lignin Hydrogenolysis in Water. *ACS Catal.* 4, 1574–1583. doi:10.1021/cs401199f

Zheng, A., Huang, Z., Wei, G., Zhao, K., Jiang, L., Zhao, Z., et al. (2020). Controlling Deoxygenation Pathways in Catalytic Fast Pyrolysis of Biomass and its Components by Using Metal-Oxide Nanocomposites. *iScience* 23, 100814. doi:10.1016/j.isci.2019.100814

Zhou, L., Yang, X., Xu, J., Shi, M., Wang, F., Chen, C., et al. (2015). Depolymerization of Cellulose to Glucose by Oxidation-Hydrolysis. *Green. Chem.* 17, 1519–1524. doi:10.1039/c4gc02151g

Conflict of Interest: The authors declare that the research was conducted in the absence of any commercial or financial relationships that could be construed as a potential conflict of interest.

frontiers in Energy Research

ORIGINAL RESEARCH
published: 22 February 2022
doi: 10.3389/fenrg.2022.851543

Efficient Swelling and Mercerization of Bagasse Fiber by Freeze-Thaw-Assisted Alkali Treatment

*Liming Cao, Jiatian Zhu, Baojuan Deng, Fanyan Zeng, Shanshan Wang, Yun Ma, Chengrong Qin and Shuangquan Yao**

Guangxi Key Laboratory of Clean Pulp and Papermaking and Pollution Control, School of Light Industrial and Food Engineering, Guangxi University, Nanning, China

The mercerization of fiber is an important method for the high-value utilization of cellulose. In this study, the bagasse fiber was mercerized by freeze–thaw-assisted alkali treatment (FT/AT). The effects of freezing temperature, freezing time, alkali concentration, and thawing temperature on cellulose and hemicellulose removal were studied. The optimal freezing temperature was −40°C, freezing time was 8.0 h, alkali concentration was 5.0%, and thawing temperature was 30°C. The highest removal rate of hemicellulose was 75.64%. It was 5.80% higher than that of alkali treatment (AT). The alkaline degradation of cellulose was inhibited. The penetration of alkaline solution to fiber was promoted by the assistance of freeze-thaw pretreatment. The effective alkali concentration (5.0%) of cellulose I completely transformed into cellulose II decreased by 66.67% compared with traditional alkaline mercerization (15.0%). The high-efficiency mercerization of fiber was achieved by FT/AT. It provides theoretical support for promoting the high-value utilization of lignocellulosic biomass.

Keywords: alkali treatment, freeze-thaw, hemicellulose, cellulose, swelling, mercerization

OPEN ACCESS

Edited by:
Jia-Long Wen,
Beijing Forestry University, China

Reviewed by:
Xin Zhou,
Nanjing Forestry University, China
Xiaolin Luo,
Fujian Agriculture and Forestry University, China

****Correspondence:***
Shuangquan Yao
yaoshuangquan@gxu.edu.cn

Specialty section:
This article was submitted to Bioenergy and Biofuels, a section of the journal Frontiers in Energy Research

Received: *10 January 2022*
Accepted: *24 January 2022*
Published: *22 February 2022*

Citation:
Cao L, Zhu J, Deng B, Zeng F, Wang S, Ma Y, Qin C and Yao S (2022) Efficient Swelling and Mercerization of Bagasse Fiber by Freeze-Thaw-Assisted Alkali Treatment. Front. Energy Res. 10:851543. doi: 10.3389/fenrg.2022.851543

INTRODUCTION

Currently, lignocellulosic biomass plays an important role in the energy, chemical, and material fields because of its zero carbon dioxide emissions, high content, and renewable properties (Luo et al., 2021; Zhu et al., 2020). Cellulose is the main component of the lignocellulosic biomass (Bian et al., 2019). In addition to pulp fibers, it is used to produce bioethanol and various functional materials, such as microcrystalline cellulose, medical cellulose, and high-absorbent cellulose materials (Alexakis et al., 2021; Li X. et al., 2021; Pang et al., 2015). The most widely used in the industry is cellulose II, although cellulose I occurs naturally (Yagura et al., 2020)' (Kita et al., 2020). Cellulose II is obtained by dissolution/regeneration (Reyes et al., 2020) or mercerization (Marzouki et al., 2019). Fibers are inflated using sodium hydroxide solution (Öztürk et al., 2006). The hemicellulose in the amorphous region is dissolved as alkali diffuses (Marzouki et al., 2019; Yu et al., 2017), and cellulose II is obtained. Smooth and round fibers are obtained by mercerization. The fiber kink index increases, and the content of fine components decreases (Noori et al., 2021). Mercerized fibers have good air permeability and chemical stability (Kumar et al., 2011; Oladele et al., 2019). They are widely used in the preparation of air filter paper, dictionary paper, and blotting paper. The color uniformity, fabric surface smoothness, and size stability of the cotton fabric is improved by printing.

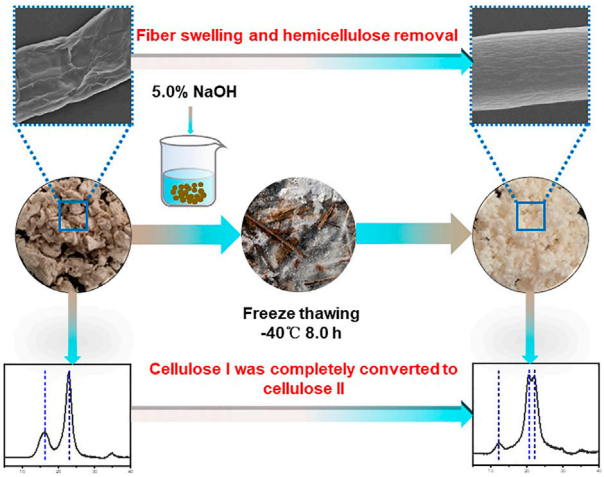

GRAPHICAL ABSTRACT |

Fibers are mercerized using traditional high alkali concentration treatments (15.00–18.00%) (Albán Reyes et al., 2016). The crystalline form of cellulose changes at full swelling. Helena et al. (Halonen et al., 2013) investigated the effect of mercerization on the cellulose supramolecular structure and water retention value. The results showed that partial cellulose II was obtained using 11.00% sodium hydroxide. Liu et al. (Liu & Hu, 2008) studied the effect of mercerization on the supramolecular structure of bamboo fibers. It was found that the crystalline form of cellulose changed when the sodium hydroxide concentration was greater than 12.00%. The effects of alkali treatment temperature and time and alkali concentration on cellulose lattice conversion were studied (SaifulAzry et al., 2017). The results showed that cellulose I was completely converted to cellulose II in a 20.00% sodium hydroxide solution. The thermal stability of the mercerized fibers improved. However, a small amount of cellulose was dissolved during the alkaline degradation, and the cellulose yield decreased. This is a technical problem that needs to be overcome in fiber mercerization. Presently, the mercerization of bleached chemical pulp is employed for the high-value utilization of the traditional pulp fiber (Albán Reyes et al., 2016). However, the mercerization effect and the swelling of the fibers are inhibited by the presence of a small amount of hemicellulose in the pulp (Chen et al., 2020). The hemicellulose is efficiently separated using a new alkali treatment. David et al. (Ibarra et al., 2010) used xylanase and endoglucanase pretreatments-assisted alkali treatment. The removal rate of hemicellulose in the sulfate bleaching chemical pulp was 82.00%. The effect of hemicellulose removal in sulfite pulp by mechanical grinding-assisted alkali treatment was studied by Li (Li et al., 2015). The pore volume and specific surface area of the pulp fibers are increased by mechanical grinding. The dissolution of hemicellulose is facilitated by alkali treatment, and the effective alkali concentration is significantly reduced. Additionally, freeze–thaw pretreatment has been employed to assist alkali treatment for the efficient separation of hemicellulose (Li J. et al., 2021). The results showed that the extraction rate of hemicellulose was 64.71%. This means that the infiltration of alkali was enhanced by the freeze–thaw pretreatment. Therefore, it is of great significance to study the mercerization of chemical pulp by freeze–thaw-assisted alkali treatment (FT/AT).

In this study, the fiber of bleached bagasse pulp was mercerized by FT/AT. The effects of freezing temperature, freezing time, alkali concentration, and thawing temperature on cellulose and hemicellulose removal were studied. The intrinsic viscosity, thermal stability, and water retention value of the fibers after the different treatments were analyzed. The morphology and physicochemical properties of the fibers were analyzed by scanning electron microscopy (SEM), specific surface area analysis (Brunauer–Emmett–Teller theory (BET)), Fourier-transform infrared spectroscopy (FTIR), X-ray diffraction (XRD), and fiber quality analysis. It provides theoretical support for the efficient mercerization of fibers.

MATERIALS AND METHODS

Materials

Bleached bagasse pulp was supplied by a local factory (Guangxi, China). The viscosity, brightness, and Kappa number of the pulp were 776 ml g^{-1}, 76 %ISO, and 3.1, respectively. The details are listed in **Table 1**. The main chemical composition was analyzed (Ge et al., 2020). The cellulose and hemicellulose contents were 80.19 and 13.56%, respectively. 90% of Sodium hydroxide solution was purchased from Sigma-Aldrich (United States). Other analytical chemicals were purchased from Aladdin Biotechnology Co., Ltd. (Shanghai, China).

Swelling of Bagasse Fiber

The bagasse fiber was swollen by FT/AT. The air-dried bagasse pulp (10 g) was thoroughly soaked in an alkali solution (240 ml). The pulp was frozen in an ultra-low temperature quick-freezing machine (ILG500DFD; Bitzer, Sindelfingen, Germany). The solid-liquid ratio was 1: 24. The pulp was treated at different freezing temperatures, freezing times, and alkali concentrations. It was

TABLE 1 | Chemical properties of bagasse fiber with different treatments.

	Bagasse pulp	AT	FT/AT
Yield (%)	100	78.35 ± 2.13	84.47 ± 2.41
Cellulose (%)	80.19 ± 0.87	71.88 ± 1.62	76.48 ± 1.34
Hemicellulose (%)	13.56 ± 0.26	4.09 ± 0.17	1.82 ± 0.13
Viscosity (ml.g^{-1})	776 ± 2.53	833 ± 2.69	845 ± 2.78
Polymerization degree	1,135 ± 3.26	1,229 ± 3.74	1,248 ± 3.82
Fiber length (mm)	0.73 ± 0.04	0.59 ± 0.01	0.59 ± 0.01
Fiber width (μm)	18.21 ± 0.27	16.96 ± 0.17	17.33 ± 0.21
Fine fiber content (%)	6.67 ± 0.29	4.43 ± 0.16	3.31 ± 0.13
Form factor (%)	89.55 ± 1.32	82.92 ± 1.48	82.41 ± 1.28
Kink angle (°)	51.63 ± 0.73	59.14 ± 0.86	61.90 ± 0.79
Kink index (mm^{-1})	0.82 ± 0.04	1.57 ± 0.02	1.68 ± 0.01
Specific surface area (m^2.g^{-1})	0.54 ± 0.03	0.63 ± 0.05	1.04 ± 0.02
Pore volume (×10^{-3} cm^{-3} g^{-1})	2.80 ± 0.05	2.65 ± 0.02	2.00 ± 0.03
Aperture (nm)	19.51 ± 0.39	12.50 ± 0.25	10.82 ± 0.32
Water retention value (%)	114 ± 2.16	149 ± 3.37	163 ± 3.41

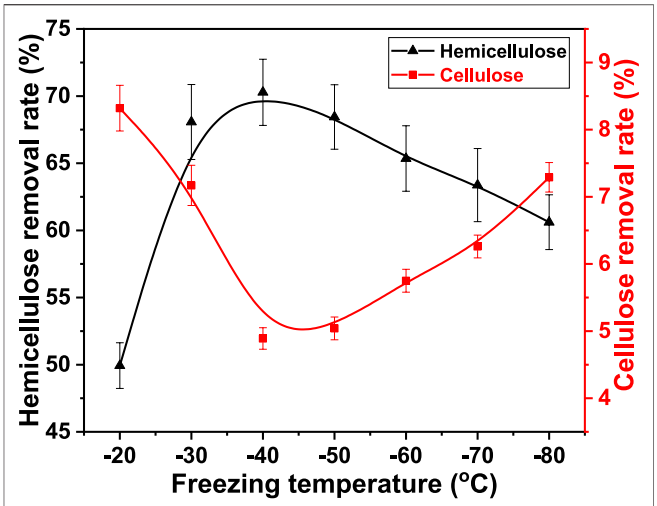

FIGURE 1 | Effect of freezing temperature on the removal rate of cellulose and hemicellulose from bagasse fiber in FT/AT.

completely thawed at different temperatures. Then, the treated pulp was obtained by vacuum extraction and filtration. The pulp was washed with pure water until after reaction. Then, it was air-dried and sealed. The swelling properties of the fiber was compared with those of traditional high-concentration AT (Halonen et al., 2013). 10 g of pulp was placed in 15.0% alkali at 50°C for 60 min.

Chemical Composition of the Pulp With Different Treatments

The contents of cellulose and hemicellulose in pulp with different treatments were analyzed (Ge et al., 2020). The specific method and process were described by Cavali and co-authors (Cavali et al., 2020). The removal rates of cellulose and hemicellulose were calculated using **Eqs 1**, **2**.

$$R_H = (C_1 - C_2)/C_2 * 100\%, \quad (1)$$

$$R_C = (C_3 - C_4)/C_3 * 100\%, \quad (2)$$

Where R_H is the removal rate of hemicellulose (%), C_1 is the hemicellulose content in the initial pulp (g), C_2 is the hemicellulose content in the treated pulp (g), R_C is the removal rate of cellulose (%), C_3 is the cellulose content in the initial pulp (g), and C_4 is the cellulose content in the treated pulp (g).

Physicochemical Properties of Fiber

The surface morphology of bagasse fiber with different treatments was characterized by SEM (Quanta FEG 250, FEI, Hills-boro, Oregon, United States) (Yao et al., 2015). The pore volume, pore diameter, and specific surface area of the fiber was analyzed using a specific surface area and porosity analyzer (ASAP 2460; Micromeritics, United States). The length, width and fine fiber content of bagasse fiber were analyzed using a fiber quality analyzer (912, Lorentze & Wettre, Sweden). The degree of hydration and swelling of the bagasse fiber was measured using the water retention value. The water retention value of the bagasse was calculated using **Eq. 3**.

$$W_{RV} = (W_2 - W_1)/W_1 * 100\%, \quad (3)$$

Where W_{RV} is the water retention value of the bagasse fiber (%), W_1 is the dry weight of the bagasse fiber (g), and W_2 is the weight of the wet bagasse fiber after centrifugation (g).

The main functional groups of the different bagasse fiber was analyzed using FTIR (IRTracer-100, Shimadzu, Japan) (Yao et al., 2015). The effect of different treatments on the cellulose crystal shape was analyzed by XRD (Mini Flex 600, Rigaku, Tokyo, Japan) (Ge et al., 2020). The XRD patterns of the monochrome Cu-Kα powders were used. The voltage and current were 40 kV and 15 mA, respectively. The scanning speed and scanning range were 0.131°.S^{-1} and 5°–50°, respectively. The thermal stability of the fiber was analyzed by thermogravimetric analysis (TGA) (STA 449F5, NETZSCH, Germany) (Tian et al., 2021).

RESULTS AND DISCUSSION

Effect of Freezing Temperature on Fiber Swelling

Wood fibers have strong thermal stability. The effective swelling of fiber is difficult to achieve at high temperatures. However, the softness of the object was enhanced by cryogenic freezing (Biglia et al., 2016). This indicates that fiber swelling can be promoted by freezing pretreatment. The key factors of freezing and thawing include freezing temperature, freezing time, and thawing temperature. Cellulose and hemicellulose were removed during the fiber swelling process. Therefore, the effect of freezing temperature on cellulose and hemicellulose removal was studied using FT/AT. It was −20, −30, −40, −50, −60, −70, and −80°C. The freezing time, alkali concentration, and thawing temperature was 6.0 h, 3.0%, and 25°C, respectively. The result is shown in **Figure 1**.

The removal rate of hemicellulose increased from 49.93 to 70.28% as the freezing temperature was increased from −20°C to −40°C. However, it decreased as the freezing temperature decreased below

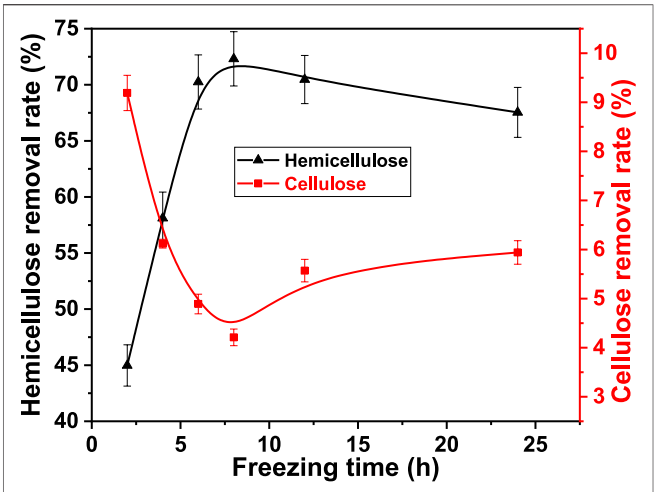

FIGURE 2 | Effect of freezing time on the removal rate of cellulose and hemicellulose from bagasse fiber in FT/AT.

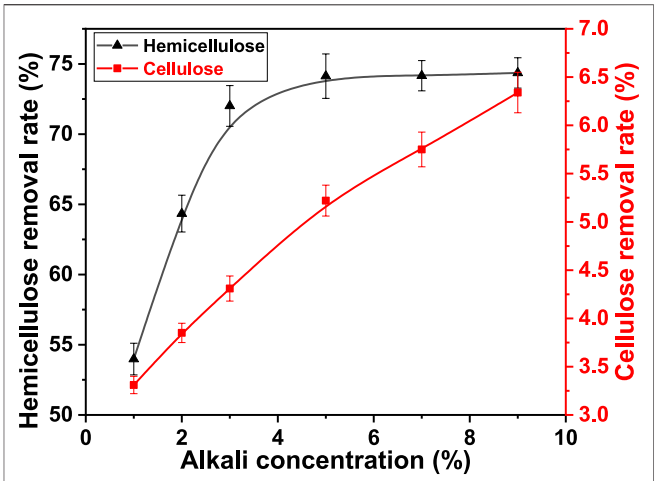

FIGURE 3 | Effect of alkali concentration on the removal rate of cellulose and hemicellulose from bagasse fiber in FT/AT.

−40°C. It was 60.61% at −80°C. The alkaline degradation of cellulose was inevitable during alkali infiltration (Liu et al., 2020). The removal rate of cellulose decreased with the decrease in freezing temperature when the freezing temperature was higher than −40°C. It decreased from 8.32 to 4.89%. The degradation of cellulose was promoted when the freezing temperature was below −40°C. The removal rate of cellulose increased to 7.29% at −80°C. Fewer ice crystals were formed inside the fibers at the beginning of freezing. The alkaline degradation of cellulose was promoted by more alkaline solution in contact with cellulose. The formation and growth of the ice crystals in the fibers as the freezing temperature decreased (Zhang et al., 2021). The number of infiltration channels increased after thawing. The osmotic effect of alkaline solution was promoted with the increase in the number of physical channels. The removal of hemicellulose was facilitated. The removal of cellulose was inhibited. Uniform and fine ice crystals were formed at −40°C. The highest removal rate of hemicellulose and the lowest removal rate of cellulose were obtained. However, the ice crystals in the fiber increased as the freezing temperature decreased. Large ice crystals were formed by gobbling up fine ice crystals. Local damage to the fibers was exacerbated. The breakdown and dissolution of cellulose was intensified. Its removal rate increased as the freezing temperature decreased. The osmosis of alkaline solution was inhibited. The dissolution of hemicellulose was inhibited with the decrease in the overall swelling property of the fiber. Therefore, the optimal freezing temperature was −40°C in FT/AT.

Effect of Freezing Time on Fiber Swelling

Freezing time is an important factor that affects food preservation during food refrigeration (Ben Haj Said et al., 2021). In fact, ice crystals grow irreversibly inside objects. Maintaining stable ice crystals is time sensitive. Therefore, the effect of freezing time on cellulose and hemicellulose removal was studied. It was 2.0, 4.0, 6.0, 8.0, 12.0, and 24.0 h. The freezing temperature was −40°C, alkali concentration was 3.0%, and thawing temperature was 25°C. The result is shown in **Figure 2**.

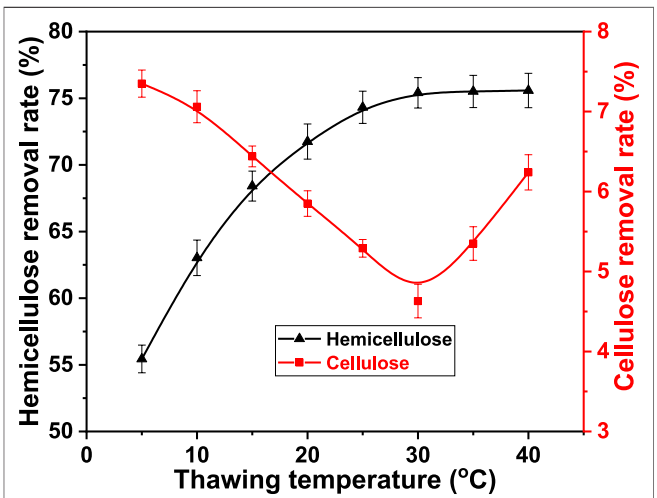

FIGURE 4 | Effect of thawing temperature on the removal rate of cellulose and hemicellulose from bagasse fiber in FT/AT.

The removal rate of hemicellulose increased with freezing time. It increased from 44.98% at 2.0 h to 72.31% at 8.0 h. However, it decreased with freezing time when the freezing time was greater than 8.0 h. It decreased to 67.54% at 24.0 h. The removal rate of cellulose decreased from 9.19 to 4.21% when the freezing time was between 2.0 and 8.0 h. The dissolution and degradation of cellulose were promoted under a relatively long freezing time. The removal rate of cellulose increased to 5.94% at 24.0 h. It was attributed to the change in the number and size of ice crystals in the fiber with freezing time. The number of fine ice crystals increased with freezing time at the beginning of freezing (Gong et al., 2020). The number of physical channels for the penetration of liquid medicine increased accordingly. Therefore, the dissolution of hemicellulose was promoted. The alkaline degradation of cellulose was suppressed. The fine ice crystals were evenly distributed inside

the fiber at 8.0 h. Large ice crystals were formed by swallowing small ice crystals as the freezing time continued to increase. The damage caused by freezing to the fiber structure changed from slight-overall to significant-local. The breaking and dissolution of cellulose was promoted, the swelling of the fiber were reduced. The dissolution of hemicellulose was suppressed. Therefore, the optimal freezing time was 8.0 h.

Effect of Alkali Concentration on Fiber Swelling

The swelling of the fiber in water was limited. However, the fiber crystallization area was permeated by acid, alkali, and salt. The swelling of the fiber was improved. The alkali concentration is an important parameter in AT. The removal of hemicellulose and alkaline degradation of cellulose are promoted. Therefore, the effect of alkali concentration on cellulose and hemicellulose removal was studied. It was 1.0, 2.0, 3.0, 5.0, 7.0, and 9.0%. The freezing temperature was −40°C, freezing time was 6.0 h, and thawing temperature was 25°C. The result is shown in **Figure 3**.

It was observed that the alkali concentration significantly affected the removal of hemicellulose when the alkali concentration was less than 5.0%. It increased from 53.98 to 74.13%. Additionally, the effect of high alkali concentration on the removal of hemicellulose was limited. The removal rate of hemicellulose was 74.36% at an alkali concentration of 9.0%. This was due to the increase in porosity indicated by the fiber after freezing. The penetration of alkali was enhanced. The effective contact between hemicellulose and alkali was strengthened. The removal rate of hemicellulose increased with the concentration of alkali. The result showed that cellulose was degraded under alkaline conditions (Zaccaron et al., 2020). The alkaline degradation of cellulose increased with the increase in alkali concentration. Therefore, the removal rate of cellulose increased linearly. It rapidly increased from 3.31 to 6.34%. The optimal alkali concentration was 5.0% in FT/AT. More efficient mercerization was obtained at relatively low alkali concentrations.

Effect of Thawing Temperature on Fiber Swelling

Alkali treatment and thawing were carried out simultaneously. The alkali treatment time was compressed to obtain a better fiber swelling effect. Thawing and alkali penetration were simultaneously carried out. The alkaline degradation of cellulose was inhibited while realizing effective contact between hemicellulose and alkali. Therefore, the effect of thawing on cellulose and hemicellulose removal was studied by adjusting the thawing temperature. The temperature was 5, 10, 15, 20, 25, 30, 35, and 40°C. The freezing temperature was −40°C, freezing time was 8.0 h, and alkali concentration was 5.0%. The result is shown in **Figure 4**.

The removal rate of hemicellulose rapidly increased with the thawing temperature and then remained stable. It increased from 55.44 to 75.41% when the thawing temperature was between 5 and 30°C. The thawing time increased as the temperature decreased. Further, the fluctuation of the temperature at the beginning of thawing directly caused the rapid formation of large ice crystals inside the fiber (Kumar et al., 2019). The destructiveness of the fiber structure was gradually enhanced. Severe local damage was formed. The infiltration effect of alkali solution was reduced in large channels formed by melting of large ice crystals. Its accessibility to hemicellulose was poor. More alkali was consumed from the alkaline degradation of cellulose. Therefore, the removal of hemicellulose was inhibited at low thawing temperatures. Conversely, the removal of cellulose was promoted. The growth of ice crystals inside the fiber was suppressed as the thawing temperature increased. The channels were quickly occupied by the alkali after the small ice crystals melted. The effective contact with the hemicellulose was strengthened. The removal rate of cellulose gradually decreased while the removal rate of hemicellulose gradually increased. It was reduced from 7.35 to 4.63% at 30°C. The removal rate of hemicellulose remained stable as the thawing temperature increased due to most of the hemicellulose was removed. It was 75.58% at 40°C. However, the alkaline degradation of cellulose was enhanced at relatively high temperatures (Knill & Kennedy, 2003). Therefore, the removal rate of cellulose decreased as the thawing temperature increased to >30°C. The rate increased to 6.24% at 40°C. The optimal thawing temperature was 30°C.

The optimal condition of FT/AT was freezing temperature −40°C, freezing time 8.0 h, alkali concentration 5.0%, and thawing temperature 30°C. The highest removal rate of hemicellulose was 75.64%. It was 5.80% higher than that of AT treatment. The lowest removal rate of cellulose was 4.63%. It was 5.73% lower than that of AT treatment. In addition, the effective alkali concentration (5.0%) was reduced by 66.67% compared to AT (15.0%). The energy consumption of freeze–thaw pretreatment was effectively compensated by the significant reduction of alkali consumption. Therefore, FT/AT is an efficient method for fiber swelling.

Properties of Bagasse Fiber With Different Treatments

The yield of bagasse fiber changed with the swelling and removal of hemicellulose. **Table 1** shows the pulp fiber yield was 78.35% with AT. It was 84.47% after FT/AT. This was attributed to the different degrees of the dissolution of the main components during swelling. The penetration of alkali was promoted by freeze–thaw pretreatment (Li J. et al., 2021). The hemicellulose in the pulp was efficiently removed, and the alkaline degradation of cellulose was inhibited. The content of cellulose decreased from 80.19 to 76.48%. The content of hemicellulose was significantly reduced from 13.56 to 1.82%. Therefore, cellulose - rich bagasse fiber was obtained by FT/AT. The viscosity and degree of polymerization of fiber was affected. **Table 1** show that the viscosity of the fiber increased from 776 ml g^{-1} to 833 ml g^{-1}. This was due to the large amount of hemicellulose dissolved during AT. Additionally, the fiber with FT/AT had greater viscosity (845 ml g^{-1}) than those treated with AT. Further, their degree of polymerization increased from 1,229 to 1,248. This was attributed to the structure of cellulose was protected while the hemicellulose was efficiently removed during FT/AT.

In fact, the morphology of the fiber is affected as the major components change. The fiber length, fiber width, and fine fiber

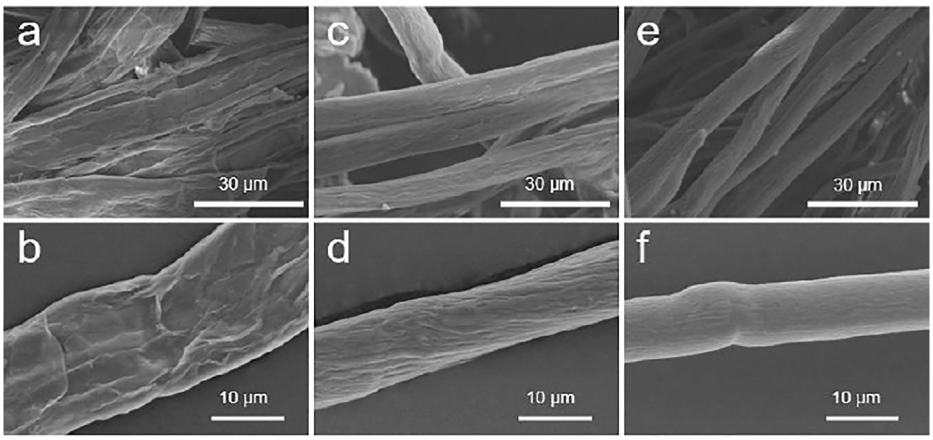

FIGURE 5 | SEM of bagasse fiber with different treatments (bleached bagasse pulp; AT; FT/AT.).

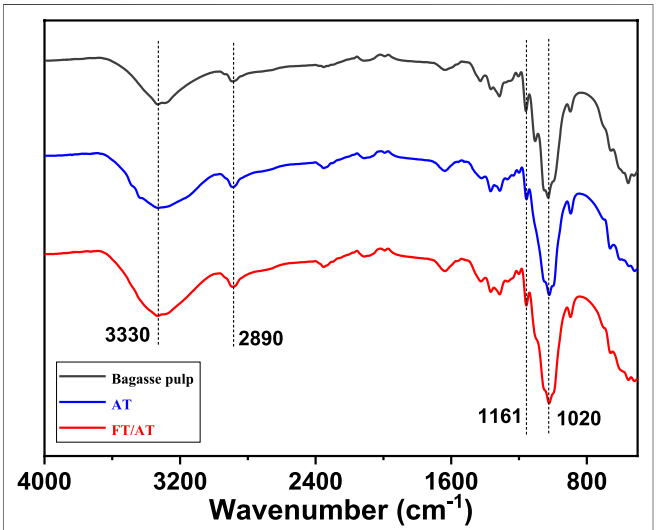

FIGURE 6 | FTIR of bagasse fiber with different treatments.

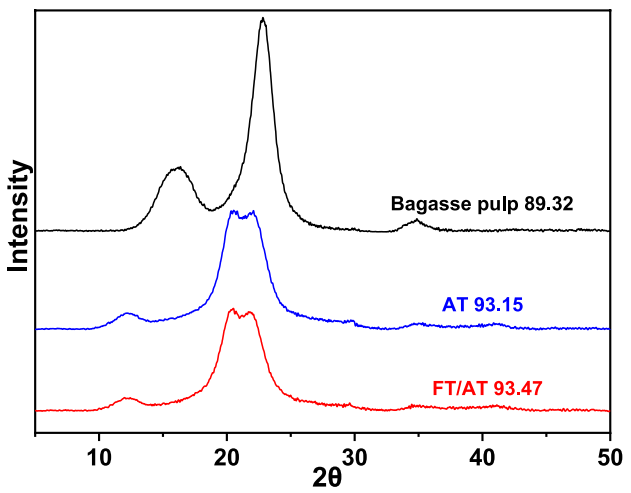

FIGURE 7 | XRD of bagasse fiber with different treatments.

content were reduced by AT. Fiber length decreased from 0.73 to 0.59 mm. Different alkali treatments had the same effect on the fiber length. However, there were differences in the fiber width. The fiber width after FT/AT treatment is larger than that after AT treatment. The fine fiber content decreased from 6.67 to 3.31%. It was reduced by 1.13% compared to that of AT. The results showed that FT/AT had a higher swelling performance than AT. The effect of fiber mercerization action is reflected not only in the swelling performance but also in the kink index of the fiber (Suizu et al., 2009). The fiber form factor, kink angle, and kink index are important indices of fiber distortion. The fiber form factor is the ratio of the projected length of the fiber to the real length. The larger the value of the form factor, the straighter the fiber. The fiber form factors were reduced by 6.63 and 7.14% by AT and FT/AT, respectively. The kink angle increased from 51.63° to 59.14° and 61.90°, respectively. The kink index increased by 0.75 mm^{-1} and 0.86 mm^{-1}, respectively. This indicates that the fiber had a relatively high kink index using FT/AT. The degree of hydration and swelling of the fiber was reflected by the water retention value. This is directly related to the specific surface area and porosity of the fiber (Arnoul-Jarriault et al., 2016). The water retention value of the bleached bagasse pulp fiber was 114%, as shown in **Table 1**. It increased to 149% with AT. It significantly increased to 163% by FT/AT. This was attributed to the relatively high specific surface area of the fibers treated with FT/AT (1.04). Moreover, the fiber had a relatively high porosity owing to the few physical channels remaining after the fine ice crystals were melted during freezing and thawing. The water absorption and swelling performance of the fibers improved. More bound water was retained inside the fibers.

Morphology and Physicochemical Properties of Bagasse Fiber With Different Treatments

First, the surface of bagasse fiber was relatively rough (**Figure 5**). This was attributed to an amount of hemicellulose in the fiber and more

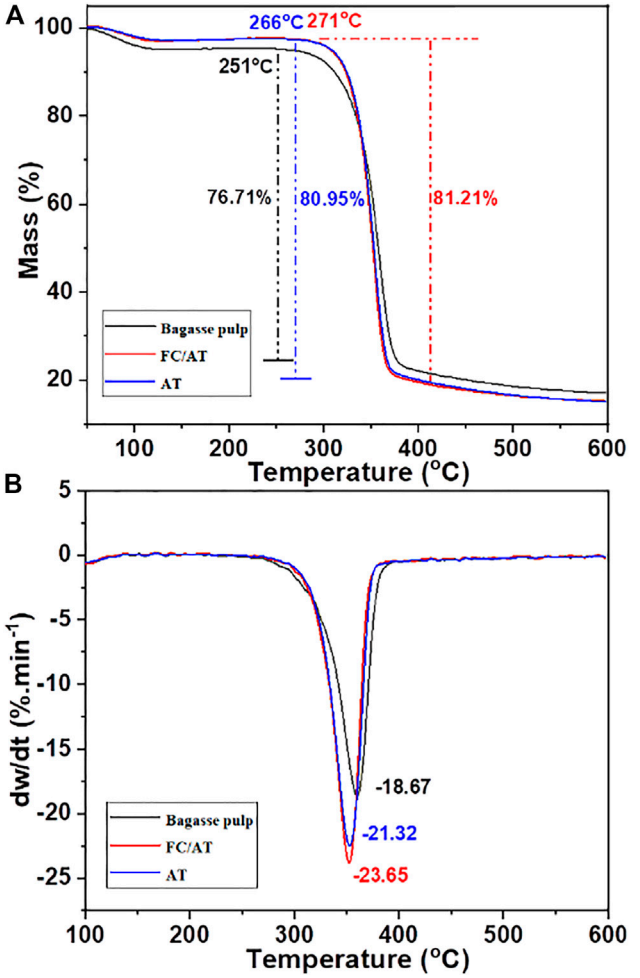

FIGURE 8 | TGA **(A)** and DTG **(B)** of bagasse fiber with different treatments.

fiber fines on the surface. The higher alkali concentration was used in AT to achieve good mercerization. Fine fibers and a large amount of hemicellulose were removed. However, the alkaline degradation of cellulose was promoted at high alkali concentration. This resulted in the presence of wrinkles on the fiber surface. Smooth, round fibers were obtained with FT/AT. This was attributed to the infiltration of alkali was promoted by FT/AT. Hemicellulose and fiber fines were efficiently removed. Further, the alkaline degradation of cellulose was inhibited at low alkali concentrations.

The changes in the fiber components before and after different treatments are shown in **Figure 6**. The characteristic peak at 3,300 cm^{-1} was attributed to the O–H stretching vibration of carbohydrate (Yao et al., 2017). The intensities of the characteristic peaks were reduced with different treatments. This was attributed to the breaking of intermolecular and intramolecular hydrogen bonds. More importantly, a large amount of hemicellulose was removed. The absorption peak at 2,890 cm^{-1} was attributed to the stretching vibration of C–H on saturated carbon. They are mainly derived from cellulose and hemicellulose. Additionally, the absorption peak intensity of C–O stretching attributed to hemicellulose at 1,020 cm^{-1} decreased (Liu et al., 2021). This showed that the C–O bond in hemicellulose was broken. A large amount of hemicellulose was removed. However, the absorption peaks at 1,161 cm^{-1} varied in the different treatments. This was attributed to the asymmetric stretching vibration of C–O–C in cellulose (Hosakun et al., 2017). Their strengths were the same in bagasse fiber and FT/AT-treated fiber. This indicates that the structure of the cellulose was protected by FT/AT. The alkaline degradation of cellulose was inhibited, while hemicellulose was efficiently removed. This was consistent with the results of the single-factor analysis.

The goal of mercerization is to change the crystal shape of cellulose. The XRD patterns of the pulp fibers are shown in **Figure 7**. The crystal peaks of the bleached bagasse pulp were observed at 16.5° and 22.5°. They belong to cellulose I (Sèbe et al., 2012). The crystallization peak at 16.5° completely disappeared after AT and FT/AT, and a new crystallization peak was observed at 12°. Additionally, the crystallization peak at 22.5° moved to 20° and 21°. These were the characteristic peaks of cellulose II(Nomura et al., 2020). That mercerization effects were obtained using different treatments. Complete mercerization was achieved at 15.0% alkali concentration with AT. The effect of different alkali concentration on cellulose crystal shape was studied by FT/AT. The lowest alkali concentration at which the crystalline form of cellulose is completely changed was 5.0% during FT/AT. The minimum alkali concentration of cellulose crystal by complete transformation was reduced by 66.67% compared with AT. This means that the efficient mercerization of the fibers was achieved by FT/AT, and relatively high fiber crystallinity was obtained (93.47). This was due to the cellulose structure was protected under low alkali concentrations.

In addition, mercerized fibers have relatively high thermal stability (Rashid et al., 2016). Therefore, the thermal decomposition behavior and thermal stability of the different fiber were analyzed. The TGA and derivative thermogravimetry (DTG) profiles of the fiber are shown in **Figure 8**.

Figure 8A shows that the initial pyrolysis temperature of the bagasse fiber was 251°C. It was raised to 266 and 271°C after mercerization. This was attributed to the removal of hemicellulose and the change of cellulose crystal shape by different mercerization. Cellulose II exhibited better thermal stability than cellulose I. Additionally, the initial pyrolysis temperatures of these two types of mercerization were different. This was attributed to the removal of more hemicellulose by FT/AT. The maximum mass loss of the bagasse fiber was 76.71%. It increased to 80.95 and 81.21% after mercerization. The alkaline degradation of cellulose was inhibited at low alkali concentrations. **Figure 8B** shows the maximum weight loss rate of the fibers under different treatment conditions. The maximum weight loss rate of the bleached bagasse fiber was 18.67%.min^{-1}. It increased by 3.65%.min^{-1} and 4.98%.min^{-1} by mercerization. This was attributed to the removal of a large amount of hemicellulose and the improvement of cellulose purity. The thermal decomposition of cellulose was enhanced (Lin et al., 2019). Therefore, the maximum weight loss rate of the cellulose increased. The results showed that the thermal stability of

cellulose was higher after FT/AT. This was attributed to a significant reduction in alkali concentration. The overall structure of cellulose was protected, while the crystalline form of cellulose was completely transformed. Further, the efficient mercerization effects were obtained. This provides a new method for the mercerization of fibers.

CONCLUSION

A new efficient mercerization for fiber has been discovered. The bleached bagasse pulp fiber was swelled by FT/AT. The bagasse hemicellulose was efficiently removed. The alkaline degradation of cellulose was inhibited at low alkali concentrations. The results showed that mercerized fibers with excellent properties were obtained. Cellulose I was completely converted into cellulose II at 5.0% alkali concentration. The minimum alkali concentration of cellulose crystal by complete transformation was reduced by 66.67% compared with AT. It provides theoretical support for the high-value utilization of cellulose.

DATA AVAILABILITY STATEMENT

The original contributions presented in the study are included in the article/Supplementary Material, further inquiries can be directed to the corresponding author.

AUTHOR CONTRIBUTIONS

LC: Conceptualization and Writing – review and editing; JZ and BD: Investigation and Writing – original draft; CQ: Funding acquisition and Resources; FZ and SW: Validation; YM: Formal analysis; SY: Project administration and Supervision.

FUNDING

This project was sponsored by the National Natural Science Foundation of China (22078075). This project was supported by the Natural Science Foundation of Guangxi Province (2020GXNSFBA297164).

REFERENCES

Albán Reyes, D. C., Skoglund, N., Svedberg, A., Eliasson, B., and Sundman, O. (2016). The Influence of Different Parameters on the Mercerisation of Cellulose for Viscose Production. *Cellulose* 23 (2), 1061–1072. doi:10.1007/s10570-016-0879-0

Alexakis, A. E., Engström, J., Stamm, A., Riazanova, A. V., Brett, C. J., Roth, S. V., et al. (2021). Modification of Cellulose Through Physisorption of Cationic Bio-Based Nanolatexes - Comparing Emulsion Polymerization and RAFT-Mediated Polymerization-Induced Self-Assembly. *Green. Chem.* 23 (5), 2113–2122. doi:10.1039/d0gc04266h

Arnoul-Jarriault, B., Passas, R., Lachenal, D., and Chirat, C. (2016). Characterization of Dissolving Pulp by Fibre Swelling in Dilute Cupriethylenediamine (CUEN) Solution in a MorFi Analyser. *HOLZFORSCHUNG* 70 (7), 611–617. doi:10.1515/hf-2015-0167

Ben Haj Said, L., Bellagha, S., and Allaf, K. (2021). Instant Controlled Pressure Drop (DIC) Assisted Dehydrofreezing for Improving Freezing/thawing Efficiency and Apple Fruit Texture. *Food Measure* 15 (1), 577–584. doi:10.1007/s11694-020-00668-x

Bian, H., Luo, J., Wang, R., Zhou, X., Ni, S., Shi, R., et al. (2019). Recyclable and Reusable Maleic Acid for Efficient Production of Cellulose Nanofibrils with Stable Performance. *ACS Sustain. Chem. Eng.* 7 (24), 20022–20031. doi:10.1021/acssuschemeng.9b05766

Biglia, A., Comba, L., Fabrizio, E., Gay, P., and Aimonino, D. R. (2016). Case Studies in Food Freezing at Very Low Temperature. *Energ. Proced.* 101, 305–312. doi:10.1016/j.egypro.2016.11.039

Cavali, M., Soccol, C. R., Tavares, D., Zevallos Torres, L. A., Oliveira de Andrade Tanobe, V., Zandoná Filho, A., et al. (2020). Effect of Sequential Acid-Alkaline Treatment on Physical and Chemical Characteristics of Lignin and Cellulose from Pine (Pinus spp.) Residual Sawdust. *Bioresour. Tech.* 316, 123884. doi:10.1016/j.biortech.2020.123884

Chen, Q., Wang, X., Huang, H., Cao, S., Chen, L., Huang, L., et al. (2020). Turkey Red Oil - An Effective Alkaline Extraction Booster for Enhanced Hemicelluloses Separation from Bamboo Kraft Pulp and Improved Fock Reactivity of Resultant Dissolving Pulp. *Ind. Crops Prod.* 145, 112127. doi:10.1016/j.indcrop.2020.112127

Ge, J., Wu, Y., Han, Y., Qin, C., Nie, S., Liu, S., et al. (2020). Effect of Hydrothermal Pretreatment on the Demineralization and Thermal Degradation Behavior of Eucalyptus. *Bioresour. Tech.* 307, 123246. doi:10.1016/j.biortech.2020.123246

Gong, Y., Xu, S., He, T., Dong, R., Ren, T., Wang, X., et al. (2020). Effect of Quick-Freezing Temperature on Starch Retrogradation and Ice Crystals Properties of Steamed Oat Roll. *J. Cereal Sci.* 96, 103109. doi:10.1016/j.jcs.2020.103109

Halonen, H., Larsson, P. T., and Iversen, T. (2013). Mercerized Cellulose Biocomposites: A Study of Influence of Mercerization on Cellulose Supramolecular Structure, Water Retention Value and Tensile Properties. *Cellulose* 20 (1), 57–65. doi:10.1007/s10570-012-9801-6

Hosakun, Y., Halász, K., Horváth, M., Csóka, L., and Djoković, V. (2017). ATR-FTIR Study of the Interaction of CO2 with Bacterial Cellulose-Based Membranes. *Chem. Eng. J.* 324, 83–92. doi:10.1016/j.cej.2017.05.029

Ibarra, D., Köpcke, V., Larsson, P. T., Jääskeläinen, A.-S., and Ek, M. (2010). Combination of Alkaline and Enzymatic Treatments as a Process for Upgrading Sisal Paper-Grade Pulp to Dissolving-Grade Pulp. *Bioresour. Tech.* 101 (19), 7416–7423. doi:10.1016/j.biortech.2010.04.050

Kita, Y., Kusumi, R., Kimura, T., Kitaoka, M., Nishiyama, Y., and Wada, M. (2020). Surface Structural Analysis of Selectively 13C-Labeled Cellulose II by Solid-State NMR Spectroscopy. *Cellulose* 27 (4), 1899–1907. doi:10.1007/s10570-019-02896-x

Knill, C. J., and Kennedy, J. F. (2003). Degradation of Cellulose Under Alkaline Conditions. *Carbohydr. Polym.* 51 (3), 281–300. doi:10.1016/s0144-8617(02)00183-2

Kumar, P. K., Bhunia, K., Tang, J., Rasco, B. A., Takhar, P. S., and Sablani, S. S. (2019). State/phase Transitions Induced by Ice Recrystallization and its Influence on the Mechanical Properties of Potatoes (Solanum tuberosum L.) Var. Russet Brown. *J. Food Eng.* 251, 45–56. doi:10.1016/j.jfoodeng.2019.02.002

Kumar, V., Kushwaha, P. K., and Kumar, R. (2011). Impedance-spectroscopy Analysis of Oriented and Mercerized Bamboo Fiber-Reinforced Epoxy Composite. *J. Mater. Sci.* 46 (10), 3445–3451. doi:10.1007/s10853-011-5249-6

Li, J., Liu, Y., Duan, C., Zhang, H., and Ni, Y. (2015). Mechanical Pretreatment Improving Hemicelluloses Removal from Cellulosic Fibers During Cold Caustic Extraction. *Bioresour. Tech.* 192, 501–506. doi:10.1016/j.biortech.2015.06.011

Li, J., Liu, Z., Feng, C., Liu, X., Qin, F., Liang, C., et al. (2021a). Green, Efficient Extraction of Bamboo Hemicellulose Using Freeze-Thaw Assisted Alkali Treatment. *Bioresour. Tech.* 333, 125107. doi:10.1016/j.biortech.2021.125107

Li, X., Du, Y., and Meng, Q. (2021b). Flexible ball-milled Bi0.4 Sb1.6 Te3/methyl Cellulose Thermoelectric Films Fabricated by Screen-Printing Method. *Funct. Mater. Lett.* 14 (06), 2151034. doi:10.1142/s1793604721510346

Lin, X., Kong, L., Cai, H., Zhang, Q., Bi, D., and Yi, W. (2019). Effects of Alkali and Alkaline Earth Metals on the Co-pyrolysis of Cellulose and High Density

Polyethylene Using TGA and Py-GC/MS. *Fuel Process. Tech.* 191, 71–78. doi:10.1016/j.fuproc.2019.03.015

Liu, P., Pang, B., Dechert, S., Zhang, X. C., Andreas, L. B., Fischer, S., et al. (2020). Structure Selectivity of Alkaline Periodate Oxidation on Lignocellulose for Facile Isolation of Cellulose Nanocrystals. *Angew. Chem. Int. Ed.* 59 (8), 3218–3225. doi:10.1002/anie.201912053

Liu, X., Renard, C. M. G. C., Bureau, S., and Le Bourvellec, C. (2021). Revisiting the Contribution of ATR-FTIR Spectroscopy to Characterize Plant Cell wall Polysaccharides. *Carbohydr. Polym.* 262, 117935. doi:10.1016/j.carbpol.2021.117935

Liu, Y., and Hu, H. (2008). X-ray Diffraction Study of Bamboo Fibers Treated with NaOH. *Fibers Polym.* 9 (6), 735–739. doi:10.1007/s12221-008-0115-0

Luo, Y., Li, Y., Cao, L., Zhu, J., Deng, B., Hou, Y., et al. (2021). High Efficiency and Clean Separation of eucalyptus Components by Glycolic Acid Pretreatment. *Bioresour. Tech.* 341, 125757. doi:10.1016/j.biortech.2021.125757

Marzouki, R., Brahmia, A., Bondock, S., Keshk, S. M. A. S., Zid, M. F., Al-Sehemi, A. G., et al. (2019). Mercerization Effect on Structure and Electrical Properties of Cellulose: Development of a Novel Fast Na-Ionic Conductor. *Carbohydr. Polym.* 221, 29–36. doi:10.1016/j.carbpol.2019.05.083

Nomura, S., Kugo, Y., and Erata, T. (2020). 13C NMR and XRD Studies on the Enhancement of Cellulose II Crystallinity with Low Concentration NaOH Post-treatments. *Cellulose* 27 (7), 3553–3563. doi:10.1007/s10570-020-03036-6

Noori, A., Lu, Y., Saffari, P., Liu, J., and Ke, J. (2021). The Effect of Mercerization on Thermal and Mechanical Properties of Bamboo Fibers as a Biocomposite Material: A Review. *Construction Building Mater.* 279, 122519. doi:10.1016/j.conbuildmat.2021.122519

Oladele, I. O., Ibrahim, I. O., Akinwekomi, A. D., and Talabi, S. I. (2019). Effect of Mercerization on the Mechanical and Thermal Response of Hybrid Bagasse Fiber/CaCO3 Reinforced Polypropylene Composites. *Polym. Test.* 76, 192–198. doi:10.1016/j.polymertesting.2019.03.021

Öztürk, H. B., Okubayashi, S., and Bechtold, T. (2006). Splitting Tendency of Cellulosic Fibers. Part 2: Effects of Fiber Swelling in Alkali Solutions. *Cellulose* 13 (4), 403–409. doi:10.1007/s10570-006-9054-3

Pang, Q., Tang, J., Huang, H., Liang, X., Hart, C., Tam, K. C., et al. (2015). A Nitrogen and Sulfur Dual-Doped Carbon Derived from Polyrhodanine@ Cellulose for Advanced Lithium-Sulfur Batteries. *Adv. Mater.* 27 (39), 6021–6028. doi:10.1002/adma.201502467

Rashid, B., Leman, Z., Jawaid, M., Ghazali, M. J., and Ishak, M. R. (2016). Physicochemical and Thermal Properties of Lignocellulosic Fiber from Sugar palm Fibers: Effect of Treatment. *Cellulose* 23 (5), 2905–2916. doi:10.1007/s10570-016-1005-z

Reyes, G., Lundahl, M. J., Alejandro-Martín, S., Arteaga-Pérez, L. E., Oviedo, C., King, A. W. T., et al. (2020). Coaxial Spinning of All-Cellulose Systems for Enhanced Toughness: Filaments of Oxidized Nanofibrils Sheathed in Cellulose II Regenerated from a Protic Ionic Liquid. *Biomacromolecules* 21 (2), 878–891. doi:10.1021/acs.biomac.9b01559

SaifulAzry, S. O. A., Chuah, T. G., Paridah, M. T., Aung, M. M., and Edi, S. Z. (2017). Effects of Polymorph Transformation via Mercerisation on Microcrystalline Cellulose Fibres and Isolation of Nanocrystalline Cellulose Fibres. *Pertanika J. Sci. Tech.* 25 (4), 1275–1290.

Sèbe, G., Ham-Pichavant, F., Ibarboure, E., Koffi, A. L. C., and Tingaut, P. (2012). Supramolecular Structure Characterization of Cellulose II Nanowhiskers Produced by Acid Hydrolysis of Cellulose I Substrates. *Biomacromolecules* 13 (2), 570–578. doi:10.1021/bm201777j

Suizu, N., Uno, T., Goda, K., and Ohgi, J. (2009). Tensile and Impact Properties of Fully Green Composites Reinforced with Mercerized Ramie Fibers. *J. Mater. Sci.* 44 (10), 2477–2482. doi:10.1007/s10853-009-3317-y

Tian, Z., Chee, T.-S., Zhang, X., Lei, L., and Xiao, C. (2021). Novel Bismuth-Based Electrospinning Materials for Highly Efficient Capture of Radioiodine. *Chem. Eng. J.* 412, 128687. doi:10.1016/j.cej.2021.128687

Yagura, T., Ikegami, W., Kamitakahara, H., and Takano, T. (2020). Synthesis of an Enantiomer of Cellulose via Cationic Ring-Opening Polymerization. *Cellulose* 27 (17), 9755–9766. doi:10.1007/s10570-020-03512-z

Yao, S., Nie, S., Yuan, Y., Wang, S., and Qin, C. (2015). Efficient Extraction of Bagasse Hemicelluloses and Characterization of Solid Remainder. *Bioresour. Tech.* 185, 21–27. doi:10.1016/j.biortech.2015.02.052

Yao, S., Nie, S., Zhu, H., Wang, S., Song, X., and Qin, C. (2017). Extraction of Hemicellulose by Hot Water to Reduce Adsorbable Organic Halogen Formation in Chlorine Dioxide Bleaching of Bagasse Pulp. *Ind. Crops Prod.* 96, 178–185. doi:10.1016/j.indcrop.2016.11.046

Yu, H., Guo, J., Chen, Y., Fu, G., Li, B., Guo, X., et al. (2017). Efficient Utilization of Hemicellulose and Cellulose in Alkali Liquor-Pretreated Corncob for Bioethanol Production at High Solid Loading by Spathaspora Passalidarum U1-58. *Bioresour. Tech.* 232, 168–175. doi:10.1016/j.biortech.2017.01.077

Zaccaron, S., Henniges, U., Potthast, A., and Rosenau, T. (2020). How Alkaline Solvents in Viscosity Measurements Affect Data for Oxidatively Damaged Celluloses. Cuoxam and Cadoxen. *Carbohydr. Polym.* 240, 116251. doi:10.1016/j.carbpol.2020.116251

Zhang, T., Wang, L., Wang, Z., Li, J., and Wang, J. (2021). Single Ice Crystal Growth with Controlled Orientation During Directional Freezing. *J. Phys. Chem. B* 125 (3), 970–979. doi:10.1021/acs.jpcb.0c11028

Zhu, H., Ma, Q., Sheng, J., and Yang, R. (2020). Freeze-thaw Repetition as an Auxiliary Method to Promote Efficient Separation of Hemicellulose from poplar. *Green. Chem.* 22 (3), 942–949. doi:10.1039/c9gc03792f

Conflict of Interest: The authors declare that the research was conducted in the absence of any commercial or financial relationships that could be construed as a potential conflict of interest.

Publisher's Note: All claims expressed in this article are solely those of the authors and do not necessarily represent those of their affiliated organizations, or those of the publisher, the editors and the reviewers. Any product that may be evaluated in this article, or claim that may be made by its manufacturer, is not guaranteed or endorsed by the publisher.

frontiers in Energy Research

ORIGINAL RESEARCH
published: 02 March 2022
doi: 10.3389/fenrg.2022.820330

Ulmus davidiana var. *japonica* Extracts Suppress Lipopolysaccharide-Induced Apoptosis Through Intracellular Calcium Modulation in U937 Macrophages

Jang-Hyuk Yun[1†], Hyun-Ouk Kim[2,3†], Jae-Hun Jeong[4], Yerin Min[5], Kwang-Hyun Park[5,6], Chuanling Si[7*] and Sun-Eun Choi[8*]*

[1]College of Veterinary Medicine and Institute of Veterinary Science, Kangwon National University, Chuncheon, South Korea, [2]Division of Chemical Engineering and Bioengineering, College of Art Culture and Engineering, Kangwon National University, Chuncheon, South Korea, [3]Biohealth-machinery Convergence Engineering, Kangwon National University, Chuncheon, South Korea, [4]Department of Food Science and Bio-Technology, Jeonnam State University, Jeonnam, South Korea, [5]Department of Emergency Medicine and BioMedical Science Graduate Program (BMSGP), Chonnam National University, Gwangju, South Korea, [6]Department of Emergency Medical Rescue, Nambu University, Gwangju, South Korea, [7]Tianjin Key Laboratory of Pulp and Paper, Tianjin University of Science and Technology, Tianjin, China, [8]Department of Forest Biomaterials Engineering, College of Forest and Environmental Sciences, Kangwon National University, Chuncheon, South Korea

This study was aimed to examine the antiapoptotic effect of *Ulmus davidiana* extracts through regulation of the intracellular cation mobilization in U937 human monocytic cells. To investigate the modulatory effects on lipopolysaccharide-induced apoptosis and the Ca^{2+} signaling pathway, we measured the levels of intracellular Ca^{2+} and various protein markers such as Bax, Bcl-2, and PARP. To isolate biopotent molecules, the branches of *U. davidiana* were processed sequentially using 60% ethanol, supercritical fluid extraction, and ethyl acetate extraction of the remaining samples to obtain single fractions and catechin-glycoside, which is one of the known bioeffector molecules of *U. davidiana*. Lipopolysaccharide increased intracellular Ca^{2+} mobilization in U937 cells by inducing transient oscillations and markedly increased Bax and PARP protein expression and decreased Bcl-2 expression. All *U. davidiana* and catechin-glycoside significantly reduced lipopolysaccharide-induced intracellular Ca^{2+} mobilization and downregulated apoptosis-related molecules. These results suggest that *U. davidiana* and catechin-glycoside may be useful for improving immune system function.

Keywords: *Ulmus davidiana* extract, supercritical fluid extraction, intracellular Ca^{2+} signaling, LPS-induced apoptosis, catechin-glycoside

OPEN ACCESS

Edited by:
Chen Huang,
Chinese Academy of Forestry, China

Reviewed by:
Weicheng Hu,
Huaiyin Normal University, China
Liqiu Hu,
Åbo Akademi University, Finland

****Correspondence:***
Kwang-Hyun Park
khpark@nambu.ac.kr
Chuanling Si
sichli@tust.edu.cn
Sun-Eun Choi
oregonin@kangwon.ac.kr

[†]These authors have contributed equally to this work and share first authorship

Specialty section:
This article was submitted to Bioenergy and Biofuels, a section of the journal Frontiers in Energy Research

Received: *22 November 2021*
Accepted: *17 January 2022*
Published: *02 March 2022*

Citation:
Yun J-H, Kim H-O, Jeong J-H, Min Y, Park K-H, Si C and Choi S-E (2022) Ulmus davidiana *var.* japonica *Extracts Suppress Lipopolysaccharide-Induced Apoptosis Through Intracellular Calcium Modulation in U937 Macrophages. Front. Energy Res. 10:820330. doi: 10.3389/fenrg.2022.820330*

INTRODUCTION

The branches of *Ulmus davidiana* var. *japonica* (ULDA) has been used as a traditional Korean medicine for the treatment of inflammatory disorders (Lee, 1966; Hong et al., 1990; Kim et al., 2010). Previous pharmacological studies have reported that ULDA possesses antioxidant, anti-angiogenic, anticancer, and neuroprotective effects (Kim et al., 2005; Si et al., 2013a).

Recently, ULDA has also been used as a functional food for supplementation of amino acids (Oh et al., 2006), oligosaccharides (Eom et al., 2006), and other unknown metabolites that are involved in many biochemical metabolic processes (Carrillo and Borthakur, 2021).

Many studies have confirmed that ULDA contains several useful ingredients (Shin et al., 2000; Eom et al., 2006; Oh et al., 2006; Lee and Lim, 2007); however, the composition of the extract varies depending on the extraction method. The beneficial effects of ULDA have been recognized worldwide, including Asia, Europe, the United States (Xiu, 1988), and Korea, but its underlying mechanism of action on innate immunity and metabolism is not clear.

Recent studies indicate that ULDA extracts have various ameliorative effects on acute inflammatory responses in rats (Lee et al., 2013a; 2013b; Si et al., 2013b; Park et al., 2020), osteopenia (Zhuang et al., 2016), and *in vitro* models (Kim et al., 2019). Moreover, the supercritical fluid of ULDA has anti-inflammatory, anti-angiogenic (Jung and Park, 2006; Si et al., 2009b), and anti-melanin effects (Jeon et al., 2020; Xiong et al., 2021a; Xiong et al., 2021b).

Lipopolysaccharide (LPS), an important molecule in the microbial challenge, exerts an effect on intracellular Ca^{2+} levels $[(Ca^{2+})_i]$, the release of cytokines, and upstream signaling pathways (Azenabor et al., 2009). Intracellular Ca^{2+}-dependent pathways mediated LPS-induced activation of transcriptional factors and iNOS expression in mouse J774 macrophages (Chen et al., 1998).

ADP-ribosyl cyclase(s) modulate concentration of $[Ca^{2+}]_i$ by mobilizing intracellular Ca^{2+} stores or by Ca^{2+} influx through plasma membrane Ca^{2+} channels in various cells (Rah et al., 2007; Kim et al., 2009; Park et al., 2011). Ca^{2+} signaling modulation *via* ADP-ribose cyclase is involved in signal transduction, including cell growth, differentiation, and death (Kim et al., 1993; Mehta et al., 1996; Liu et al., 2022). In this study, we investigated whether pharmaceutical inhibition of Ca^{2+} could be effective in protecting cells against programmed cell death. To test this hypothesis, we compared Ca^{2+} signals and apoptosis markers such as Bcl-2, Bax, and PARP-1 in LPS and supercritical fluid-fractionated ULDA-treated LPS groups of U937 cells.

Therefore, this study was performed to investigate the effects of supercritical fluid-fractionated ULDA, including initial fractions of polyphenols, hydrophobic substances, and flavonoids, on innate immunity modulation and recovery of innate immune function in an *in vitro* model.

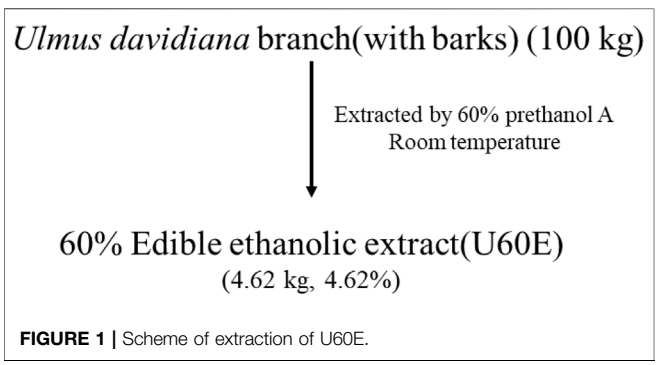

FIGURE 1 | Scheme of extraction of U60E.

MATERIALS AND METHODS

Extraction and Isolation of *U. davidiana*

In this study, extraction equipment was used for supercritical fluid extraction of *U. davidiana* branch (with bark). *U. davidiana* branch (with bark) was purchased from the Yangnyeongsi Medicine Market (Seoul, Korea), and impurities were removed, cleaned, and shaded for use as experimental material. One hundred kilograms of *Ulmus davidiana* branch (with bark) was extracted once with 60% edible ethanol at room temperature. The extract was then concentrated by removing 60% edible ethanol under vacuum to yield a quantity of 4.62 kg (U60E) (**Figure 1**). The dried sample was pulverized by passing through a 200 mesh screen and maintained at a temperature of 50°C in the pulverization tank. When the temperature stabilized, *U. davidiana* branch (with bark) samples were kept under CO_2 gas at an equilibrium pressure of 400 bar, which was maintained through a control valve controlled by a high-pressure pump. After reaching the set pressure, extraction was performed by injecting 100 L of ethanol (300 ml/min) for 333 min to the bottom of the extraction tank. The high-pressure pump was set at a specific pressure and temperature for 30 min to remove the residual ethanol in the sample, and the extraction was completed by flowing CO_2 gas. As described above, after supercritical extraction of 100 kg of *U. davidiana* branch (with bark) with 60% alcohol at room temperature, the extract was filtered, concentrated under vacuum, and freeze-dried to obtain 4.81 kg of the final product (USCFR) (Jeon et al., 2020). The filtrate (USCFR, 1 kg) was fractionated with ethyl acetate, and the ethyl acetate extract was concentrated under vacuum and freeze-dried to obtain 185.2 g of the final product (USCFREA) (**Figure 2**), which was dissolved in water and filtered through filter paper no. 20 (Hyundai Micro, Seoul, South Korea). Purification and isolation were performed by liquid column chromatography with TLC monitoring. In addition, 185 g of USCFREA on Disogel (300 g, 3 × 50 cm) with 30% methanol under isocratic conditions in a Prep-LC system (20 ml/min, 280 nm) yielded catechin 7-O-β-D-apiofuranoside (compound 1) (**Figure 3**).

Cell Culture

U937 cells were obtained from the American Type Culture Collection and maintained in complete RPMI 1640 medium supplemented with 10% fetal bovine serum and 1% antibiotics. After at least 14 days of proliferation, U937 cells were used for *in vitro* experiments.

Intracellular Ca^{2+} Measurement

Intracellular Ca^{2+} mobilization was measured as previously described (Park et al., 2011). Cells were plated manually on poly-L-lysine–coated confocal dishes (#100350; SPL, Pochun, Korea) and loaded with 1 mM Fluo-4 AM (Molecular Probes, CA, United States) at 37°C for 30 min. After washing with Hanks' balanced salt solution medium containing 0.1% bovine serum albumin, changes in fluorescence were determined at 488 nm

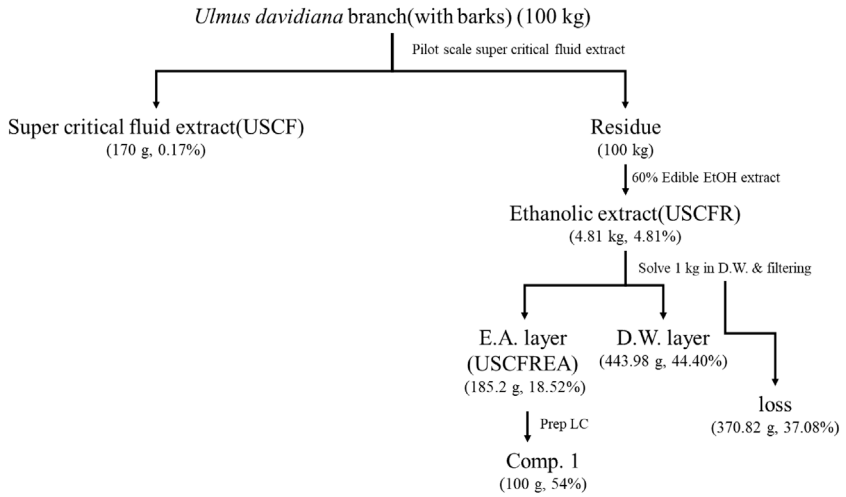

FIGURE 2 | Scheme of extraction of USCFR and USCFREA.

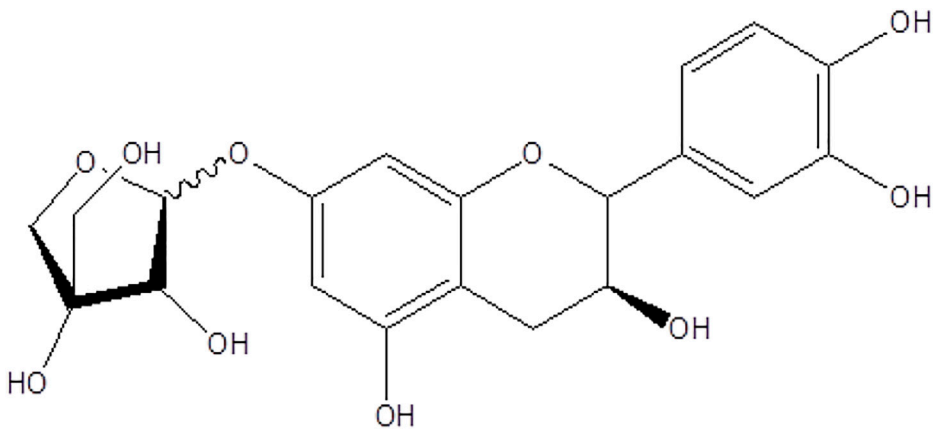

FIGURE 3 | Chemical structure of compound 1 isolated from *Ulmus davidiana* branch (with bark).

excitation/530 nm emission using an air-cooled argon laser system with a TE-2000 inverted microscope (Nikon, Tokyo, Japan) equipped with a temperature-controlled metal stage (Tokai Hit Co., Ltd., Shizuoka-ken, Japan). The emitted fluorescence at 530 nm was measured using a photomultiplier, and time series were acquired with a frame interval of 4 s. For the calculation of $[Ca^{2+}]i$, the method described by Tsien et al. (1982) was applied with *Kd* for Fluo-4 using the equation $[Ca^{2+}]i = Kd(F - F_{min})/(F_{max} - F)$. Each tracing was calibrated for maximal intensity (F_{max}) by adding 8 mM ionomycin and for minimal intensity (F_{min}) by adding 50 mM ethylene glycol tetraacetic acid at the end of each measurement.

Western Blot Analysis

Cell protein extracts were prepared immediately before use as follows: cells were solubilized by mixing with ice-cold lysis buffer [20 mM HEPES (pH 7.2), 1% Triton X-100, 10% glycerol, 1 mM EDTA, 1 mM phenylmethylsulfonyl fluoride, 50 mM NaF, 1 mM Na_3VO_4, leupeptin (10 mg/ml), pepstatin (10 mg/ml), and aprotinin (10 mg/ml)] by repeated trituration using a micropipette. The samples were then incubated for 1 h at 4°C. The supernatants were obtained after centrifugation at 20,000 × g for 10 min. The concentration of the extracted proteins in the supernatant was determined by the Bradford assay using bovine serum albumin as a standard protein. Equivalent micrograms of proteins per lane were resolved on 7–12% SDS-polyacrylamide gel and electrotransferred to a polyvinylidene difluoride membrane (GE Healthcare). Antibodies against Bax, Bcl-2, PARP, and actin were used. Horseradish peroxidase-conjugated secondary antibodies (Santa Cruz Biotechnology) were used and visualized using

enhanced chemiluminescence (ECL). All immunoreactive signals were analyzed using densitometric scanning (LAS4000; GE Healthcare, United States).

Quantitative Chromatographic Analysis of *U. davidiana* Branch (With Bark)

HPLC analysis was conducted using a Waters 2,695 Separation Module (Waters Co., Milford, MA, United States) with a vacuum degasser, a binary pump, a 2,487 dual λ absorbance detector, a column compartment, and Empower software for data acquisition and integration. HPLC-grade reagents (J.T. Baker Co., Ltd., United States) were used for HPLC analysis (Si et al., 2008b, 2009a; An et al., 2019; Liu et al., 2021f). All solvents were filtered and degassed prior to use. The branches (with bark) of *U. davidiana* were accurately weighed to 2 g and dissolved in 50 ml of methanol. Samples were ultrasonicated for 15 min and filtered through filter paper no. 20 (600 × 600 mm, HYUNDAI Micro, Korea). The filtrate was further filtered through a 0.45-μm syringe filter (PVDF, Gelman, United States). Catechin 7-O-β-D apiofuranoside (**1**) was separated on a Phenomenex KJ0-4282 guard column and a SkyPakC18 column (5 μm C^{18} HPLC column, 5 μm, 250 × 4.6 mm; SK Chemical) with a linear gradient of [D.W.MeOH: P_2HO_4 (940:50:1)]: [MeOH:P_2HO_4 (990:1)] = 100:0 to 0:100 for 30 min. The column temperature was maintained at room temperature, and the flow rate was maintained at 1.0 ml/min. The sample injection volume was 20 μL. Eluted samples were monitored at 280 nm, and compound 1 was eluted at 14.45 ± 0.14 min. Compound 1 was detected in *U. davidiana* extracts. For these experiments, compound 1, U60E, USCFR, and USCFREA were prepared at a concentration of 1 mg/ml in methanol; the stock solutions were then diluted to 1,000, 500, 250, 125, and 62.5 ppm.

Statistical Analysis

All data are expressed as the mean ± SEM. One-way analysis of variance followed by Tukey's multiple range test was used to compare each group (Si et al., 2008a; Du et al., 2019, 2022; Li et al., 2019, 2020; Liu et al., 2020a). Student's *t*-test was used for comparison between the groups. Statistical analyses were conducted using SPSS for Windows (version 10.0; Chicago, IL, United States), and data indicated with different superscript letters represent significant difference at $p < .05$.

RESULTS AND DISCUSSION

Identification of Single Compound and Function

Catechin 7-O-β-D-apiofuranoside (**Figure 3**) from the U60E [12.16 ± 0.15 μg/ml], USCFR [131.45 ± 0.18 ppm (μg/ml)], and USCFREA [350.98 ± 0.16 ppm (μg/ml)] fractions and the catechin-glycoside–rich fraction (Com.1 rich fraction) were determined using a calibration equation (y = 6,857.3x–42,331; R^2 = 0.9985) (**Figures 2**, **3**) (**Table 1** and **Table 2**). The chemical structure of purified compound 1 (**Figure 3**) was determined using ChemDraw (PerkinElmer, MA, United States).

TABLE 1 | Retention time of compound **1** from *Ulmus davidiana* branch (with bark).

Material	Retention time (min)
	Compound 1
Standard	14.449 ± 0.14
U60E	14.271 ± 0.12
USCFR	14.482 ± 0.16
USCFREA	14.687 ± 0.15

The results are expressed as the mean ± S.D. (n = 3).

Definition of Compounds

In this study, we established a methodology to produce a high-content extract (Com.1 rich fraction) having a content of Com.1 10–30 times higher than that in general alcohol extracts, which overcame the obstacle to developing pharmaceuticals or functional materials derived from natural products. We believe that this new method will be helpful in obtaining large quantities of active substances (**Figure 4**).

Regulation of Ca^{2+} Signal by ULDA Extracts and Catechin-Glycoside

We assessed whether LPS would increase intracellular Ca^{2+} mobilization in U937 cells, mimicking cell exposure to Gram-negative bacteria, and whether ULDA extracts and catechin-glycoside could protect cells from LPS exposure (**Figure 5**). Intracellular Ca^{2+} mobilization in LPS-treated U937 cells was monitored by confocal microscopy. We observed that LPS at micromolar concentration induced transient Ca^{2+} oscillations with medium amplitude in U937 cells (**Figures 5B,E,H,K**). Therefore, we determined whether ULDA extracts and catechin-glycoside (each 50 μg/ml) reduced Ca^{2+} mobilization in response to LPS treatment (**Figures 5C,F,I,L**). All types of ULDA extracts (U60E: **Figures 5A–C** panels; USCFR: **Figures 5D–F** panels; USCFREA: **Figures 5G–I** panels) and catechin-glycoside (**Figures 5J–L** panels) reduced LPS-induced Ca^{2+} mobilization within a few minutes of pretreatment. These results suggest that LPS induces Ca^{2+} mobilization and that ULDA extracts and catechin-glycoside can reduce LPS-induced damage signals in U937 cells.

TABLE 2 | Concentration of compound 1 from *Ulmus davidiana* branch (with bark).

Material	Concentration (μg/ml)
	Compound 1
U60E	12.16 ± 0.15
USCFR	131.45 ± 0.18
USCFREA	350.98 ± 0.16

The results are expressed as the mean ± S.D. (n = 3).

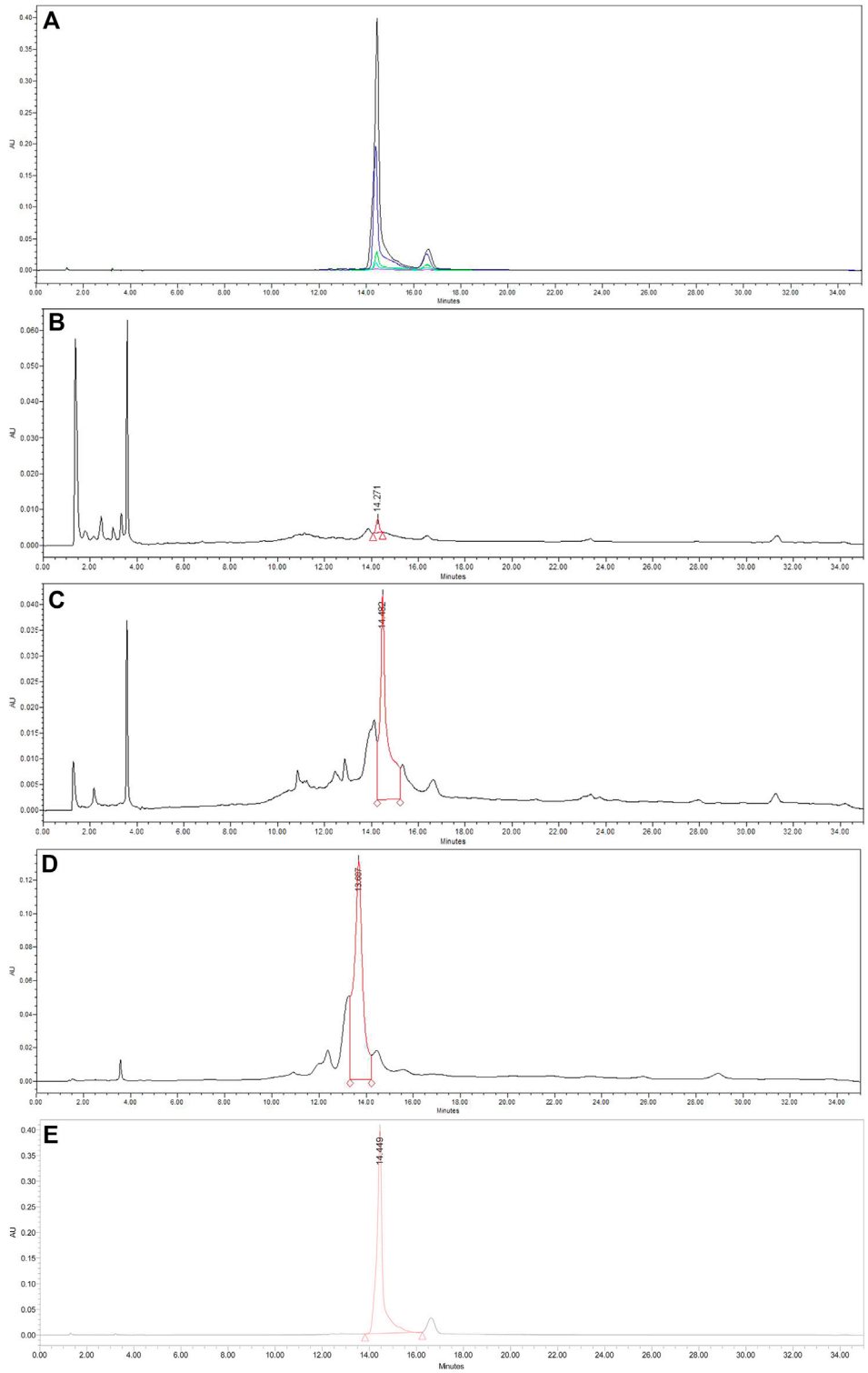

FIGURE 4 | Representative HPLC chromatograms of **(A)** compound standard, **(B)** U60E [branch (with bark) 60% pre-ethanol A extract], **(C)** USCFR [branch (with bark) supercritical extraction residue 60% edible ethanolic extract from *U. davidiana*], **(D)** USCFREA [ethyl acetate layer extract of USCFR], and **(E)** catechin-glycoside–rich fraction. U60E = 1,000 ppm, USCFREA = 1,000 ppm, USCFR = 1,000 ppm, and catechin-glycoside–rich fraction = 1,000 ppm.

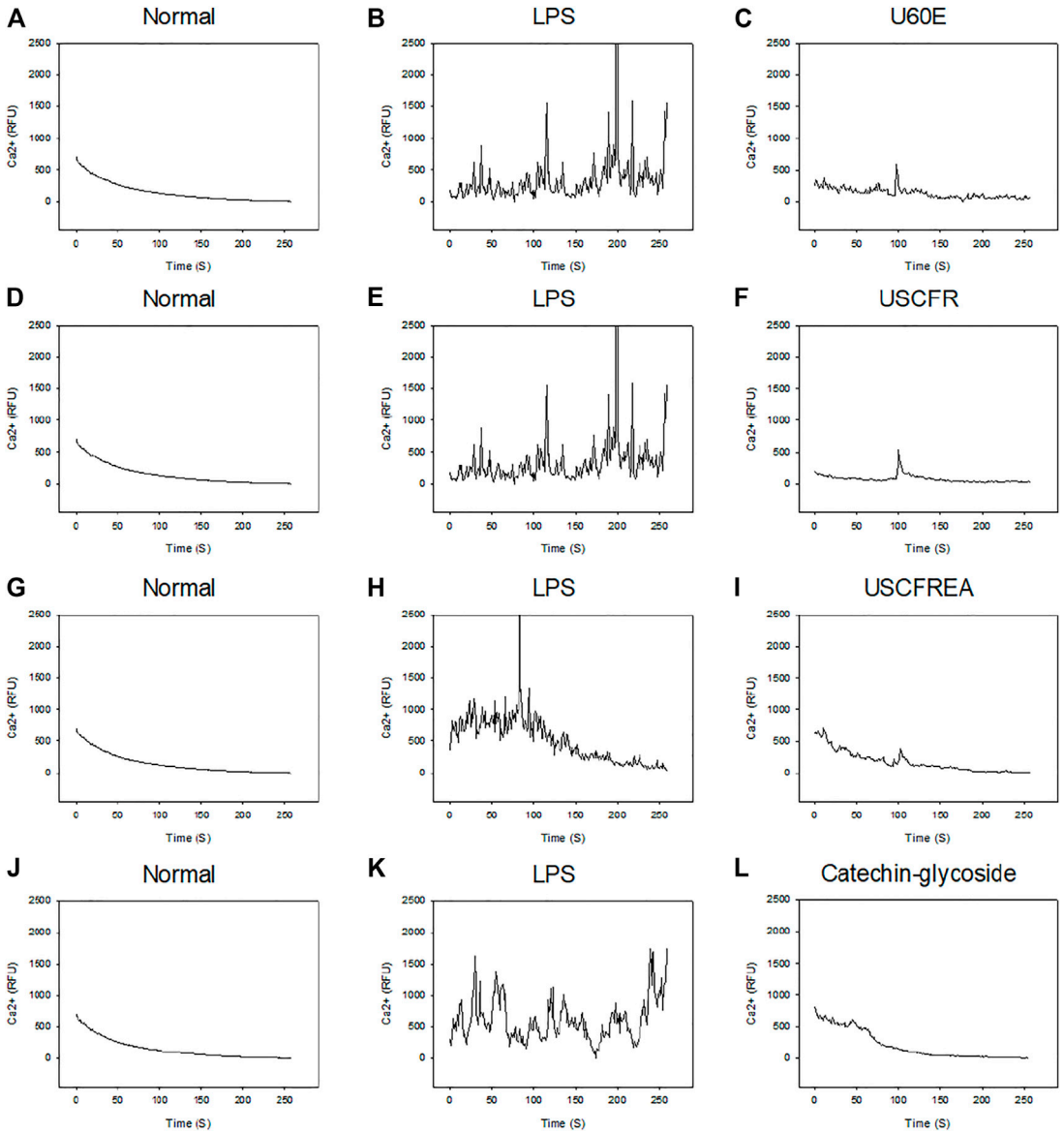

FIGURE 5 | LPS-induced Ca^{2+} signaling and inhibition effects of U60E, USCFR, USCFREA, and catechin-glycoside–rich fraction. Cells were plated on confocal dishes and loaded with Ca^{2+}-specific dye as detailed in Materials and Methods. LPS (1 μg/ml) was added and Ca^{2+} mobilization was monitored at the indicated time points. Normal **(A,D,G,J)** and LPS **(B,E,H,K)**. **(C)** U60E, **(F)** USCFREA, **(I)** USCFR, and **(L)** catechin-glycoside–rich fraction (each 50 μg/ml) were pretreated for 10 min before LPS treatment. Data are representative of three independent experiments and values are expressed.

Antiapoptotic Effects on U937 Cells

Next, we examined apoptotic signaling response in U937 cells treated with 1 μg/ml LPS (**Figures 6A–D**). Administration of LPS increased the expression of apoptosis markers such as Bax and PARP and reduced the expression of Bcl-2, an antiapoptotic protein. Pretreatment with ULDA extracts (**Figures 6A–C**) and catechin-glycoside (**Figure 6D**) markedly reversed Bax and PARP protein expression levels; moreover, Bcl-2 expression was significantly elevated in a dose-dependent manner. Future comprehensive experimental studies might improve our understanding of other molecular pathways activated by ULDA extracts and catechin-glycosides in various disease-related signaling processes and help guide prospective clinical studies evaluating their effects and appropriate usage.

Lipopolysaccharide is a major virulence factor, and previous studies have demonstrated that LPS induces apoptosis in the murine macrophage-like cell line J744.1 (Suzuki et al., 2008; Ude et al., 2020), but not in humans. In this study, we emphasized the important role of the nuclear apoptotic pathway leading to Bax and PARP activation in LPS-induced apoptosis of human macrophages, U937 cells, and suggested that catechin-glycoside is a good candidate for amelioration of inflammatory disorders. However, when using natural materials with excellent physiological activity, it is necessary

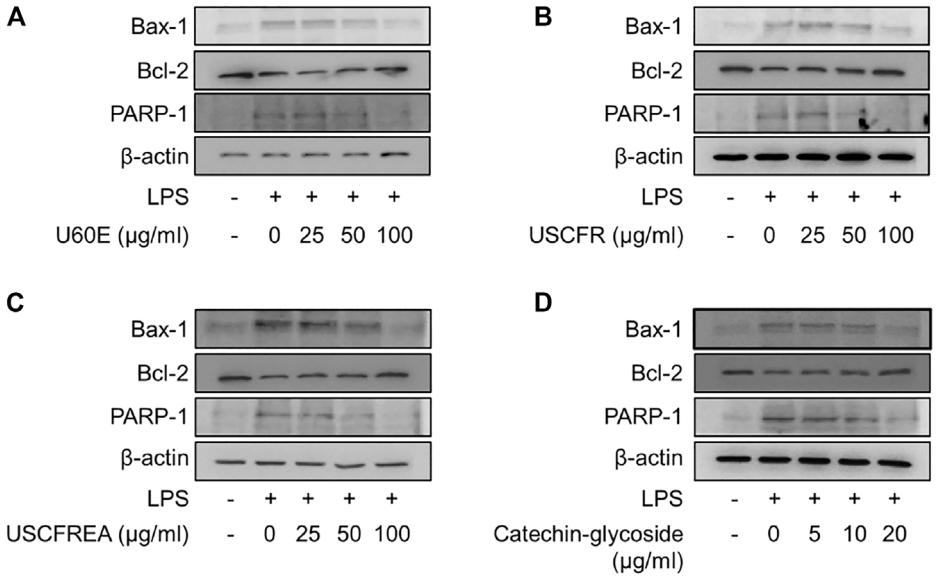

FIGURE 6 | Inhibition effects of U60E, USCFREA, USCFR, and catechin-glycoside–rich fraction on LPS-induced apoptosis signaling in U937 cells. Cells were treated with LPS (1 μg/ml) in the presence or absence of the indicated doses of **(A)** U60E, **(B)** USCFR, **(C)** USCFREA, and **(D)** catechin-glycoside–rich fraction. Lysed cell extracts were analyzed by Western blotting using the indicated antibodies. U60E, USCFREA, USCFR, and catechin-glycoside–rich fraction were pretreated for 10 min before LPS treatment. The Western blot is representative of three independent experiments.

to review and consider the optimal process for biological manufacturing.

Intracellular Ca^{2+} mobilization is a universal signaling pathway in which cells respond to a wide range of external stimuli such as hormones, chemicals, and other organic/inorganic compounds (Lee and Zhao, 2019; Dara et al., 2021). Stimulation of Ca^{2+} mobilization is initiated by the activation of second messenger production in the cytosol, which activates Ca^{2+} release from stores, such as the endoplasmic reticulum and endolysosomes (Streb et al., 1983). Ca^{2+} influx played an important role in the $[Ca^{2+}]i$ mobilization pathway in U937 cells and well-defined LPS-induced cytokine production (Wehrhahn et al., 2010) *via* the transient receptor potential melastatin 2 (TRPM2) pathway. In addition, LPS-induced U937 apoptotic signaling is mediated by the transient receptor potential vanilloid subtype 1 (TRPV1) channel along with the cytosolic ROS signaling pathways (Güzel and Akpınar, 2021). These LPS-induced apoptotic signals are dependent upon mitochondrial dysfunction (Kuwabara and Imajoh-Ohmi, 2004), which is expected to be a parallel mechanism. In this study, we observed the effect of $[Ca^{2+}]i$ mobilization on LPS-induced cell apoptosis and inhibitory effects of ULDA extract fractions and catechin-glycoside in U937 cells, but the critical pathway was not defined clearly and needs to be further investigated.

In many similar studies, an optimal extraction method was developed to obtain large quantities of effective substances from the same amount of natural raw materials while considering cost, space, facilities, and infrastructure (Liu et al., 2017; Hu et al., 2018; Lu et al., 2019; Kumar et al., 2020; Wang et al., 2020; Xu et al., 2020c; Yang et al., 2020; Ha et al., 2021; Huang et al., 2021; Zheng et al., 2021). Accordingly, the most commonly used extraction methods in academia and industry include hot water extraction, ethanol extraction, ultrasonic extraction, pressurized extraction, and supercritical extraction (Si et al., 2011; Chen et al., 2016; Hu et al., 2017; Xie et al., 2018, 2019; Yang et al., 2019; Xu et al., 2020a, Xu et al., 2020b, Xu et al., 2021a, Xu et al., 2021b; Wang et al., 2021a; Liu et al., 2021a, 2021b, 2021c). Each extraction method has its advantages and disadvantages that should be considered in many ways at the laboratory level and future commercialization level (Dai et al., 2020a; Liu et al., 2020b; Liu et al., 2021d; Liu et al., 2021e; Dai et al., 2020b; Chen et al., 2020; Chen et al., 2021; Ma et al., 2021; Zhang et al., 2021). Among various extraction methods, supercritical extraction technology has the advantages of being eco-friendly, use of safe organic solvents, and avoidance of environmental pollution. Thus, we used supercritical extraction technology for obtaining *U. davidiana* extracts with low cytotoxicity (Mun et al., 2018; Seo et al., 2018). Traditionally, water and alcohols (methanol or ethanol) have been used for the extraction of basic ingredients in local and industrial fields, but the risks and advantages of nonspecific classification between molecules exist (Cho et al., 2017). Therefore, fractionation with various solvents following polarity, ionic strength, hydrophilicity, and hydrophobicity along with purification has been performed worldwide, and techniques for the synthesis of the same molecules have been developed (Rho et al., 2004; Nan et al., 2013; Ravichandiran et al., 2019; Fang et al., 2020; Wang et al., 2021b). In this study, we extracted effective molecules from the residual material by supercritical fluidic extraction (Mun et al., 2018; Seo et al., 2018). Considering that these residues could retain relatively

hydrophilic molecules after supercritical fluid extraction, we performed common hydrophilic and hydrophobic extraction methods using 60% edible ethanol and ethyl acetate, respectively.

In this study, to examine the value of the supercritical extraction residue, physiological activity study was performed by extracting the supercritical extract of *U. davidiana* using 60% alcohol. In addition, ethyl acetate solvent analysis was conducted as a part of the production method to examine the added physiological value of *U. davidiana* supercritical extract and to verify the possibility of *U. davidiana* supercritical extraction residue as a new natural material.

CONCLUSION

The branches of *Ulmus davidiana* var. *japonica* (ULDA) has traditionally been used in Korea and other Asian countries. ULDA extracts are complex substances consisting of many components; a few of them have pharmaceutical applications in various diseases, such as inflammation and other chronic problems, and as antimicrobial agents.

In this study, we investigated the effects of supercritical fluid-fractionated ULDA, including initial fractions of polyphenols, hydrophobic substances, and flavonoids, on innate immunity modulation and recovery of innate immune function in an *in vitro* model. Future experiments are needed to investigate the beneficial effects of these resources in other diseases using *in vivo* models.

DATA AVAILABILITY STATEMENT

The original contributions presented in the study are included in the article/Supplementary Material; further inquiries can be directed to the corresponding authors.

AUTHOR CONTRIBUTIONS

Investigation, J-HY, YM, and H-OK; Supervision, CS, K-HP, and S-EC; Writing—original draft, S-EC and K-HP; Writing—review and editing, CS and J-HJ.

FUNDING

This research was supported by 2021 Universities Leading Lab-Specific Start-Ups through the National Research Foundation of Korea (NRF) grant funded by the Korean government (MSIT), the Key Technology Research and Development Program of Tianjin (19YFZCSN00950), the R and D program for Forest Science Technology (201703B10-1819-BA01, 2019151D10-2023-0301 and 2019151D10-2223-0301) provided by the Korea Forest Service (Korea Forestry Promotion Institute), and partially supported by the Technology Development Program (S3030198) funded by the Ministry of SMEs and Startups (MSS, Korea) to S-EC. This work was also partially supported by the National Research Foundation of Korea grant funded by the Korean government (2019R1I1A1A01057005 to H-OK, 2021R1A2C1091322 to K-HP, and NRF-2020R1I1A3071928 to H-JY).

REFERENCES

An, L., Si, C., Wang, G., Sui, W., and Tao, Z. (2019). Enhancing the Solubility and Antioxidant Activity of High-Molecular-Weight Lignin by Moderate Depolymerization via *In Situ* Ethanol/acid Catalysis. *Ind. Crops Prod.* 128, 177–185. doi:10.1016/j.indcrop.2018.11.009

Azenabor, A. A., Kennedy, P., and York, J. (2009). Free Intracellular Ca2+ Regulates Bacterial Lipopolysaccharide Induction of iNOS in Human Macrophages. *Immunobiology* 214, 143–152. doi:10.1016/j.imbio.2008.06.001

Carrillo, J. T., and Borthakur, D. (2021). Do Uncommon Plant Phenolic Compounds have Uncommon Properties? A Mini Review on Novel Flavonoids. *J. Bioresour. Bioprod.* 6 (4), 279–291. doi:10.1016/j.jobab.2021.09.001

Chen, B.-C., Chou, C.-F., and Lin, W.-W. (1998). Pyrimidinoceptor-mediated Potentiation of Inducible Nitric-Oxide Synthase Induction in J774 Macrophages. *J. Biol. Chem.* 273, 29754–29763. doi:10.1074/jbc.273.45.29754

Chen, S., Wang, G., Sui, W., Parvez, A. M., Dai, L., and Si, C. (2020). Novel Lignin-Based Phenolic Nanosphere Supported Palladium Nanoparticles with Highly Efficient Catalytic Performance and Good Reusability. *Ind. Crops Prod.* 145, 112164. doi:10.1016/j.indcrop.2020.112164

Chen, T., Liu, H., Liu, J., Li, J., An, Y., Zhu, M., et al. (2021). Carboxymethylation of Polysaccharide Isolated from Alkaline Peroxide Mechanical Pulping (APMP) Waste Liquor and Its Bioactivity. *Int. J. Biol. Macromol.* 181, 211–220. doi:10.1016/j.ijbiomac.2021.03.125

Chen, X., Yang, Q., Si, C.-L., Wang, Z., Huo, D., Hong, Y., et al. (2016). Recovery of Oligosaccharides from Prehydrolysis Liquors of poplar by Microfiltration/ultrafiltration Membranes and Anion Exchange Resin. *ACS Sustainable Chem. Eng.* 4, 937–943. doi:10.1021/acssuschemeng.5b01029

Cho, E., Chung, E. Y., Jang, H.-Y., Hong, O.-Y., Chae, H. S., Jeong, Y.-J., et al. (2017). Anti-cancer Effect of Cyanidin-3-Glucoside from Mulberry via Caspase-3 Cleavage and DNA Fragmentation *In Vitro* and *In Vivo*. *Acamc* 17, 1519–1525. doi:10.2174/1871520617666170327152026

Dai, L., Cao, Q., Wang, K., Han, S., Si, C., Liu, D., et al. (2020a). High Efficient Recovery of L-Lactide with Lignin-Based Filler by thermal Degradation. *Ind. Crops Prod.* 143, 111954. doi:10.1016/j.indcrop.2019.111954

Dai, L., Ma, M., Xu, J., Si, C., Wang, X., Liu, Z., et al. (2020b). All-lignin-based Hydrogel with Fast pH-Stimuli Responsiveness for Mechanical Switching and Actuation. *Chem. Mater.* 32, 4324–4330. doi:10.1021/acs.chemmater.0c01198

Dara, P. K., Geetha, A., Mohanty, U., Raghavankutty, M., Mathew, S., Nagarajarao, R. C., et al. (2021). Extraction and Characterization of Myofibrillar Proteins from Different Meat Sources: A Comparative Study. *J. Bioresour. Bioprod.* 6 (4), 367–378. doi:10.1016/j.jobab.2021.04.004

Du, H., Liu, W., Zhang, M., Si, C., Zhang, X., and Li, B. (2019). Cellulose Nanocrystals and Cellulose Nanofibrils Based Hydrogels for Biomedical Applications. *Carbohydr. Polym.* 209, 130–144. doi:10.1016/j.carbpol.2019.01.020

Du, H., Zhang, M., Liu, K., Parit, M., Jiang, Z., Zhang, X., et al. (2022). Conductive PEDOT:PSS/cellulose Nanofibril Paper Electrodes for Flexible Supercapacitors with superior Areal Capacitance and Cycling Stability. *Chem. Eng. J.* 428, 131994. doi:10.1016/j.cej.2021.131994

Eom, S. Y., Chung, C. B., Kim, Y. S., Kim, J. H., Kim, K. S., Kim, Y. H., et al. (2006). Cosmeceutical Properties of Polysaccharides from the Root Bark of *Ulmus Davidiana* Var. *Japonica*. *J. Cosmet. Sci.* 57, 355–367.

Fang, X., Zhou, J., Wang, J., Tang, F., and Zhao, L. (2020). Preparation of Flavonoids from Osmanthus Dregs and Enzymatic Modification. *J. For. Eng.* 5, 99–105. doi:10.13360/j.issn.2096-1359.202006009

Güzel, M., and Akpınar, O. (2021). Hydroxychloroquine Attenuates Acute Inflammation (LPS)-Induced Apoptosis via Inhibiting TRPV1 Channel/ROS Signaling Pathways in Human Monocytes. *Biology* 10, 967. doi:10.3390/biology10100967

Ha, E. J., Yun, J.-H., Si, C., Bae, Y. S., Jeong, Y.-H., Park, K.-H., et al. (2021). Application of Ethanol Extracts from Alnus Sibirica Fisch. Ex Turcz in Hair Growth Promotion. *Front. Bioeng. Biotechnol.* 9, 673314. doi:10.3389/fbioe.2021.673314

Hong, N. D., Kim, N. J., No, Y. S., and Kim, J. S. (1990). A Study on Efficacy of Ulmi Cortex. *Kor. J. Phamacogn.* 21, 217–222.

Hu, L., Du, H., Liu, C., Zhang, Y., Yu, G., Zhang, X., et al. (2018). Comparative Evaluation of the Efficient Conversion of Corn Husk Filament and Corn Husk Powder to Valuable Materials via a Sustainable and Clean Biorefinery Process. *ACS Sustainable Chem. Eng.* 7, 1327–1336. doi:10.1021/acssuschemeng.8b05017

Hu, L., Wang, K., Li, G., Zhang, R., Luo, Y., Si, C.-L., et al. (2017). Isolation and Structural Elucidation of Heartwood Extractives of Juglans Sigillata. *Holzforschung* 71, 785–791. doi:10.1515/hf-2017-0036

Huang, L.-Z., Ma, M.-G., Ji, X.-X., Choi, S.-E., and Si, C. (2021). Recent Developments and Applications of Hemicellulose from Wheat Straw: a Review. *Front. Bioeng. Biotechnol.* 9, 690773. doi:10.3389/fbioe.2021.690773

Jeon, G., Ko, J.-Y., Mun, M.-J., Min, J., Choi, S.-E., and Bang, S. H. (2020). Effect of Melanin Reduction by Extracts from *Ulmus Davidiana* by Supercritical Fluid Extraction. *Toxicol. Environ. Health Sci.* 12, 325–329. doi:10.1007/s13530-020-00057-3

Jung, H. J., and Park, E. H. (2006). "Anti-inflanunatory, Anti-angiogenic and Analgesic Activities of *Ulmus Davidiana* Var. Japonica," in *Proceeding of the Convention of the Pharmaceutical Society of Korea* (Busan, Seoul: The Pharmaceutical Society of Korea), 138–139.

Kim, E.-J., Jang, M.-K., Yoon, E.-H., Jung, C.-Y., Nam, D.-W., Lee, S.-D., et al. (2010). Efficacy of Pharmacopuncture Using Root Bark of *Ulmus Davidiana* Planch in Patients with Knee Osteoarthritis: a Double-Blind Randomized Controlled Trial. *J. Acupuncture Meridian Stud.* 3, 16–23. doi:10.1016/S2005-2901(10)60003-9

Kim, K.-S., Lee, S.-D., Kim, K.-H., Kil, S.-Y., Chung, K.-H., and Kim, C.-H. (2005). Suppressive Effects of a Water Extract of *Ulmus Davidiana* Planch (Ulmaceae) on Collagen-Induced Arthritis in Mice. *J. Ethnopharmacology* 97, 65–71. doi:10.1016/j.jep.2004.10.011

Kim, M., Park, K.-H., and Choi, S. E. (2019). Protective Effects of Supercritical Fluid Extracts of *Ulmus Daviana* Var. Japonica on LPS-Induced Immune Responses. *ksbbj* 34, 216–220. doi:10.7841/ksbbj.2019.34.3.216

Kim, S.-Y., Park, K.-H., Gul, R., Jang, K. Y., and Kim, U.-H. (2009). Role of Kidney ADP-Ribosyl Cyclase in Diabetic Nephropathy. *Am. J. Physiology-Renal Physiol.* 296, F291–F297. doi:10.1152/ajprenal.90381.2008

Kim, U.-H., Han, M.-K., Park, B.-H., Kim, H.-R., and An, N.-H. (1993). Function of NAD Glycohydrolase in ADP-Ribose Uptake from NAD by Human Erythrocytes. *Biochim. Biophys. Acta (Bba) - Mol. Cell Res.* 1178, 121–126. doi:10.1016/0167-4889(93)90001-6

Kumar, A., Sharma, G., Naushad, M., Al-Muhtaseb, A. a. H., García-Peñas, A., Mola, G. T., et al. (2020). Bio-inspired and Biomaterials-Based Hybrid Photocatalysts for Environmental Detoxification: A Review. *Chem. Eng. J.* 382, 122937. doi:10.1016/j.cej.2019.122937

Kuwabara, T., and Imajoh-Ohmi, S. (2004). LPS-induced Apoptosis Is Dependent upon Mitochondrial Dysfunction. *Apoptosis* 9, 467–474. doi:10.1023/B:APPT.0000031453.90821.6a

Lee, E.-H., Park, C.-W., and Jung, Y.-J. (2013a). Anti-inflammatory and Immune-Modulating Effect of *Ulmus Davidiana* Var. Japonica Nakai Extract on a Macrophage Cell Line and Immune Cells in the Mouse Small Intestine. *J. Ethnopharmacology* 146, 608–613. doi:10.1016/j.jep.2013.01.035

Lee, H.-S., Jang, M. S., Kim, J.-H., Hong, C.-P., Lee, E.-J., Jeun, E. J., et al. (2013b). *Ulmus Davidiana* Var. Japonica Nakai Upregulates Eosinophils and Suppresses Th1 and Th17 Cells in the Small Intestine. *PLoS One* 8, e76716. doi:10.1371/journal.pone.0076716

Lee, H. C., and Zhao, Y. J. (2019). Resolving the Topological enigma in Ca2+ Signaling by Cyclic ADP-Ribose and NAADP. *J. Biol. Chem.* 294, 19831–19843. doi:10.1074/jbc.REV119.009635

Lee, S.-J., and Lim, K.-T. (2007). Inhibitory Effect of Phytoglycoprotein on Tumor Necrosis Factor-α and Interleukin-6 at Initiation Stage of colon Cancer in 1,2-Dimethylhydrazine-Treated ICR Mice. *Toxicol. Appl. Pharmacol.* 225, 198–205. doi:10.1016/j.taap.2007.07.010

Lee, S. J. (1966). *Korean Folk Medicin*, Vol. 39. Seoul: Seoul National University.

Li, X., Lu, X., Nie, S., Liang, M., Yu, Z., Duan, B., et al. (2020). Efficient Catalytic Production of Biomass-Derived Levulinic Acid over Phosphotungstic Acid in Deep Eutectic Solvent. *Ind. Crops Prod.* 145, 112154. doi:10.1016/j.indcrop.2020.112154

Li, X., Xu, R., Yang, J., Nie, S., Liu, D., Liu, Y., et al. (2019). Production of 5-hydroxymethylfurfural and Levulinic Acid from Lignocellulosic Biomass and Catalytic Upgradation. *Ind. Crops Prod.* 130, 184–197. doi:10.1016/j.indcrop.2018.12.082

Liu, C., Wang, G., Sui, W., An, L., and Si, C. (2017). Preparation and Characterization of Chitosan by a Novel Deacetylation Approach Using Glycerol as green Reaction Solvent. *ACS Sustainable Chem. Eng.* 5, 4690–4698. doi:10.1021/acssuschemeng.7b00050

Liu, H., Du, H., Zheng, T., Liu, K., Ji, X., Xu, T., et al. (2021a). Cellulose Based Composite Foams and Aerogels for Advanced Energy Storage Devices. *Chem. Eng. J.* 426, 130817. doi:10.1016/j.cej.2021.130817

Liu, H., Xu, T., Cai, C., Liu, K., Liu, W., Zhang, M., et al. (2022). Multifunctional Superelastic, Superhydrophilic, and Ultralight Nanocellulose-Based Composite Carbon Aerogels for Compressive Supercapacitor and Strain Sensor. *Adv. Funct. Mater.* 32, 2113082. doi:10.1002/adfm.202113082

Liu, H., Xu, T., Liu, K., Zhang, M., Liu, W., Li, H., et al. (2021b). Lignin-based Electrodes for Energy Storage Application. *Ind. Crops Prod.* 165, 113425. doi:10.1016/j.indcrop.2021.113425

Liu, K., Du, H., Liu, W., Liu, H., Zhang, M., Xu, T., et al. (2021c). Cellulose Nanomaterials for Oil Exploration Applications. *Polym. Rev.* 0, 1–41. doi:10.1080/15583724.2021.2007121

Liu, K., Du, H., Zheng, T., Liu, H., Zhang, M., Zhang, R., et al. (2021d). Recent Advances in Cellulose and its Derivatives for Oilfield Applications. *Carbohydr. Polym.* 259, 117740. doi:10.1016/j.carbpol.2021.117740

Liu, K., Du, H., Zheng, T., Liu, W., Zhang, M., Liu, H., et al. (2021e). Lignin-containing Cellulose Nanomaterials: Preparation and Applications. *Green. Chem.* 23, 9723–9746. doi:10.1039/D1GC02841C

Liu, W., Du, H., Liu, H., Xie, H., Xu, T., Zhao, X., et al. (2020a). Highly Efficient and Sustainable Preparation of Carboxylic and Thermostable Cellulose Nanocrystals via FeCl3-Catalyzed Innocuous Citric Acid Hydrolysis. *ACS Sustainable Chem. Eng.* 8, 16691–16700. doi:10.1021/acssuschemeng.0c06561

Liu, W., Du, H., Liu, K., Liu, H., Xie, H., Si, C., et al. (2021f). Sustainable Preparation of Cellulose Nanofibrils via Choline Chloride-Citric Acid Deep Eutectic Solvent Pretreatment Combined with High-Pressure Homogenization. *Carbohydr. Polym.* 267, 118220. doi:10.1016/j.carbpol.2021.118220

Liu, W., Du, H., Zhang, M., Liu, K., Liu, H., Xie, H., et al. (2020b). Bacterial Cellulose-Based Composite Scaffolds for Biomedical Applications: A Review. *ACS Sustainable Chem. Eng.* 8, 7536–7562. doi:10.1021/acssuschemeng.0c00125

Lu, J., Zhu, W., Dai, L., Si, C., and Ni, Y. (2019). Fabrication of Thermo- and pH-Sensitive Cellulose Nanofibrils-Reinforced Hydrogel with Biomass Nanoparticles. *Carbohydr. Polym.* 215, 289–295. doi:10.1016/j.carbpol.2019.03.100

Ma, C., Ma, M. G., Si, C., Ji, X. X., and Wan, P. (2021). Flexible MXene-Based Composites for Wearable Devices. *Adv. Funct. Mater.* 31, 2009524. doi:10.1002/adfm.202009524

Mehta, K., Shahid, U., and Malavasi, F. (1996). Human CD38, a Cell-surface Protein with Multiple Functions. *FASEB j.* 10, 1408–1417. doi:10.1096/fasebj.10.12.8903511

Mun, M.-J., Park, K.-H., and Choi, S. E. (2018). Biological Activity of Supercritical Extraction Residue 60% Ethanolic Extracts from Ulmus Davidiana. *J. Converg. Inf. Technol.* 8, 29–36. doi:10.22156/CS4SMB.2018.8.5.029

Nan, H., Yoo, D. J., and Kang, S. H. (2013). Fast Parallel Detection of Feline Panleukopenia Virus DNA by Multi-Channel Microchip Electrophoresis with Programmed Step Electric Field Strength. *J. Sep. Sci.* 36, 350–355. doi:10.1002/jssc.201200721

Oh, P. S., Lee, S. J., and Lim, K. T. (2006). Glycoprotein (116 kD) Isolated from *Ulmus Davidiana* Nakai Protects from Injury of 12-O-Tetradecanoylphorbol 13-acetate (TPA)-treated BNL CL.2 Cells. *Pharmacol. Rep.* 58, 67–74.

Park, K.-H., Chung, E.-Y., Choi, Y.-N., Jang, H.-Y., Kim, J.-S., and Kim, G.-B. (2020). Oral Administration of Ulmus Davidiana Extract Suppresses Interleukin-1β Expression in LPS-Induced Immune Responses and Lung Injury. *Genes Genom.* 42, 87–95. doi:10.1007/s13258-019-00883-x

Park, K.-H., Kim, B.-J., Kang, J., Nam, T.-S., Lim, J. M., Kim, H. T., et al. (2011). Ca 2+ Signaling Tools Acquired from Prostasomes Are Required for Progesterone-Induced Sperm Motility. *Sci. Signal.* 4 (173), ra31. doi:10.1126/scisignal.2001595

Rah, S.-Y., Park, K.-H., Nam, T.-S., Kim, S.-J., Kim, H., Im, M.-J., et al. (2007). Association of CD38 with Nonmuscle Myosin Heavy Chain IIA and Lck Is Essential for the Internalization and Activation of CD38. *J. Biol. Chem.* 282, 5653–5660. doi:10.1074/jbc.m609478200

Ravichandiran, P., Subramaniyan, S. A., Kim, S.-Y., Kim, J.-S., Park, B.-H., Shim, K. S., et al. (2019). Synthesis and Anticancer Evaluation of 1,4-Naphthoquinone Derivatives Containing a Phenylaminosulfanyl Moiety. *ChemMedChem* 14, 532–544. doi:10.1002/cmdc.201800749

Rho, Y. S., Kim, S. Y., Kim, W. J., Yun, Y. K., Sin, H. S., and Yoo, D. J. (2004). Convenient Syntheses of Daunomycinone-7-D-Glucuronides and Doxorubicinone-7-D-Glucuronides. *Synth. Commun.* 34, 3497–3511. doi:10.1081/scc-200030978

Seo, J.-H., Lee, Y.-J., Jo, Y.-I., Ko, J.-Y., Mun, M.-J., Park, K.-H., et al. (2018). Anti-fungal, Anti-oxidant, and Anti-inflammatory Effects of Supercritical Fluid Extracts from Ulmus Davidiana. *J. Korea Convergence Soc.* 9, 225–233. doi:10.15207/JKCS.2018.9.8.225

Shin, D.-Y., Kim, H.-S., Min, K.-H., Hyun, S.-S., Kim, S.-A., Huh, H., et al. (2000). Isolation of a Potent Anti-MRSA Sesquiterpenoid Quinone from Ulmus Davidiana Var. Japonica. *Chem. Pharm. Bull.* 48, 1805–1806. doi:10.1248/cpb.48.1805

Si, C.-L., Deng, X.-J., Liu, Z., Kim, J.-K., and Bae, Y.-S. (2008a). Studies on the Phenylethanoid Glycosides with Anti-complement Activity fromPaulownia tomentosavar.Tomentosawood. *J. Asian Nat. Prod. Res.* 10, 1003–1008. doi:10.1080/10286020802242364

Si, C.-L., Jiang, J.-Z., Liu, S.-C., Hu, H.-Y., Ren, X.-D., Yu, G.-J., et al. (2013a). A New Lignan Glycoside and Phenolics from the branch wood of Pinus Banksiana Lambert. *Holzforschung* 67, 357–363. doi:10.1515/hf-2012-0137

Si, C.-L., Kim, J.-K., Bae, Y.-S., and Li, S.-M. (2009a). Phenolic Compounds in the Leaves ofPopulus Ussuriensisand Their Antioxidant Activities. *Planta Med.* 75, 1165–1167. doi:10.1055/s-0029-1185476

Si, C.-L., Liu, Z., Kim, J.-K., and Bae, Y.-S. (2008b). Structure Elucidation of Phenylethanoid Glycosides from Paulownia Tomentosa Steud. Var. Tomentosa wood. *Holzforschung* 62, 197–200. doi:10.1515/hf.2008.047

Si, C.-L., Shen, T., Jiang, Y.-Y., Wu, L., Yu, G.-J., Ren, X.-D., et al. (2013b). Antioxidant Properties and Neuroprotective Effects of Isocampneoside II on Hydrogen Peroxide-Induced Oxidative Injury in PC12 Cells. *Food Chem. Toxicol.* 59, 145–152. doi:10.1016/j.fct.2013.05.051

Si, C.-L., Wu, L., and Zhu, Z.-Y. (2009b). Phenolic Glycosides from Populus Davidiana Bark. *Biochem. Syst. Ecol.* 37, 221–224. doi:10.1016/j.bse.2009.01.007

Si, C.-L., Xu, J., Kim, J.-K., Bae, Y.-S., Liu, P.-T., and Liu, Z. (2011). Antioxidant Properties and Structural Analysis of Phenolic Glucosides from Bark of Populus Ussuriensis Kom. *Wood Sci. Technol.* 45, 5–13. doi:10.1007/s00226-009-0286-x

Streb, H., Irvine, R. F., Berridge, M. J., and Schulz, I. (1983). Release of Ca2+ from a Nonmitochondrial Intracellular Store in Pancreatic Acinar Cells by Inositol-1,4,5-Trisphosphate. *Nature* 306, 67–69. doi:10.1038/306067a0

Suzuki, C., Kimoto-Nira, H., Kobayashi, M., Nomura, M., Sasaki, K., and Mizumachi, K. (2008). Immunomodulatory and Cytotoxic Effects of Various Lactococcus Strains on the Murine Macrophage Cell Line J774.1. *Int. J. Food Microbiol.* 123, 159–165. doi:10.1016/j.ijfoodmicro.2007.12.022

Tsien, R. Y., Pozzan, T., and Rink, T. J. (1982). Calcium Homeostasis in Intact Lymphocytes: Cytoplasmic Free Calcium Monitored with a New, Intracellularly Trapped Fluorescent Indicator. *J. Cell Biol.* 94, 325–334. doi:10.1083/jcb.94.2.325

Ude, M. U., Oluka, I., and Eze, P. C. (2020). Optimization and Kinetics of Glucose Production via Enzymatic Hydrolysis of Mixed Peels. *J. Bioresour. Bioprod.* 5, 283–290. doi:10.1016/j.jobab.2020.10.007

Wang, H., Du, H., Liu, K., Liu, H., Xu, T., Zhang, S., et al. (2021a). Sustainable Preparation of Bifunctional Cellulose Nanocrystals via Mixed H2SO4/formic Acid Hydrolysis. *Carbohydr. Polym.* 266, 118107. doi:10.1016/j.carbpol.2021.118107

Wang, H., Xie, H., Du, H., Wang, X., Liu, W., Duan, Y., et al. (2020). Highly Efficient Preparation of Functional and Thermostable Cellulose Nanocrystals via H2SO4 Intensified Acetic Acid Hydrolysis. *Carbohydr. Polym.* 239, 116233. doi:10.1016/j.carbpol.2020.116233

Wang, S., Liu, F., Zhou, Q., Xu, S., Huang, S., and Luo, J. (2021b). Preparation of Cedrol and Cedryl Acetate and Their Antifungal Activities. *J. For. Eng.* 6, 74–80. doi:10.13360/j.issn.2096-1359.202007036

Wehrhahn, J., Kraft, R., Harteneck, C., and Hauschildt, S. (2010). Transient Receptor Potential Melastatin 2 Is Required for Lipopolysaccharide-Induced Cytokine Production in Human Monocytes. *J.I.* 184, 2386–2393. doi:10.4049/jimmunol.0902474

Xie, H., Du, H., Yang, X., and Si, C. (2018). Recent Strategies of Cellulose Nanocrystals and Cellulose Nanofibrils Derived from Raw Cellulose Materials. *Int. J. Polym. Sci.* 2018, 7923068. doi:10.1155/2018/7923068,7923068

Xie, H., Zou, Z., Du, H., Zhang, X., Wang, X., Yang, X., et al. (2019). Preparation of Thermally Stable and Surface-Functionalized Cellulose Nanocrystals via Mixed H2SO4/Oxalic Acid Hydrolysis. *Carbohydr. Polym.* 223, 115116. doi:10.1016/j.carbpol.2019.115116

Xiong, R., Hua, D., Hoeck, J. V., Berdecka, D., Léger, M., Munter, S. D., et al. (2021a). Photothermal Nanofibres Enable Safe Engineering of Therapeutic Cells. *Nat. Nanotechnol.* 16, 1281–1291. doi:10.1038/s41565-021-00976-3

Xiong, R., Xu, R. X., Huang, C., De Smedt, S., and Braeckmans, K. (2021b). Stimuli-responsive Nanobubbles for Biomedical Applications. *Chem. Soc. Rev.* 50, 5746–5776. doi:10.1039/C9CS00839J

Xiu, R. J. (1988). Microcirculation and Traditional Chinese Medicine. *JAMA* 260, 1755–1757. doi:10.1001/jama.260.12.1755

Xu, J., Li, C., Dai, L., Xu, C., Zhong, Y., Yu, F., et al. (2020a). Biomass Fractionation and Lignin Fractionation towards Lignin Valorization. *ChemSusChem* 13, 4284–4295. doi:10.1002/cssc.202001491

Xu, R., Du, H., Liu, C., Liu, H., Wu, M., Zhang, X., et al. (2021a). An Efficient and Magnetic Adsorbent Prepared in a Dry Process with Enzymatic Hydrolysis Residues for Wastewater Treatment. *J. Clean. Prod.* 313, 127834. doi:10.1016/j.jclepro.2021.127834

Xu, R., Liu, K., Du, H., Liu, H., Cao, X., Zhao, X., et al. (2020c). Falling Leaves Return to Their Roots: A Review on the Preparation of γ-Valerolactone from Lignocellulose and Its Application in the Conversion of Lignocellulose. *ChemSusChem* 13, 6461–6476. doi:10.1002/cssc.202002008

Xu, R., Si, C., Kong, F., and Li, X. (2020b). Synthesis of γ-valerolactone and its Application in Biomass Conversion. *J. For. Eng.* 5, 20–28. doi:10.13360/j.issn.2096-1359.201904004

Xu, T., Du, H., Liu, H., Liu, W., Zhang, X., Si, C., et al. (2021b). Advanced Nanocellulose-Based Composites for Flexible Functional Energy Storage Devices. *Adv. Mater.* 33, 2101368. doi:10.1002/adma.202101368

Yang, J., Si, C., Liu, K., Liu, H., Li, X., and Liang, M. (2020). Production of Levulinic Acid from Lignocellulosic Biomass and Application. *J. For. Eng.* 5, 21–27. doi:10.13360/j.issn.2096-1359.201905013

Yang, X., Xie, H., Du, H., Zhang, X., Zou, Z., Zou, Y., et al. (2019). Facile Extraction of Thermally Stable and Dispersible Cellulose Nanocrystals with High Yield via a Green and Recyclable FeCl3-Catalyzed Deep Eutectic Solvent System. *ACS Sustainable Chem. Eng.* 7, 7200–7208. doi:10.1021/acssuschemeng.9b00209

Zhang, M., Du, H., Liu, K., Nie, S., Xu, T., Zhang, X., et al. (2021). Fabrication and Applications of Cellulose-Based Nanogenerators. *Adv. Compos. Hybrid Mater.* 4, 865–884. doi:10.1007/s42114-021-00312-2

Zheng, X., Zhao, Y., Pan, B., and Wang, X. (2021). Extraction, Distribution and Composition of Tannin in Picea Sitchensis. *J. For. Eng.* 6, 108–113. doi:10.13360/j.issn.2096-1359.202007026

Zhuang, X., Fu, C., Liu, W., Wang, Y., Xu, F., Zhang, Q., et al. (2016). *Ulmus Davidiana* Extract Improves Lumbar Vertebral Parameters in Ovariectomized Osteopenic Rats. *Am. J. Transl. Res.* 8, 298–313.

Conflict of Interest: The authors declare that the research was conducted in the absence of any commercial or financial relationships that could be construed as a potential conflict of interest.

Publisher's Note: All claims expressed in this article are solely those of the authors and do not necessarily represent those of their affiliated organizations, or those of the publisher, the editors, and the reviewers. Any product that may be evaluated in this article, or claim that may be made by its manufacturer, is not guaranteed or endorsed by the publisher.

frontiers in Energy Research

ORIGINAL RESEARCH
published: 04 March 2022
doi: 10.3389/fenrg.2022.841169

Mass Transport Limitations and Kinetic Consequences of Corn Stover Deacetylation

Nicholas E. Thornburg[1], Ryan M. Ness[2], Meagan F. Crowley[2], Lintao Bu[2], M. Brennan Pecha[2], Francois L. E. Usseglio-Viretta[3], Vivek S. Bharadwaj[2], Yudong Li[4], Xiaowen Chen[4], David A. Sievers[4], Edward J. Wolfrum[2], Michael G. Resch[4] and Peter N. Ciesielski[2]**

[1]Center for Integrated Mobility Sciences, National Renewable Energy Laboratory, Golden, CO, United States , [2]Renewable Resources and Enabling Sciences Center, National Renewable Energy Laboratory, Golden, CO, United States, [3]Center for Energy Conversion and Storage Systems, National Renewable Energy Laboratory, Golden, CO, United States, [4]Catalytic Carbon Transformation and Scale-Up Center, National Renewable Energy Laboratory, Golden, CO, United States

OPEN ACCESS

Edited by:
Xiaojun Shen,
Dalian Institute of Chemical Physics (CAS), China

Reviewed by:
Tae Hyun Kim,
Hanyang Universiy, Erica, South Korea
Venkatesh Balan,
University of Houston, United States

***Correspondence:**
Nicholas E. Thornburg
Nicholas.Thornburg@nrel.gov
Peter N. Ciesielski
Peter.Ciesielski@nrel.gov

Specialty section:
This article was submitted to Bioenergy and Biofuels, a section of the journal Frontiers in Energy Research

Received: 22 December 2021
Accepted: 31 January 2022
Published: 04 March 2022

Citation:
Thornburg NE, Ness RM, Crowley MF, Bu L, Pecha MB, Usseglio-Viretta FLE, Bharadwaj VS, Li Y, Chen X, Sievers DA, Wolfrum EJ, Resch MG and Ciesielski PN (2022) Mass Transport Limitations and Kinetic Consequences of Corn Stover Deacetylation. Front. Energy Res. 10:841169. doi: 10.3389/fenrg.2022.841169

Alkaline pretreatment of herbaceous feedstocks such as corn stover prior to mechanical refining and enzymatic saccharification improves downstream sugar yields by removing acetyl moieties from hemicellulose. However, the relationship between transport phenomena and deacetylation kinetics is virtually unknown for such feedstocks and this pretreatment process. Here, we report the development of an experimentally validated reaction–diffusion model for the deacetylation of corn stover. A tissue-specific transport model is used to estimate transport-independent kinetic rate constants for the reactive extraction of acetate, hemicellulose and lignin from corn stover under representative alkaline conditions (5–7 g L^{-1} NaOH, 10 wt% solids loadings) and at low to mild temperatures (4–70°C) selected to attenuate individual component extraction rates under differential kinetic regimes. The underlying transport model is based on microstructural characteristics of corn stover derived from statistically meaningful geometric particle and pore measurements. These physical descriptors are incorporated into distinct particle models of the three major anatomical fractions (cobs, husks and stalks) alongside an unsorted, aggregate corn stover particle, capturing average Feret lengths of 917–1239 μm and length-to-width aspect ratios of 1.8–2.9 for this highly heterogeneous feedstock. Individual reaction–diffusion models and their resulting particle model ensembles are used to validate and predict anatomically-specific and bulk feedstock performance under kinetic-controlled vs. diffusion-controlled regimes. In general, deacetylation kinetics and mass transfer processes are predicted to compete on similar time and length scales, emphasizing the significance of intraparticle transport phenomena. Critically, we predict that typical corn stover particles as small as ~2.3 mm in length are entirely diffusion-limited for acetate extraction, with experimental effectiveness factors calculated to be 0.50 for such processes. Debilitatingly low effectiveness factors of 0.021–0.054 are uncovered for cobs—implying that intraparticle mass transfer resistances may impair observable kinetic measurements of this anatomical fraction by up to 98%. These first-reported quantitative maps of reaction vs. diffusion control link fundamental insights into corn stover anatomy, biopolymer composition, practical size reduction

thresholds and their kinetic consequences. These results offer a guidepost for industrial deacetylation reactor design, scale-up and feedstock selection, further establishing deacetylation as a viable biorefinery pretreatment for the conversion of lignocellulosics into value-added fuels and chemicals.

Keywords: biomass pretreatment, biomass reaction kinetics, computational fluid dynamics, corn stover, deacetylation, transport phenomena

INTRODUCTION

Lignocellulosic biomass has long been investigated as a renewable feedstock for the production of biofuels and bio-based chemicals. Modern biorefinery strategies employ chemical pretreatment steps to alter feedstock structure and composition in order to enhance downstream bioproduct yields (Mosier et al., 2005; Rollin et al., 2011; Yang et al., 2017). One such pretreatment is deacetylation, or the selective, reactive removal of enzyme-inhibiting (Palmqvist and Hahn-Hägerdal, 2000; Mills et al., 2009) acetyl functionalities from the hemicellulose component of herbaceous feedstocks such as corn stover (Chen et al., 2012; Chen et al., 2016). Deacetylation features advantages of mild temperature and ambient pressure chemical processing and occurs prior to mechanical refining (a combination termed DMR) and enzymatic saccharification (Chen et al., 2019). Corn stover DMR enables high sugar monomer concentrations ($\leq$230 g L^{-1}) and subsequent ethanol titers ($\leq$86 g L^{-1}) at substantial projected cost savings (Tao et al., 2012; Chen et al., 2016). Basic environments enhance deacetylation rates in aqueous media, and the treatment introduces nanoscale porosity via mesoscale plant tissue-loosening for increased enzyme accessibility (Lima et al., 2018). Lignin and small amounts of hemicellulose are also co-extracted under these conditions. Separately, extracted DMR lignin is a promising access point for co-valorization and has received recent literature attention (Karp et al., 2014; Katahira et al., 2016; Kruger et al., 2016; Rodriguez et al., 2017; Xu et al., 2020).

Nonetheless, little is known about the coupled chemistry and physics of deacetylation processes, particularly at the biomass particle scale where such phenomena are known to compete in other biorefinery steps (Luterbacher et al., 2013; Thornburg et al., 2020; Ciesielski et al., 2021). While biomass transport phenomena are typically discussed qualitatively (Viamajala et al., 2010), studies on alkaline deacetylation often only quantitatively emphasize end-of-experiment performance metrics such as liquor yield, molecular weight (MW) distribution or residual solids compositional analysis (Karp et al., 2014; Lima et al., 2018), which do not account for transient behaviors, such as diffusion or heat transfer, that occur throughout the course of reaction. Others have reported alkaline decomposition kinetics of lignin model compounds (Gierer et al., 1977; Shimizu et al., 2012; Shimizu et al., 2013), although these insights are not readily extensible to real biomass, where cell wall biopolymer assemblies and tissue pore structures at the nanoscale and mesoscale, respectively, heavily influence experimental kinetic measurements (Min et al., 2014; Lima et al., 2018). Indeed, given the complexity surrounding experimental diffusion measurements (Jakes et al., 2020), few reports attempt to quantify the significant mass or heat transfer effects that accompany deacetylation of real biomass (Costanza and Costanza, 2002), especially as they apply to complicated continuous reactor configurations such as packed corn stover beds (Sahayaraj et al., 2021) or twin-screw extruders (Morales-Huerta et al., 2021). Lastly, the vast majority of these studies employ whole (unsorted) corn stover as the feedstock, despite the known structural and compositional differences among its major anatomical fractions (Min et al., 2014), which are expected to imbue unique kinetic and physical transport properties.

Ultimately, the untangling of chemical kinetics from mass and heat transfer and from plant anatomy is paramount to reconcile laboratory reactor data, practical feedstock comminution targets, and engineering scaling principles in overall biorefinery process development (Ciesielski et al., 2021). Some of us have recently utilized a generalizable mesoscale modeling framework to determine the transport-independent kinetics of condensed-phase biomass fractionation processes, first demonstrated for the methanolysis of poplar hardwood (Thornburg et al., 2020). These models leverage feedstock-specific measurements of particle geometries and tissue microstructures to inform assumptions of mass transport phenomena, while experimental reactor temperature profiles capture the non-isothermality of such dynamic pretreatment systems. Batch reactor experiment campaigns using known biomass particle size ranges then enable the mathematical regression of kinetic rate parameters within non-isothermal reaction–diffusion simulations evaluated for representative particle sizes and pretreatment conditions.

Here, we extend this two-dimensional (2D) mesoscale modeling approach to the sodium hydroxide-mediated deacetylation of corn stover. We develop first-principled reaction–diffusion models (i) to calculate transport-independent, anatomically-specific kinetic rate parameters describing corn stover deacetylation and (ii) to identify practical particle size thresholds for kinetic vs. mass transfer control. These actionable, quantitative relationships connect key insights of corn stover anatomy with biorefinery reactor performance, informing new best practices for feedstock preparation, experimentation and scaling.

EXPERIMENTAL AND COMPUTATIONAL METHODS

While brief descriptions are provided below, full details of feedstock preparation, batch kinetics, liquor analysis, imaging

and computational techniques are included in Supplementary Material (SM).

Materials Preparation and Characterization

Unsorted (whole, WH) corn stover received from Idaho National Laboratory (INL) was manually separated into cob (CB), husk (HS) and stalk (SK) anatomical fractions, and each of the four fractions was milled with a 2-mm screen in a laboratory-scale Wiley mill. Kramer corn stover (KR) was cultivated on Kramer farm in Wray, Colorado, and prior to experimental use at the National Renewable Energy Laboratory (NREL), KR was Wiley milled through a 2-mm screen without additional sorting. Compositional analysis was performed for each milled fraction following standard NREL Laboratory Analytical Protocols (Sluiter et al., 2005; Sluiter et al., 2008b). Particle size measurements were collected via external analysis performed by Microtrac, Inc. for each corn stover sample, while data distributions were analyzed in MATLAB R2021a. Select particles were imaged via X-ray computed tomography (XCT) in three vertical segments while rotating a complete 360° revolution; resultant radiographs were dimensionally reconstructed before data processing and visualization using the open-source NREL Microstructure Analysis Toolbox, MATBOX (Cooper et al., 2016; Arganda-Carreras et al., 2017; Usseglio-Viretta et al., 2020; Pettersen et al., 2021; Sun et al., 2021; Usseglio-Viretta et al., 2022). Segmentation and characterization methods leverage threshold selection and denoising methods developed by others (Otsu, 1979; Buades et al., 2005; Villanova et al., 2013; Tanaka, 2021). See **Supplementary Table S1** and SM methods discussion for details.

Batch Kinetics and Product Characterization

Batch reactor experiments were conducted with a 10 wt% solids loading (500 ± 5 mg feedstock) in 10-ml glass reactor vials placed in the center wells of an aluminum block subjected to temperature-regulated heating (40°C, 70°C and higher-temperature experiments) or cooling in an ice-water bath (4°C experiments). Final sodium hydroxide (NaOH) concentrations in the 5.00 mL total reaction volume were either 5.00, 7.00 or 9.00 g L^{-1} (preliminary screening only). While some experiments were subjected to periodic vortexing, typical batch experiments remained unagitated for a prescribed reaction duration (0, 2, 5, 10, 20, 60 min or longer) before being quenched via vacuum filtration.

Upon neutralization, filtrate liquors were analyzed for total sugars (via 4% sulfuric acid hydrolysis), acetate (via sulfuric acidification) and soluble lignin (via dilution in water) by high-performance liquid chromatography (HPLC) following standard NREL Laboratory Analytical Protocols (Sluiter et al., 2008a; Sluiter et al., 2008b).

Computational Modeling

2D axisymmetric corn stover models were constructed and tetrahedrally meshed directly in COMSOL Multiphysics 5.6 for finite-element computational fluid dynamics (CFD) simulations. Kinetic rate coefficients were regressed to experimental batch reactor data via the COMSOL–MATLAB R2021a API using an iterative generalized least-squares estimation procedure. Initial guesses for coefficients were randomly perturbed by ±20% via an exterior function, and parameters were iteratively re-fit to prevent convergence of the algorithm onto local minima. Classical molecular dynamics (MD) simulations were conducted using CHARMM program (MacKerell et al., 1998; Hynninen and Crowley, 2014) along with SHAKE and PME algorithms (Darden et al., 1993; Kräutler et al., 2001) to estimate diffusion coefficients (see **Supplementary Equation S1**) in NaOH solution (Jorgensen et al., 1983) at 4–90°C for solutes xylan (Guvench et al., 2008; Hatcher et al., 2009) [degree of polymerization (DP) 1–5, 10], lignin (Orella et al., 2019; Vermaas et al., 2019) [DP 1–5, 10; see **Supplementary Table S2** for decamer linkage details (Min et al., 2014)], and acetate (Vanommeslaeghe et al., 2010) and hydroxide anions.

RESULTS AND DISCUSSION

Deacetylation Activity Benchmarking and Experimental Design

The first objective of this study is to determine suitable laboratory reaction conditions amenable to analytical measurements of individual corn stover components (i.e., acetate, xylan and lignin) within differential kinetic (i.e., <15 wt% extraction) regimes. Notably, the intended goal is not to maximize yield, but rather to identify reaction conditions that elucidate important kinetic and mass transport information. Key handles for such laboratory experiments include reactor volume, temperature, corn stover loading, NaOH concentration and agitation. A highly characterized NREL Kramer corn stover (KR) sample was selected for initial activity screening and selection of reaction conditions given its similarity in composition to whole (WH) corn stover received from INL and its anatomical fractions (CB, HS, SK) (**Supplementary Table S3**). As a preliminary trial set, KR deacetylation was examined at 10 wt % solids loading in 5–9 g L^{-1} NaOH in 5 mL total reaction volume at 85–95°C for durations of up to 120 min (Chen et al., 2012; Tao et al., 2012; Chen et al., 2016; Katahira et al., 2016), with subsequent HPLC analysis conducted on soluble acetate, xylan and lignin products in the resultant vacuum-filtered liquor phase (Sluiter et al., 2008a); we note that structural glucan is not extractable for any corn stover feedstock under any condition reported here. Further, lignin extracted during the course of deacetylation is likely to be non-structural in nature, or possibly bound through lignin–carbohydrate complex ester linkages (akin to the ester cleavages required to remove acetate). However, alternate mechanisms such as de-etherification or de-esterification of structural lignin polymers are known to require significantly higher reaction temperatures (e.g., 270–300°C) than those studied here (Katahira et al., 2016). Results are summarized in **Supplementary Figure S1**. While NaOH concentration is monotonically related to overall component yield, each yield profile illustrates minimal time or temperature dependence,

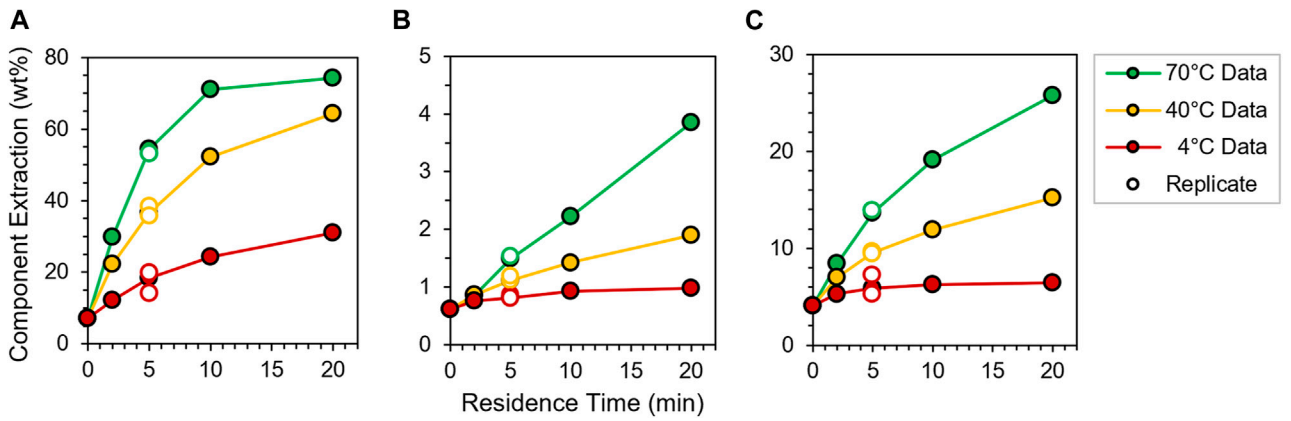

FIGURE 1 | Time-course deacetylation profiles for **(A)** acetate, **(B)** xylan and **(C)** lignin extraction from WH corn stover at 4, 40 and 70°C and 5 g L^{-1} NaOH concentration. Component extraction (wt%) determined from analyte yield of filtered liquor relative to fresh biomass composition (**Supplementary Table S3**). Connecting lines included for visual clarity.

suggesting that deacetylation chemistries occur too rapidly at such conditions to allow for insightful kinetic measurements.

Hence, to slow observable reaction rates, KR was next screened at 4 and 20°C for 5–9 g L^{-1} NaOH loadings with and without periodic vial vortexing (**Supplementary Figure S2**) to assess the impact of agitation on time-course yields for reaction times up to 30 min. Overall, yields of each acetate, xylan and lignin plateau around 20 min, with similar extents of extraction observed for 5 and 7 g L^{-1} conditions and higher final yields for 9 g L^{-1}. Importantly, minimal differences are observed between vortexed and unagitated data sets (**Supplementary Figure S2**), implying that external (film) mass transfer at the exterior corn stover surface does not impact liquid-phase yield measurements at this reactor scale. This finding allows for important simplifications to particle-scale reaction–diffusion models developed and validated later in this study (*vide infra*).

From the initial KR trials, a final set of reaction conditions is selected for the primary study of WH corn stover deacetylation and that of its anatomical fractions, CB, HS and SK: each fraction is Wiley milled to <2 mm and evaluated at 500 mg loadings in 5 mL total reaction volume, without agitation, at initial NaOH concentrations (C_{NaOH}) of 5 and 7 g L^{-1}. Batch deacetylation is conducted at temperatures of 4, 40 and 70°C for batch reaction times of 0, 2, 5, 10, 20 and 60 min, after which the liquid phases are vacuum-filtered to quench the reaction. Initial feedstock compositions are determined using standard biomass compositional analysis protocols developed by NREL (Sluiter et al., 2005; Sluiter et al., 2008b), and maximum extractable components are gleaned from 60-min residence time experiments at each C_{NaOH} (**Supplementary Table S3**). Finally, anatomical fraction sorting data summarized in **Supplementary Table S4** reveals the overall breakdown on a mass basis of the WH bulk feedstock as received.

Apparent Trends in Deacetylation Kinetics

Batch deacetylation was first evaluated for the WH feedstock at 4–70°C and 5–7 g L^{-1} NaOH for residence times of 0–20 min. Individual component yields of acetate, xylan and lignin in the liquid phase are traced as a function of residence time and C_{NaOH} for a suite of reactions conducted at the 5-mL scale, and data are summarized in **Figure 1** and **Supplementary Figure S3**. Additionally, given the rapid nature of deacetylation chemistries, apparent time-zero yields (i.e., upon instantaneous fluid–solid contact) are quantified for each C_{NaOH} and feedstock (**Supplementary Table S5**) to establish reactor "start-up" behavior, which practically manifests as the *y*-axis intercept on time-course yield plots (**Figure 1, Supplementary Figure S3**). These time-zero yields are also important for defining proper initial conditions for reaction–diffusion models developed later in this study (*vide infra*).

Several readily observable kinetic trends arise. First, as expected, relative rates of component extraction rise with increasing C_{NaOH}, consistent with its role as a stoichiometric reagent for deacetylation. Second, xylan extraction proceeds at controllably slow rates across all conditions, while immobilized lignin converts to soluble products at sufficiently slow rates only at the two lower temperatures. In contrast, acetate production proceeds rapidly at all temperatures, but rates observed at the 4°C condition are manageably slow for the kinetic regression and modeling purposes of this study. To this end, kinetic fitting generally requires at least a subset of data to be collected under differential conditions, wherein total extents of component extraction (i.e., conversion) are kept at or below ~15 wt%; conditions here were deliberately selected from screening experiments described in the previous section to enable differential kinetic measurements and subsequent model regression for acetate, xylan and lignin components (*vide infra*). Third, time-course component yields across all conditions are highly reproducible (±14% maximum relative error), as shown by the close agreement among open and closed circles plotted in **Figure 1** and **Supplementary Figure S3**.

Next, CB, HS and SK were assessed at the same conditions as WH, and results are illustrated in **Supplementary Figures S4–S6**.

TABLE 1 | Summary of mean particle size and porosity attributes.

Corn stover fraction	L_{Feret}[a] (μm)	W_{Feret}[a] or t_{Feret}[a] (μm)	Aspect ratio[b]	ε_P[c]	τ[c]
WH	1101 ± 161[d]	433 ± 206[d]	2.54	--	--
CB	1239 ± 141	689 ± 225	1.80	0.129	10.3
HS	1181 ± 172[d]	413 ± 204[d]	2.86	0.640	1.12
SK	917 ± 184	355 ± 172	2.58	0.671	1.36

[a]*Mean Feret length (L_{Feret}, longer dimension) or Feret width or thickness (W_{Feret} or t_{Feret}, shorter dimension) computed from 2D particle size distribution statistics. Latter values denote a single standard deviation from the mean. See* ***Supplementary Figures S8, S9****.*

[b]*Dimensionless ratio of mean L_{Feret} to mean W_{Feret} or t_{Feret}. See* ***Supplementary Figure S9****.*

[c]*Internal void fraction ε_P and tortuosity τ directly calculated from XCT reconstructions via MATBOX tool (Cooper et al., 2016; Usseglio-Viretta et al., 2022). See* ***Supplementary Table S1*** *and SM methods description.*

[d]*Volume-weighted average derived from two largest volumetric bins. See* ***Supplementary Figures S8A,C****.*

Intriguingly, acetate extraction profiles observed for WH closely match that of SK (24 wt% of WH, **Supplementary Table S4**), suggesting this anatomical fraction's deacetylation behavior is highly representative of the parent unsorted material. In contrast, HS (18 wt% of WH, **Supplementary Table S4**) exhibits slightly enhanced acetate removal profiles relative to the other fractions, while CB (8 wt% of WH, **Supplementary Table S4**) yield profiles for all components and conditions appear to lag across the entire feedstock series. Lastly, replicates performed for 5- and 20-min residence times once again illustrate high reproducibility of kinetic measurements taken at this millireactor scale.

Taken together, these data indicate that each aggregate feedstock and anatomically-specific kinetic parameters may be confidently determined using reaction–diffusion models and parameter regression methods. However, the experimental results also reveal several non-obvious complexities underlying batch deacetylation pretreatment:

1) Broad differences are observed in component extraction rates, temperature dependencies and feedstock anatomy, requiring a wide range of experimental conditions to access differential kinetic regimes (**Figure 1, Supplementary Figures S3–S6**).
2) Particle size effects are known to influence apparent yield for condensed-phase biomass pretreatment (Thornburg et al., 2020) and hence must also be quantified (*vide infra*).
3) Reactor heating (40°C, 70°C) and cooling (4°C) timescales are on the order of reaction–diffusion phenomena (**Supplementary Figure S7**, **Supplementary Equations S2, S3**), meaning observable kinetic measurements are non-isothermal—thus complicating the interpretation of temperature dependencies.

Therefore, conclusions may not be drawn simply from the suite of experimental data presented in this section. Particle-scale modeling emerges as a critical tool to account for the non-isothermality and transport phenomena that accompany experimental biomass extraction measurements, and reaction–diffusion models developed here enable the decoupling of these physics to determine the underlying chemical kinetic information.

Corn Stover Particle Model Construction

Milled biomass contains a heterogeneous mixture of different particle sizes and aspect ratios, which in turn plays an important role in the physical behavior of such particles when immersed in chemically reactive fluid environments. To understand these behaviors, we first examined statistically meaningful distributions of corn stover particle sizes and aspect ratios obtained from tens of thousands of individual 2D particle measurements via a commercial particle size analysis service. Data and statistics were analyzed using MATLAB R2021a. Mean values of Feret lengths, widths/thicknesses and aspect ratios resulting from volume-binning of each corn stover sample output are summarized in **Table 1**, while histograms and aspect ratio trends are illustrated in **Supplementary Figures S8, S9**, respectively.

Three conclusions are made from these analyses. First, WH and SK exhibit nearly identical aspect ratios, highlighting physical similarities between these samples that complement their closely related acetate extraction profiles (**Figure 1**, **Supplementary Figures S3–S6**). Second, CB once again emerges as an outlier among the set of feedstocks, further emphasizing the unique characteristics of this fraction. And third, the relatively small (11–20%) standard deviations observed per sample volume bin imply that the geometric descriptors reported in **Table 1** are representative of a majority of each sample volume, and hence should adequately describe the typical length scales associated with their particle-scale physics.

Separately, we assessed the internal microstructures of each anatomical fraction using X-ray computed tomography. Cross-sectional images extracted from the 3D control volumes are shown in **Figure 2** after contrast correction. The slice through the SK reconstruction (**Figure 2A**) reveals that both vascular bundles, comprised of thick, heavily lignified cell walls, and pith, which consists of thinner walls with lower lignin content, are present in the sample. The slice through the HS reconstruction (**Figure 2B**) reveals mostly leaf tissue, although some xylem and phloem domains are also observed. However, the microstructure revealed by the CB reconstruction (**Figure 2C**) is notably different than the other tissue types, exhibiting densely-packed cells that generally lack the elongated shape and regularly arrayed configuration characteristic to the vascular and leaf tissues. Post-processed 3D radiographs collected for each CB, HS and SK were analyzed using MATBOX, a custom image processing toolbox that enables direct calculation of particle-scale porosity features (Cooper et al., 2016; Usseglio-Viretta et al., 2020; Usseglio-Viretta et al., 2022). Specifically, we compute void fraction ε_P and tortuosity τ for each anatomical fraction, and calculated values are reported in **Table 1**. Values must be considered with caution, however, as segmentation was performed without prior knowledge of the true volume fractions (i.e., blind segmentation) and with limited XCT image resolution (see SM methods and **Supplementary Table S1** for details); however, the selected fields of view capture spatially distributed patterns that appear periodically throughout the whole microstructure by

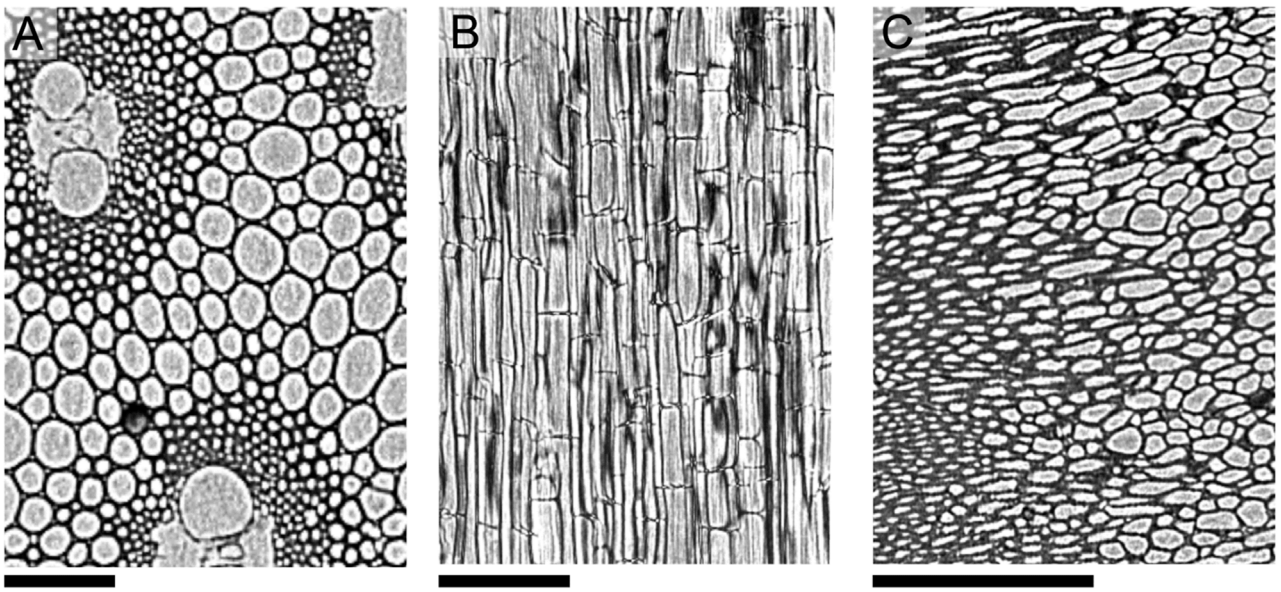

FIGURE 2 | Select 2D slices through X-ray computed tomographic reconstructions taken after contrast correction of **(A)** SK, **(B)** HS and **(C)** CB corn stover tissues. All scale bars are 200 μm.

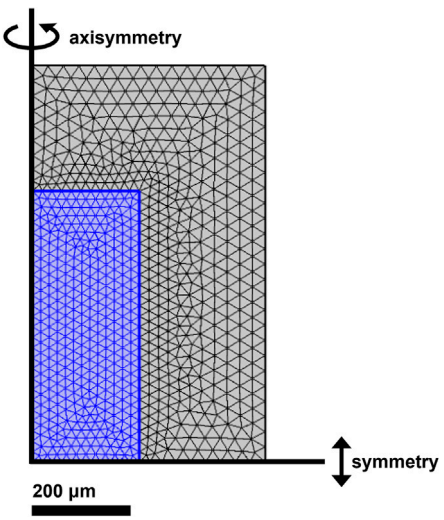

FIGURE 3 | 2D axisymmetric meshed model geometry for WH particle (blue) and aqueous solution (grey) domains constructed in COMSOL Multiphysics 5.6. Inset text indicates scale bar and (axi)symmetry boundary conditions; no-flux boundary conditions are imposed at the unmarked grey solution domain edges.

visual inspection, providing some confidence in the calculated results. Accordingly, the pore descriptors of HS and SK share clear similarities. Void fractions of ~0.65 have been assumed in other lignocellulosic biomass types (Thornburg et al., 2020), and τ values close to unity indicate straight pore channels easily traversed by diffusing solutes. However, CB is yet again remarkably distinct from the other anatomical fractions, and its low ε_P of 0.129 and extremely high τ of 10.3 suggest severe mass transport limitations through this tissue anatomy (**Figure 2C**). Finally, given the strong similarity between WH and SK, the calculated ε_P of 0.671 and τ of 1.36 for SK are also assumed for WH particle models.

Armed with external and internal physical descriptors, we then construct model geometries for finite-element simulations. 2D axisymmetric models are selected here based on their advantages of mathematical simplicity and known agreement with more computationally intensive 3D microstructural models, as validated in prior biomass conversion modeling studies performed by some of us (Ciesielski et al., 2015; Pecha et al., 2018; Thornburg et al., 2020). Characteristic particle Feret lengths and widths/thicknesses (i.e., averaged to radii) are gleaned from **Table 1**; axisymmetry is enforced along the tall axis of the particle with a separate symmetry boundary condition along its short axis. Next, porosity metrics from **Table 1** describe the porous portion of the particle domain. In addition, a 100-fold diffusion penalty is imposed in the radial direction to account for anisotropic biases of longitudinal diffusion, similar to other well-characterized feedstocks (Comstock, 1970). Specifically, 2D porous geometries are assumed to have uniformly distributed pores, and thus spatially uniform porosity along a given diffusion coordinate, as per Darcy's law. Initial chemical compositions of extractable acetate, extractable xylan, extractable lignin and the balance of unextractable components are imported from compositional data in **Supplementary Table S3**. Furthermore, the particle domain is enveloped by an equidistantly spaced aqueous fluid domain that is prescribed the identical initial C_{NaOH} and solid:fluid volumetric ratios (0.169) as in batch deacetylation experiments, and a no-flux boundary condition at the exterior edges. As a final step, the final dual-domain geometries undergo finite-element meshing to prepare them for CFD simulation

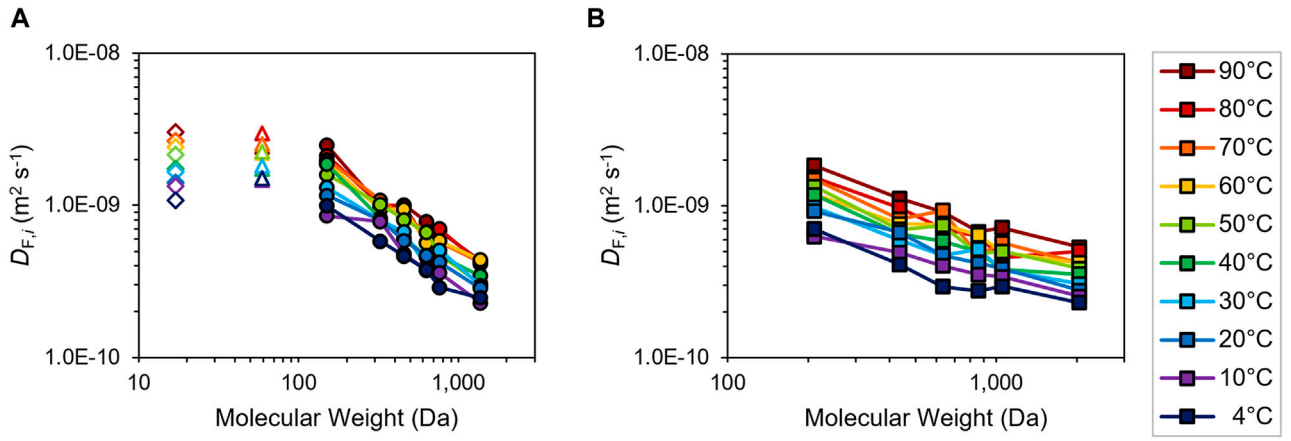

FIGURE 4 | Logarithmic plots of fluid diffusion coefficients $D_{F,i}$ from MD calculations vs. solute molecular weight of **(A)** hydroxide anion (open diamonds), acetate anion (open triangles) and xylan oligomers (filled circles; DP 1–5, 10) and of **(B)** lignin oligomers (filled squares; DP 1–5, 10) in 5 g L^{-1} NaOH at temperatures of 4–90°C (inset color legend). Connecting lines drawn for visual clarity.

in COMSOL Multiphysics 5.6. An example of the meshed 2D WH particle is illustrated in **Figure 3**.

Reaction–Diffusion Model Development

A primary objective of this study is to determine non-isothermal, transport-independent kinetic rate parameters for the reactive extraction of acetate, xylan and lignin from three major corn stover anatomical fractions (CB, HS, SK). Geometries and pore structure descriptors are now incorporated into 2D axisymmetric reaction–diffusion models to describe the chemistry and physics of mesoscale deacetylation processes. Mass transfer is described by various physical equations and assumptions described below, while the system's heat transfer is handled explicitly by global, time-dependent temperature profiles characteristic of experimental reactor temperatures (**Supplementary Figure S7**, **Supplementary Equations S2, S3**). Treatment of temperature as a time-dependent function allows temperature-dependent rate constants and diffusion coefficients each to be implicit functions of residence time, further reducing complexity in the subsequent finite-element calculations.

First, the effective diffusivity $D_{\mathrm{eff},i}$ of species i is defined by **Eq. 1**, where $D_{\mathrm{F},i}$ is the fluid diffusion coefficient and i refers to reactant species acetate (act), xylan (xyl), lignin (lig) or hydroxide (OH^-). Void fraction ε_P and tortuosity τ vary by anatomical fraction (**Table 1**) and are assumed to be constant throughout the reactive extraction process, whereas $D_{\mathrm{F},i}$ is specific to each solute's molecular diffusivity in aqueous alkaline solutions.

$$D_{\mathrm{eff},i} = \frac{\varepsilon_P}{\tau} D_{\mathrm{F},i} \tag{1}$$

Fluid diffusion coefficients $D_{\mathrm{F},i}$ are estimated via classical MD simulations of the various solute species diffusing in 0.125 M (i.e., 5 g L^{-1}) and 0.175 M (i.e., 7 g L^{-1}) NaOH solutions for quasi-equilibrated system temperatures of 4–90°C. Acetate (Vanommeslaeghe et al., 2010) diffusion and hydroxide self-diffusion are readily calculated using straightforward anion assemblies (Jorgensen et al., 1983), while xylan and lignin oligomer structures (DP 1–5, 10) are constructed using internal coordinates of the appropriate xylose (Guvench et al., 2008; Hatcher et al., 2009) or lignin monomers and linkages (Min et al., 2014), with the latter assigned via the Lignin–KMC tool (Orella et al., 2019; Vermaas et al., 2019) (**Supplementary Table S2**). Estimates of $D_{\mathrm{F},i}$ at the two C_{NaOH} are illustrated in **Figure 4** and **Supplementary Figure S10**. Diffusion coefficients generally decrease with increasing solute MW and increase with increasing temperature, albeit varying within the same orders of magnitude. Temperature-dependent exponential functions are then determined from log-linear plots of $\ln(D_{\mathrm{F},i})$ vs. $1/T$ (K^{-1}) (**Supplementary Figures S11, S12**) for incorporation into **Eq. 1** and subsequent model physics. Similar to the authors' prior study on lignin solvolysis (Thornburg et al., 2020), base-case models assume trimeric structures (DP 3) of each xylan and lignin as intermediate-MW reactive solutes. Sensitivity analyses are assessed following kinetic parameter determination in the next section to validate these speciation assignments (*vide infra*).

Second, simultaneous diffusion (**Eq. 1**) and chemical reaction (R_i) are described by mass continuity equations in porous media and in free solution. As noted above, Darcy's law and Fick's second law (**Eq. 2**) describe the reaction and diffusion of species i at local concentration C_i within uniformly distributed pores of the 2D particle domain (**Figure 3**, blue portion). Complementarily, mass continuity (**Eq. 3**) captures the equivalent competing phenomena occurring in aqueous solution (**Figure 3**, grey portion). The authors note the explicit residence time and implicit temperature dependencies of each expression's reaction and diffusion terms, which are handled by finite-element calculations of material fluxes for each mesh element illustrated in **Figure 3**.

$$\frac{\partial(\varepsilon_P C_i)}{\partial t} + \nabla \cdot \left(- D_{\mathrm{eff},i} \nabla C_i \right) = R_i \tag{2}$$

TABLE 2 | Best-fit deacetylation kinetic rate constants (mean values and standard deviations) across ten independent regression rounds[a] using individual particle models and data[b] evaluated at 4–70°C and 5 g L^{-1} NaOH.

Fraction	Parameter[a]	Best-fit values for component *i*		
		Acetate (act)	Xylan (xyl)	Lignin (lig)
WH	$k_{0,i}$ (m^3 mol^{-1} s^{-1})	$7.58 \times 10^1 \pm 1.16 \times 10^1$	$4.97 \times 10^2 \pm 6.54 \times 10^1$	$9.92 \times 10^0 \pm 1.16 \times 10^0$
	$E_{a,i}$ (kJ mol^{-1})	38.2 ± 0.39	49.8 ± 7.29	36.3 ± 0.28
CB[c]	$k_{0,i}$ (m^3 mol^{-1} s^{-1})	$>7.74 \times 10^1 \pm 9.99 \times 10^0$	$>>5.74 \times 10^2 \pm 1.54 \times 10^2$	$>1.04 \times 10^1 \pm 2.27 \times 10^0$
	$E_{a,i}$ (kJ mol^{-1})	<31.9 ± 0.34	<<59.5 ± 7.44	<32.3 ± 0.62
HS	$k_{0,i}$ (m^3 mol^{-1} s^{-1})	$8.45 \times 10^1 \pm 1.49 \times 10^1$	$4.96 \times 10^2 \pm 7.68 \times 10^1$	$9.78 \times 10^0 \pm 1.53 \times 10^0$
	$E_{a,i}$ (kJ mol^{-1})	38.5 ± 0.45	48.2 ± 1.64	36.2 ± 0.44
SK	$k_{0,i}$ (m^3 mol^{-1} s^{-1})	$8.12 \times 10^1 \pm 1.13 \times 10^1$	$4.96 \times 10^2 \pm 9.11 \times 10^1$	$1.07 \times 10^1 \pm 1.12 \times 10^0$
	$E_{a,i}$ (kJ mol^{-1})	39.2 ± 0.35	49.2 ± 6.30	35.5 ± 0.30

[a]*Initial guess values were perturbed by ten unique random number matrices, and parameters were independently regressed to experimental data for each perturbed guess matrix to generate ten distinct rate constant fits. Best-fit values reported here denote the arithmetic mean and standard deviation of outputs resulting from the ten rounds. See* ***Eqs 4***, ***5*** *and discussion of parameter regression techniques in SM.*

[b]*Time-course acetate, xylan and lignin yield data collected for each feedstock at 4, 40 and 70°C and 5 g L^{-1} NaOH, for 0, 2, 5, 10 and 20 min residence times. See* ***Figure 1*** *and* ***Supplementary Figures S4–S6****.*

[c]*Rate constants generated for cob fraction do not adequately represent experimental data (****Supplementary Figures S4–S6, S16****) and are thus reported as lower ($k_{0,i}$) or upper ($E_{a,i}$) boundary values. See* ***Supplementary Figure S16*** *and discussion in main text.*

$$\frac{\partial C_i}{\partial t} + \nabla \cdot \left(- D_{\mathrm{F},i} \nabla C_i \right) = R_i \tag{3}$$

Finally, reaction rate expressions are defined in **Eq. 4** for the sodium hydroxide-mediated extraction of corn stover. Note that **Eq. 4** describes rates of consumption of each biomass-derived species *i* in the particle domain P, thus assigning a negative sign convention ($-R_i$, mol m^{-3} s^{-1}) along with reactant concentrations specific to the solid corn stover phase ($C_{i,\mathrm{P}}$). Pseudo-second order rate laws are prescribed following the assumption of pseudo-first order behavior in each reactant. Arrhenius-type rate constants k_i (m^3 mol^{-1} s^{-1}; **Eq. 5**) describe the temperature dependence of these parameters, where $k_{0,i}$ (m^3 mol^{-1} s^{-1}) is the pre-exponential factor, $E_{a,i}$ (kJ mol^{-1}) is the activation barrier, R is the universal gas constant and T is the absolute reaction temperature (K; **Supplementary Equations S2, S3**).

$$-R_i = k_i C_{i,\mathrm{P}} C_{\mathrm{NaOH}}, \text{where} \tag{4}$$

$$k_i = k_{0,i} e^{-E_{a,i}/RT} \tag{5}$$

Each species' maximum extent of extraction (i.e., conversion) is a function of feedstock identity and C_{NaOH}, and experimentally determined values reported in **Supplementary Table S3** are used to normalize the individual component extraction profiles calculated from $-R_i$. The authors note that alternate rate expressions (e.g., reversible rate laws, non-integer reaction orders) were assessed early into our study, but none except **Eq. 4** provided adequate representation of time-course extraction data (**Figure 1**, **Supplementary Figures S4–S6**). Although other rate expressions may be possible, the assigned rate form of **Eq. 4** is phenomenologically relevant to deacetylation processes and is appropriately selected here.

Kinetic Rate Constant Determination

Upon defining model geometry (**Table 1**; **Figure 3**), physics (**Eqs 1–3**, **Supplementary Equations S2, S3**; **Figure 4**) and chemistry (**Eqs. 4–5**) of deacetylation, kinetic rate constants in **Eqs 4**, **5** may be regressed to experimental data illustrated in **Figure 1** and **Supplementary Figures S4–S6** using a COMSOL–MATLAB R2021a API. Specifically, pre-exponential factors $k_{0,i}$ and activation barriers $E_{a,i}$ of **Eq. 5** were systematically fitted to time-course acetate, xylan and lignin extraction data measured at the 5 g L^{-1} NaOH condition as a basis for parameter regression. In a typical fitting routine, an outer MATLAB function randomly perturbs a set of initial parameter guesses by ±20% of the base value before feeding the values to an inner fitting function. The inner function supplies the perturbed guesses as rate parameter inputs to the specified 2D COMSOL model (WH, CB, HS or SK), which calculates and returns to MATLAB the individual component extraction extents at simulated residence times of 0, 2, 5, 10 and 20 min. Model outputs are compared to experimental values for each species, and an iterative generalized least-squares regression routine modifies the rate parameters to minimize the residual objective function until an exit criterion is satisfied. The entire procedure is repeated an additional 9 times with uniquely perturbed initial parameters fed each round to assess the sensitivity of initial guesses (Thornburg et al., 2020). About 110–140 iterations were required to obtain satisfactory fits in a given round; full details are described in SM.

The resultant best-fit parameters averaged across ten independent fitting rounds are reported in **Table 2**. Several key observations are made across the parameter collection. First, WH, HS and SK yield statistically identical pre-exponential factors and activation barriers for all three reactants, further reinforcing the performance similarities of these three fractions; this observation is also consistent with HS and SK anatomies comprising the majority of WH on a weight basis (**Supplementary Table S4**). Second, while pre-exponential factors remain consistent for CB, this fraction's activation barriers are notably lower for acetate and lignin while considerably higher for xylan. These differences may be attributed to the expectedly different types of lignin and hemicellulose—and thereby to the emergent differences in the cell wall nanoscale architecture—present in this portion of plant tissue (thus bearing different reactivities), and/or as a

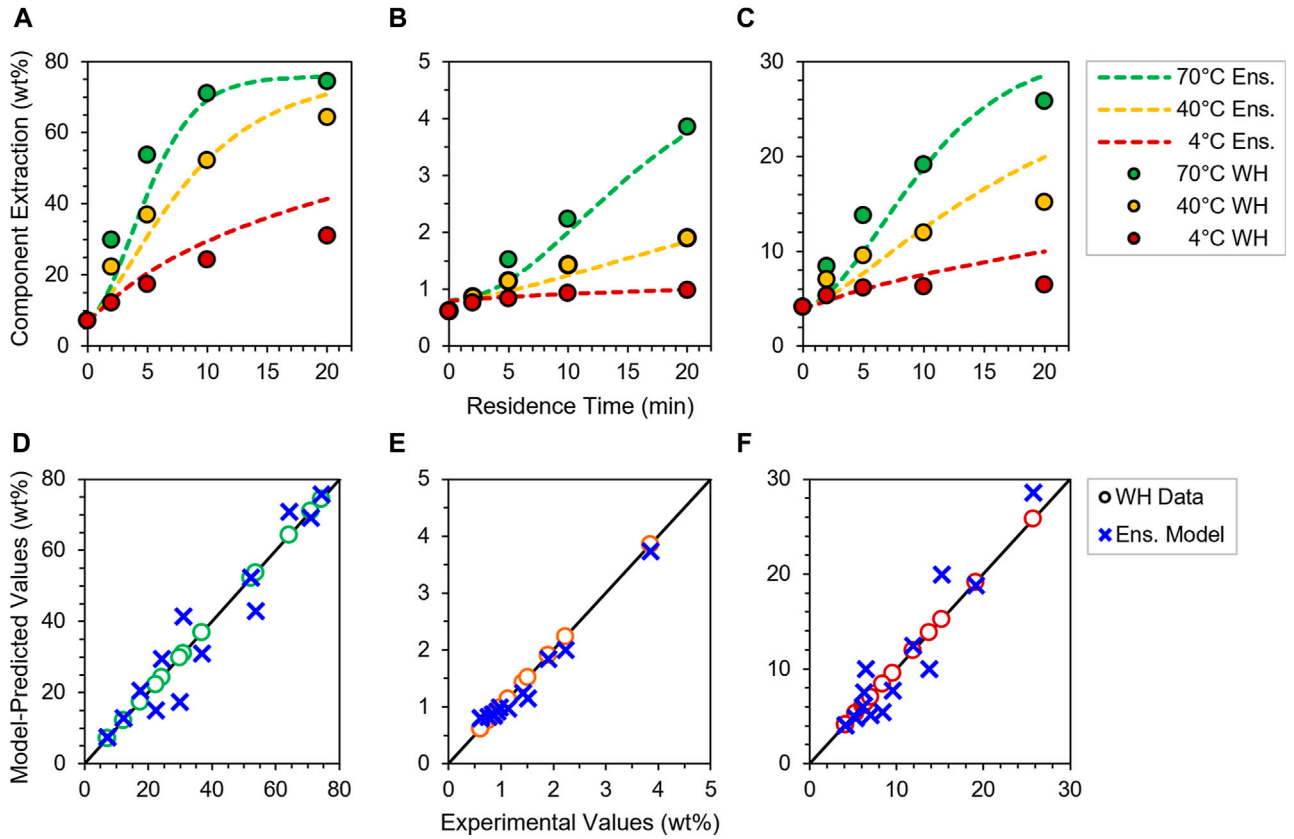

FIGURE 5 | Ensemble model predictions (dashed lines) at 4–70°C and 5 g L^{-1} NaOH of **(A)** acetate, **(B)** xylan and **(C)** lignin extraction profiles compared to experimental data collected for WH at the same deacetylation conditions (filled circles), and parity plots of **(D)** acetate, **(E)** xylan and **(F)** lignin model values (blue crosses), with individual species data from WH experiments (open circles) at all three temperatures plotted along a 45° parity line (black) for visual reference. See **Figure 1** and **Supplementary Table S4**.

compensating consequence of the relatively severe mass transport limitations inherent to CB (**Table 1**; **Figure 2C**); nonetheless, we qualify **Table 2** values for CB as approximate upper or lower boundaries rather than definitive coefficients. Third, among the three species studied, acetate and lignin share similar activation barriers across different tissue types, whereas $k_{0,act}$ values are nearly an order of magnitude larger than $k_{0,lig}$ in all cases. These results suggest that while the two species may share similar temperature dependencies, lignin extraction may suffer pronounced entropic penalties (e.g., strong surface adsorption of extracted products, inferior hydrogen bonding, unfavorable local solvation) that may ultimately belie the major differences in each reactant's apparent extraction kinetics. Such kinetic considerations are worthy of further investigation and may help inform on suitable lignin extraction technique(s) for a given biorefinery strategy (Schutyser et al., 2018). Fourth, WH, HS and SK all feature standard deviations of <18% for each parameter, suggesting reasonably low initial guess sensitivity during fitting; CB fits are demonstrably worse (i.e., parameter standard deviations <27%), which may be a mathematical consequence of the severely counteractive transport resistances discussed later (*vide infra*). Lastly, the authors note that each reactive species' rate coefficients are valid only when taken as a duet (i.e., $k_{0,i}$ and $E_{a,i}$) and that other, mathematically equivalent local solution pairs likely exist.

Next, mean rate constants from **Table 2** are incorporated directly into 2D reaction–diffusion models of each particle type to inspect the goodness of fit. **Supplementary Figure S13** illustrates the resulting best-fit WH simulated extraction profiles and individual component parity plots at the three deacetylation temperatures, highlighting reasonably good fits for all three species. In general, simulated lignin and acetate profiles are slightly overpredictive at longer residence times, while the xylan model trace slightly underpredicts this component's experimental trends. Similar patterns of strong model agreement are observed for HS (**Supplementary Figure S14**) and SK (**Supplementary Figure S15**). However, CB yet again emerges as an outlier feedstock fraction (**Supplementary Figure S16**). While reasonable fits are observed for lignin at 4 and 40°C, the best-fit curve for this species at 70°C falls significantly short, with concomitantly worse agreement among acetate and xylan data sets. Acetate and xylan traces effectively collapse to single profiles at all three temperatures, albeit for distinct reasons. Given the rapid kinetics anticipated by

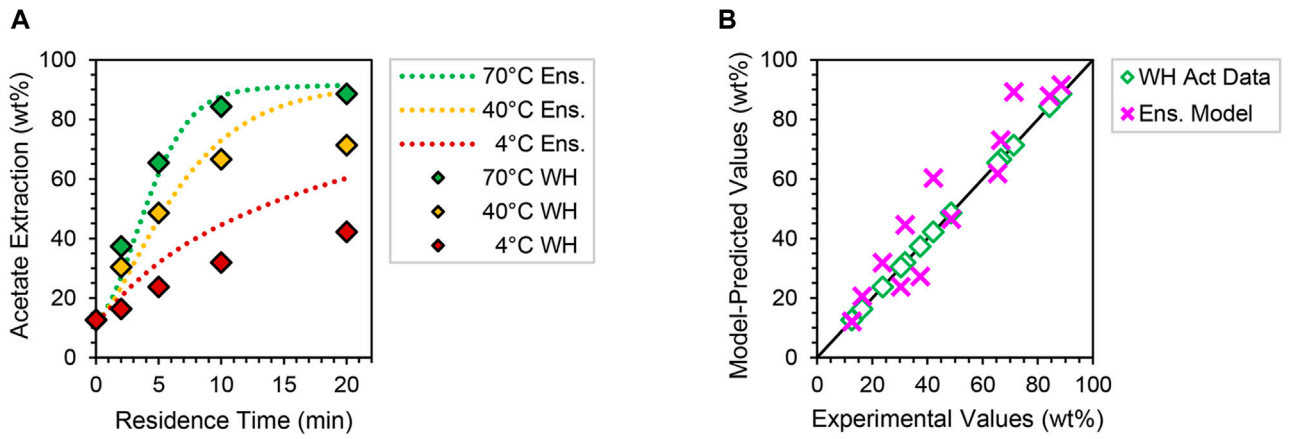

FIGURE 6 | (A) Ensemble model predictions (dotted lines) at 4–70°C and 7 g L^{-1} NaOH of acetate extraction in comparison to WH data collected at the same deacetylation conditions (filled diamonds). **(B)** Parity plot of the 7 g L^{-1} NaOH acetate extraction model predictions (pink crosses) compared to WH acetate extraction data (open diamonds) at all three temperatures plotted along a 45° parity line (black) for visual reference. See **Supplementary Figure S20** for analogous xylan and lignin trends.

Table 2 parameters, supposedly fast rates of acetate extraction are likely to be severely outcompeted by mass transfer resistance, mathematically dampening any practical influence of reaction temperature on the simulated response. Conversely, CB xylan rate parameters predict considerably slower kinetics than other feedstocks, and the presence of strongly limiting transport effects leads to zero-rate model responses and thus considerable error in this component's best fits (**Table 2**). The quantitative consequences of mass transfer resistance on apparent extraction kinetics are discussed at length in the final Results and Discussion subsection of this study (*vide infra*).

As a final validation exercise, myriad sensitivity analyses were carried out to evaluate the influence of various mass transport parameters, none of which appear to be highly sensitive to the resultant WH model outputs. Results are summarized in **Supplementary Figures S17–S19** and further confirm the validity of transport assumptions incorporated into base-case reaction–diffusion models.

Anatomical Ensemble Calculations and Model Predictions

Upon fitting kinetic rate coefficients, we now seek to test the validity of our four individual particle models as aggregate ensembles and also under deacetylation conditions beyond the original regression data set. First, we create a simulated ensemble of the collective feedstock by weighting the responses of anatomical particle models by their mass fractions within the bulk corn stover feedstock (**Supplementary Table S4**); here, the balance of feedstock that is not cobs, husks or stalks is deemed to be "whole" material, and hence is used to weight the extraction response of the WH model. **Figure 5** shows the aggregate ensemble model responses and experimental data comparison for acetate, xylan and lignin at 4–70°C and 5 g L^{-1} NaOH. Excellent fits are seen for all species and conditions, as illustrated by each species' parity plot in **Figures 5D–F** with no greater than 13% variance from any experimental batch reactor measurement. Thus, calculations of corn stover ensemble responses demonstrate the robustness and versatility of 2D axisymmetric models in capturing experimental deacetylation trends.

Next, models are extended beyond their original reaction condition to assess their predictive capability under different circumstances. While 5 g L^{-1} NaOH data are used for kinetic rate parameter fitting, the 7 g L^{-1} NaOH data sets of **Supplementary Figures S3–S6** are now utilized to evaluate the four particle models' predictivities. Select input parameters in WH, CB, HS and SK models are now adjusted for the 7 g L^{-1} NaOH condition, including initial C_{NaOH} in the aqueous domain (**Figure 3**), apparent time-zero yields (**Supplementary Table S5**), mass fractions of extractable material (**Supplementary Table S3**), maximum extents of component extraction (**Supplementary Table S3**), diffusion coefficients (**Supplementary Figure S10**) and their temperature profiles (**Supplementary Figure S12**).

Figure 6 shows the predicted 7 g L^{-1} acetate extraction profiles and corresponding parity plot for an anatomically weighted corn stover particle ensemble (**Supplementary Table S4**); analogous xylan and lignin model responses are included in **Supplementary Figure S20**. Importantly, model simulations at this deacetylation condition have not been regressed to experimental data, and time-course responses thus may be considered as blind predictions for validation purposes. Despite slight overprediction at late residence times, good agreement is observed for acetate and xylan extraction kinetics at this higher C_{NaOH} condition, with no greater than 21% variance from experiment—further implying high fidelity of these two component models under extrapolative deacetylation conditions. However, lignin profiles are significantly overpredictive in this case (**Supplementary Figure S20B**). This may be attributable to realistic lignin solubility limitations at higher alkalinity that are

TABLE 3 | Thiele moduli and effectiveness factors for WH calculated at 4–70°C and 5 g L^{-1} NaOH.

Species	T (°C)	φ_i[a]	η_i[a,b]	Regime[a]
Acetate	4	0.58	0.90	Intermediate
	40	1.2	0.70	Intermediate
	70	1.9	0.50	Intermediate
Xylan	4	0.13	0.99	Kinetically limited
	40	0.36	0.96	Kinetically limited
	70	0.70	0.86	Intermediate
Lignin	4	0.26	0.98	Kinetically limited
	40	0.50	0.92	Intermediate
	70	0.78	0.84	Intermediate

[a]*See* ***Eq. 6*** *for definition and surrounding discussion.*
[b]*See* ***Eq. 7*** *for definition and surrounding discussion.*

TABLE 4 | Computed values of Thiele moduli and effectiveness factors for CB, HS and SK component extraction performed at 4 and 70°C and at 5 g L^{-1} NaOH.

Species	T (°C)	CB[a]		HS		SK	
		φ_i[b]	η_i[b,c]	φ_i[b]	η_i[b,c]	φ_i[b]	η_i[b,c]
Acetate	4	>19	<0.054	0.62	0.89	0.42	0.95
	70	>47	<0.021	2.1	0.47	1.4	0.62
Xylan	4	>0.15	<0.99	0.19	0.99	0.12	1.0
	70	>1.2	<0.70	0.97	0.77	0.60	0.89
Lignin	4	>4.7	<0.21	0.25	0.98	0.28	0.98
	70	>12	<0.084	0.76	0.84	0.81	0.83

[a]*Cob parameters listed in* ***Table 3*** *represent lower boundaries of k_i, and thus lower boundaries of φ_i and upper boundaries of η_i. See* ***Eq. 5***, ***Supplementary Figure S16*** *and discussion in main text.*
[b]*See* ***Eq. 6*** *for definition and surrounding discussion.*
[c]*See* ***Eq. 7*** *for definition and surrounding discussion.*

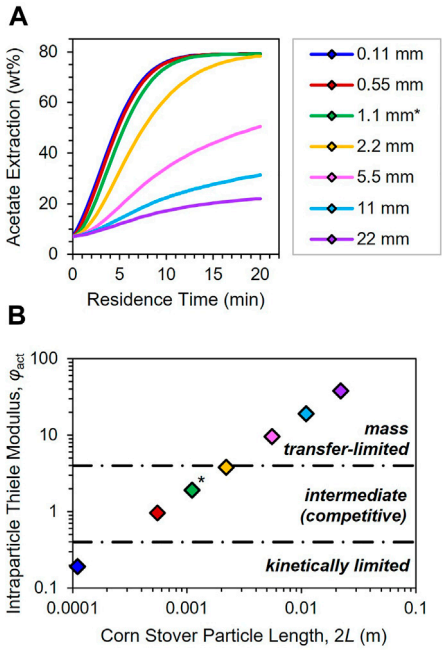

FIGURE 7 | (A) Acetate extraction profiles and **(B)** intraparticle Thiele moduli φ_{act} (see **Eq. 6**) as a function of corn stover particle length. Isotropically scaled 2D WH particle models simulated at deacetylation conditions of 70°C and 5 g L^{-1} NaOH. Asterisk (*) label in each denotes 1.1-mm-long WH base case particle (green; see **Figure 3**). Dot-dashed lines in **(B)** divide regimes by their controlling phenomena (inset italicized labels). See **Eq. 6**, **Supplementary Table S7** and discussion in main text for regime definitions.

not captured in the idealized model physics, which would practically raise entropic barriers and thus uniquely reduce the value of $k_{0,lig}$ at this condition. Future investigations at high C_{NaOH} may seek to incorporate solubility effects into mesoscale models to reconcile these apparent prediction gaps. Overall, however, 2D reaction–diffusion models and their aggregate ensembles appear to be valid and reasonably predictive of corn stover deacetylation behaviors at two process-relevant alkaline conditions.

Intraparticle Mass Transfer Resistance and Kinetic Consequences

Actionable insights into corn stover deacetylation may be gleaned from the foundational reaction–diffusion models developed in this report. Of particular value are questions of mass transfer rates and how they may (or may not) compete with the kinetic rates of deacetylation chemistry. An historical approach to achieve this rate comparison is to calculate the Thiele modulus for the case of a reactive solute undergoing simultaneous diffusion and chemical reaction (Thiele, 1939; Froment and Bischoff, 1990; Levenspiel, 1998). An adaptation of the intraparticle Thiele modulus φ_i for incompletely convertible chemical reactions is described by:

$$\varphi_i = \sqrt{\frac{\text{reaction rate}}{\text{diffusion rate}}} = L\sqrt{\frac{k_i'}{(D_{\text{eff,OH}^-})(Y_{\max,i})}} \qquad (6)$$

where L (m) is the characteristic path length, k_i' (s^{-1}) is the pseudo-first-order rate coefficient of species i extraction, $D_{\text{eff,OH}^-}$ ($m^2\ s^{-1}$) is the effective diffusivity of the mobile OH^- reactant and $Y_{\max,i}$ is the maximum extractable yield of component i (non-dimensionalized and normalized to a value between 0 and 1) observed at long residence times (**Supplementary Table S3**); the latter term is included to account for incomplete extraction (i.e., incomplete conversion). Subscript i again refers to acetate, xylan or lignin, the immobile, corn stover-bound reactants, and k_i' is calculated by multiplying k_i (mol $m^{-3}\ s^{-1}$; **Table 2**) by the initial molar content of each solid-bound species (mol; see **Supplementary Table S3** and MW values in **Figure 4** and **Supplementary Figure S17**). Path length L of the diffusing reactant is defined as half the particle length; this characteristic length may be visualized as the long axis of the blue 2D WH particle illustrated in **Figure 3**. We note that φ_i is dimensionless, and calculated values indicate whether the deacetylation process is either effectively controlled (i.e., limited) by the reaction rate ($\varphi_i < 0.4$) or the diffusion rate ($\varphi_i > 4.0$), or instead governed by an intermediate regime ($0.4 < \varphi_i < 4.0$) where reaction kinetics and mass transfer compete along similar time and length scales (Levenspiel, 1998).

A related dimensionless expression that quantifies reaction vs. diffusion control is the effectiveness factor η_i, defined by **Eq. 7** for arbitrary geometries (Aris, 1957; Levenspiel, 1998) applicable to biomass particles (Thornburg et al., 2020):

$$\eta_i = \frac{\tanh(\varphi_i)}{\varphi_i} \quad (7)$$

Values of η_i are bounded by 0 and 1. Like φ_i, the magnitude of η_i indicates whether a process is kinetically limited ($\eta_i > 0.95$), mass transport-limited ($\eta_i < 0.25$) or in between; note that a low φ_i indicates a high η_i and vice versa. The effectiveness factor also bears tangible interpretations: for example, if $\eta_i = 0.40$, apparent kinetic measurements observed via experiment may actually be attenuated by up to 60% due to diffusion limitations.

The Thiele modulus φ_i and the related effectiveness factor η_i are therefore important descriptors of mass transport resistances in biomass pretreatment and conversion (Ciesielski et al., 2021), and here we use them to interpret the observable and predicted performance of corn stover deacetylation. Calculated values of φ_i and η_i are reported in **Table 3** for each acetate, xylan and lignin extracted from WH with 5 g L^{-1} NaOH and at temperatures of 4–70°C. In general, Thiele moduli increase with increasing temperature, indicating that diffusion limitations become more pronounced at high temperatures where kinetic rates expectedly become very rapid, and thus non-controlling. This is especially true for acetate extraction, which faces severe mass transfer resistances at 70°C (η_i = 0.50) while curiously approaching kinetic limitations at 4°C (η_i = 0.90). In contrast, effectiveness factors for lignin and xylan are generally high at all conditions, although mass transfer does appear to compete somewhat with extraction kinetics at the two elevated temperatures (η_i ~ 0.84–0.92).

Next, we compare intraparticle reaction and diffusion rates across the family of anatomical fractions. **Table 4** lists the computed φ_i and η_i values for each CB, HS and SK at 4 and 70°C for the three reactive components. Trends in reaction vs. diffusion resistance for HS and SK are remarkably similar to WH (**Table 3**), further reinforcing the similar performance attributes among these corn stover fractions. As expected, CB remains a significant outlier among the material set, and given the uncertainty in determining accurate kinetic parameters (*vide supra*), values reported in **Table 4** for CB should be regarded as approximate boundaries rather than definitive metrics. Even so, debilitating mass transport resistances are identified for the extraction of lignin and especially acetate, with η_{act} as low as 0.021—suggesting laboratory deacetylation measurements may be impaired by nearly 98% due to mass transport phenomena! Remarkably, however, external (film) mass transfer resistances (Frössling, 1938; Levenspiel, 1998) at the exterior particle surface are negligible across all four corn stover samples, including CB (see **Supplementary Table S6**, **Supplementary Equation S4** and surrounding SM discussion). Such alarming findings further edify the critical importance of mesoscale modeling in biomass pretreatment and conversion by illuminating these obscured, but crucial performance-limiting bottlenecks.

Processing conditions and feedstock anatomy clearly influence the phenomena that control alkaline deacetylation, as do the size of the feedstock particles. We now isotropically scale the WH model to simulate deacetylation across proportionally smaller and larger 2D particles; results for acetate extraction at 70°C and 5 g L^{-1} are illustrated in **Figure 7A**, while Thiele moduli are plotted as a function of full particle length $2L$ in **Figure 7B**. Corn stover particle size indeed has a pronounced impact on acetate removal: precipitous drops in yield are predicted for particles larger than 2.2 mm, with the largest 22-mm particle achieving only 22% extraction after 20 min reaction time (**Figure 7A**). Size-dependent mass transport consequences are accordingly witnessed in **Figure 7B** by the span of φ_{act} from 0.19 to 38, the largest of which corresponds to an η_{act} of 0.026.

Finally, we propose actionable insights into feedstock size thresholds for corn stover deacetylation by back-calculating from critical values of φ_{act} (*vide supra*). **Eq. 6** is rearranged to solve for L_{crit} at the two $\varphi_{crit,act}$ boundaries to determine anatomically-specific particle size thresholds of mass transfer resistance at 4 and 70°C. Full particle lengths $2L_{crit}$ are reported in **Supplementary Table S7** alongside physical interpretations. Crucially, unsorted corn stover particles as little as 2.3 mm in length are predicted to be entirely diffusion-limited for acetate extraction at the higher temperature—approximately the average Feret length of milled WH, HS and SK particles used in this study (**Table 1**), and nearly identical to hardwood size limits determined in the authors' previous study on poplar methanolysis (Thornburg et al., 2020). Size thresholds for these three corn stover fractions are indeed similar, whereas CB particles will virtually always be subjected to mass transfer control despite any practical attempt at size reduction. Conversely, kinetic control may be achieved for WH, HS and SK if particle lengths are kept below 0.23 mm; in other words, finely milled corn stover is predicted to enable laboratory kinetic measurements of deacetylation chemistry devoid of transport limitations. However, milling feedstock to this size range is impractical for pilot- and industrial-scale applications, where mass transport is anticipated to play a dominant role in deacetylation process performance. Additional strategies such as air classification (Thompson et al., 2016) may enable the practically scalable removal of cob fractions to obviate their severe mass transfer penalties in processing contexts. Overall, the predictors proposed in **Supplementary Table S7** will inform both biomass conversion researchers and biorefinery practitioners of practical feedstock size reduction targets to properly account for mesoscale mass transfer resistances in pretreatment systems that straddle myriad time and length scales.

CONCLUSION

Alkaline deacetylation prior to mechanical refining is an emerging biorefinery pretreatment strategy to improve enzymatic saccharification yields of herbaceous feedstocks such as corn stover. In this study, we develop first-principled reaction–diffusion models of three primary anatomical fractions of milled corn stover (cobs, husks and stalks) and of an aggregate particle representative of the unsorted (whole) feedstock to understand and corroborate how microscopic differences in biopolymer and tissue assemblies impact

observable deacetylation performance at 4–70°C and 5–7 g L^{-1} NaOH for residence times of 0–20 min. Anatomically-specific 2D models then incorporate key physical and chemical descriptors of corn stover particle microstructure, geometry and biopolymer composition.

With appropriate assumptions for particle-scale physics, such as condensed-phase mass transfer, kinetic rate constants for acetate, xylan and lignin extraction are regressed from experimental data sets at 5 g L^{-1} NaOH and subsequently validated by 7 g L^{-1} data and anatomically-weighted ensemble calculations. Individual and ensemble model responses provide excellent fits to experimental data and offer reasonably valid predictions of reaction–diffusion behavior at extrapolated conditions. Crucially, mass transfer resistances are predicted to dominate acetate extraction kinetics at moderate temperatures for all feedstock fractions, but especially so for cobs, which demonstrate vanishingly small effectiveness factors of 0.021 for deacetylation at 70°C. Indeed, unsorted corn stover particles as small as 2.3 mm in length are expected to be completely mass transfer-limited for deacetylation—therefore establishing critical particle size reduction guidelines for laboratory and industrial practitioners to heed when studying this important pretreatment process.

Mesoscale modeling is a vital tool to uncover performance-controlling phenomena and to decouple chemical kinetics from mass and heat transfer in multiphase systems. Historical reaction engineering theories such as the Thiele modulus and effectiveness factor offer a renewed perspective on modern approaches to biomass deconstruction. Transport phenomena indeed lie at the heart of most biomass conversion processes, and the unique model frameworks developed in this report provide both scale-unifying information and actionable guideposts for chemical reactor design, scale-up and deployment of future biorefineries.

DATA AVAILABILITY STATEMENT

The original contributions presented in the study are included in the article/**Supplementary Material**. Further inquiries can be directed to the corresponding authors.

AUTHOR CONTRIBUTIONS

NT conceived the study, designed kinetic experiments, executed all CFD simulations and MATLAB programs, and wrote the article. RN conducted all kinetic and analytical experiments and designed the experimental apparatuses under the advisement of EW, XC, DS and MR. MC and PC performed XCT experiments, post-processing and visualization while FU performed XCT data analysis in MATBOX. LB and VB executed MD simulations, and VB determined lignin decamer structures and MD coordinates. YL assisted with design of kinetic experiments and coordinated corn stover feedstock sorting, milling, storage, and material and data transfers. MR, XC and DS advised experimental campaigns, equipment resources and project timelines while EW oversaw analytical measurement needs and data quality assurance. MP assisted with reaction–diffusion model development and co-wrote and debugged algorithms. PC directed the scientific project, developed particle model frameworks, wrote data regression algorithms with NT and MP, and advised the overall scientific objectives of the study.

FUNDING

Funding provided by the U.S. Department of Energy Office of Energy Efficiency and Renewable Energy Bioenergy Technologies Office through the Feedstock-Conversion Interface Consortium. A portion of this research was performed using computational resources sponsored by the Department of Energy's Office of Energy Efficiency and Renewable Energy and located at the National Renewable Energy Laboratory.

ACKNOWLEDGMENTS

NT and YL acknowledge corn stover hand fractionation activities and information provided by Amber Hoover, Neal Yancey and Allison Ray of Idaho National Laboratory. NT and RN further acknowledge Brittany Thornton, Darren Peterson and William Michener of NREL for their assistance with analytical characterization. VB and LB acknowledge Heather Mayes of NREL for her assistance with lignin MD structures.

SUPPLEMENTARY MATERIAL

The Supplementary Material for this article can be found online at: https://www.frontiersin.org/articles/10.3389/fenrg.2022.841169/full#supplementary-material

REFERENCES

Arganda-Carreras, I., Kaynig, V., Rueden, C., Eliceiri, K. W., Schindelin, J., Cardona, A., et al. (2017). Trainable Weka Segmentation: a Machine Learning Tool for Microscopy Pixel Classification. *Bioinformatics* 33 (15), 2424–2426. doi:10.1093/bioinformatics/btx180

Aris, R. (1957). On Shape Factors for Irregular Particles-I. *Chem. Eng. Sci.* 6 (6), 262–268. doi:10.1016/0009-2509(57)85028-3

Buades, A., Coll, B., and Morel, J. "(Year). "A Non-local Algorithm for Image Denoising," in 2005 IEEE Computer Society Conference on Computer Vision and Pattern Recognition (CVPR'05)), 60–65.62

Chen, J., Adjallé, K., Barnabé, S., Perrier, M., and Paris, J. (2019). Mechanical and Thermal Pretreatment Processes for Increasing Sugar Production from Woody Biomass via Enzymatic Hydrolysis. *Waste Biomass Valor.* 10 (7), 2057–2065. doi:10.1007/s12649-018-0217-x

Chen, X., Kuhn, E., Jennings, E. W., Nelson, R., Tao, L., Zhang, M., et al. (2016). DMR (Deacetylation and Mechanical Refining) Processing of Corn stover

Achieves High Monomeric Sugar Concentrations (230 G L−1) during Enzymatic Hydrolysis and High Ethanol Concentrations (>10% V/v) during Fermentation without Hydrolysate Purification or Concentration. *Energy Environ. Sci.* 9 (4), 1237–1245. doi:10.1039/C5EE03718B

Chen, X., Tao, L., Shekiro, J., Mohaghaghi, A., Decker, S., Wang, W., et al. (2012). Improved Ethanol Yield and Reduced Minimum Ethanol Selling Price (MESP) by Modifying Low Severity Dilute Acid Pretreatment with Deacetylation and Mechanical Refining: 1) Experimental. *Biotechnol. Biofuels* 5 (1), 60. doi:10.1186/1754-6834-5-60

Ciesielski, P. N., Crowley, M. F., Nimlos, M. R., Sanders, A. W., Wiggins, G. M., Robichaud, D., et al. (2015). Biomass Particle Models with Realistic Morphology and Resolved Microstructure for Simulations of Intraparticle Transport Phenomena. *Energy Fuels* 29 (1), 242–254. doi:10.1021/ef502204v

Ciesielski, P. N., Pecha, M. B., Thornburg, N. E., Crowley, M. F., Gao, X., Oyedeji, O., et al. (2021). Bridging Scales in Bioenergy and Catalysis: A Review of Mesoscale Modeling Applications, Methods, and Future Directions. *Energy Fuels* 35 (18), 14382–14400. doi:10.1021/acs.energyfuels.1c02163

Comstock, G. L. (1970). Directional Permeability of Softwoods. *Wood Fiber* 1 (4), 283–289.

Cooper, S. J., Bertei, A., Shearing, P. R., Kilner, J. A., and Brandon, N. P. (2016). TauFactor: An Open-Source Application for Calculating Tortuosity Factors from Tomographic Data. *SoftwareX* 5, 203–210. doi:10.1016/j.softx.2016.09.002

Costanza, V., and Costanza, P. (2002). Estimating Pure Diffusion Contributions in Alkaline Pulping Processes. *Lat. Am. Appl. Res.* 32, 151–159.

Darden, T., York, D., and Pedersen, L. (1993). Particle Mesh Ewald: AnN·Log(N) Method for Ewald Sums in Large Systems. *J. Chem. Phys.* 98 (12), 10089–10092. doi:10.1063/1.464397

Froment, G. F., and Bischoff, K. B. (1990). *Chemical Reactor Analysis and Design*, Ch 3. New York, NY, U.S.A.: John Wiley & Sons.

Frössling, N. (1938). Uber die Verdunstung Fallender Tropfen (The Evaporation of Falling Drops). *Gerlands Beitr. Geophys.* 52, 107–216.

Gierer, J., Imsgard, F., Norén, I., Stilkerieg, B., Christensen, A., and Schroll, G. (1977). Studies on the Degradation of Phenolic Lignin Units of the Beta-Aryl Ether Type with Oxygen in Alkaline Media. *Acta Chem. Scand.* 31b, 561–572. doi:10.3891/acta.chem.scand.31b-0561

Guvench, O., Greene, S. N., Kamath, G., Brady, J. W., Venable, R. M., Pastor, R. W., et al. (2008). Additive Empirical Force Field for Hexopyranose Monosaccharides. *J. Comput. Chem.* 29 (15), 2543–2564. doi:10.1002/jcc.21004

Hatcher, E. R., Guvench, O., and MacKerell, A. D. (2009). CHARMM Additive All-Atom Force Field for Acyclic Polyalcohols, Acyclic Carbohydrates, and Inositol. *J. Chem. Theor. Comput.* 5 (5), 1315–1327. doi:10.1021/ct9000608

Hynninen, A. P., and Crowley, M. F. (2014). New Faster CHARMM Molecular Dynamics Engine. *J. Comput. Chem.* 35 (5), 406–413. doi:10.1002/jcc.23501

Jakes, J. E., Zelinka, S. L., Hunt, C. G., Ciesielski, P., Frihart, C. R., Yelle, D., et al. (2020). Measurement of Moisture-dependent Ion Diffusion Constants in wood Cell wall Layers Using Time-Lapse Micro X-ray Fluorescence Microscopy. *Sci. Rep.* 10 (1), 9919. doi:10.1038/s41598-020-66916-8

Jorgensen, W. L., Chandrasekhar, J., Madura, J. D., Impey, R. W., and Klein, M. L. (1983). Comparison of Simple Potential Functions for Simulating Liquid Water. *J. Chem. Phys.* 79 (2), 926–935. doi:10.1063/1.445869

Karp, E. M., Donohoe, B. S., O'Brien, M. H., Ciesielski, P. N., Mittal, A., Biddy, M. J., et al. (2014). Alkaline Pretreatment of Corn Stover: Bench-Scale Fractionation and Stream Characterization. *ACS Sust. Chem. Eng.* 2 (6), 1481–1491. doi:10.1021/sc500126u

Katahira, R., Mittal, A., McKinney, K., Chen, X., Tucker, M. P., Johnson, D. K., et al. (2016). Base-Catalyzed Depolymerization of Biorefinery Lignins. *ACS Sust. Chem. Eng.* 4 (3), 1474–1486. doi:10.1021/acssuschemeng.5b01451

Kräutler, V., van Gunsteren, W. F., and Hünenberger, P. H. (2001). A Fast SHAKE Algorithm to Solve Distance Constraint Equations for Small Molecules in Molecular Dynamics Simulations. *J. Comput. Chem.* 22 (5), 501–508. doi:10.1002/1096-987X(20010415)22:5<501:AID-JCC1021>3.0.CO;2-V

Kruger, J. S., Cleveland, N. S., Zhang, S., Katahira, R., Black, B. A., Chupka, G. M., et al. (2016). Lignin Depolymerization with Nitrate-Intercalated Hydrotalcite Catalysts. *ACS Catal.* 6 (2), 1316–1328. doi:10.1021/acscatal.5b02062

Levenspiel, O. (1998). *Chemical Reaction Engineering*, Ch 18. New York, NY, U.S.A: John Wiley & Sons.

Lima, C. S., Rabelo, S. C., Ciesielski, P. N., Roberto, I. C., Rocha, G. J. M., and Driemeier, C. (2018). Multiscale Alterations in Sugar Cane Bagasse and Straw Submitted to Alkaline Deacetylation. *ACS Sust. Chem. Eng.* 6 (3), 3796–3804. doi:10.1021/acssuschemeng.7b04158

Luterbacher, J. S., Parlange, J.-Y., and Walker, L. P. (2013). A Pore-Hindered Diffusion and Reaction Model Can Help Explain the Importance of Pore Size Distribution in Enzymatic Hydrolysis of Biomass. *Biotechnol. Bioeng.* 110 (1), 127–136. doi:10.1002/bit.24614

MacKerell, A. D., Jr., Brooks, B., Brooks, C. L., III, Nilsson, L., Roux, B., Won, Y., et al. (1998). "CHARMM: The Energy Function and its Parameterization," in *Encyclopedia of Computational Chemistry*.

Mills, T. Y., Sandoval, N. R., and Gill, R. T. (2009). Cellulosic Hydrolysate Toxicity and Tolerance Mechanisms in *Escherichia coli*. *Biotechnol. Biofuels* 2 (1), 26. doi:10.1186/1754-6834-2-26

Min, D.-Y., Chang, H.-M., Jameel, H., Lucia, L., Wang, Z.-G., and Jin, Y.-C. (2014). The Structure of Lignin of Corn stover and its Changes Induced by Mild Sodium Hydroxide Treatment. *BioResources* 9 (2), 2405–2414. doi:10.15376/biores.9.2.2405-2414

Morales-Huerta, J. C., Hernández-Meléndez, O., Hernández-Luna, M. G., Manero, O., Bárzana, E., and Vivaldo-Lima, E. (2021). An Experimental and Modeling Study on the Pretreatment and Alkaline Hydrolysis of Blue Agave Bagasse in Twin-Screw Extruders. *Ind. Eng. Chem. Res.* 60 (34), 12449–12460. doi:10.1021/acs.iecr.1c02175

Mosier, N., Wyman, C., Dale, B., Elander, R., Lee, Y. Y., Holtzapple, M., et al. (2005). Features of Promising Technologies for Pretreatment of Lignocellulosic Biomass. *Bioresour. Tech.* 96 (6), 673–686. doi:10.1016/j.biortech.2004.06.025

Orella, M. J., Gani, T. Z. H., Vermaas, J. V., Stone, M. L., Anderson, E. M., Beckham, G. T., et al. (2019). Lignin-KMC: A Toolkit for Simulating Lignin Biosynthesis. *ACS Sust. Chem. Eng.* 7 (22), 18313–18322. doi:10.1021/acssuschemeng.9b03534

Otsu, N. (1979). A Threshold Selection Method from Gray-Level Histograms. *IEEE Trans. Syst. Man. Cybern.* 9 (1), 62–66. doi:10.1109/TSMC.1979.4310076

Palmqvist, E., and Hahn-Hägerdal, B. (2000). Fermentation of Lignocellulosic Hydrolysates. II: Inhibitors and Mechanisms of Inhibition. *Bioresour. Tech.* 74 (1), 25–33. doi:10.1016/S0960-8524(99)00161-3

Pecha, M. B., Ramirez, E., Wiggins, G. M., Carpenter, D., Kappes, B., Daw, S., et al. (2018). Integrated Particle- and Reactor-Scale Simulation of Pine Pyrolysis in a Fluidized Bed. *Energy Fuels* 32 (10), 10683–10694. doi:10.1021/acs.energyfuels.8b02309

Pettersen, E. F., Goddard, T. D., Huang, C. C., Meng, E. C., Couch, G. S., Croll, T. I., et al. (2021). UCSF ChimeraX : Structure Visualization for Researchers, Educators, and Developers. *Protein Sci.* 30 (1), 70–82. doi:10.1002/pro.3943

Rodriguez, A., Salvachúa, D., Katahira, R., Black, B. A., Cleveland, N. S., Reed, M., et al. (2017). Base-Catalyzed Depolymerization of Solid Lignin-Rich Streams Enables Microbial Conversion. *ACS Sust. Chem. Eng.* 5 (9), 8171–8180. doi:10.1021/acssuschemeng.7b01818

Rollin, J. A., Zhu, Z., Sathitsuksanoh, N., and Zhang, Y.-H. P. (2011). Increasing Cellulose Accessibility Is More Important Than Removing Lignin: A Comparison of Cellulose Solvent-Based Lignocellulose Fractionation and Soaking in Aqueous Ammonia. *Biotechnol. Bioeng.* 108 (1), 22–30. doi:10.1002/bit.22919

Schutyser, W., Renders, T., Van den Bosch, S., Koelewijn, S.-F., Beckham, G. T., and Sels, B. F. (2018). Chemicals from Lignin: an Interplay of Lignocellulose Fractionation, Depolymerisation, and Upgrading. *Chem. Soc. Rev.* 47 (3), 852–908. doi:10.1039/C7CS00566K

Shimizu, S., Posoknistakul, P., Yokoyama, T., and Matsumoto, Y. (2013). Quantitative Difference in the Rates of the β-O-4 Bond Cleavage between Lignin Model Compounds with and without γ-Hydroxymethyl Groups during the Alkaline Pulping Process. *BioResources* 8 (3), 11. doi:10.15376/biores.8.3.4312-4322

Shimizu, S., Yokoyama, T., Akiyama, T., and Matsumoto, Y. (2012). Reactivity of Lignin with Different Composition of Aromatic Syringyl/Guaiacyl Structures and Erythro/Threo Side Chain Structures in β-O-4 Type during Alkaline Delignification: As a Basis for the Different Degradability of Hardwood and Softwood Lignin. *J. Agric. Food Chem.* 60 (26), 6471–6476. doi:10.1021/jf301329v

Sluiter, A., Hames, B., Ruiz, R., Scarlata, C., Sluiter, J., and Templeton, D. (2008a). *Determination of Sugars, Byproducts, and Degradation Products in Liquid Fraction Process Samples*. Golden, CO: National Renewable Energy Laboratory. Technical Report NREL/TP-510-42623.

Sluiter, A., Hames, B., Ruiz, R., Scarlata, C., Sluiter, J., Templeton, D., et al. (2008b). *Determination of Structural Carbohydrates and Lignin in Biomass*. Golden, CO:

National Renewable Energy Laboratory. Technical Report NREL/TP-510-42618.

Sluiter, A., Ruiz, R., Scarlata, C., Sluiter, J., and Templeton, D. (2005). *Determination of Extractives in Biomass*. Golden, CO: National Renewable Energy Laboratory. Technical Report NREL/TP-510-42619.

Sun, Q., Xia, Y., Klinger, J., Seifert, R., Kane, J., Thompson, V., et al. (2021). X-ray Computed Tomography-Based Porosity Analysis: Algorithms and Application for Porous Woody Biomass. *Powder Tech.* 388, 496–504. doi:10.1016/j.powtec.2021.05.006

Tanaka, M. (2021). Noise Level Estimation from a Single Image (Available at: https://www.mathworks.com/matlabcentral/fileexchange/36921-noise-level-estimation-from-a-single-image)[Online]. MATLAB Central File Exchange. [Accessed December 21, 2021].

Tao, L., Chen, X., Aden, A., Kuhn, E., Himmel, M. E., Tucker, M., et al. (2012). Improved Ethanol Yield and Reduced Minimum Ethanol Selling price (MESP) by Modifying Low Severity Dilute Acid Pretreatment with Deacetylation and Mechanical Refining: 2) Techno-Economic Analysis. *Biotechnol. Biofuels* 5 (1), 69. doi:10.1186/1754-6834-5-69

Thiele, E. W. (1939). Relation between Catalytic Activity and Size of Particle. *Ind. Eng. Chem.* 31 (7), 916–920. doi:10.1021/ie50355a027

Thompson, V. S., Lacey, J. A., Hartley, D., Jindra, M. A., Aston, J. E., and Thompson, D. N. (2016). Application of Air Classification and Formulation to Manage Feedstock Cost, Quality and Availability for Bioenergy. *Fuel* 180, 497–505. doi:10.1016/j.fuel.2016.04.040

Thornburg, N. E., Pecha, M. B., Brandner, D. G., Reed, M. L., Vermaas, J. V., Michener, W. E., et al. (2020). Mesoscale Reaction-Diffusion Phenomena Governing Lignin-First Biomass Fractionation. *ChemSusChem* 13 (17), 4495–4509. doi:10.1002/cssc.202000558

Usseglio-Viretta, F. L. E., Patel, P., Bernhardt, E., Mistry, A., Mukherjee, P. P., Allen, J., et al. (2020). MATBOX: An Open-Source Microstructure Analysis Toolbox for Microstructure Generation, Segmentation, Characterization, Visualization, Correlation, and Meshing Available at: (https://github.com/NREL/MATBOX_Microstructure_analysis_toolbox) [Online]. GitHub. [Accessed December 20, 2021].

Usseglio-Viretta, F. L. E., Patel, P., Bernhardt, E., Mistry, A., Mukherjee, P. P., Allen, J., et al. (2022). MATBOX: An Open-Source Microstructure Analysis Toolbox for Microstructure Generation, Segmentation, Characterization, Visualization, Correlation, and Meshing. *SoftwareX* 17, 100915. doi:10.1016/j.softx.2021.100915

Vanommeslaeghe, K., Hatcher, E., Acharya, C., Kundu, S., Zhong, S., Shim, J., et al. (2009). CHARMM General Force Field: A Force Field for Drug-like Molecules Compatible with the CHARMM All-Atom Additive Biological Force fields. *J. Comput. Chem.* 31 (4), NA. doi:10.1002/jcc.21367

Vermaas, J. V., Petridis, L., Ralph, J., Crowley, M. F., and Beckham, G. T. (2019). Systematic Parameterization of Lignin for the CHARMM Force Field. *Green. Chem.* 21 (1), 109–122. doi:10.1039/C8GC03209B

Viamajala, S., Donohoe, B. S., Decker, S. R., Vinzant, T. B., Selig, M. J., Himmel, M. E., et al. (2010). "Heat and Mass Transport in Processing of Lignocellulosic Biomass for Fuels and Chemicals," in *Sustainable Biotechnology: Sources of Renewable Energy*. Editors O. V. Singh and S. P. Harvey (Dordrecht: Springer Netherlands), 1–18. doi:10.1007/978-90-481-3295-9_1

Villanova, J., Laurencin, J., Cloetens, P., Bleuet, P., Delette, G., Suhonen, H., et al. (2013). 3D Phase Mapping of Solid Oxide Fuel Cell YSZ/Ni Cermet at the Nanoscale by Holographic X-ray Nanotomography. *J. Power Sourc.* 243, 841–849. doi:10.1016/j.jpowsour.2013.06.069

Vincent Sahayaraj, D., Lusi, A., Mitchell, E. M., Bai, X., and Tessonnier, J.-P. (2021). Comparative Study of the Solvolytic Deconstruction of Corn stover Lignin in Batch and Flow-Through Reactors. *Green. Chem.* 23 (19), 7731–7742. doi:10.1039/D1GC02420E

Xu, L., Zhang, S.-J., Zhong, C., Li, B.-Z., and Yuan, Y.-J. (2020). Alkali-Based Pretreatment-Facilitated Lignin Valorization: A Review. *Ind. Eng. Chem. Res.* 59 (39), 16923–16938. doi:10.1021/acs.iecr.0c01456

Yang, B., Tao, L., and Wyman, C. E. (2017). Strengths, Challenges, and Opportunities for Hydrothermal Pretreatment in Lignocellulosic Biorefineries. *Biofuels, Bioproducts and Biorefining*, n/a. doi:10.1002/bbb.1825

Author's Disclaimer: The views expressed in the article do not necessarily represent the views of the DOE or the U.S. Government. The U.S. Government retains and the publisher, by accepting the article for publication, acknowledges that the U.S. Government retains a nonexclusive, paid-up, irrevocable, worldwide license to publish or reproduce the published form of this work, or allow others to do so, for U.S. Government purposes.

Conflict of Interest: All authors were employed by the National Renewable Energy Laboratory, operated by Alliance for Sustainable Energy, LLC, for the U.S. Department of Energy (DOE) under Contract No. DE-AC36-08GO28308.

Publisher's Note: All claims expressed in this article are solely those of the authors and do not necessarily represent those of their affiliated organizations, or those of the publisher, the editors, and the reviewers. Any product that may be evaluated in this article, or claim that may be made by its manufacturer, is not guaranteed or endorsed by the publisher.

frontiers in Energy Research

ORIGINAL RESEARCH
published: 07 March 2022
doi: 10.3389/fenrg.2022.849949

Performance and Economic Analysis of Organosolv Softwood and Herbaceous Lignins to Activated Carbons as Electrode Materials in Supercapacitors

Lu Yu[1,2], Kendhl Seabright[1], Ishan Bajaj[3], David J. Keffer[2], David M. Alonso[4], Chien-Te Hsieh[5], Mi Li[1], Hao Chen[6], Sheng Dai[6,7], Yasser Ashraf Gandomi[8], Christos T. Maravelias[3,9] and David P. Harper[1]**

[1]Center for Renewable Carbon, Institute of Agriculture, The University of Tennessee, Knoxville, TN, United States, [2]Department of Materials Science and Engineering, The University of Tennessee, Knoxville, TN, United States, [3]Andlinger Center for Energy and the Environment, Princeton University, Princeton, NJ, United States, [4]Glucan Biorenewables LLC, Madison, WI, United States, [5]Department of Chemical Engineering and Materials Science, Yuan Ze University, Taoyuan, Taiwan, [6]Department of Chemistry, The University of Tennessee, Knoxville, TN, United States, [7]Chemical Sciences Division, Oak Ridge National Laboratory, Oak Ridge, TN, United States, [8]Department of Chemical Engineering, Massachusetts Institute of Technology, Cambridge, MA, United States, [9]Department of Chemical and Biological Engineering, Princeton University, Princeton, NJ, United States

OPEN ACCESS

Edited by:
Xiaojun Shen,
Dalian Institute of Chemical Physics (CAS), China

Reviewed by:
Kunfeng Chen,
Shandong University, China
Maria Gonzalez Alriols,
University of the Basque Country, Spain
Yun Ji,
University of North Dakota, United States

***Correspondence:**
Chien-Te Hsieh
cthsieh@saturn.yzu.edu.tw
David P. Harper
dharper4@utk.edu

Specialty section:
This article was submitted to Bioenergy and Biofuels, a section of the journal Frontiers in Energy Research

Received: 06 January 2022
Accepted: 03 February 2022
Published: 07 March 2022

Citation:
Yu L, Seabright K, Bajaj I, Keffer DJ, Alonso DM, Hsieh C-T, Li M, Chen H, Dai S, Gandomi YA, Maravelias CT and Harper DP (2022) Performance and Economic Analysis of Organosolv Softwood and Herbaceous Lignins to Activated Carbons as Electrode Materials in Supercapacitors. Front. Energy Res. 10:849949. doi: 10.3389/fenrg.2022.849949

In this work, yellow pine (YP, softwood) and switchgrass (SG, grass) lignins were extracted as a coproduct of an organosolv γ-valerolactone (GVL) biorefinery that also produces biofuels and furfural. The extracted lignins were converted to carbon precursors for synthesizing porous activated carbon electrodes for high energy-density supercapacitors. This research details the impact of lignin composition on the derived porous structures and electrochemical properties of activated carbons. Lignin precursors with various syringyl (S) to guaiacyl (G) contents were characterized using ^{31}P nuclear magnetic resonance (NMR) and two-dimensional ^{1}H–^{13}C NMR. A two-step activation process, using steam and carbon dioxide as the activating agents, enabled the formation of porous carbons structures with high surface area. The capacitive behavior of supercapacitors was systematically characterized by cyclic voltammetry, charge-discharge cycling, and electrochemical impedance spectroscopy. The specific capacitance of YP and SG capacitors reached 367 and 221 F g^{-1}, respectively. Both types of capacitors demonstrated remarkably stable capacitance (capacitance retention >90%) along with excellent Coulombic efficiency (>99%) over 10,000 cycles. Compared to SG electrode, the better electrochemical performance achieved with YP electrodes was mainly due to shorter diffusion path, improved ionic mobility, and increased active surface area. The inexpensive lignin-based porous electrodes synthesized in this work can be used for various electrochemical devices for improved performance, decreased cost, and enhanced durability. This work also demonstrates that the selection of feedstock and appropriate processing conditions can tailor the structure of carbon composites for targeted applications. Techno-economic analysis indicates that YP and SG activated carbons can be produced at a minimum selling price of $8,493 and $6,670 per ton,

respectively, which is competitive with the commercially available supercapacitor-grade activated carbons.

Keywords: lignin, economic analysis, γ-valerolactone, activated carbon, supercapacitors

1 INTRODUCTION

Lignin is a natural aromatic polymer composed of phenylpropane units with various interunit linkages, such as ether and C–C bonds (Pandey and Kim, 2011; Azadi et al., 2013; Rodríguez Correa et al., 2017). As one of the major components of terrestrial plants, about 70 million tons of lignin are produced as the by-product from pulp/paper industry annually (Gosselink et al., 2004; Liu et al., 2015). However, *ca.* 95% of the available lignin is combusted to generate a low-grade heat source and the remaining amount is used for preparing specialty products for various markets (Gosselink et al., 2004; Liu et al., 2015). Considering lignin's high carbon content and unique aromatic structure, it is desirable to use lignin for synthesizing high value-added products, such as carbon fiber, carbon black, dyes, and paints (Carrott and Ribeiro Carrott, 2007). Manufacturing porous carbon structures from lignin precursors is another promising application given the important role of porous carbon electrodes for different electrochemical devices. Activated carbons (ACs) can be prepared using a variety of raw materials including peanut shell, sugarcane bagasse and corn syrup (see **Supplementary Table S1**). Lignin can be considered a potential precursor in preparing highly porous ACs due to its high carbon content, low cost, and large-scale availability as a major byproduct of paper and biofuel production (Souto et al., 2018).

Selecting an appropriate lignin precursor is challenging due to lignin's highly complex structure that varies as a function of the biomass source and isolation methods adopted (Rowlandson et al., 2020). The basic constituent of lignin is phenylpropane (C6–C3), which tends to form a three-dimensional complex structure through ether or C–C bonds (Han et al., 2018). Lignin is composed of varying ratios of three aromatic monomers depending mainly on botanical origin, including *p*-coumaryl alcohol, coniferyl alcohol, and sinapyl alcohol (McKendry, 2002; Calvo-Flores and Dobado, 2010). According to the composition of the structural units, lignin can be classified into three broad classes: softwood, hardwood, and grass lignin.(Adler, 1977; Roberts, 1996). Normally, softwood lignin predominantly contains coniferyl alcohols (~90%) with a minor amount of *p*-coumaryl alcohols (Pandey and Kim, 2011). Hardwood lignin possess similar amounts of coniferyl and sinapyl alcohol units, while grass lignin is composed of all three major units with high ratio of coniferyl and sinapyl alcohols (Kubo and Kadla, 2005). Softwood lignin has a more crosslinked network structure due to the availability of the C_5 position of the coniferyl alcohol units for coupling. Hardwood and grass lignin have a more linear structure as a result of the sinapyl alcohol units that contain extra methoxy groups on the aromatic rings, which limit the formation of coupling and cross-linking branches (Kubo and Kadla, 2005; Liu et al., 2015).

For industrial-scale manufacturing of ACs, a consistent feedstock supply is essential to ensure relatively uniform product quality. High surface area ACs are commonly used for catalysis, purification, decolorization, deodorization, separation, and energy storage (Hsieh and Teng, 2000; Hsieh and Lin, 2006). The application of activated porous carbon electrodes within electric double-layer capacitors (so-called "supercapacitors") has received a surge in attention as high surface areas (i.e., electrolyte/electrode interface) enabled through activated porous electrodes for double-layer formation and subsequent energy storage (Liu and Osaka, 1997; Qu and Shi, 1998). Many physical and chemical approaches have been reported for preparing activated carbon structures, which vary in electrode performance based upon pore size distribution, surface functional groups, and surface heterogeneity (Hsieh and Teng, 2002; Huang et al., 2020). However, there is limited understanding of the chemical and physical process to convert lignin from different precursors into ACs. Herein, we establish processing-structure-property-performance relationships (PSPP) through an efficient activation method for preparing activated carbons from different lignin precursors with enhanced electrochemical properties (e.g., surface accessibility).

In this work, a novel activation technique was developed for preparing activated carbons from two types of lignin, yellow pine (YP, softwood lignin) and switchgrass (SG, grass lignin). The influence of lignin molecular structure on both surface texture and pore size distribution of the activated carbons was systematically examined. The electrochemical performance of supercapacitors assembled with carbon electrodes was also explored using cyclic voltammetry (CV), charge-discharge cycling, and electrochemical impedance spectroscopy (EIS) in aqueous electrolytes. Techno-economic analysis was performed to assess the economic viability of the process and demonstrate the efficacy of using lignin with different chemical constituents as precursors for preparing highly porous activated carbons used as electrode material in supercapacitors.

2 EXPERIMENTAL

2.1 Preparation of Activated Carbons From Lignin

The YP and SG were obtained from Genera Energy LLC (Vonore, TN). Lignin was isolated using an γ-valerolactone organosolv fractionation technology described by Alonso et al. (2017) at the lab scale. YP and SG lignin were carbonized in a ceramic boat inserted in an alumina tube furnace with nitrogen gas flowing (3 L min^{-1}) at 1,000°C for 1 h. After naturally cooling down with N_2 flow, the carbonized samples were pulverized by ball-milling (PM100 RETSCH model), using 2- and 10-mm stainless steel balls in a stainless-steel container at 350 rpm for 30 min. The

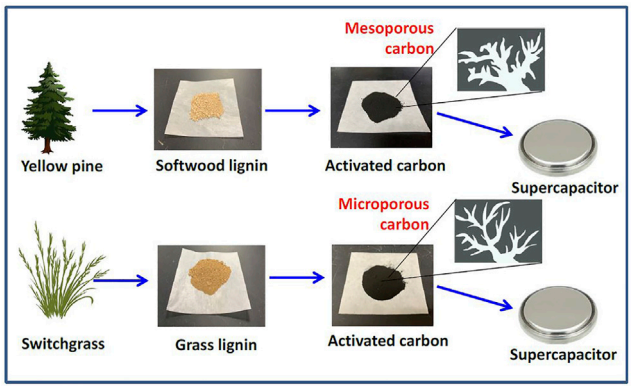

FIGURE 1 | Schematic diagram for illustrating the flowchart of supercapacitor using two kinds of electrode materials, where activated carbons were derived from different raw materials and lignin precursors.

grounded carbon powders were separated from the grinding balls using sieves and then placed into the tube furnace for steam activation at 800°C for 1 h with a ramping rate of 10°C min^{-1}. After steam activation, the carbon sample was placed in the furnace under CO_2 atmosphere for physical activation at 800°C for 1 h to yield the final samples. **Figure 1** illustrates the schematic diagram for the experimental design for the supercapacitor using two kinds of electrode materials (i.e., YP and SG), where activated carbons (YP-AC and SG-AC) were derived from different raw materials and lignin precursors.

2.2 Materials Characterization

Thermogravimetric analyzer (TGA, Perkin Elmer Pyris 1) and differential scanning calorimetry (DSC, Perkin Elmer Diamond DSC) were adopted to measure thermal stability of lignin precursors in an inert nitrogen environment. The TGA analysis was conducted by heating lignin samples from 100 to 800°C at a heating rate of 10°C min^{-1}. The DSC procedure involved three heating and cooling cycles performed at a rate of 100°C min^{-1}. The lignin samples were initially heated for two cycles from 25 to 160°C, and then heated to 230°C.

The structural morphology images of the carbon samples were collected by using scanning electron microscope (SEM, Phenom ProX). Surface characteristics of the carbon samples were analyzed by an automated adsorption apparatus (Micromeritics Instrument Co., TriStar 3000) using N_2 physisorption at -196°C. Total and mesopore surface areas of the carbon samples were calculated by using Brunauer–Emmett–Teller (BET) and Barrett–Joyner–Halenda (BJH) equations. Pore-size distributions were analyzed from the N_2-adsorption branch using density functional theory (DFT) method.

Surface functional groups on the activated carbon samples were characterized by attenuated total reflectance Fourier transform infrared (FTIR) spectroscopy (Perkin Elmer, Spectrum II). FTIR spectra were collected from 4,000—600 cm^{-1} using 16 scans with a resolution of 4 cm^{-1}. Additional surface chemical composition was collected by X-ray photoelectron spectroscopy (XPS, Fison VG ESCA210). Elemental (i.e., CHN) analysis of lignin samples was performed by combustion analysis (Perkin Elmer) to determine amounts of carbon, hydrogen, and nitrogen. To quantify the amount of oxygen, a differential technique was adopted where the samples were assumed to be composed of solely C, H, N, and O elements. Gel permeation chromatography (GPC) was used to determine the number average molecular weight (Mn), weight average molecular weight (Mw), and molar-mass dispersity ($Đ_M$) index of the lignin samples. GPC analysis was conducted by dissolving lignin in tetrahydrofuran (THF) at 1 mg ml^{-1} and injecting into an EcoSec GPC Instrument (Tosoh), with two columns (TSKgel SuperMultipore HZ-M, 4.6 × 150 mm, 4 μm) and a guard column held at 40°C. Acetobromination of the lignin was required prior to dissolution in THF for GPC analysis (Guerra et al., 2008).

^{31}P-NMR measurements were carried out using a Varian 400-MR spectrometer. Lignin samples, approximately 60 mg, were dissolved in 0.4 ml NMR solvent (deuterated chloroform and pyridine (1:1.6 v/v)). Then, 0.1 ml internal standard solution (21.5 mg endo-N-hydroxy-5-norbornene-2,3-dicarboximide in 1 ml NMR solvent) and 0.05 ml relaxation reagent (11.4 mg chromium (III) acetylacetonate in 1 ml NMR solvent) were added. Immediately before NMR analysis, 0.1 ml phosphorylating reagent, 2-chloro-4,4,5,5-tetramethyl-1,3,2-dioxaphospholane (Santa Cruz Biotechnology) was added to the sample. Acquisition parameters were set to collect 512 scans, with 1 s acquisition time and 5 s relaxation delay. Spectral data were analyzed using MestReNova software.

Two-dimensional (2D) ^{1}H −^{13}C NMR spectra were conducted on a Bruker Avance III 500-Hz NMR spectrometer, and spectral processing was carried out using a Bruker Topspin 3.5 software. The lignin samples (30 mg) were dissolved in 0.4 ml DMSO-d_6 in an NMR tube independently. Heteronuclear single quantum coherence (HSQC) experiments were perfomed with a Bruker pulse sequence (hsqcetgpspsi 2.2) on an N_2 cryoprobe (BBO ^{1}H&^{19}F-5mm) with the following acquisition parameters: spectra width 12 ppm in F2 (^{1}H) dimension with 1,024 data points (acquisition time 85.2 ms), 200 ppm in F1 (^{13}C) dimension with 256 increments (acquisition time 5.1 ms), a 1.0-s delay, a $^{1}J_{C–H}$ of 145 Hz, and 128 scans. The central DMSO-d_6 solvent peak ($^{™}$C/$^{™}$H at 39.5/2.49) was used to calibrate the chemical shift position. Assignment and the relative abundance of lignin compositional subunits and inter-unit linkage were estimated using volume integration of contours in HSQC spectra according to published literature (Das et al., 2018). The abundances of aromatic units and side-chain linkages were presented as percentage of total SGH units and total side-chain linkages, respectively.

2.3 Electrochemical Performance

Prior to working electrode preparation, the electrode slurries were first prepared by mixing 94.0 wt% activated carbon powder, 5.0 wt% polyvinylidene fluoride (Kynar) and 1.0 wt% black carbon (Super C65) in N-methyl-2-pyrrolidone (NMP) solvent. Subsequently, the stainless-steel substrate was coated with the electrode slurry to obtain a flexible electrode with an area of 2 × 1 cm^2.

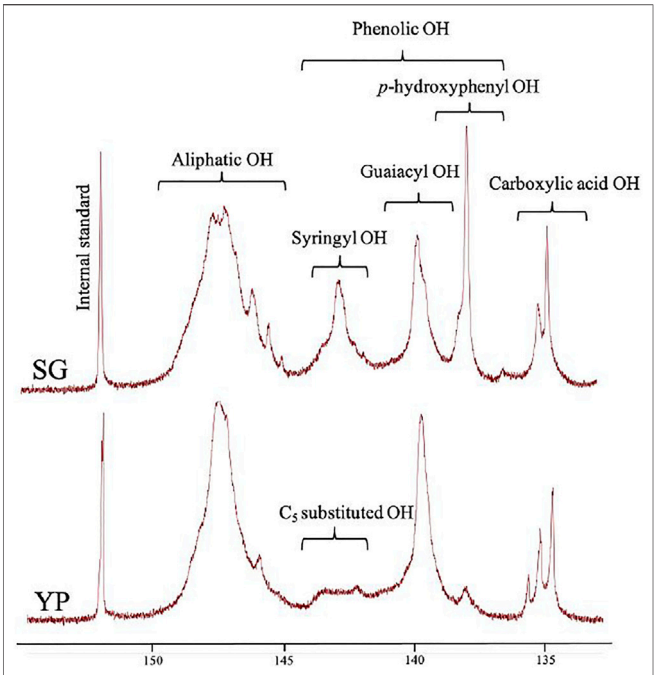

FIGURE 2 | Quantitative ^{31}P NMR spectra of SG and YP lignin samples.

Electrochemical measurements were conducted in a three-electrode system with a Pt wire as the counter electrode and an Ag/AgCl electrode as the reference electrode. Sulfuric acid (H_2SO_4, 1 M) was used as the electrolyte solution. The CV measurements were conducted at different scan rates (10, 30, 50, and 100 mV s^{-1}) within the potential range of 0–1 V. The capacitance was measured by charging and discharging from 1 to 0 V at different current densities. The impedance spectra were recorded with the AC frequency ranging from 100 kHz to 1 mHz. The resulting Nyquist plots were analyzed using the *Z*-view software package.

3 RESULTS AND DISCUSSION

3.1 Physicochemical Properties of Lignin

The compositional and elemental analysis of various lignin precursors are provided in the Electronic Supporting Information (see **Supplementary Table S2**). **Supplementary Table S2** includes the purity analysis, average molecular weight, and elemental analysis. **Supplementary Table S2** details that there is less than 4 and 6% of contaminants for YP and SG, respectively. Additionally, the ash contents are low, 0.02 and 0.03% for YP and SG, respectively, indicating that YP lignin has higher purity than SG lignin. GPC analysis details that YP lignin possesses similar molar-mass dispersity ($Đ_M$) index (M_w/M_n: 3.00 (YP) and 2.96 (SG)) with SG lignin, which reveals the dispersion of the distribution of molar masses in YP and SG lignin (Kilpelaeinen et al., 1994; Kubo and Kadla, 2005). The quantitative CHN of these two lignin sources are summarized in the elemental analysis, showing that YP lignin possesses a higher carbon content than SG, whereas SG lignin has higher oxygen and nitrogen content.

Hydroxyl units are a key factor that affect the product's thermal and physical properties, which was quantified using ^{31}P NMR (Hosseinaei et al., 2016; Hosseinaei et al., 2017). As shown in **Figure 2** and **Table 1**, YP and SG have similar amount of aliphatic hydroxyl groups, while SG possess a higher amount of phenolic hydroxy groups and carboxylic acid groups. The higher level of carboxylic acid in SG lignin is likely a result of higher concentration of phenolic acids (*p*CA and FA) being present in grasses (Hosseinaei et al., 2016). Since YP lignin predominantly contains guaiacol (G) units, the amount of *p*-hydroxyphenyl OH groups in SG lignin are higher than YP. To further confirm above results, we used 2D NMR analysis quantify the aromatic and aliphatic region in both lignin types, as illustrated in **Figure 3**. **Supplementary Table S3** includes the relative abundance of lignin linkages assessed using ^{13}C-^{1}H NMR analysis. The results agree with ^{31}P NMR results confirming higher degree of lignin condensation in YP relative to SG due to the presence of the C_5 position of G units, which provide coupling and cross-linking sites. The linkages of methoxyl (OMe), γ-hydroxylated (A_γ), β-5′ phenylcoumaran (B_γ and B_β) groups and β- O-4' (A_α/A_α') can be observed for both lignins. However, SG lignin contains resinol (C_β and C_γ) substructures, which YP lignin does not possess.

Lignin's chemical composition depends on the botanical source and isolation method. Lignin from grasses (e.g., SG) usually possesses all three units (H-, G-, and S-type), whereas softwood lignin (e.g., YP) are primarily composed of G-type units (Yoshida et al., 2004). As shown in **Figure 3** S– and G-units and H-units are clearly observed in the aromatic region of the SG sample, while YP predominantly possess G-units along with a small quantity of H-units. The S-units show strong signals for C_2/H_2 and C_6/H_6 in correlation with δC/δH 103.9/6.65 ($S_{2/6}$), the G-units display strong correlations at δC/δH: 110.9/7.00 (G_2), 115.1/6.72and6.98 (G_5), and 118.7/6.77 (G_6), and the peaks of H-units are observed at 114.8/6.73 ($H_{3,5}$) and 127.8/7.20 ($H_{2,6}$).

Aromaticity, an indicator of a product's quality as well as its thermal stability, was evaluated for the precursors using TGA, as shown in **Figure 4A**. The pyrolysis of both lignin types presents a similar trend of weight loss starting at 200°C, which corresponds to the breaking of the weaker bonds such as hydrogen bonds and C-OH binding (Liu et al., 2015). Decomposition is observed in the range of 200–300°C, which proceeded faster for SG due to its

TABLE 1 | Hydroxyl group contents of YP and SG lignin samples obtained by^{31}P NMR.

Lignin functional group	Chemical shift (ppm)	YP	SG
Internal standard	152.50–151.50	0.20	0.20
Aliphatic OH	150.00–145.00	2.79	2.76
Syringyl OH	145.00–141.00	0.73*	1.07
Guaiacyl OH	141.00–138.50	1.28	0.99
p-hydroxyphenyl OH	138.50–136.50	0.19	0.70
Total phenolic OH	145.00–136.50	2.20	2.76
Carboxylic acid	136.00–133.50	0.48	0.57

**C5-substituted OH*

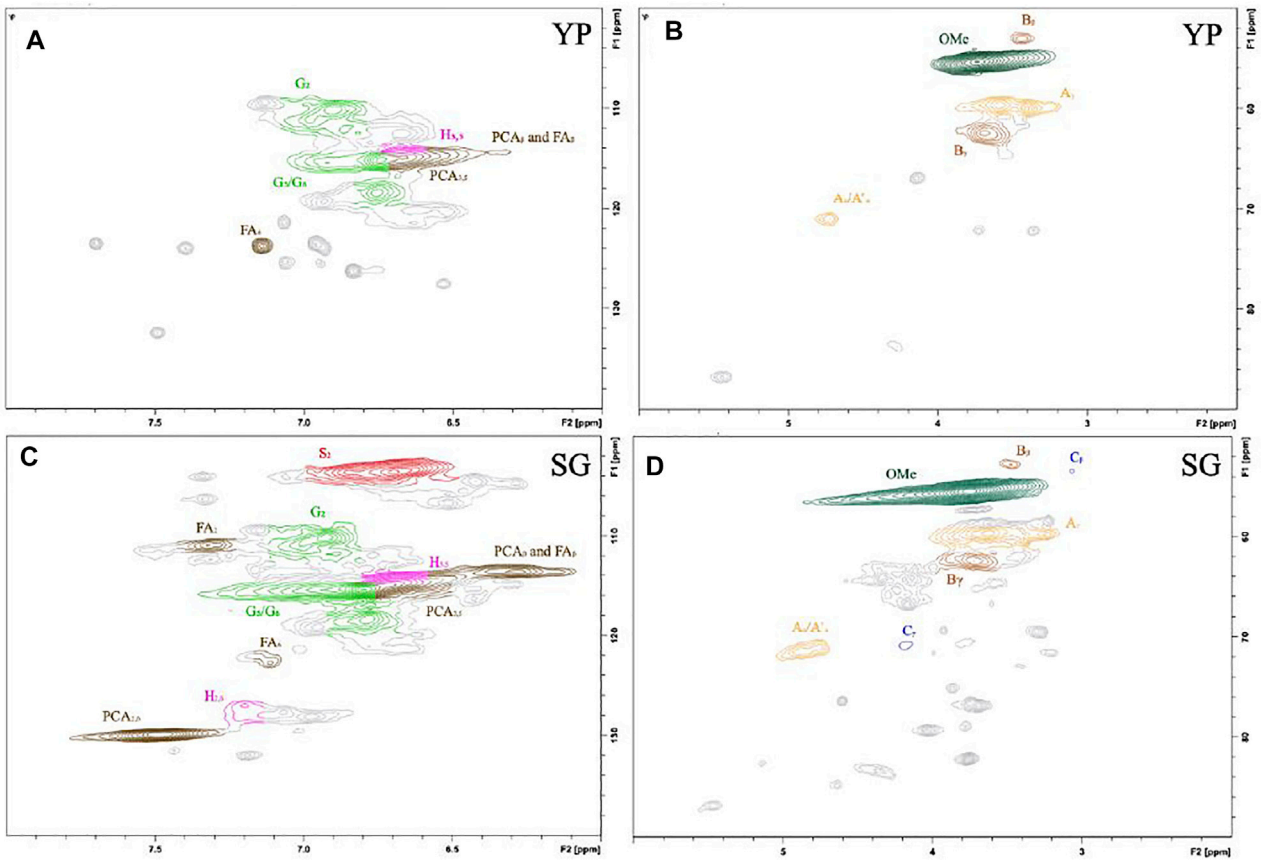

FIGURE 3 | 2D^{13}C-^{1}H NMR spectra for different lignin precursors **(A,B)** YP and **(C,D)** SG.

higher number of linkages. The maximal loss occurs at 380–390°C, where the cleavage of stronger bonds, such as β-O-4 linkages begins to degrade (Liu et al., 2015). The maximal decomposition temperature of YP is higher than that of SG, at 395 and 385°C respectively. This implies that YP lignin is more thermally stable compared to SG lignin with the presence of a more condensed molecular structure. Eventually, a carbon residue forms at 700°C with approximately 40 wt% fixed carbon. **Figure 4B** presents typical DSC curves of both lignin structures, which is used to determine the glass transition behaviors of the lignins. The glass transition temperature (T_g) of SG lignin (155°C) is higher than that of YP lignin (142°C) due to more hydroxyl groups in SG samples. Hydroxyl groups play an important role in affecting the thermal properties of lignin, especially the T_g. The existence of hydroxyl groups leads to the formation of hydrogen bonds that subsequently limits molecular movement (Kubo and Kadla, 2005; Hosseinaei et al., 2017).

3.2 Surface Characteristics of Activated Carbons

Figures 5A,B demonstrate SEM images of pyrolyzed lignin from YP and SG lignin (i.e., YP-py and SG-py) obtained upon thermal pyrolysis at 1,000°C. As illustrated in **Figure 5**, the pyrolyzed lignin exhibits contiguous morphology where the YP-py appears as flat sheets containing numerous cavities, while the SG-py is formed as curved structure. This observation reflects that lignin carbonization occurs during the pyrolysis process, inducing decomposition along with char formation. This dynamic interaction results in releasing gaseous compounds, including oxygen and hydrogen in the form of CO, CO_2, H_2, CH_4, *etc.* (Rodríguez Correa et al., 2017). This promotes the formation of condensable volatiles due to free radicals generated after the cleavage of inner bonds, usually the C–O bond in the *β*- O-4' substructures (Britt, 1995). Of note, S-type lignin includes a higher amount of C–O bonds compared to H- and G-type lignin. The quantitative CHN comparison between these two lignin structures also confirms this trend (i.e., the SG lignin contains higher O/C ratio (~50.4%) than YP (~44.3%), as summarized in **Supplementary Table S2**). This correlation implies the SG lignin is more easily decomposed compared to the YP lignin upon thermal pyrolysis. After pyrolysis, the lignin is converted into char with high carbon content and abundant surface functional groups, but limited surface area (Liu et al., 2015). As shown in **Supplementary Figure S1**, XPS survey-scan spectra confirms the presence of carbon (C 1s) and oxygen (O 1s) in both pyrolyzed lignin samples. In addition, it is notable that

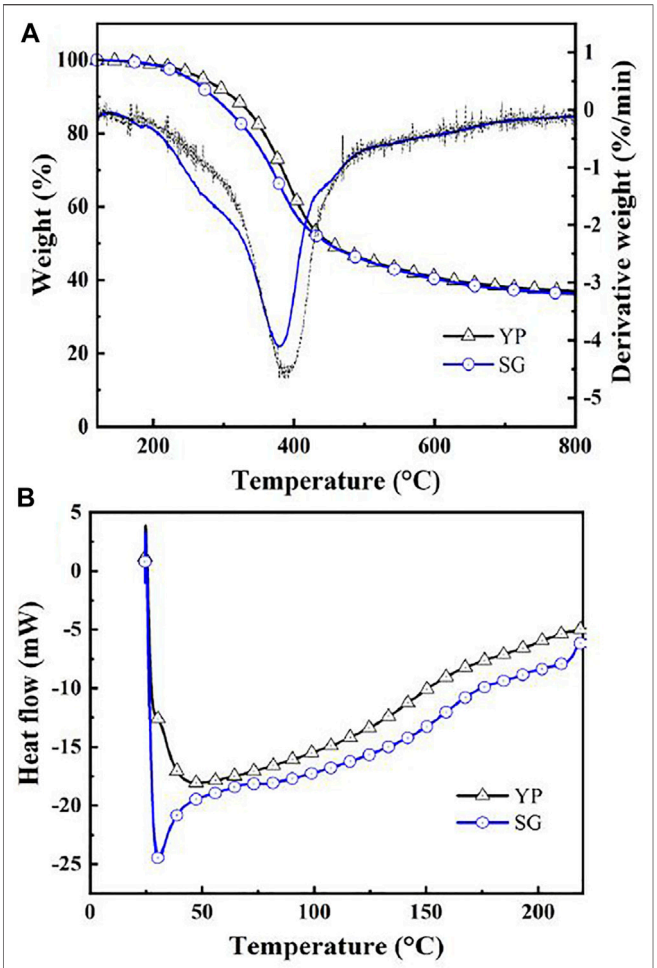

FIGURE 4 | (A) TGA and **(B)** DSC curves of YP and SG lignin precursors.

there is a small amount of inorganic impurity, which is sodium (Na 1s) peak located at ~1,072 eV, in YP-py sample. Elemental analysis shows the O/C ratio of SG-py (~8.1%) is lower than YP-py (~15.2%), and there is ~3.6% Na in YP-py. The surface area obtained by BET measurements of YP-py and SG-py samples are all negligible (YP-py: 0.02 $m^2 g^{-1}$ and SG-py: 0.11 $m^2 g^{-1}$). It is well documented that both surface area and pore volume increase as a result of the activation process (C.-T, 1998). The increase in porosity of YP-AC and SG-AC can be attributed to the opening of closed pores and/or enlarging of the micropores due to gasification of the carbon during the activation process (Kinoshita, 1988).

SEM images of activated carbons prepared from YP and SG lignin are illustrated in **Figures 5C,D**, respectively. According to **Figure 5**, it is obvious that the smaller carbonaceous aggregate size, and greater porosity is present with YP-AC compared with SG-AC. **Supplementary Table S4** includes characteristics of different porous carbons determined from analysis of the N_2 adsorption isotherms at -196°C. Based on BET measurements, the YP-AC sample possesses a specific surface area of ~1,070 $m^2 g^{-1}$, which is approximately two times higher than that of SG-AC (~507 $m^2 g^{-1}$). The YP-AC sample contains a higher percentage of mesopore (~44%), whereas the SG-AC is mainly microporous due to the presence of 89% micropore volume. The DFT method was employed to analyze the full-range pore size distribution of both carbon samples, as shown in **Supplementary Figure S2**. The DFT analysis reveals different pore size distributions within the structure, where the YG-AC sample possesses a sharp peak at the pore size of *ca.* 1–2 nm, and a smaller but broad distribution ranging up to 50 nm, while the SG-AC sample exhibits one major lump at *ca.* 1–2 nm. Since both carbon samples were thermally treated through a similar pyrolysis and two-step activation method, this variation in the morphology of the activated porous electrodes implies that surface area, porosity, and pore size distribution is strongly dependent on the lignin nature.

Physical activation usually involves three mechanisms, including surface burn-off, pore deepening, and pore widening during the carbon gasification (i.e., activation process). For the YP carbon with high O/C ratio, it is more prone to surface burn off and the oxidation reaction induced by the oxygen functional groups that facilitate the pore widening by destroying the microporous structures (Teng and Hsieh, 1998). On the other hand, the extent of carbon agglomeration in YP-py is less than that in SG-py, indicating more surface area of YP-py is accessible to CO_2/H_2O upon activation. More pores could be evenly widened and the closed micropores are allowed to be opened during gasification (Teng et al., 1996). In addition, it has been demonstrated that the presence of Na has a significant catalytic effect during the activation, (Rodrguez-Mirasol et al., 1993; Liu et al., 2015), which contributes to the high surface area of YP-AC. As for the SG carbon, with relatively low O/C ratio, the accessibility of the activation agents, H_2O and CO_2, increases with the extent of the burn-off and subsequently results in a parallel reaction step with pore deepening and pore widening. The difference between the YP and SG chars results in different porosities as well as pore size distributions. Therefore, the O/C ratio, char structure, and inorganic impurities are key factors that lead to highly porous ACs.

Elemental analysis shows that the YP-AC and SG-AC contain high O/C atomic ratios of 7.3 and 10.5%, respectively. This observation reveals that both produced ACs possess high oxidation levels (i.e., many oxygen functionalities attached to porous carbon). XPS spectra (see **Figure 6A,B**) were obtained to confirm the presence of surface functional groups on the carbons. The full spectra are presented in **Figure 6A** with the typical C 1s and O 1s peaks located at ~285 and ~531 eV, respectively. The C 1s peak (shown in **Figure 6B**) was split into three peaks located at 284.6 ± 0.1 eV (C=C or C–C), 286.5 ± 0.1 eV (C-O) and 288.9 ± 0.1 eV (C=O or O-C=O). This result is further confirmed by FTIR spectra, which are displayed in **Figure 6C,D**. The peak occurring at ca. 1,540 cm^{-1} is assigned to the presence of C=C stretching (Tang et al., 2012). The strong peaks in the range of 800–1,300 cm^{-1} are due to stretching of the C–O and–COOH bonds (Yang et al., 2012; Russo et al., 2014; Vinayan et al., 2016). The transmittance peak appears at around 1740 cm^{-1}, mainly originating from the C=O stretch in various functional groups (i.e. ketones, carbonyls, esters, carboxylic acid groups, etc.) (Periasamy et al., 2009;

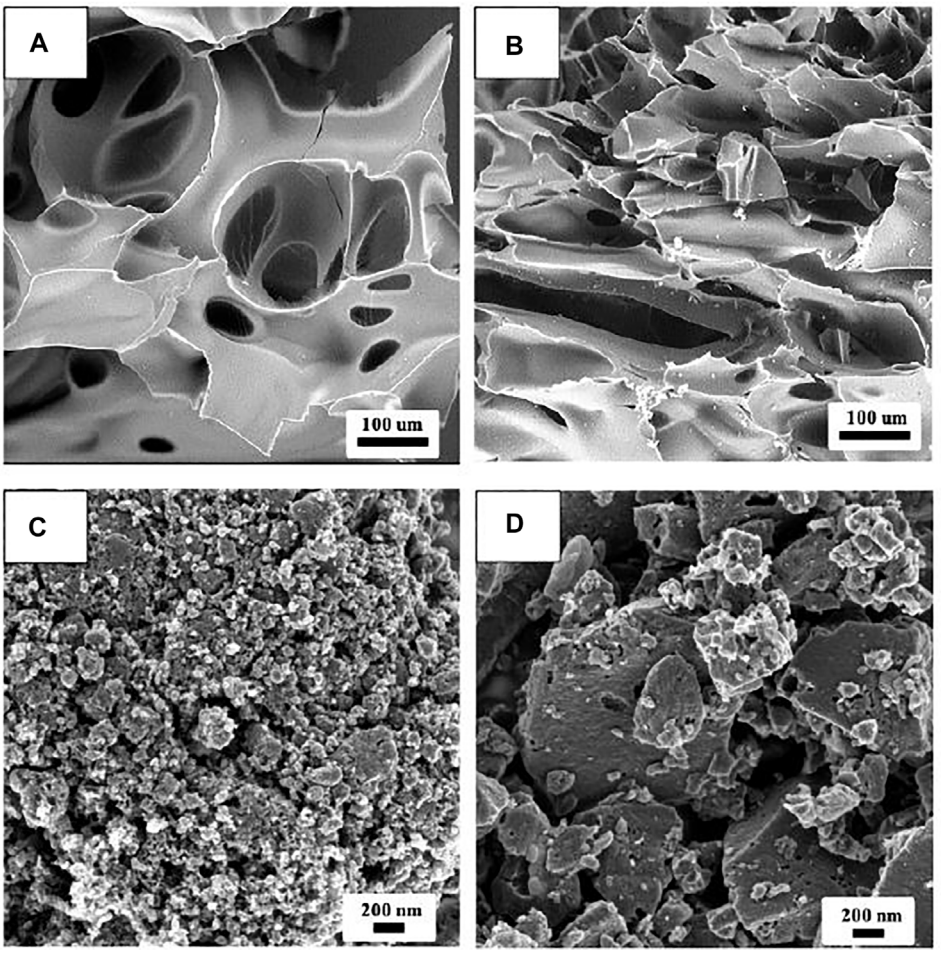

FIGURE 5 | SEM images of different lignin precursors: **(A)** YP-py and **(B)** SG-py and SEM images of different ball-milled AC samples: **(C)** YP-AC and **(D)** SG-AC.

Kharangarh et al., 2018). Based on the FTIR spectra, oxygen functional groups exist on both activated carbons samples, attached to edge or basal plane of carbons.

3.3 Electrochemical Performance of Supercapacitors

Typical CV curves of capacitors assembled with YP and SG carbons were recorded within the potential range of 0–1 V at various sweep rates as illustrated in **Figure 7A,B**. As shown in **Figure 7**, the voltammograms of the carbon electrodes display an obvious pair of redox peaks at 0.3–0.5 V. The CV profiles demonstrate a pseudo capacitance behavior where the induced current increases with increasing sweep rate. Additionally, a rectangular voltammogram, in which the current quickly reaches and maintains a relatively constant magnitude (**Figure 7**) upon reversal of the potential sweep can be maintained, although it shows current leakage at such high sweep rates (e.g., 100 mV s^{-1}) for both capacitors. The current density of the supercapacitors assembled with the YP carbon electrode was higher compared to that of SG electrodes due to larger available surface area of the YP carbon structure, enabling 1) the formation of electric double-layer and 2) the redox reaction in the presence of oxygen functionalities.

The formation of carbon electric double layer with acidic electrolyte and subsequent charge/discharge processes can be formulated using equation (R1) (Zheng et al., 1997; Hsieh and Teng, 2002):

$$C^{*} + H^{+} \leftrightarrow C^{*}//H^{+} \quad \text{(R1)}$$

Here, C* is the active carbon sites, H^{+} represents the protons, and the double layer where the charges accumulated separately on two sides of the interface is shown as//. It formulates a physical adsorption process induced by electrostatic forces between the carbon substrate and the protons. The pseudocapacitance, originated from the oxygen functional groups with electron-accepting properties, such as carbonyl and quinone groups, also induces redox reactions during the electron transfer process (Hsieh and Teng, 2002; Conway, 2013):

$$C_xO^{*} + H^{+} + e^{-} \leftrightarrow C_xOH \quad \text{(R2)}$$

where C_xO^{*} represents carbonyl and quinone groups. Since YP carbon has higher porosity with an increased oxidation level, it

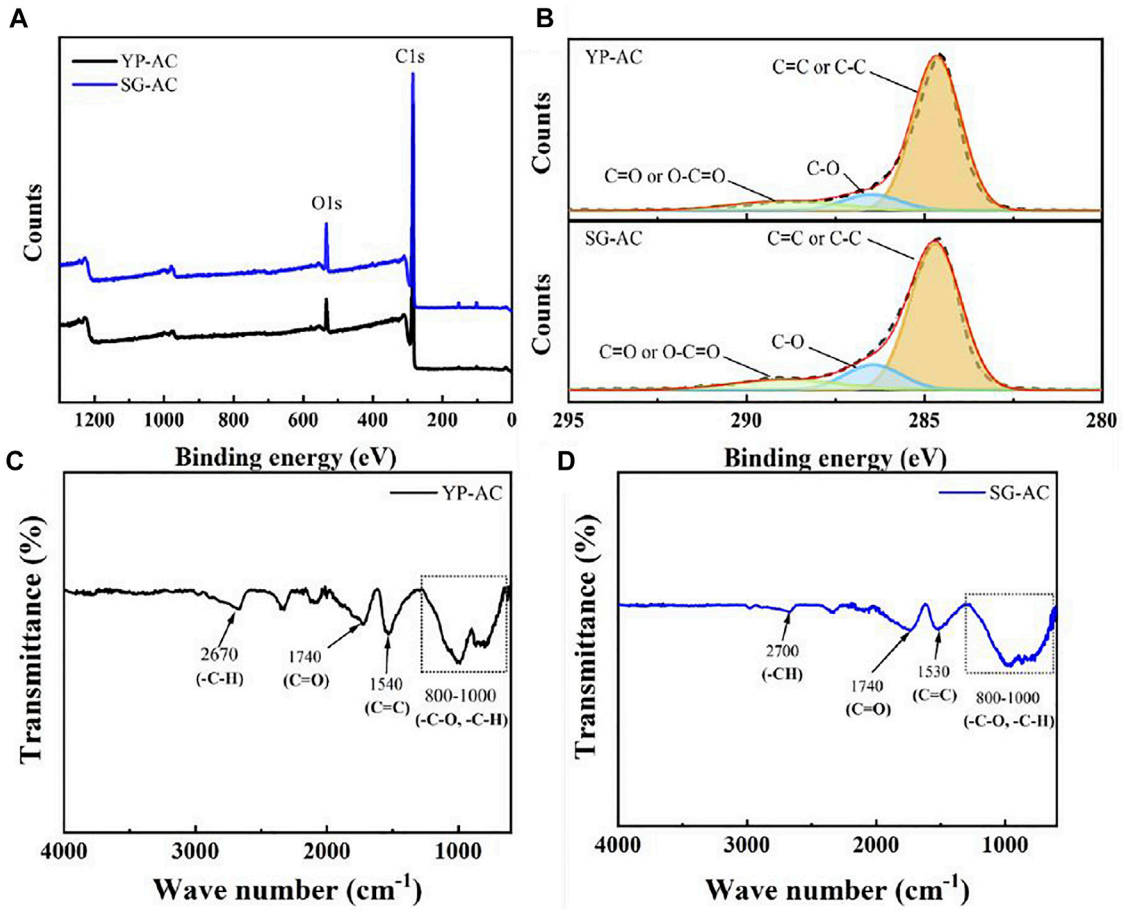

FIGURE 6 | (A) Survey-scan XPS spectra of YP-AC and SF-AC samples, **(B)** C 1s peak of YP-AC and SG-AC samples. FTIR spectra of activated carbons **(C)** YP-AC and **(D)** SG-AC.

provides more hydrophilic sites accessible for the double-layer formation and redox reaction, promoting the progress of (R1) and (R2) reactions.

Figure 8A,B show typical charge-discharge profiles of YP and SG capacitors at 0.5 and 2.5 mA cm^{-2}, respectively. The YP capacitor exhibits higher capacitance for both charge and discharge cycles and demonstrates reduced 'IR drop' at the beginning of discharge. Such a small "IR drop" is mostly due to higher ionic conductivity and lower diffusion resistance of the electrolyte within the porous carbon structure (Conway, 2013). Also, as shown in **Figure 8**, one charge-discharge plateau at 0.4–0.5 V, attributed to the pseudocapacitance from the redox reaction step (R2). The variation of specific capacitance with discharge current density, from 0.1 to 2.5 mA cm^{-2}, is depicted in **Figure 8C**. At 0.1 mA cm^{-2}, the specific capacitances of YP and SG were ~367 and 221 F g^{-1}, respectively. The specific capacitance was found to decrease with increasing discharge current, which displays a trend confirmed by other research (Hsieh et al., 2010).

To assess the stability of as-prepared porous electrodes, extended charge-discharge cycling was performed at 10 mA cm^{-2}. The capacitors equipped with YP-AC and SG-AC electrodes were charged and discharged between 0 and 1 V repeatedly, as shown in **Figure 8D**. Analyzing the variation of discharge capacitance with cycle number revealed that the YP capacitor has superior and stable capacitance (capacitance retention >90%) and exhibits excellent Coulombic efficiency (>99%) over long-term cycling (>10,000 cycles). The weakening of the Faraday reactions after long-term cycling is one of the reasons that cause the slight decrease of capacitance retention (~94%) after 10,000 cycles. We also noticed that both capacitors show the trend during cycling: the capacitance first decreases then increases. We speculate that this phenomenon results from the electrodes needing time to fully wet the complex porous structures, especially at fast charge and discharge rates. YP-AC electrode took a longer time than SG-AC, as the surface area of YP-AC is doubled that of SG-AC.

The EIS technique was employed to analyze the electrochemical behavior of the capacitors assembled with various lignin-based electrodes. The impedance spectra of different capacitors are shown as Nyquist plots in **Figure 9A**.

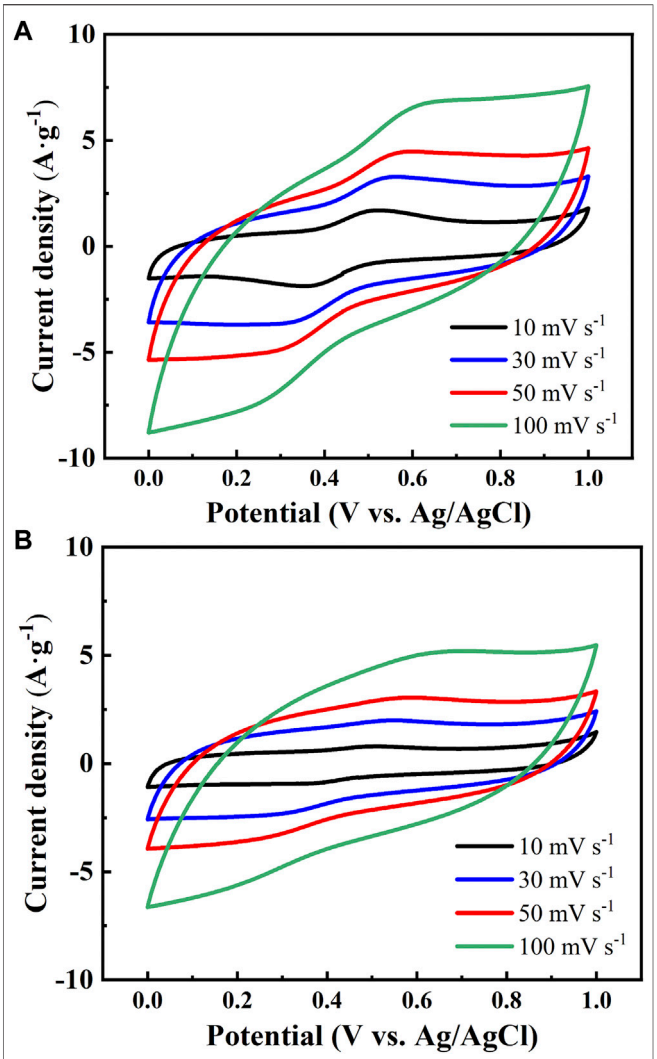

FIGURE 7 | Cyclic voltammetry profiles of **(A)** YP-AC and **(B)** SG-AC electrodes in 1 M H_2SO_4 at different scan rates.

As illustrated in **Figure 9**, the high-frequency intersection with the real axis represents the electrolyte resistance (R_E), followed by a single quasi-semicircle in the high-frequency region (100 kHz - 1 Hz). The semicircle in the high-frequency region is due to combined effect of interfacial resistances (between activated carbon composites and current collector (R_I//C_I)), as well as the charge transfer impedance (R_{CT}//C_{DL}, a double-layer capacitance in parallel with a resistance) (Kinoshita, 1988). The EIS spectra also include a linear regime in the low frequency region corresponding to the capacitive response of the porous carbons (McCreery et al., 1994). The equivalent circuit model used for simulating the impedance behavior of the capacitors is shown in the inset of **Figure 9A**. The *Z*-view software package was adopted for fitting the EIS spectra with the equivalent circuit model. The overall resistance, so-called "equivalent series resistance", R_{ES} (= R_E + R_I + R_{CT}), was composed of the electrolyte resistance, interfacial impedance, and charge transfer resistance. The R_{ES} values were 28.7 and 24.8 Ω for YP and SG capacitors, respectively. The slightly higher R_{ES} value of YP electrode is attributed to higher surface area and more complex porous structure, resulting in the high resistance for charge transfer within the pore structure.

As shown in **Figure 9A**, the Nyquist plot displays an inclined line at low frequencies (<1 Hz), resulting from the solid-state diffusion process of protons within the porous electrodes. Meanwhile, Warburg impedance (Z_D) in the electrodes can be formulated as $Z_D = k_W\ \omega^{-1/2}\ (1 - j)$, based on semi-infinite diffusion model. Here, k_W represents the Warburg coefficient and ω (= $2\pi f$) is the angular frequency (f). **Figure 9B** presents the "Randles plot", Re Z' versus $\omega^{-1/2}$, for both capacitors. The diffusion coefficients (D) determined from the k_W value were 4.77×10^{-10} and 2.16×10^{-10} $cm^2\ s^{-1}$ for the YP and SG capacitors, respectively, detailing the D value of YP capacitor was more than two times higher than that of SG. This finding reveals that the ionic diffusion resistance is significantly alleviated for the YP electrodes, leading to fast redox reaction (i.e., R2) and rapid formation of electric double-layer (i.e., R1) in the mesoporous carbon. Accordingly, the unique pore texture of the YP structure significantly facilitates the electrochemical reactions. Shorter diffusion path, along with increased mesopores and surface area available for energy storage with the YP carbon structure, were the major contributing factors for the improved performance.

3.4 Techno-Economic Analysis

To demonstrate the economic feasibility of the approach, the minimum selling price (MSP) of activated carbons produced by using YP and SG as feedstocks is estimated. Four steps are taken to perform techno-economic analysis.

3.4.1 Process Synthesis

First, a process is designed to convert biomass to activated carbons. The process consists of eight areas as shown in **Figure 10**, resulting in the production of cellulose, furfural, and activated carbons. Fractionations were performed in 1 L reactors with 30% biomass loading scale. The purpose of the biomass fractionation area (A100) is to isolate the solid cellulose fraction from the dissolved hemicellulose and lignin fractions. The liquid fraction from A100, containing C_5 sugars and lignin is sent to lignin recovery area (A200). While GVL solubilizes lignin, by adding water lignin is precipitated, while the C_5 sugars remain soluble. The liquid stream containing C_5 sugars from A200 is concentrated and sent to furfural production area (A300) for converting it to furfural. The effluent stream from the furfural production reactor contains water, GVL, and furfural. To obtain pure furfural as an additional co-product, it needs to be separated from GVL and water. Furfural and water are readily separated from the high-boiling point GVL (208°C), facilitated by the low boiling point of the furfural/water azeotrope. Separation of furfural and water is similar to the distillation step currently used in the commercial production of furfural (Zeitsch, 2000). More details regarding the areas A100, A200, and A300 were previously reported by Alonso et al. (Alonso et al., 2017).

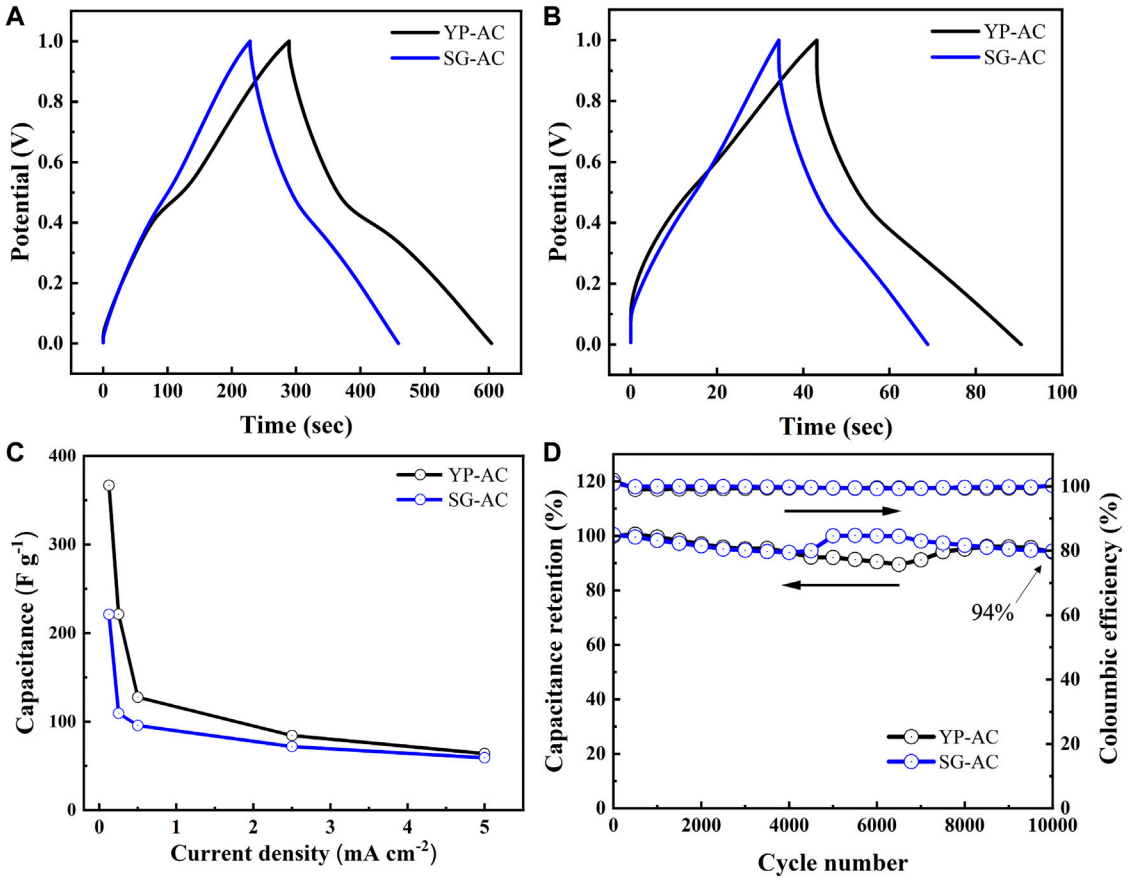

FIGURE 8 | Charge-discharge curves of different capacitors at **(A)** 0.5 and **(B)** 2.5 mA cm^{-2}, **(C)** variation of specific capacitance with current density, and **(D)** cyclic performance of different capacitors at 10 mA cm^{-2}.

Lignin recovered from A200 is sent to the lignin activation area (A400), where it is reduced to activated carbons. Lignin is carbonized in a nitrogen atmosphere at 1,000°C and 1 bar. We assumed that an air separation unit is installed onsite for supplying the required N_2. The required mass ratio of N_2/lignin is 11 for both YP and SG lignin. The reactor effluent contains components in solid and gas phases, which are separated by a cyclone. The activation takes place in a mixed atmosphere of steam and nitrogen in a reactor operating at 800°C and 1 bar. The required mass ratio of gas to inlet solid is 13 for SG and 14.4 for YP lignin. The solids from the second activation reactor are further reduced in the presence of CO_2 in the third reactor operating at 800°C and 1 bar. We assume that the required amount of CO_2 is available for purchase. The mass ratio of solid to gas required for SG and YP lignin are 2.9 and 2.2, respectively. According to the process described 1 MT of YP is converted to 521 kg of cellulose (70% pure), 40 kg of activated carbons, and 50 kg of furfural (99% pure) and 1 MT of SG is converted to 410 kg of cellulose (83% pure), 55 kg of activated carbons, and 149 kg of furfural (99% pure).

Ancillary areas including heat and power generation (A500), wastewater treatment (A600), storage (A700), and utilities (A800) are included in the design. Unrecoverable lignin and natural gas required to meet the process heating and electricity requirements are combusted in A500. Most of the heating demand is met from the evaporators used to recover GVL and distillation columns and the electricity demand is met from the compressors and the air separation unit. The process wastewater streams are treated by anerobic and aerobic digestion in A600. Area A700 is used to store bulk chemicals. Area A800 includes a cooling water system, chilled-water system, process water manifold, and power systems.

3.4.2 Process Modeling

Second, based on experimental results, Aspen Plus process models are developed to estimate material and energy flows. The base design considers annual production rate of 5.5 kton of activated carbons. This production rate is chosen to mitigate the risks associated with initial investment scale and ensure that only a fraction of the current market volume of supercapacitor-grade carbon is produced. The NRTL model is used as the thermodynamic model used for the simulation. The material flow information for the main streams and energy consumption in each process areas are given in **Supplementary Table S5** and

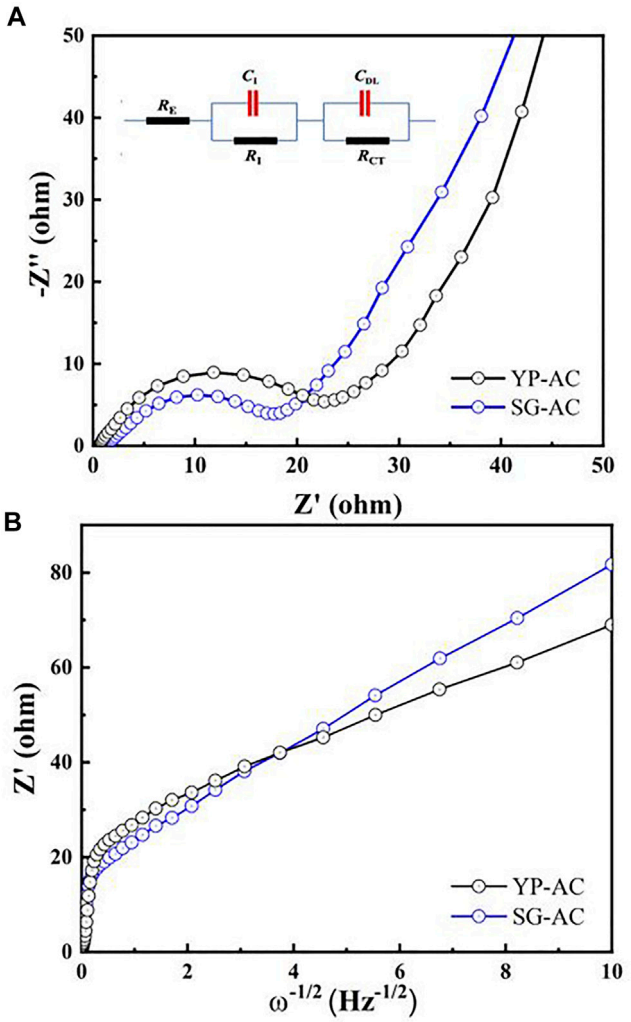

FIGURE 9 | (A) Nyquist plots of different capacitors at OCV, where an equivalent circuit was proposed for describing the impedance behavior within the frequency range between 100 kHz and 1 Hz. **(B)** Randles plots of different capacitors at open circuit voltage.

the process flow diagram of the Aspen Plus model is shown in **Supplementary Figure S3**.

Next, the total energy requirements of the process are estimated after heat integration is performed. The heating, cooling, and power requirements of the process with YP as the feedstock are 10.8, 17.1, and 3.5 MW, respectively. When SG is used as the feedstock, the heating, cooling, and power requirements are 8 MW, 12.4 MW, and 2.5 MW, respectively. A part of the heating and electricity requirements are satisfied by combusting biomass residues and the remaining are satisfied by natural gas.

3.4.3 Estimating Capital and Operating Costs

Third, the capital costs as well as the variable and fixed operating costs are estimated. All equipment costs are adjusted to a common year (2019) using appropriate cost indices. The installed costs of all the areas except A400 are estimated based on the article by Alonso et al. (Alonso et al., 2017) using appropriate scaling factors. Detailed installed equipment costs of A400 are given in **Supplementary Table S6** and a summary of the capital costs of different areas are provided in **Supplementary Table S7**. Total capital investment (TCI) is obtained by adding equipment installed costs to the costs associated with warehouse, site development, piping, office construction, project contingency, etc. (Davis et al., 2018). A summary of different components of TCI is given in **Supplementary Table S8**. The TCI of YP and SG biorefineries are estimated to be $229 million and $189 million, respectively. The main reason for the higher TCI of the YP-based biorefinery is the lower yield of activated carbons. The annual fixed operating costs accounting for salaries, maintenance, and insurance are estimated to be $9.3 million and $8.5 million for YP and SG biorefineries, respectively. Based on the raw material prices listed in **Supplementary Table S9**, the annual variable operating costs of YP and SG biorefineries are estimated to be $15.2 million and $12.1 million, respectively. The main reason for the higher TCI and operating costs of the YP-based biorefinery is the lower yield of activated carbons. Thus, to obtain the produce the same amount of activated carbon, YP-based biorefinery requires larger equipment and more energy to process higher material flows.

3.4.4 Process Economics

Fourth, a discounted cash flow analysis is used to determine the minimum selling price of activated carbons, under the financial assumptions given in **Supplementary Table S10**. The internal rate of return has been set at 30% instead of the typical 10% to reflect the higher risk of investing in a new technology. We assume that cellulose and furfural can be sold as coproducts. In recent years, cellulose price has varied between $700 - $900 per ton (Itlia, 2015). Because of the initial technical risk, a lower selling price of $700/ton is used for the SG-based cellulose. Since cellulose produced using YP is 70% pure, a selling price of $600/ton is assigned. Furfural price has ranged between $1,000-1800 per ton in the recent years (CN Chemicals, 2016). In our analysis, the price of furfural is fixed to $1,000 per ton, which is competitive in the current market. All coproducts (cellulose and furfural) are treated using a market value allocation approach in a consistent manner with the NREL's studies (Biddy et al., 2016).

The results of the analysis are shown in **Figure 11**. The process areas for biomass fractionation, lignin recovery, and heat and power generation are the major cost contributors. The revenues from the production of cellulose and furfural significantly reduce the MSP of activated carbons. The activated carbons from YP and SG can be produced at an MSP of $8,493 and $6,670 per ton, respectively. Notably, the current selling price of supercapacitor-grade activated carbon is $13600/ton (Weinstein and Dash, 2013). The activated carbons produced, especially from YP lignin, demonstrated remarkable electrochemical performance.[49] This illustrates that the

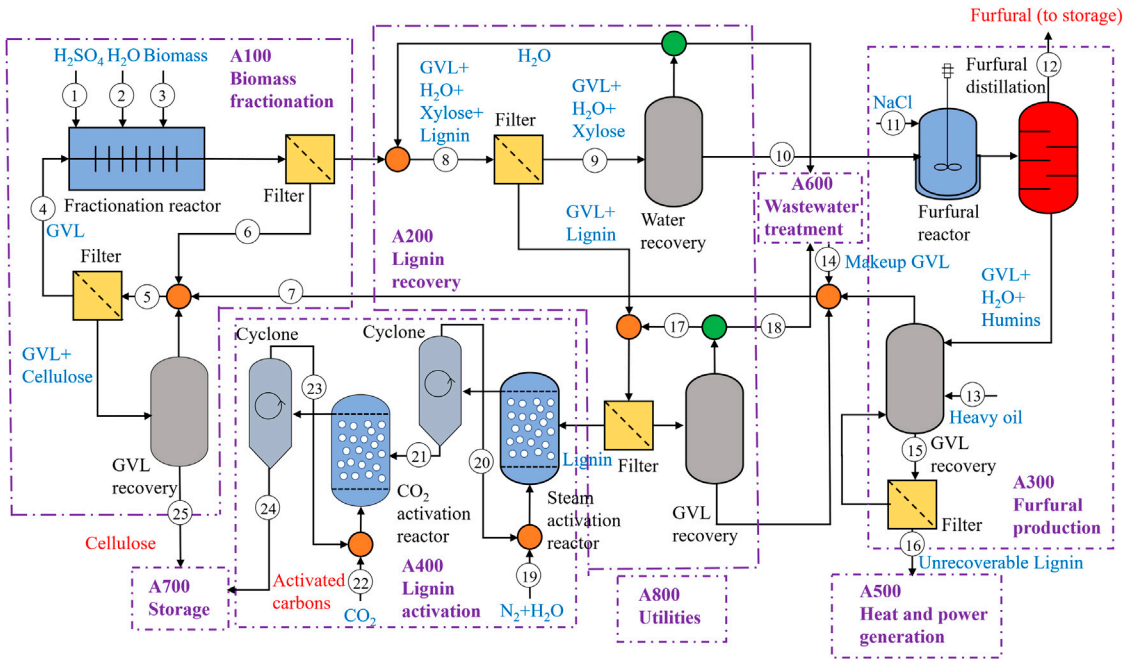

FIGURE 10 | Simplified process flow diagram to produce activated carbons, furfural, and cellulose from biomass.

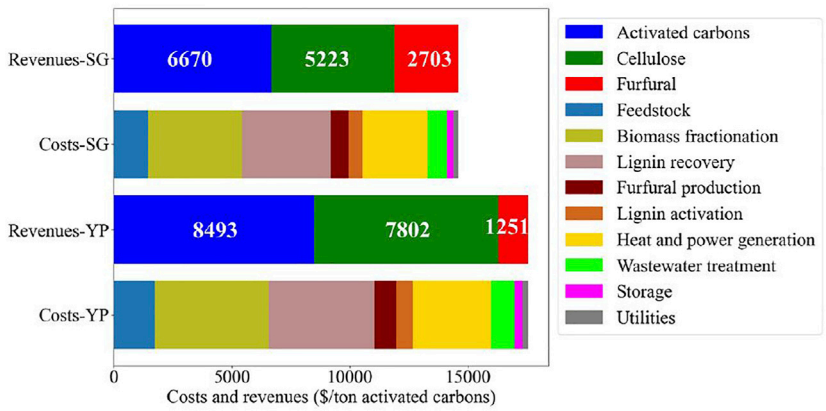

FIGURE 11 | Cost breakdown by process area for SG and YP-based biorefineries.

proposed strategy of utilizing a lignin stream to produce activated carbons is promising and provides an opportunity for successful translation to an economically viable commercial process. The impact of the prices of cellulose and furfural on the MSP of activated carbons (shown in **Figure 12**) was also studied. If the price of cellulose is varied between $500-$1,000/ton and the furfural price varies in the range of $1,000-$1,500/ton, the MSP of YP and SG activated carbons range from $2,666-9,793/ton and $3080-8,162/ton, respectively. Because of the higher yield of furfural from SG, the furfural price impacts the MSP of SG activated carbons to a higher degree than YP-ACs.

4 CONCLUSION

This research employed two types of lignin (YP and SG) as the precursors for synthesizing porous activated carbon electrodes for supercapacitors. The pyrolysis and activation of lignin feedstocks results in porous activated carbons, with surface area and pore size distributions that can be tailored by feedstock choice and processing conditions. The structure of the ACs dictates adsorptive capacity and the diffusion rates of penetrating ions, which are reflected in the electrochemical performance of these materials as supercapacitors. 2D ^{1}H–^{13}C NMR were used to characterize the S/G/H alcohol units of lignin-

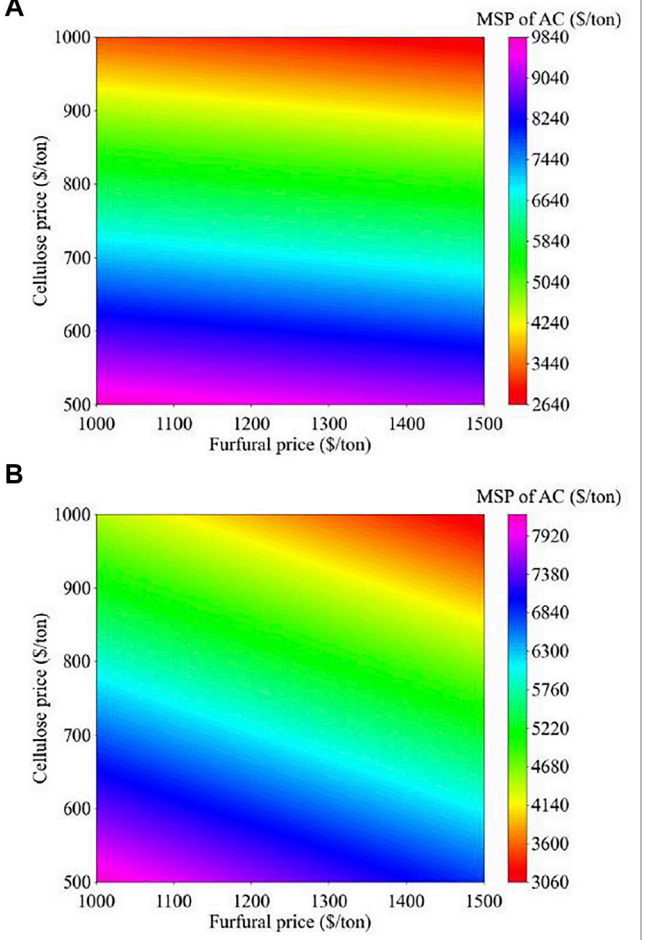

FIGURE 12 | Impact of furfural and cellulose price on the MSP of activated carbons produced in **(A)** YP and **(B)** SG-based biorefineries.

based electrodes, which are important indices in evaluating biochar structures and pore characteristics of the activated carbons. The different O/C ratios, carbon aggregations, and inorganic impurities between the YP and SG chars were determined to be critical factors inducing differing porosities and pore size distributions through a two-step activation process. Higher O/C ratios, less extent of carbon aggregations, and presence of inorganic impurities were easier to achieve for highly porous activated carbon structures. Based on the electrochemical performance of as-prepared electrodes, the specific capacitances of YP and SG capacitors reached 367 and 221 $F\,g^{-1}$, respectively. The YP capacitor displayed stable capacitance (the capacitance retention: > 90%) and excellent Coulombic efficiency (>99%) over 10,000 cycles. Analyzing the Randles plots, the apparent D values, was determined to be 4.77×10^{-10} and 2.16×10^{-10} $cm^2\,s^{-1}$ for the YP and SG capacitors, respectively. This remarkable performance improvement of the YP carbon electrodes was likely the result of a shorter diffusion path and higher available active surface area for energy storage. Techno-economic analysis indicates that YP and SG capacitors can be produced at a minimum selling price of $8,493 and $6,670 per ton, respectively, which is competitive with the price of commercially produced supercapacitors. The novel lignin-based activated porous carbon electrodes developed in this work paves the way for engineering inexpensive and high-performance electrode materials for various electrochemical energy devices.

DATA AVAILABILITY STATEMENT

The raw data supporting the conclusions of this article will be made available by the authors, without undue reservation.

AUTHOR CONTRIBUTIONS

Conceptualization, LY, C-TH, DA, IB, DH; methodology, LY, KS, IB, C-TH, ML, SD, YG, CM, DH; validation, LY, KS, IB, ML, HC.; formal analysis, LY, IB, C-TH, ML; resources, DK, SD, CM, DH; data curation, KS, DH.; writing—original draft preparation, LY, IB; writing—review and editing, KS, DK, DA, C-TH, ML, HC, SD, YG, DH; visualization, LY, IB; supervision, DH, DK, SD, CM; project administration, DH; funding acquisition, DH, DA, CM, SD. All authors have read and agreed to the published version of the manuscript.

FUNDING

This research was supported by a grant from the U.S. Department of Energy BioEnergy Technologies Office through the Biomass Research and Development Initiative award DE-EE0008353.0000. LY received partial support from the Center for Materials Processing, a Tennessee Higher Education Commission (THEC). DH acknowledges support from the USDA National Institute of Food and Agriculture, Hatch Project 1012359.

SUPPLEMENTARY MATERIAL

The Supplementary Material for this article can be found online at: https://www.frontiersin.org/articles/10.3389/fenrg.2022.849949/full#supplementary-material

REFERENCES

Adler, E. (1977). Lignin Chemistry?past, Present and Future. *Wood Sci. Technol.* 11, 169–218. doi:10.1007/bf00365615

Alonso, D. M., Hakim, S. H., Zhou, S., Won, W., Hosseinaei, O., Tao, J., et al. (2017). Increasing the Revenue from Lignocellulosic Biomass: Maximizing Feedstock Utilization. *Sci. Adv.* 3, e1603301. doi:10.1126/sciadv.1603301

Azadi, P., Inderwildi, O. R., Farnood, R., and King, D. A. (2013). Liquid Fuels, Hydrogen and Chemicals from Lignin: A Critical Review. *Renew. Sustain. Energ. Rev.* 21, 506–523. doi:10.1016/j.rser.2012.12.022

Biddy, M. J., Davis, R., Humbird, D., Tao, L., Dowe, N., Guarnieri, M. T., et al. (2016). The Techno-Economic Basis for Coproduct Manufacturing to Enable Hydrocarbon Fuel Production from Lignocellulosic Biomass. *ACS Sustain. Chem. Eng.* 4, 3196–3211. doi:10.1021/acssuschemeng.6b00243

Britt, P. F., Buchanan, A. C., Thomas, K. B., and Lee, S.-K. (1995). Pyrolysis Mechanisms of Lignin: Surface-Immobilized Model Compound Investigation of Acid-Catalyzed and Free-Radical Reaction Pathways. *J. Anal. Appl. Pyrolysis* 33, 1–19. doi:10.1016/0165-2370(94)00846-s

Calvo-Flores, F. G., and Dobado, J. A. (2010). Lignin as Renewable Raw Material. *ChemSusChem* 3, 1227–1235. doi:10.1002/cssc.201000157

Carrott, S. P. J. M., and Ribeiro Carrott, M. M. (2007). Lignin--from Natural Adsorbent to Activated Carbon: A Review. *Bioresour. Technol.* 98, 2301–2312. doi:10.1016/j.biortech.2006.08.008

CN Chemicals (2016). *CCM: Furfural: export price Falls to Record Low in May 2016*. [Online]. Kcomber Inc. Available: http://www.cnchemicals.com/Press/87387-CCM:%20Furfural:%20export%20price%20falls%20to%20record%20low%20in%20May%202016.html (Accessed June 2021).

Conway, B. E. (2013). *Electrochemical Supercapacitors: Scientific Fundamentals and Technological Applications*. Ottawa, Ontario: Springer US.

Das, L., Li, M., Stevens, J., Li, W., Pu, Y., Ragauskas, A. J., et al. (2018). Characterization and Catalytic Transfer Hydrogenolysis of Deep Eutectic Solvent Extracted Sorghum Lignin to Phenolic Compounds. *ACS Sustain. Chem. Eng.* 6, 10408–10420. doi:10.1021/acssuschemeng.8b01763

Davis, R. E., Grundl, N. J., Tao, L., Biddy, M. J., Tan, E. C., Beckham, G. T., et al. (2018). *Process Design and Economics for the Conversion of Lignocellulosic Biomass to Hydrocarbon Fuels and Coproducts: 2018 Biochemical Design Case Update; Biochemical Deconstruction and Conversion of Biomass to Fuels and Products via Integrated Biorefinery Pathways (No. NREL/TP-5100-71949)*. Golden, CO: National Renewable Energy Lab (NREL).

Gosselink, R. J. A., De Jong, E., Guran, B., and Abächerli, A. (2004). Co-ordination Network for Lignin-Standardisation, Production and Applications Adapted to Market Requirements (EUROLIGNIN). *Ind. Crops Prod.* 20, 121–129. doi:10.1016/j.indcrop.2004.04.015

Guerra, A., Lucia, L. A., and Argyropoulos, D. S. (2008). Isolation and Characterization of Lignins from Eucalyptus Grandis Hill Ex Maiden and Eucalyptus Globulus Labill. By Enzymatic Mild Acidolysis (EMAL). *Holzforschung* 62, 24–30. doi:10.1515/hf.2008.004

Han, J., Jeong, S.-Y., Lee, J. H., Choi, J. W., Lee, J.-W., and Roh, K. C. (2018). Structural and Electrochemical Characteristics of Activated Carbon Derived from Lignin-Rich Residue. *ACS Sustain. Chem. Eng.* 7, 2471–2482. doi:10.1021/acssuschemeng.8b05351

Hosseinaei, O., Harper, D. P., Bozell, J. J., and Rials, T. G. (2016). Role of Physicochemical Structure of Organosolv Hardwood and Herbaceous Lignins on Carbon Fiber Performance. *ACS Sustain. Chem. Eng.* 4, 5785–5798. doi:10.1021/acssuschemeng.6b01828

Hosseinaei, O., Harper, D. P., Bozell, J. J., and Rials, T. G. (2017). Improving Processing and Performance of Pure Lignin Carbon Fibers through Hardwood and Herbaceous Lignin Blends. *Int. J. Mol. Sci.* 18, 1410. doi:10.3390/ijms18071410

Hsieh, C.-T., and Lin, Y.-T. (2006). Synthesis of Mesoporous Carbon Composite and its Electric Double-Layer Formation Behavior. *Micropor. Mesopor. Mater.* 93, 232–239. doi:10.1016/j.micromeso.2006.02.017

Hsieh, C.-T., and Teng, H. (2000). Influence of Mesopore Volume and Adsorbate Size on Adsorption Capacities of Activated Carbons in Aqueous Solutions. *Carbon* 38, 863–869. doi:10.1016/s0008-6223(99)00180-3

Hsieh, C.-T., and Teng, H. (2002). Influence of Oxygen Treatment on Electric Double-Layer Capacitance of Activated Carbon Fabrics. *Carbon* 40, 667–674. doi:10.1016/s0008-6223(01)00182-8

Hsieh, C.-T., Chen, W.-Y., and Cheng, Y.-S. (2010). Influence of Oxidation Level on Capacitance of Electrochemical Capacitors Fabricated with Carbon Nanotube/Carbon Paper Composites. *Electrochim. Acta* 55, 5294–5300. doi:10.1016/j.electacta.2010.04.085

Huang, J. B., Patra, J., Lin, M. H., Ger, M. D., Liu, Y. M., Pu, N. W., et al. (2020). A Holey Graphene Additive for Boosting Performance of Electric Double-Layer Supercapacitors. *Polymers (Basel)* 12, 765. doi:10.3390/polym12040765

Itlia, C. (2015). *The International Cellulose Market*. [Online]. Tecniche Nuove Spa. Available at: https://www.paperindustryworld.com/the-international-cellulose-market/(Accessed, June 2021).

Kharangarh, P. R., Umapathy, S., and Singh, G. (2018). Thermal Effect of Sulfur Doping for Luminescent Graphene Quantum Dots. *ECS J. Solid State. Sci. Technol.* 7, M29–M34. doi:10.1149/2.0041803jss

Kilpelaeinen, I., Sipilae, J., Brunow, G., Lundquist, K., and Ede, R. M. (1994). Application of Two-Dimensional NMR Spectroscopy to Wood Lignin Structure Determination and Identification of Some Minor Structural Units of Hard- and Softwood Lignins. *J. Agric. Food Chem.* 42, 2790–2794. doi:10.1021/jf00048a026

Kinoshita, K. (1988). *Carbon: Electrochemical and Physicochemical Properties*. New York: Wiley.

Kubo, S., and Kadla, J. F. (2005). Hydrogen Bonding in Lignin: A Fourier Transform Infrared Model Compound Study. *Biomacromolecules* 6, 2815–2821. doi:10.1021/bm050288q

Liu, X., and Osaka, T. (1997). Properties of Electric Double-Layer Capacitors with Various Polymer Gel Electrolytes. *J. Electrochem. Soc.* 144, 3077–3071. doi:10.1149/1.1837960

Liu, W.-J., Jiang, H., and Yu, H.-Q. (2015). Thermochemical Conversion of Lignin to Functional Materials: a Review and Future Directions. *Green. Chem.* 17, 4888–4907. doi:10.1039/c5gc01054c

McCreery, R. L., Cline, K. K., Mcdermott, C. A., and Mcdermott, M. T. (1994). Control of Reactivity at Carbon Eletrode Surfaces. *Colloids Surf. A.* 93, 211–219. doi:10.1016/0927-7757(94)02899-0

McKendry, P. (2002). Energy Production from Biomass (Part 2): Conversion Technologies. *Bioresour. Techn.* 83, 47–54. doi:10.1016/s0960-8524(01)00119-5

Pandey, M. P., and Kim, C. S. (2011). Lignin Depolymerization and Conversion: A Review of Thermochemical Methods. *Chem. Eng. Technol.* 34, 29–41. doi:10.1002/ceat.201000270

Periasamy, A., Muruganand, S., and Palaniswamy, M. (2009). Vibrational Studies of Na2SO4, K2SO4, NaHSO4 and KHSO4 Crystals. *Rasayan J.Chem.* 2, 981–989. Available at: http://rasayanjournal.co.in/vol-2/issue

Qu, D., and Shi, H. (1998). Studies of Activated Carbons Used in Double-Layer Capacitors. *J. Power Sourc.* 74, 99–107. doi:10.1016/s0378-7753(98)00038-x

Roberts, J. C. (1996). "The Chemistry of Lignin and its Removal," in *The Chemistry of Paper*. Manchester, UK: The Royal Society of Chemistry, 26–51.

Rodrguez-Mirasol, J., Cordero, T., and Rodriguez, J. (1993). Activated Carbons from Carbon Dioxide Partial Gasification of eucalyptus Kraft Lignin. *Energy Fuels* 7, 133–138.

Rodríguez Correa, C., Stollovsky, M., Hehr, T., Rauscher, Y., Rolli, B., and Kruse, A. (2017). Influence of the Carbonization Process on Activated Carbon Properties from Lignin and Lignin-Rich Biomasses. *ACS Sustain. Chem. Eng.* 5, 8222–8233. doi:10.1021/acssuschemeng.7b01895

Rowlandson, J. L., Edler, K. J., Tian, M., and Ting, V. P. (2020). Toward Process-Resilient Lignin-Derived Activated Carbons for Hydrogen Storage Applications. *ACS Sustain. Chem. Eng.* 8, 2186–2195. doi:10.1021/acssuschemeng.9b05869

Russo, P., Hu, A., Compagnini, G., Duley, W. W., and Zhou, N. Y. (2014). Femtosecond Laser Ablation of Highly Oriented Pyrolytic Graphite: A Green Route for Large-Scale Production of Porous Graphene and Graphene Quantum Dots. *Nanoscale* 6, 2381–2389. doi:10.1039/c3nr05572h

Souto, F., Calado, V., and Pereira, N. (2018). Lignin-based Carbon Fiber: a Current Overview. *Mater. Res. Express* 5, 1–30. doi:10.1088/2053-1591/aaba00

Tang, L., Ji, R., Cao, X., Lin, J., Jiang, H., Li, X., et al. (2012). Deep Ultraviolet Photoluminescence of Water-Soluble Self-Passivated Graphene Quantum Dots. *ACS Nano* 6, 5102–5110. doi:10.1021/nn300760g

Teng, H., and Hsieh, C.-T. (1998). Influence of Surface Characteristics on Liquid-phase Adsorption of Phenol by Activated Carbons Prepared from Bituminous Coal. *Ind. Eng. Chem. Res.* 37, 3618–3624. doi:10.1021/ie970796j

Teng, H., Ho, J.-A., Hsu, Y.-F., and Hsieh, C.-T. (1996). Preparation of Activated Carbons from Bituminous Coals with CO2 Activation. 1. Effects of Oxygen Content in Raw Coals. *Ind. Eng. Chem. Res.* 35, 4043–4049. doi:10.1021/ie960170d

Vinayan, B. P., Zhao-Karger, Z., Diemant, T., Chakravadhanula, V. S. K., Schwarzburger, N. I., Cambaz, M. A., et al. (2016). Performance Study of Magnesium-Sulfur Battery Using a Graphene Based Sulfur Composite Cathode Electrode and a Non-nucleophilic Mg Electrolyte. *Nanoscale* 8, 3296–3306. doi:10.1039/c5nr04383b

Weinstein, L., and Dash, R. (2013). Supercapacitor Carbons. *Mater. Today* 16, 356–357. doi:10.1016/j.mattod.2013.09.005

Yang, Z., Yao, Z., Li, G., Fang, G., Nie, H., Liu, Z., et al. (2012). Sulfur-Doped Graphene as an Efficient Metal-free Cathode Catalyst for Oxygen Reduction. *ACS Nano* 6, 205–211. doi:10.1021/nn203393d

Yoshida, T., Oshima, Y., and Matsumura, Y. (2004). Gasification of Biomass Model Compounds and Real Biomass in Supercritical Water. *Biomass Bioenergy* 26, 71–78. doi:10.1016/s0961-9534(03)00063-1

Zeitsch, K. J. (2000). *The Chemistry and Technology of Furfural and its Many By-Products*. Köln, Germany: Elsevier.

Zheng, J. P., Huang, J., and Jow, T. R. (1997). The Limitations of Energy Density for Electrochemical Capacitors. *J. Electrochem. Soc.* 144, 2026–2031. doi:10.1149/1.1837738

Conflict of Interest: Author D. M. A. is employed by Glucan Biorenewables LLC.

The remaining authors declare that the research was conducted in the absence of any commercial or financial relationships that could be construed as a potential conflict of interest.

Publisher's Note: All claims expressed in this article are solely those of the authors and do not necessarily represent those of their affiliated organizations, or those of the publisher, the editors and the reviewers. Any product that may be evaluated in this article, or claim that may be made by its manufacturer, is not guaranteed or endorsed by the publisher.

frontiers | Frontiers in Energy Research

ORIGINAL RESEARCH
published: 08 April 2022
doi: 10.3389/fenrg.2022.868181

Comparative Study on the Pretreatment of Aspen and Maple With 1-Ethyl-3-methylimidazolium Acetate and Cholinium Lysinate

Hemant Choudhary[1,2], *Blake A. Simmons*[1,3] *and John M. Gladden*[1,2]*

[1]Deconstruction Division, Joint BioEnergy Institute, Emeryville, CA, United States, [2]Department of Biomaterials and Biomanufacturing, Sandia National Laboratories, Livermore, CA, United States, [3]Biological Systems and Engineering Division, Lawrence Berkeley National Laboratory, Berkeley, CA, United States

The efficiency of the enzymatic digestibility of certain lignocellulosic biomass has been observed as a function of their structural and chemical changes which in turn depends on the ionic liquid (IL) used as the pretreatment solvent. This study demonstrated and compared the feasibility of the IL pretreatment process for two woody biomasses, namely maple and aspen, using two mechanistically distinct ILs, i.e., 1-ethyl-3-methylimidazolium acetate (C_2mim][OAc]) and cholinium lysinate ([Ch][Lys]) as the solvent. The pretreatment was performed at three different temperatures of 100°C, 140°C, and 160°C at a high solid loading of 25 wt% to understand the impact of lignin content and crystallinity index on enzymatic digestibility. Saccharification of the biomass obtained after the IL pretreatment afforded 30–85% glucan conversions. For aspen, both [C_2mim][OAc] and [Ch][Lys] exhibited the highest glucan conversion at 140°C. For maple, the highest glucan conversion was obtained at 140°C with [C_2mim][OAc], whereas [Ch][Lys] had an optimum glucan conversion at 160°C. These pretreatments resulted in negligible delignification irrespective of the IL used. A significant loss of crystallinity was observed for all [C_2mim][OAc]-pretreated biomasses, whereas the pretreatment with [Ch][Lys] resulted in an increase in the crystallinity index.

Keywords: ionic liquid, woody biomass, enzymatic hydrolysis, biofuel, sustainability, delignification, cellulose crystallinity

OPEN ACCESS

Edited by:
Chen Huang,
Chinese Academy of Forestry, China

Reviewed by:
Zhe Ling,
Nanjing Forestry University, China
Xuelian Zhou,
Nanjing Forestry University, China

***Correspondence:**
John M. Gladden
jmgladden@lbl.gov

Specialty section:
This article was submitted to Bioenergy and Biofuels, a section of the journal Frontiers in Energy Research

Received: *02 February 2022*
Accepted: *11 March 2022*
Published: *08 April 2022*

Citation:
Choudhary H, Simmons BA and Gladden JM (2022) Comparative Study on the Pretreatment of Aspen and Maple With 1-Ethyl-3-methylimidazolium Acetate and Cholinium Lysinate. Front. Energy Res. 10:868181. doi: 10.3389/fenrg.2022.868181

INTRODUCTION

The depletion of fossil resources and stricter environmental regulations, along with an increasing demand for renewable carbon-based fuels and chemicals, have led to the need to find alternatives such as human-inedible lignocellulosic biomass (Bastidas-Oyanedel and Schmidt, 2019; Wang et al., 2020). The use of clean and sustainable energy along with the promotion of decarbonization processes is driving the economic recovery in the energy sectors. For instance, according to the 2021 report on World Total Primary Energy Supply in 2019, biofuels and waste were a leading contributor (>9%) other than non-renewable energy sources (IEA 2021).

Lignocellulosic biomass comprising agricultural, forest, and herbaceous residues serves as a good source for carbon-neutral and renewable carbon resources. Nevertheless, owing to the structural complexity of the constituent cellulose, hemicellulose, and lignin, the facile utilization of biomass is

challenging (Gibson, 2012). Among the various cutting-edge technologies developed to tackle the recalcitrance issues, pretreatment with ionic liquids (ILs, organic salts with a melting point below 100°C) has attracted significant attention (Usmani et al., 2020; Yao et al., 2021).

The properties of ILs including basicity and H-bonding ability can be tuned to dissolve, fractionate, and even convert the lignocellulosic components by changing the ion composition(s) (Yao et al., 2021). This ability of ILs makes them a powerful solvent for lignocellulose processing. For instance, imidazolium-based ILs with adequate basicity of the anion are reported to dissolve cellulose under mild conditions of time and temperature by disrupting the existing interunit H-bonds in cellulose and establishing new H-bonds with the polymer chain (Da Costa Lopes et al., 2018; Jian Sun et al., 2016, Shaoni Sun et al., 2016). However, the major concerns associated with the imidazolium ILs involve high cost, high viscosity, and limited compatibility with the downstream processes. The use of aqueous solutions of imidazolium ILs was suggested as a probable solution to the aforementioned issues. For a non-woody biomass pretreatment with an aqueous solution of 1-ethyl-3-methylimidazolium acetate ($[C_2mim][OAc]$) and 1-butyl-3-methylimidazolium acetate ($[C_4mim][OAc]$), no significant decrease in the pretreatment efficacy was observed with water content up to 40% (Perez-Pimienta et al., 2017).

The search for biocompatible ILs to facilitate a consolidated biomass processing, cholinium cations coupled with amino acid anions [e.g., cholinium lysinate (Ch)(Lys)] were introduced (Sun et al., 2014). This class of ILs was generally found to be less toxic to enzymes and microorganisms than the imidazolium ILs and had a high delignification ability at a higher biomass loading and lower temperatures (Perez-Pimienta et al., 2020; Sun et al., 2014, Jian Sun et al., 2016; Shaoni Sun et al., 2016).

In addition to the pretreatment solvents and efficient processes, the identification of appropriate bioenergy feedstock is equally important given the availability of a variety of lignocellulosic feedstock depending on the geographical location (White, 2010; Gelfand et al., 2020). In this regard, woody biomasses are promising candidates owing to their higher carbohydrate content, availability, abundance, and reduced logistic expenses including storage (Socha et al., 2013; Lauri et al., 2014; Das et al., 2021). Lauri et al. (2014) predicted that woody biomass, if utilized to its full potential, could provide up to 40% of the total global energy consumption in 2050. Nevertheless, woody biomass has a higher lignin content and higher cellulose crystallinity that further complicates the direct or facile utilization for energy (or chemical) applications. This necessitates the development of pretreatment processes to identify potential woody biomass feedstock for sustainable future biorefinery and energy applications.

In this work, we compared the feasibility of IL pretreatment processes for two woody biomasses, namely, maple and aspen, using two mechanistically distinct ILs i.e., $[C_2mim][OAc]$ and [Ch][Lys] (see **Scheme 1**) at different pretreatment temperatures. To the best of our knowledge, no reports exist in the literature studying the effect of temperature on the delignification and crystallinity of aspen and maple during their pretreatment with $[C_2mim][OAc]$ and [Ch][Lys]. Furthermore, saccharification of the pretreated biomass was evaluated as a measure of the pretreatment efficacy and understanding the potential of the woody biomass under study.

EXPERIMENTAL SECTION

Materials

All materials were used as supplied unless otherwise noted. Water was deionized, with a specific resistivity of 18 MΩ cm at 25°C, from Purelab Flex (ELGA, Woodridge, IL). Cholinium lysinate ([Ch][Lys]) was purchased from Proioincs GmbH (Grambach, Austria), while 1-ethyl-3-methylimidazolium acetate ($[C_2mim][OAc]$) was procured from BASF (Ludwigshafen, Germany). Citric acid (ACS reagent ≥99.5%), sodium citrate tribasic dihydrate (ACS reagent, ≥99.0%), and sodium azide were obtained from Sigma-Aldrich (St. Louis, MO). Sulfuric acid (72% and 95–98%) was purchased from VWR. Ethanol (200 proof) was purchased from Decon Labs, Inc. (King of Prussia, PA). Sulfuric acid (72%) was procured from RICCA Chemical Company (Arlington, TX). J. T. Baker, Inc. (Phillipsburg, NJ) supplied hydrochloric acid. Analytical standard grade glucose and xylose were also obtained from Sigma-Aldrich (St. Louis, MO) and used for calibration.

The biomass studied here were aspen and maple, which were dried for 24 h in a 40°C oven. Subsequently, it was knife-milled with a 1 mm screen (Thomas-Wiley Model 4, Swedesboro, NJ). The resulting biomass was then placed in a leak-proof bag and stored in a dry cool place. The moisture content of the dried biomass was determined gravimetrically by subtracting the weight of the oven-dried biomass (105°C, overnight) and starting biomass. The content of extractives was determined using the protocol reported elsewhere (Mansfield et al., 2012).

Commercial cellulase (Cellic® CTec3, 1853 BHU-2-HS g^{-1}, 1.212 g ml^{-1}) and hemicellulase (Cellic® HTec3, 1760 FXU g^{-1}, 1.210 g ml^{-1}) mixtures were provided by Novozymes, North America (Franklinton, NC).

Compositional Analysis

All compositional analysis experiments were conducted in duplicate. The compositional analysis of the biomass before and after pretreatment was performed using the National Renewable Energy Laboratory (NREL) two-step acid hydrolysis protocols (LAP) LAP-002 and LAP-005 (Sluiter et al., 2011). Briefly, 300 mg of extractive-free biomass and 3 ml of 72% sulfuric acid (H_2SO_4) were incubated at 30°C while shaking at 200 rpm for 1 h. The solution was diluted to 4% H_2SO_4 with 84 ml of DI water and autoclaved at 121°C for 1 h. The reaction was quenched by cooling down the flasks before removing the solids by filtration using medium-porosity filtering crucibles. The filtrates were spectrophotometrically analyzed for the acid-soluble lignin or ASL (NanoDrop 2000; Thermo Fisher Scientific, Waltham, MA) using the absorbance at 240 nm. Additionally, monomeric sugars (glucose and

xylose) were determined by HPLC using an Agilent 1200 series instrument equipped with a refractive index detector and a Bio-Rad Aminex HPX-87H column. An aqueous solution of H_2SO_4 (4 mM) was used as the mobile phase (0.6 ml min^{-1}, column temperature 60°C) for the separation of products (total run time being 20 min). The amount of glucan and xylan was calculated from the glucose and xylose content multiplied by the anhydro correction factors of 162/180 and 132/150, respectively. Finally, acid-insoluble lignin was quantified gravimetrically from the solid after heating overnight at 105°C (the weight of acid-insoluble lignin and ash) and then at 575°C for at least 6 h (the weight of ash).

Biomass Pretreatment With [C_2mim][OAc]

All pretreatment reactions were conducted in duplicate. Aspen or maple samples of 1 mm and [C_2mim][OAc] were mixed in a 1:3 ratio (w/w) to afford a biomass loading of 25 wt% in a 38 ml capped glass pressure tube and pretreated for 3 h in an oil bath heated at 100, 140, and 160°C, respectively. After pretreatment, the samples were removed from the oil bath and allowed to cool. A measure of 10 ml DI water was slowly added to the biomass-IL slurry and mixed well. The mixture was transferred to 50 ml Falcon tubes and the pressure tubes were washed with additional water to obtain a total volume of 40 ml. The mixture was centrifuged at high speed (4000 rpm) to separate solids and remove any residual IL. The water-washed solid was freeze-dried to obtain dried pretreated biomass for further analysis.

Biomass Pretreatment With [Ch][Lys]

All pretreatment reactions were conducted in duplicate. The 1 mm aspen or maple samples, [Ch][Lys], and DI water were mixed in a 5:2:13 ratio (w/w) to afford a biomass loading of 25 wt % in a 38 ml capped glass pressure tube and pretreated for 3 h in an oil bath heated at 100, 140, and 160°C. After pretreatment, the samples were removed from the oil bath and allowed to cool. Then 10 ml DI water was slowly added to the biomass-IL slurry and mixed well. The mixture was transferred to 50 ml Falcon tubes and the pressure tubes were washed with additional water to obtain a total volume of 40 ml. The mixture was centrifuged at high speed (4000 rpm) to separate solids and remove any residual IL. The water-washed solid was freeze-dried to obtain dried pretreated biomass for further analysis.

Enzymatic Saccharification

All enzymatic saccharification was conducted in duplicate. Enzymatic saccharification of the pretreated biomass was carried out using commercially available enzymes, Cellic® CTec3 and HTec3 (9:1 v/v) from Novozymes, at 50°C in a rotary incubator (Enviro-Genie, Scientific Industries, Inc.). All the reactions were performed at 2.5 wt% biomass loading in a 15 ml glass tube. The pH of the mixture was adjusted to 5 with 50 mM sodium citrate buffer supplemented with 0.02% sodium azide to prevent microbial contamination. The total reaction volume included a total protein content of 10 mg per g biomass. The amount of sugar released was measured by HPLC as described previously.

TABLE 1 | Compositions of the biomass employed in this study.

	Aspen	Maple
Moisture	5.76 ± 0.01	6.64 ± 0.03
Extractives	6.82 ± 0.02	6.92 ± 0.08
Glucan	41.85 ± 0.08	36.63 ± 0.79
Xylan	15.32 ± 0.38	13.97 ± 1.13
ASL	6.15 ± 0.15	6.31 ± 0.20
AIL	18.50 ± 0.05	21.69 ± 0.44
Ash	0.71 ± 0.31	1.10 ± 0.26

ASL, acid-soluble lignin; AIL, acid-insoluble lignin

Powder X-Ray Diffraction Analysis

The crystallinity index of untreated and pretreated biomass was analyzed using a PANalytical Empyrean X-ray diffractometer equipped with a PIXcel3D detector and operated at 45 kV and 40 mA using Cu Kα radiation (λ = 1.5418 Å). The diffraction patterns were collected in the 2θ range of 5–55° with a step size of 0.026° and an exposure time of 300 s. A reflection-transmission spinner was used as a sample holder and the spinning rate was set at 8 rpm throughout the experiment. The crystallinity index (CI) was determined from the crystalline and amorphous peak areas of the measured diffraction patterns using the following equation as reported previously (Park et al., 2010).

$\%CI = [(I_{002} — I_{am})/I_{002}]*100$, where I_{002} is the intensity of the crystalline plane (002) and I_{am} is the minimum between (002) and (101) peaks and is at about 18°.

RESULTS AND DISCUSSION

The composition of the two woody biomasses, namely, aspen and maple, were determined as per the NREL protocol and the results are summarized in **Table 1**. There were <7% extractives found to be present in both biomasses. Higher glucan content of 41.85% was found in aspen compared with that of 36.63% glucan in maple. On the other hand, the acid-insoluble lignin (or AIL) content was higher in maple amounting to 21.69% compared to 18.5% in aspen.

Solid Recovery and Composition

As described earlier, pretreatment is a critical step to enhance the accessibility of the cellulosic component of the biomass. In general, the effective pretreatment of woody biomasses with both [C_2mim][OAc] and [Ch][Lys] has been reported at temperatures between 90 and 160°C, mostly with a time interval of 3 h to achieve high sugar yields (Sun et al., 2014; Yoo et al., 2017; Usmani et al., 2020; Das et al., 2021; Yao et al., 2021). The influence of the temperature was examined on the pretreatment efficacy of the ILs under investigation on aspen and maple as a function of solid recovery and biomass composition. In this study, we have chosen three pretreatment temperatures 100, 140, and 160°C, respectively. Although a higher temperature has been shown to favor delignification and thus a higher sugar yield, the stability of the IL at higher temperatures is always a subject to consider. It should be noted that we expect a small

TABLE 2 | Compositional analysis of aspen and maple after IL pretreatments at different temperatures.

Pretreatment			Composition of biomass (%)			% Loss/removal		
IL	T (°C)	Solid recovery (%)	Glucan	Xylan	AIL	Glucan	Xylan	AIL
			Aspen					
-[a]			41.8 ± 0.1	15.3 ± 0.4	18.5 ± 0.1			
[C_2mim][OAc]	100	90.0 ± 0.5	36.7 ± 0.1	13.6 ± 0.6	16.9 ± 0.2	21.0 ± 0.2	20.0 ± 0.2	17.8 ± 0.3
	140	81.4 ± 0.7	44.4 ± 0.1	13.5 ± 0.0	16.3 ± 0.1	13.5 ± 0.7	28.2 ± 0.1	28.3 ± 0.7
	160	80.5 ± 0.1	42.1 ± 0.3	13.7 ± 0.1	18.4 ± 2.9	18.9 ± 2.19	27.9 ± 0.1	19.9 ± 0.2
[Ch][Lys]	100	88.9 ± 1.1	41.1 ± 0.8	15.1 ± 0.3	16.5 ± 0.9	12.6 ± 0.0	12.3 ± 0.6	20.7 ± 0.1
	140	88.3 ± 0.2	45.0 ± 0.4	15.1 ± 0.4	16.7 ± 1.4	4.9 ± 0.2	12.9 ± 0.2	20.3 ± 0.2
	160	67.3 ± 1.4	44.2 ± 0.8	15.2 ± 1.4	13.8 ± 0.4	28.8 ± 0.1	33.1 ± 0.0	49.8 ± 2.9
			Maple					
-[a]			36.6 ± 0.8	14.0 ± 1.1	21.7 ± 0.4			
[C_2mim][OAc]	100	88.7 ± 0.9	38.8 ± 0.0	15.9 ± 0.0	20.2 ± 0.1	6.0 ± 0.1	-0.7 ± 0.3	17.4 ± 0.7
	140	80.9 ± 2.5	41.5 ± 0.4	13.0 ± 0.1	19.1 ± 0.4	8.3 ± 0.0	24.9 ± 0.1	28.8 ± 0.2
	160	84.9 ± 0.6	31.5 ± 1.4	10.6 ± 1.0	22.9 ± 0.4	26.9 ± 1.2	35.7 ± 0.5	10.4 ± 1.1
[Ch][Lys]	100	89.4 ± 0.9	39.2 ± 0.2	15.4 ± 0.0	21.4 ± 0.1	4.2 ± 0.3	1.7 ± 0.2	11.8 ± 0.2
	140	84.8 ± 1.3	39.0 ± 0.0	14.3 ± 0.1	19.5 ± 0.3	9.6 ± 0.6	13.4 ± 0.3	23.8 ± 0.6
	160	66.9 ± 3.6	40.9 ± 0.8	14.6 ± 0.1	17.2 ± 0.5	25.2 ± 0.1	30.2 ± 0.3	47.0 ± 0.5

Biomass loading (25 wt%), 3 h. [C_2mim][OAc] loading (75 wt%). [Ch][Lys] loading (10 wt%) along with 65 wt% water.
[a]*Untreated biomass.*

percentage of both [C_2mim][OAc] and [Ch][Lys] to decompose when heated at 160°C for 3 h (Clough et al., 2013; Yao et al., 2021).

The glucan, xylan, and AIL content of aspen and maple before and after pretreatment with [C_2mim][OAc] and [Ch][Lys] at 100, 140, and 160°C, respectively, for 3 h is tabulated in **Table 2**. While considering the amount of dried biomass recovered after pretreatment with ILs followed by washing (see Experimental Section for details), termed here as solid recovery, a significant impact of temperature was observed for [Ch][Lys]-based pretreatments. For both aspen and maple, a high solid recovery between 80 and 90% was afforded under all temperature conditions with [C_2mim][OAc] and at 100 and 140°C with [Ch][Lys]. Only ~67% solids were recovered after pretreatment of these woody biomasses with [Ch][Lys] at 160°C. In general, [C_2mim][OAc] is reported to have a higher solid recovery for woody biomass irrespective of the temperature employed for the pretreatment (Torr et al., 2016), whereas [Ch][Lys] is reported to have lower solid recovery at higher pretreatment temperatures (Sun et al., 2014; Yao et al., 2021).

The carbohydrate (including glucan and xylan) and lignin amount of the IL-pretreated biomass was also determined to understand the impact of pretreatment as a function of IL and pretreatment temperature. Interestingly, the carbohydrate and lignin content was found to be similar to that of the untreated aspen and maple woody biomass. For aspen, the glucan, xylan, and AIL content were in the range of 36–45%, 13–15%, and 13–18%, respectively, compared with the 41.8, 15.3, and 18.5% glucan, xylan, and AIL content in untreated aspen. Similarly, untreated maple contained 36.6% glucan, 14% xylan, and 21.7% AIL, whereas the IL-pretreated samples were composed of 31–42% glucan, 10–16% xylan, and 17–23% AIL (see **Table 2**).

To realize the actual loss or removal of the holocellulosic or lignin component, the percentage removal of each component was also calculated as follows:

$$\%\text{Removal} = \left[100 - \left\{\left(\%\text{solid recovery}\right)* \left(\text{composition of the pretreated biomass}/\text{composition of the untreated biomass}\right)\right\}\right].$$

Although the carbohydrate and lignin content were similar for the untreated and IL-pretreated biomasses, the inclusion of solid recovery into the calculation in the form of percentage removal highlighted the differences between the efficacies of the pretreatment. In general, a higher loss of glucan, xylan, and AIL was observed at 160°C. Overall, [C_2mim][OAc] pretreatment resulted in higher loss of glucan (up to 27%) and xylan (up to 36%), whereas [Ch][Lys] removed up to 47% AIL from maple wood. On the contrary, in the case of aspen, [Ch][Lys] pretreatment resulted in the maximum loss of glucan (28.8%), xylan (33.1%), and AIL (49.8%). These result of higher lignin removal by [Ch][Lys] in comparison to the [C_2mim][OAc] was consistent with the previous reports (Sun et al., 2014; Usmani et al., 2020; Yao et al., 2021). It should be noted that [C_2mim][OAc] was reported to dissolve higher amounts of lignin compared with [Ch][Lys], but the use of water (anti-solvent) to remove the IL crashes out the soluble biopolymers in the solution in the case of [C_2mim][OAc]. On the

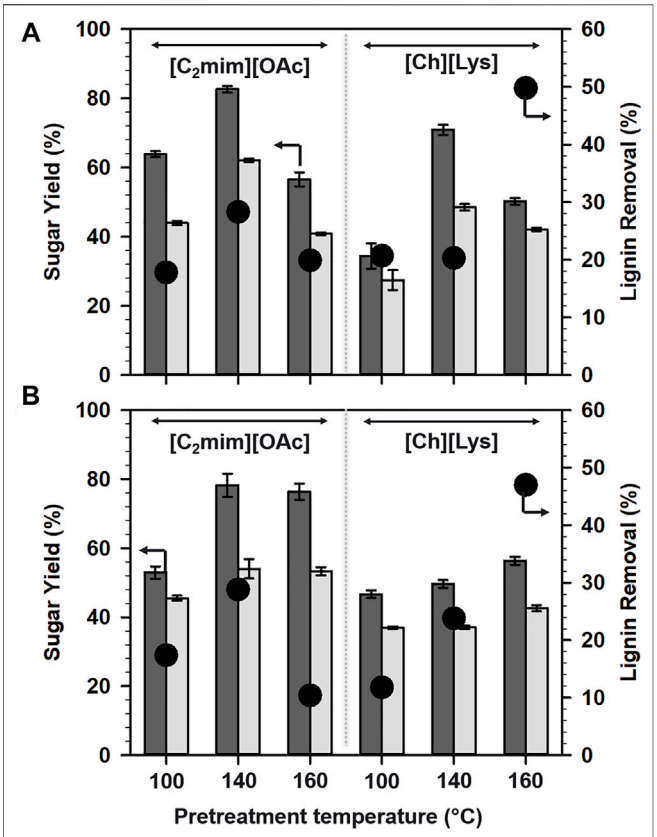

FIGURE 1 | Sugar yields from **(A)** aspen and **(B)** maple after IL pretreatments at different temperatures. Glucose (dark gray bars) and xylose (light gray bars). The percentage of lignin removal is shown in black closed circles.

other hand, [Ch][Lys] with a higher pK_a value than [C_2mim][OAc] results in higher removal of lignin from the slurry when washed with water.

Saccharification of the Pretreated Residues

To further elucidate the impact of IL pretreatment on the woody biomass, the glucan, and xylan digestibility was measured using commercial enzyme cocktails (Novozymes Cellic CTec3 and HTec3) as shown in **Figure 1**. The saccharification of the pretreated biomass was carried out at a protein loading of 10 mg per g of biomass at 50°C for 72 h.

Among [C_2mim][OAc]- and [Ch][Lys]-based pretreatments, [C_2mim][OAc] pretreatment enhanced the glucan digestibility and hence, glucose yields. Interestingly, the pretreatment of aspen at 160°C was not favorable for higher sugar release for both ILs under study (**Figure 1A**). The yields of glucose after pretreatment with [C_2mim][OAc] was in the following order: 140°C (82.7%) > 100°C (63.9%) > 160°C (56.6%). However, the glucan digestibility after [Ch][Lys] pretreatment of aspen follows the order: 140°C (70.9%) > 160°C (50.2%) > 100°C (34.4%).

In the case of maple (**Figure 1B**), the highest glucose yield, that is 78.2%, was achieved at 140°C after the pretreatment with [C_2mim][OAc] and the order of the glucose yields could be summarized as 140°C (78.2%) > 160°C (76.4%) > 100°C (53%). Switching the pretreatment solvent from [C_2mim][OAc] to [Ch][Lys] demanded a higher temperature to release sugar from the pretreated biomass, 160°C (56.4%) > 140°C (49.6%) > 100°C (46.7%).

Because lignin is considered to limit cellulose accessibility, delignification (or lignin removal) is the most common strategy to improve cellulose accessibility. Consequently, the amount of lignin removal was plotted against the sugar yield, however, no significant relationship was derived from the plots. This indicated that factors other than lignin removal govern the saccharification of the woody biomass.

Xylose yields were also observed to have a trend similar to glucose yields and were in the range of 27–62%. For both [C_2mim][OAc] and [Ch][Lys]-pretreated aspen solids, maximum xylose yields were attained at 140°C (**Figure 1A**). For maple (**Figure 1B**), 140°C was found to be optimal for maximum xylose when pretreated with [C_2mim][OAc], whereas pretreatment with [Ch][Lys] was more effective at 160°C.

Crystallinity of the Pretreated Residues

A majority of the effort in the lignocellulosic pretreatment has been made to disrupt the crystallinity of cellulose and enhance the accessibility for an accelerated conversion (Park et al., 2010; Karimi and Taherzadeh 2016; Baruah et al., 2018; Pena et al., 2019; Usmani et al., 2020). PXRD patterns were recorded for untreated and IL-pretreated biomass to determine the crystalline (cellulose forms and the degree of crystallinity) and non-crystalline components (amorphous cellulose, hemicellulose, and lignin). A change in the crystallinity index is an indication of structural changes, however, the crystallinity of the overall biomass depends on both 1) amount of crystalline cellulose dissolved and precipitated during biomass pretreatment, and 2) loss of non-crystalline components during washing of the pretreatment solvent (IL in the present study).

PXRD patterns of untreated and IL-pretreated woody biomass were plotted as shown in **Figure 2**. As shown in **Figures 2A,C**, [C_2mim][OAc]-pretreated woody biomass was highly amorphous after the IL-pretreatment. This could be explained based on the H-bond disruption ability of [C_2mim][OAc] to swell and/or dissolve cellulose in the lignocellulosic biomass (Swatloski et al., 2002). Typically, for any given biomass, maxima at 2θ = ~16° is assigned to the (101) plane of the cellulose I form, while the dominant (002) plane of cellulose II form is observed at 2θ = ~22°. Pretreatment with [C_2mim][OAc] resulted in the disappearance of the (101) plane with an increase in the pretreatment temperature resulting in a broad peak around 2θ = 20°. These patterns are clearly different from the untreated biomass and indicate the disruption of interunit H-bonding in crystalline cellulose of woody biomass.

On the other hand, [Ch][Lys]-pretreated samples (**Figures 2B,D**) were less amorphous compared with the untreated biomass accounted for by the loss of non-crystalline components. The peak for the crystalline component (002) plane of cellulose II increased in intensity with the increase in temperature suggesting a decrease in the non-crystalline

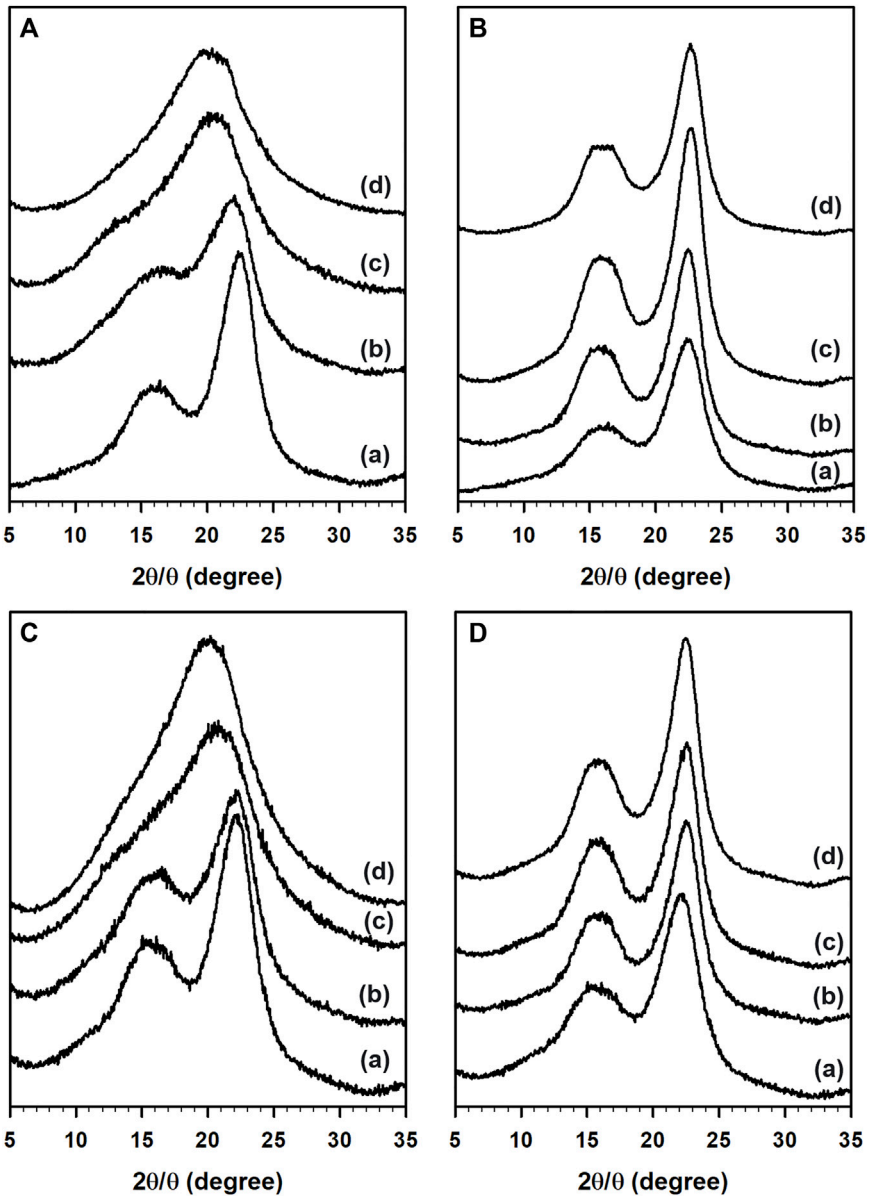

FIGURE 2 | PXRD patterns of aspen (top; **(A,B)**) and maple (bottom; **(C,D)**) in the presence of [C_2mim][OAc] (left; **(A,C)**) and [Ch][Lys] (right; **(B,D)**). **(A)** Untreated biomass and pretreatment at **(B)** 100°C, **(C)** 140°C, and **(D)** 160°C.

components from the woody biomass. This agreed with the compositional data of the IL-pretreated woody biomass shown in **Table 2**.

The crystallinity index of untreated and pretreated biomass was calculated as reported previously (Park et al., 2010) and plotted as shown in **Figure 3**. The crystallinity index of the untreated and IL pretreated maple was in the following order: [Ch][Lys]/160°C (57.5%) ~ [Ch][Lys]/140°C (58.3%) > [Ch][Lys]/100°C (55.8%) > untreated maple (47.7%) > [C_2mim][OAc]/100°C (34.7%) >> [C_2mim][OAc]/140°C (19.1%) > [C_2mim][OAc]/160°C (13.9%). Similar to this trend, the crystallinity index of untreated and pretreated aspen was in the following order: [Ch][Lys]/160°C (62.1%) ~ [Ch][Lys]/140°C (61.7%) > [Ch][Lys]/100°C (60.2%) > untreated aspen (55.8%) > [C_2mim][OAc]/100°C (34.3%) >> [C_2mim][OAc]/140°C (20.2%) > [C_2mim][OAc]/160°C (16.9%).

CONCLUSION

In summary, the pretreatment efficacy of two woody biomass (aspen and maple) with two distinct ILs ([C_2mim][OAc] and [Ch][Lys]) was compared at three different temperatures. Pretreatment with [C_2mim][OAc] afforded the highest

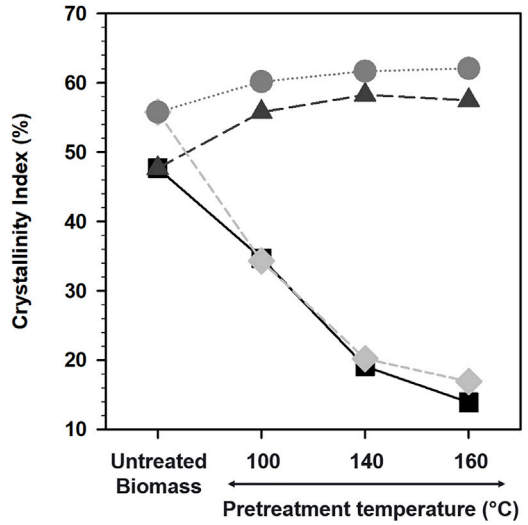

FIGURE 3 | Crystallinity index of biomass pretreated with [C_2mim][OAc] and [Ch][Lys] at different temperatures. Maple pretreated with [C_2mim][OAc] (black squares), maple pretreated with [Ch][Lys] (dark gray triangles), aspen pretreated with [Ch][Lys] (gray circles), and aspen pretreated with [C_2mim][OAc] (light gray diamonds).

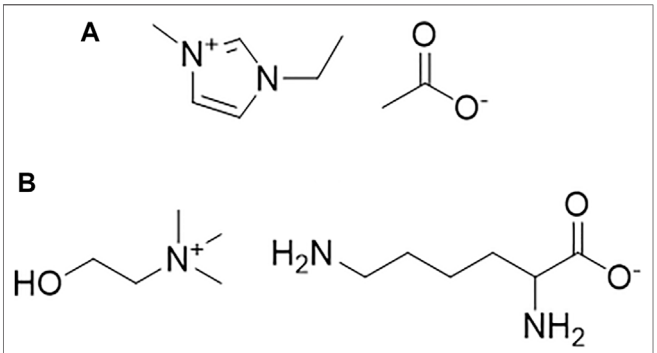

SCHEME 1 | Chemical structures of **(A)** 1-ethyl-3-methylimidazolium acetate ([C_2mim][OAc]) and **(B)** Cholinium lysinate ([Ch][Lys]).

sugar yields for both aspen and maple. At 140°C, 82.7% glucose and 62.1% xylose were released from aspen, whereas 78.2% glucose and 54% xylose yields were obtained. The comparisons of the IL at different temperatures suggested aspen to be the better source as an energy crop owing to the sugar release efficacy even with diluted [Ch][Lys]. Based on the compositional data, negligible delignification was observed for all pretreatment conditions other than the biomass pretreated with [Ch][Lys] at 160°C. In agreement with previous reports, pretreatment with [C_2mim][OAc] resulted in reduced crystallinity due to the swelling/dissolution of crystalline cellulose, whereas the pretreatment with [Ch][Lys] removed non-crystalline components from the biomass, enhancing the overall crystallinity of the biomass sample.

DATA AVAILABILITY STATEMENT

The original contributions presented in the study are included in the article/Supplementary Material; further inquiries can be directed to the corresponding author.

AUTHOR CONTRIBUTIONS

HC collected and analyzed data and wrote the original draft. BAS supervised the project and edited the draft. JMG supervised the project and edited the draft.

FUNDING

This work was part of the DOE Joint BioEnergy Institute (http://www.jbei.org) supported by the U.S. Department of Energy, Office of Science, Office of Biological and Environmental Research, through contract DE-AC02-05CH11231 between Lawrence Berkeley National Laboratory and the U.S. Department of Energy.

ACKNOWLEDGMENTS

The authors acknowledge Novozymes for providing the CTec3 and HTec3 enzymes used in this work. They are thankful to Dr. Vitalie Stavila of Sandia National Laboratories for assistance in collecting the PXRD data.

REFERENCES

Baruah, J., Nath, B. K., Sharma, R., Kumar, S., Deka, R. C., Baruah, D. C., et al. (2018). Recent Trends in the Pretreatment of Lignocellulosic Biomass for Value-Added Products. *Front. Energ. Res.* 6, 141. doi:10.3389/fenrg.2018.001410.3389/fenrg.2018.00141

J. -R. Bastidas-Oyanedel and J. E. Schmidt (Editors) (2019). "Biorefinery," *Integrated Sustainable Processes for Biomass Conversion to Biomaterials, Biofuels, and Fertilizers* (Cham: Springer Nature). doi:10.1007/978-3-030-10961-5

Clough, M. T., Geyer, K., Hunt, P. A., Mertes, J., and Welton, T. (2013). Thermal Decomposition of Carboxylate Ionic Liquids: Trends and Mechanisms. *Phys. Chem. Chem. Phys.* 15, 20480–20495. doi:10.1039/C3CP53648C

Da Costa Lopes, A. M., Lins, R. M. G., Rebelo, R. A., and Łukasik, R. M. (2018). Biorefinery Approach for Lignocellulosic Biomass Valorisation with an Acidic Ionic Liquid. *Green. Chem.* 20, 4043–4057. doi:10.1039/c8gc01763h

Das, L., Achinivu, E. C., Barcelos, C. A., Sundstrom, E., Amer, B., Baidoo, E. E. K., et al. (2021). Deconstruction of Woody Biomass via Protic and Aprotic Ionic Liquid Pretreatment for Ethanol Production. *ACS Sust. Chem. Eng.* 9, 4422–4432. doi:10.1021/acssuschemeng.0c07925

Gelfand, I., Hamilton, S. K., Kravchenko, A. N., Jackson, R. D., Thelen, K. D., and Robertson, G. P. (2020). Empirical Evidence for the Potential Climate Benefits of Decarbonizing Light Vehicle Transport in the U.S. With Bioenergy from Purpose-Grown Biomass with and without BECCS. *Environ. Sci. Technol.* 54, 2961–2974. doi:10.1021/acs.est.9b07019

Gibson, L. J. (2012). The Hierarchical Structure and Mechanics of Plant Materials. *J. R. Soc. Interf.* 9 (76), 2749–2766. doi:10.1098/rsif.2012.0341

IEA (2021). *IEA World Total Energy Supply*. Available from: https://www.iea.org/reports/key-world-energy-statistics-2021/supply.

Jian Sun, J., Konda, N. V. S. N. M., Shi, J., Parthasarathi, R., Dutta, T., Xu, F., et al. (2016). CO2 Enabled Process Integration for the Production of Cellulosic Ethanol Using Bionic Liquids. *Energy Environ. Sci.* 9, 2822–2834. doi:10.1039/C6EE00913A

Karimi, K., and Taherzadeh, M. J. (2016). A Critical Review of Analytical Methods in Pretreatment of Lignocelluloses: Composition, Imaging, and Crystallinity. *Bioresour. Tech.* 200, 1008–1018. doi:10.1016/j.biortech.2015.11.022

Lauri, P., Havlík, P., Kindermann, G., Forsell, N., Böttcher, H., and Obersteiner, M. (2014). Woody Biomass Energy Potential in 2050. *Energy Policy* 66, 19–31. doi:10.1016/j.enpol.2013.11.033

Mansfield, S. D., Kim, H., Lu, F., and Ralph, J. (2012). Whole Plant Cell wall Characterization Using Solution-State 2D NMR. *Nat. Protoc.* 7, 1579–1589. doi:10.1038/nprot.2012.064

Park, S., Baker, J. O., Himmel, M. E., Parilla, P. A., and Johnson, D. K. (2010). Cellulose Crystallinity index: Measurement Techniques and Their Impact on Interpreting Cellulase Performance. *Biotechnol. Biofuels* 3, 10. doi:10.1186/1754-6834-3-10

Pena, C. A., Soto, A., King, A. W. T., and Rodríguez, H. (2019). Improved Reactivity of Cellulose via its Crystallinity Reduction by Nondissolving Pretreatment with an Ionic Liquid. *ACS Sust. Chem. Eng.* 7, 9164–9171. doi:10.1021/acssuschemeng.8b06357

Perez-Pimienta, J. A., Sathitsuksanoh, N., Thompson, V. S., Tran, K., Ponce-Noyola, T., Stavila, V., et al. (2017). Ternary Ionic Liquid-Water Pretreatment Systems of an Agave Bagasse and Municipal Solid Waste Blend. *Biotechnol. Biofuels* 10–15. doi:10.1186/s13068-017-0758-4

Pérez-Pimienta, J. A., Icaza-Herrera, J. P. A., Méndez-Acosta, H. O., González-Álvarez, V., and Méndoza-Pérez, J. (2020). Bioderived Ionic Liquid-Based Pretreatment Enhances Methane Production from Agave Tequilana Bagasse. *RSC Adv.* 10, 14025–14032. doi:10.1039/d0ra01849j

Sluiter, A., Hames, B., Ruiz, R., Scarlata, C., Sluiter, J., Templeton, D., et al. (2011). *Determination of Structural Carbohydrates and Lignin in Biomass*. Golden, CO: National Renewable Energy Laboratory (NREL) Analytical Procedures. TP-510-42618 Available from: https://www.nrel.gov/docs/gen/fy11/42618.pdf.

Socha, A. M., Plummer, S. P., Stavila, V., Simmons, B. A., and Singh, S. (2013). Comparison of Sugar Content for Ionic Liquid Pretreated Douglas-fir Woodchips and Forestry Residues. *Biotechnol. Biofuels* 6, 61. doi:10.1186/1754-6834-6-61

Sun, N., Parthasarathi, R., Socha, A. M., Shi, J., Zhang, S., Stavila, V., et al. (2014). Understanding Pretreatment Efficacy of Four Cholinium and Imidazolium Ionic Liquids by Chemistry and Computation. *Green. Chem.* 16, 2546–2557. doi:10.1039/c3gc42401d

Shaoni Sun, S., Sun, S., Cao, X., and Sun, R. (2016). The Role of Pretreatment in Improving the Enzymatic Hydrolysis of Lignocellulosic Materials. *Bioresour. Tech.* 199, 49–58. doi:10.1016/j.biortech.2015.08.061

Swatloski, R. P., Spear, S. K., Holbrey, J. D., and Rogers, R. D. (2002). Dissolution of Cellose with Ionic Liquids. *J. Am. Chem. Soc.* 124, 4974–4975. doi:10.1021/ja025790m

Torr, K. M., Love, K. T., Simmons, B. A., and Hill, S. J. (2016). Structural Features Affecting the Enzymatic Digestibility of pine wood Pretreated with Ionic Liquids. *Biotechnol. Bioeng.* 113, 540–549. doi:10.1002/bit.25831

Usmani, Z., Sharma, M., Gupta, P., Karpichev, Y., Gathergood, N., Bhat, R., et al. (2020). Ionic Liquid Based Pretreatment of Lignocellulosic Biomass for Enhanced Bioconversion. *Bioresour. Tech.* 304, 123003. doi:10.1016/j.biortech.2020.123003

Wang, C., Zhang, X., Liu, Q., Zhang, Q., Chen, L., and Ma, L. (2020). A Review of Conversion of Lignocellulose Biomass to Liquid Transport Fuels by Integrated Refining Strategies. *Fuel Process. Tech.* 208, 106485. doi:10.1016/j.fuproc.2020.106485

White, E. M. (2010). *Woody Biomass for Bioenergy and Biofuels in the United States: A Briefing Paper*. Gen. Tech. Rep. PNW-GTR-825. Portland, OR: U.S. Department of Agriculture, Forest Service, Pacific Northwest Research Station, 45.

Yao, A., Choudhary, H., Mohan, M., Rodriguez, A., Magurudeniya, H., Pelton, J. G., et al. (2021). Can Multiple Ions in an Ionic Liquid Improve the Biomass Pretreatment Efficacy? *ACS Sust. Chem. Eng.* 9, 4371–4376. doi:10.1021/acssuschemeng.0c09330

Yoo, C. G., Pu, Y., and Ragauskas, A. J. (2017). Ionic Liquids: Promising green Solvents for Lignocellulosic Biomass Utilization. *Curr. Opin. Green Sust. Chem.* 5, 5–11. doi:10.1016/j.cogsc.2017.03.003

Conflict of Interest: The authors declare that the research was conducted in the absence of any commercial or financial relationships that could be construed as a potential conflict of interest.

Publisher's Note: All claims expressed in this article are solely those of the authors and do not necessarily represent those of their affiliated organizations, or those of the publisher, the editors, and the reviewers. Any product that may be evaluated in this article, or claim that may be made by its manufacturer, is not guaranteed or endorsed by the publisher.

frontiers | Frontiers in Energy Research

REVIEW
published: 11 April 2022
doi: 10.3389/fenrg.2022.857621

Beyond Crystallinity: Using Raman Spectroscopic Methods to Further Define Aggregated/Supramolecular Structure of Cellulose

Umesh P. Agarwal *

Forest Products Laboratory, USDA FS, Madison, WI, United States

In the bio-based economy, conversion of biomass to biofuels and other products is essential for developing a sustainable alternative to fossil fuels. For this to become a reality, understanding of the biomass ultrastructure is critically important. For instance, to enhance the yield of fermentable sugars from enzymatic hydrolysis of cellulose, the understanding of the latter's supramolecular structure and the ability to modify it appropriately is essential. Although cellulose crystallinity is one way to define the aggregated structure, previous research has shown that merely studying how cellulose crystallinity influences the hydrolysis is not good enough. This deduction is based on the fact that not only most crystallinity estimation methods have limitations but also crystallinity measurement inadequately defines the aggregated state of cellulose. Therefore, better approaches to describe the ultrastructure are needed. Raman spectroscopy is particularly well suited to this task because, in addition to crystallinity, several pieces of structure-related information can be generated, which when combined provide a more comprehensive description of the aggregated state. Additionally, the information derived using Raman spectroscopy is more resolved because it comes from spectral features that represent both the aggregated and the molecular states of cellulose. Few examples will be presented to illustrate this capability.

Keywords: cellulose, crystallinity, lignocellulose, biofuels, bio-based economy, supramolecular structure

OPEN ACCESS

Edited by:
Jia-Long Wen,
Beijing Forestry University, China

Reviewed by:
Yunqiao Pu,
Oak Ridge National Laboratory (DOE), United States
Samarthya Bhagia,
Oak Ridge National Laboratory, United States

***Correspondence:**
Umesh P. Agarwal
umesh.p.agarwal@usda.gov

Specialty section:
This article was submitted to Bioenergy and Biofuels, a section of the journal Frontiers in Energy Research

Received: *18 January 2022*
Accepted: *15 March 2022*
Published: *11 April 2022*

Citation:
Agarwal UP (2022) Beyond Crystallinity: Using Raman Spectroscopic Methods to Further Define Aggregated/Supramolecular Structure of Cellulose. Front. Energy Res. 10:857621. doi: 10.3389/fenrg.2022.857621

INTRODUCTION

Wood and other lignocellulosic biomass contain a significant amount of carbohydrate polymers that can be enzymatically converted to ethanol and other useful products (Huber et al., 2006; Zhu et al., 2009; Chundawat et al., 2011; Zhou et al., 2018). However, prior to their conversion, the native polymers need to be hydrolyzed to lower molecular weight sugars. A review of the literature on this subject shows that the recalcitrancy of biomass to enzyme hydrolysis is due to two factors—inaccessibility of cellulose and crystallinity of cellulose (Fan et al., 1980; Himmel and Picataggio, 2008; Johnson and Elander, 2008; Agarwal et al., 2013a; Leu and Zhu, 2013). To make cellulose accessible to enzymes, typically a pretreatment is required where one or more of the non-cellulosic polymers are either partly removed or modified (Himmel and Picataggio, 2008; Zhu et al., 2009; Yu et al., 2022). Such pretreated biomass then becomes more amenable to conversion to sugars. On the other hand, the negative effect of cellulose crystallinity (CrI) on the conversion is controversial. There are studies that support its negative impact (Fan et al., 1980; Ohmine et al.,

1983; Mosier et al., 2005; Ibbett, et al., 2013) and reports that show that the CrI by itself is not a problem (Jeoh et al., 2007; Gierlinger et al., 2008; Rollin et al., 2010; Foston et al., 2011; Agarwal et al., 2013a; Aldaeus et al., 2015; Gao et al., 2021). It may be that the size of the cellulose crystals plays a role, highly crystalline and thicker crystals may pose a problem, but nano-sized crystalline cellulose may not (as in the G-layer in tension wood). If true, the latter is likely to be due to the increased surface area that the smaller size crystals provide. In any case, this aspect needs to be further investigated.

Although cellulose CrI is often measured and reported using one of the many available methods (e.g., XRD, IR, NMR, and Raman spectroscopy), considering that there are significant limitations associated with most of the methods, it seems that its estimation is not very accurate (Park et al, 2009; Park et al., 2010; Agarwal et al., 2010; Agarwal et al., 2018; Agarwal et al., 2021a). For instance, XRD methods are often used but because the obtained diffractogram is a convolution of contributions from many sources (e.g., crystalline and non-crystalline cellulose, amorphous cellulose, hemicellulose, and lignin), the obtained data need to be deconvoluted. However, there is no unique way to accomplish this (Madams, 1980; Park et al, 2009; Park et al., 2010). Similarly, some other methods (e.g., Rietveld analysis) (De Figueiredo and Ferreira, 2014; Ling et al., 2019) need prior crystalline knowledge of the sample components in order to model a fit to the obtained diffractogram. This also introduces subjectivity in the analysis, and hence, the obtained result is influenced. Furthermore, it has been reported that the XRD-estimated CrI is impacted by the water content of the sample (Agarwal et al., 2017). The reason for this is the ability of non-crystalline and amorphous cellulose to reorganize in the presence of water (Agarwal et al., 2017; Agarwal et al., 2021a; Agarwal et al., 2021b). Similarly, as was recently reported using IR and Raman spectroscopies, non-crystalline cellulose is capable of contributing in the same wavenumber and X-ray diffraction regions as the crystalline form (Agarwal et al., 2021a). Therefore, when present, such non-crystalline cellulose would contribute toward the estimated CrI of a material. Likewise, in solid-state MAS–NMR, it is well recognized that the CrI depends on the amount of water in the sample (Park et al, 2009; Agarwal et al., 2021b). To obtain well-resolved peaks in NMR, as a standard sampling protocol, certain amount of water is regularly added to the sample (Wickholm et al., 1998). This neglects the fact that the water addition causes reorganization of the less-than-fully-crystalline cellulose. And consequently, higher CrI values are obtained. Similarly, in 380-Raman, involved band intensities are slightly impacted by the sample's water content (Agarwal et al., 2021b). Given this situation, it is clear that to estimate cellulose CrI more accurately, better methods are needed. It appears that two recently developed methods, 93-Raman (Agarwal et al., 2018) and 3-THz (terahertz spectroscopy) (Vieira and Pasquini, 2014; Wang et al., 2020; Wang et al., 2021) are promising. Both these methods, although based on different spectroscopy techniques, estimate CrI using the same cellulose-crystal mode. Nevertheless, these methods need to be applied to a wide variety of cellulose materials before either one or both can be considered precise.

Many forms of aggregated cellulose are far from fully crystalline or amorphous, and it is vitally important to fully characterize them. Considering that not only cellulose CrI measurement has limited accuracy but also it is only one of the many characteristics of cellulose supramolecular structure, use of methods that give additional structural information is desirable. One such technique is MAS–NMR, where in addition to CrI, other structural parameters, such as lateral fibril dimension and *tg*/*gt* ratio, can be estimated (Wickholm et al., 1998; Peciulyte et al., 2015; Agarwal et al., 2021b). Nevertheless, additional methods are needed to further define the ultrastructure. For this purpose, applications of Raman spectroscopy have been developed in the laboratory of the author. Over the years, many of these methods have provided detailed structural information on cellulose. Here, such methods are briefly reviewed, and a case is made for their broader applicability so that the changes in the cellulose supramolecular structure can be more precisely evaluated. It is projected that improved understanding of the structure would yield to improved valorization of biomass largely due to better appraisal of the ways in which process conditions impact the supramolecular structure of cellulose.

Raman Spectroscopy of Cellulose

In the studies of cellulose, although Raman spectroscopy was first applied a long time ago (Atalla and Dimick, 1975), the technological evolution of the instrumentation has led to countless advances in the area (Baldwin et al., 2002; Adar et al., 2007). Consequently, by means of modern instrumentation, the applications to the fields of cellulose and lignocellulose have greatly advanced (Agarwal, 2019). In particular, two classes of the applications stand out—applications based on Raman imaging and analysis using the 1,064-nm excitation-based FT–Raman technique. In the imaging, capability exists to chemically map the distribution of the material components at submicron level. On the other hand, the use of FT–Raman permits acquisition of high-quality fluorescence-free spectra. Raman spectroscopy is being increasingly applied to many areas of cellulose research, and the obtained information has proven to be highly valuable. Recently, a review focusing on such advances was published (Agarwal, 2019). In this study, the focus is on those features in the Raman spectra of celluloses that have generated useful information in the context of aggregated structure of cellulose. A significant amount of the reported work was carried out in the laboratory of the author. However, where appropriate, the information from the literature is also included.

In the Raman spectra of celluloses, the assignments of most of the bands are available in the literature (Wiley and Atalla, 1987; Edwards et al., 1997). In **Table 1**, only those bands and their assignments are listed that are used in the information presented here.

Cellulose Crystallinity

To estimate cellulose CrI, three Raman spectroscopy-based methods are used. They are based on the spectral

TABLE 1 | Selected Raman frequencies and their assignments (70–1,550 cm^{-1}) of cellulose I (Avicel I), cellulose II (Avicel II), and amorphous cellulose (Avicel amorphous).

Avicel I	Avicel II	Avicel amorphous	Most assignments* (Wiley and Atalla, 1987; Edwards et al., 1997)
93(m)**	—	—	Crystal lattice mode
348(w)	353(m)	356(m)	Some heavy-atom stretching
381(m)	376(sh)	—	Some heavy-atom stretching; δ(CCC) ring
—	577(m)	—	Some heavy-atom stretching
898(m)	—	—	ν(COC) in-plane symmetric
912(sh)	—	—	HCC and HCO bending at C-6; ν(COC) in-plane symmetric
1,096(s)	1,097(s)	1,092(s)	Stretching, C-C and C-O; ν(COC) glycosidic asymmetric
1,380(m)	1,374(m)	1,377(s)	HCC, HCO, and HOC bending; δ(CH2)
1,463(sh)	1,462(m)	1,463(m)	HCH and HOC bending; δ(CH2) scissors
1,476(m)	—	—	HCH and HOC bending; δ(CH2) scissors

*ν = stretching, δ = in plane scissoring, ρ = in-plane rocking, τ = out-of-plane twisting, **relative band intensities in a spectrum are indicated by s = strong, m = medium, w = weak, and sh = shoulder.

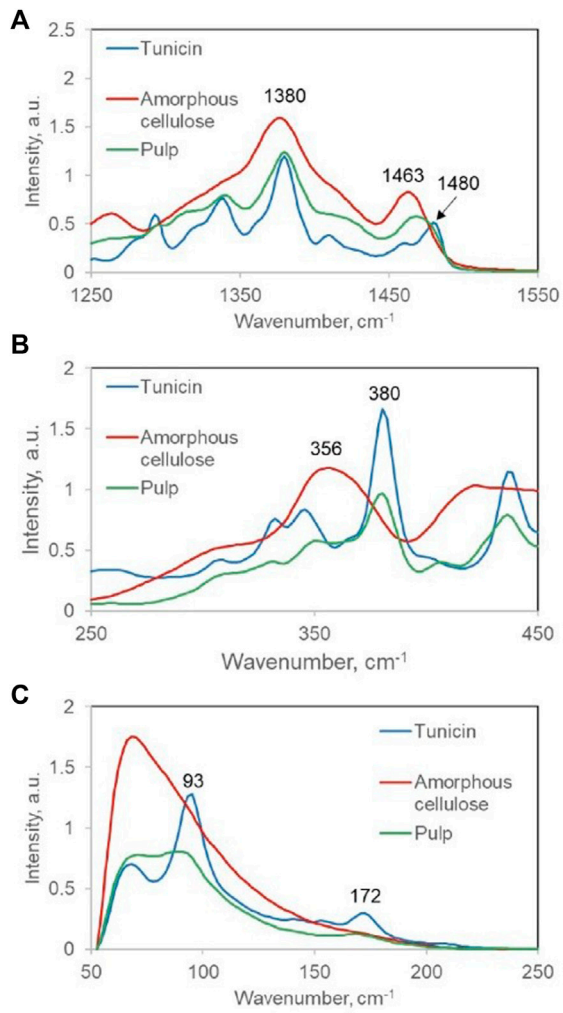

FIGURE 1 | Raman spectra of tunicin (very high CrI), bleached hardwood kraft pulp (medium CrI), and completely amorphous cellulose (zero CrI) in the regions on which the three Raman methods are based; **(A)** 1,481 cm^{-1}, **(B)** 380 cm^{-1}, and **(C)** 93 cm^{-1}.

contributions of crystalline cellulose at 1,481, 380, and 93 cm^{-1} (**Figure 1**), and these are, respectively, referred to as 1481-Raman, 380-Raman, and 93-Raman (Schenzel et al., 2005; Agarwal et al., 2010; Agarwal et al., 2018, respectively). Of the three methods, the 1481-Raman method, which was developed first and is based on the ratio of the 1,481 to 1,460 cm^{-1} band intensities, is most limited. Even for pure celluloses, not only the bands at 1,481 and 1,460 cm^{-1} have medium intensities but they also overlap significantly. Therefore, one needs to deconvolute them prior to intensity calculation. Added complexity arises for samples that contain other components such as hemicelluloses and lignin because Raman contributions of these are also present in the same spectral region (Agarwal and Ralph, 1997).

The second method, 380-Raman, developed in 2010, seems to suffer the characteristic that it fails to differentiate between organized and crystalline cellulose. As was reported earlier by Agarwal et al. (2018), the method estimated CrI values of 49.9 and 57.4% for aspen and red pine woods, respectively (Agarwal et al., 2013b), but in fact, later, the native cellulose in the wood cell wall was found to be non-crystalline (Agarwal et al., 2016). This further supported the argument that cellulose that is simply spatially organized/ordered and not crystalline is capable of making contributions in the spectral/diffraction regions that are typically associated with crystalline cellulose. The supporting evidence for this argument was recently obtained from the research that was based on ball-milled celluloses (Agarwal et al., 2021a), which clearly established that non-crystalline cellulose is indeed capable of making contributions where the contributions of crystalline cellulose are usually detected.

Contrary to the aforementioned two Raman methods, the third method, the 93-Raman, seems to accurately estimate the crystallinity. This method is synonymous with the 3 THz method in terahertz spectroscopy (Parrott and Zeitler, 2015; Agarwal et al., 2018; Wang et al., 2020; Wang et al., 2021) since both the methods detect the same lattice mode of crystalline cellulose. Moreover, as would be expected, the two spectroscopic energies

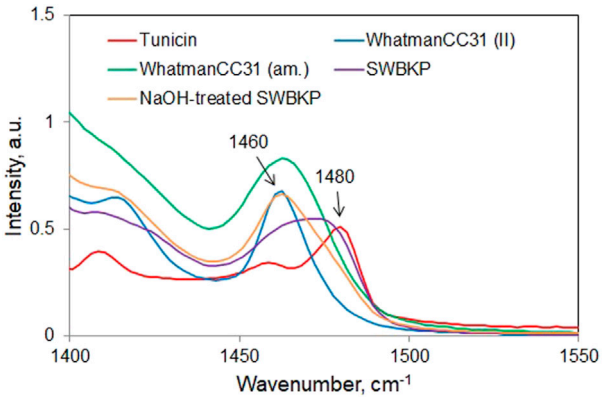

FIGURE 2 | Raman spectra of selected samples in 1400- to 1,550-cm^{-1} region.

are approximately equivalent (99 cm^{-1} = 3 THz). Nevertheless, because these methods were recently developed, they have yet not been applied widely.

Conformation of Exocyclic CH_2OH

In the Raman spectra of celluloses, the contributions of CH_2 bending modes that are sensitive to *tg* and *gt* conformation appear at 1,480 and 1,460 cm^{-1}, respectively (**Figure 2**). Whereas *tg* conformation containing cellulose I allomorph gives rise to a peak at 1,480 cm^{-1}, the *gt* conformation-rich cellulose II, cellulose III, and amorphous phase all appear at 1,460 cm^{-1}. Therefore, from the Raman spectrum of a sample, exocyclic CH_2OH conformational information can be derived from the relative intensities at these two wavenumber positions. Based on **Eqn. 1**, the data in **Table 2** summarize such information for a number of cellulose materials including those that are highly crystalline (e.g., #1 and #9). Whatman CC31 (II), a highly crystalline cellulose II sample, was produced from the previously obtained Whatman CC31 (II) sample (Agarwal et al., 2017) by additionally treating it with 2.5 N HCl at 100°C for 60 min. Further details on the other listed materials in **Table 2** can be obtained from the following references: Whatman CC31 amorphous (Agarwal et al., 2010), softwood bleached kraft pulp (SWBKP), never-dried NaOH-treated aspen wood holocellulose, HCl- and NaOH-treated aspen wood holocellulose, Avicel PH-101, Avicel PH-101 + 10% xylan, Whatman CC31 (cotton microcrystalline cellulose or MCC), tunicin, 95.6% crystalline (Agarwal et al., 2016), and 10% NaOH (at 170°C)-treated SWBKP (Agarwal et al., 2021c). In materials that are composed of only cellulose I allomorph, meaning that in addition to crystalline domains, only the amorphous phase is present, the *gt*/*tg* ratio is a measure of the disordered form of cellulose (Schenzel et al., 2005). As pointed out earlier, for cellulose I materials, one of the Raman CrI methods is based on the *tg*/*gt* ratio (1481-Raman). From the *gt*/*tg* ratio data given in **Table 2**, tunicin, a highly crystalline cellulose Iβ material, showed the lowest *gt*/*tg* ratio (0.36).

$$gt\Big/tg\ Ratio\ =\ I_{1460}/I_{1480}. \tag{1}$$

In **Table 2**, considering the ratio data of the cellulose I and non-crystalline materials (see classification column) and excluding those that have cellulose II (#1 and #4, **Table 2**) or are completely amorphous (#2), the highest ratio is for #5 (never-dried NaOH-treated aspen wood holocellulose), implying that it is the most disordered. However, it is important to note that this sample was classified as non-crystalline and not as cellulose I (Agarwal et al., 2017; Agarwal et al., 2018). Compared to its ratio value (0.82, **Table 2**), the cellulose I samples (#3, #6, #7 - #10) all showed lower values implying reduced degree of the CH_2OH *gt* conformational disorder.

Accessibility to Water

Accessibility to water (A) of a cellulose sample is based on the ratio of two numbers. The numbers, for the sample and for the completely amorphous cellulose (which is taken as 100% accessible to water), are increases in the relative intensity of

TABLE 2 | *gt*/*tg* CH_2OH conformational ratio (I_{1460}/I_{1480}) and accessibility to water (A).

Sample[a]	Description	*gt*/*tg* ratio[b]	Accessibility to water (A) (%)	Classification
1	Whatman CC31 (II), 100% crystalline[c]	11.05	57.2	Cellulose II
2	Whatman CC31, amorphous	2.89	100.0	Amorphous
3	Softwood bleached kraft pulp (SWBKP)	0.77	25.5	Cellulose I and amorphous
4	10% NaOH (at 170°C)-treated SWBKP	2.34	86.5	Cellulose I, cellulose II, and amorphous
5	NaOH-treated aspen wood holocellulose, never-dried	0.82	49.0	Non-crystalline cellulose
6	HCl- and NaOH-treated aspen wood holocellulose	0.63	23.6	Cellulose I and amorphous
7	Avicel PH-101 (wood pulp)	0.55	24.4	Microcrystalline cellulose I
8	Avicel PH-101 + 10% xylan	0.60	24.5	Mixture of cellulose I and xylan
9	Whatman CC31 (cotton)	0.46	12.3	Microcrystalline cellulose I
10	Tunicin, 95.6% crystalline[d]	0.36	1.0	Cellulose I

[a]*Except sample #1, further details can be found in Agarwal et al., 2017.*
[b]*In all cases, the SD was <8%.*
[c]*CrI estimated as in Agarwal et al., 2021c.*
[d]*Segal-WAXS CrI.*

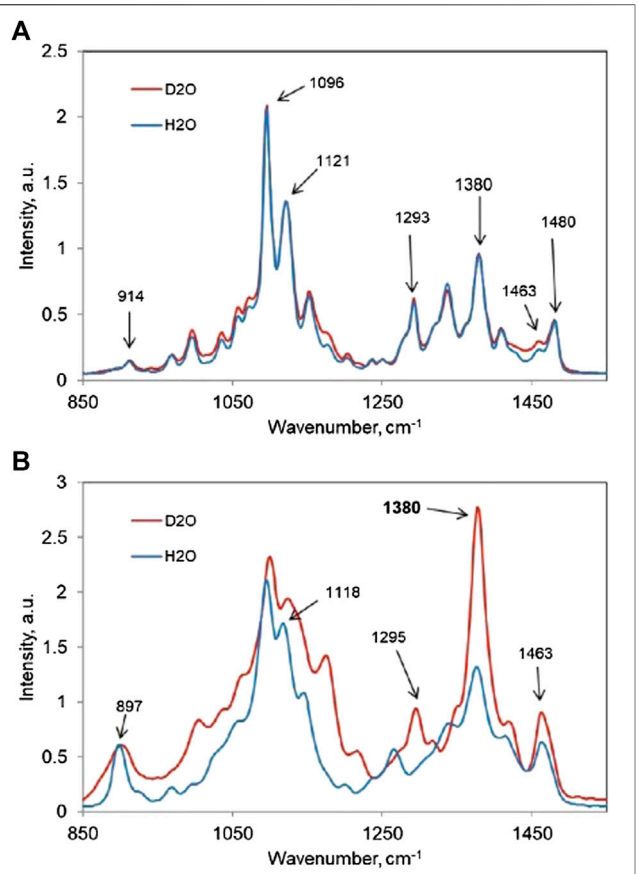

FIGURE 3 | In H_2O and D_2O Raman spectra, in 850- to 1,550-cm^{-1} region, of **(A)** tunicin and **(B)** completely amorphous cellulose.

the 1,380-cm^{-1} band (I_{1380}/I_{1096} ratio), when all the D_2O-accessible C_6 OHs are converted to C_6 OD groups. As reported previously (Agarwal et al., 2016; Agarwal et al., 2021a), **Eq. 2** was used to calculate A. The A data are listed in **Table 2**.

$$A\,(Raman) = \frac{\Delta I_{1380}\,(sample)*100}{\Delta I_{1380}\,(amorphous)}. \quad (2)$$

In **Figure 3**, two sets of spectra are shown, one for tunicin—a highly crystalline Iβ cellulose, which showed no increase (**Figure 3A**), and the other set for completely amorphous cellulose, which showed a 154% increase (**Figure 3B**). Moreover, considering that there are two types of accessible C6 OHs located either on the surface or in the interior of cellulose that can contribute to such an intensity increase, the "A" value represents the sum of both such contributions. However, depending on the characteristics of a sample, one or the other contribution type may dominate. For instance, in mostly crystalline nano-size celluloses, the surface contribution would be dominant.

In the case of tunicin (**Figure 3A**), hardly any intensity increase at 1,380 cm^{-1} is seen because nearly all cellulose is present in the crystalline state and the size of the crystal is substantial (10 nm) (Agarwal et al., 2017). This implies that the contribution from the surfaces is minimal due to fewer surface CH_2OH groups being available for the OH-to-OD exchange. Moreover, because the measurement of A does not discriminate between the accessible surface and interior CH_2OH groups, a thin crystal, although fully crystalline, might produce a higher A value than a thick crystal that, in the interior, is not completely crystalline.

Chain Conformational Disorder

Recently, using Raman spectroscopy, we have introduced a new cellulose parameter "chain conformational disorder" (CCONDIS), which is yet another feature of the aggregated cellulose structure (Agarwal et al., 2021b). For a material, CCONDIS is defined as the intensity ratio I_{900}/I_{1096}, where 120-min ball-milled cotton MCC is taken as being 100% disordered (CCONDIS = 100). It has been observed that with the increased chain conformational disorder, the intensities of Raman bands at 900 and 1,096 cm^{-1} are impacted the most, whereas the intensity of the former band increases, and it declines in the case of the 1,096 cm^{-1} band (Agarwal et al., 2010; Agarwal et al., 2021b). Therefore, the ratio of these two intensities (**Eq. 3**) is a good measure of this disorder.

$$CCONDIS = \frac{\left(\frac{I_{900}}{I_{1096}}\right)sample*100}{\left(\frac{I_{900}}{I_{1096}}\right)amorphous}. \quad (3)$$

In the publication (Agarwal et al., 2021b), CCONDIS data were generated for a set of cellulose nanocrystals (CNCs) that were obtained from a variety of sources, and it was found that in all the cases, compared to the wet state, the disorder was higher in the freeze-dried state (Agarwal et al., 2021b). Moreover, among the CNCs, wet *Cladophora* CNCs showed the least amount of the conformational disorder, whereas the freeze-dried pulp CNCs had the most disorder. Nevertheless, the observed trend in the wet state was not necessarily maintained on freeze-drying. In **Table 3**, CCONDIS data are reported for a number of samples.

Additional details on the samples can be obtained from the author's earlier publications: amorphous cellulose and Whatman CC31 MCC (Agarwal et al., 2010); never-dried and freeze-dried SWBKPs (Agarwal et al., 2021b); 5% NaOH-treated (at 170°C) SWBKP (Agarwal et al., 2021c); and never-dried and oven-dried 4% NaOH-treated aspen wood holocellulose, 4% NaOH- and 4 N HCl (100°C, 6 h)-treated aspen wood holocellulose, wet Avicel PH-101, wet (Avicel PH-101 + 10% xylan), tunicin, and 95.6% crystalline (Agarwal et al., 2016).

Moreover, in **Table 3**, the sample compositions have been classified in terms of presence of cellulose and hemicellulose. This gives some information about the components that are responsible for the spectral contributions. Most of the samples contain crystalline cellulose I together with some amorphous cellulose. However, several samples that are obtained from wood (#2 - #4; #5 - #7) also contain some hemicellulose.

Of the samples listed in **Table 3**, normalized Raman spectra of five samples (#1, #2, #5, #8, #11, respectively, amorphous cellulose, never-dried SWBKP, never-dried 4% NaOH-treated aspen wood holocellulose, wet Avicel PH-101, and tunicin), are

TABLE 3 | Chain conformational disorder (CCONDIS).

Sample	Description	CCONDIS (%)	Classification
1	Amorphous cellulose (Whatman CC31)	100.0	Amorphous cellulose
2	Never-dried softwood bleached kraft pulp (SWBKP)	40.6	Cellulose I, amorphous cellulose, and hemicellulose
3	Freeze-dried SWBKP	51.2	Cellulose I, amorphous cellulose, and hemicellulose
4	5% NaOH-treated (at 170°C) SWBKP[a]	50.2	Cellulose I, amorphous cellulose, and some hemicellulose
5	Never-dried 4% NaOH-treated aspen wood holocellulose	33.1	Non-crystalline cellulose and _ hemicelluloses
6	4% NaOH-treated aspen wood holocellulose, oven-dried (at 110°C)	52.4	Cellulose, mostly non-crystalline, and hemicelluloses
7	4% NaOH- and 4 N HCl (100°C, 6 h)-treated aspen wood holocellulose[a]	45.4	Cellulose I and some amorphous cellulose
8	Wet Avicel PH-101[b]	25.3	MCC cellulose I
9	Wet (Avicel PH-101 + 10% xylan)	28.2	Mixture of Cellulose I and 10% xylan
10	Whatman CC31 (cotton MCC)	27.5	MCC cellulose I
11	Tunicin, 95.6% crystalline[c]	16.1	Cellulose I

[a]*After treatment, the sample was dried at 25°C.*
[b]*Microcrystalline cellulose (MCC) obtained from softwood pulp.*
[c]*Segal-WAXS crystallinity.*

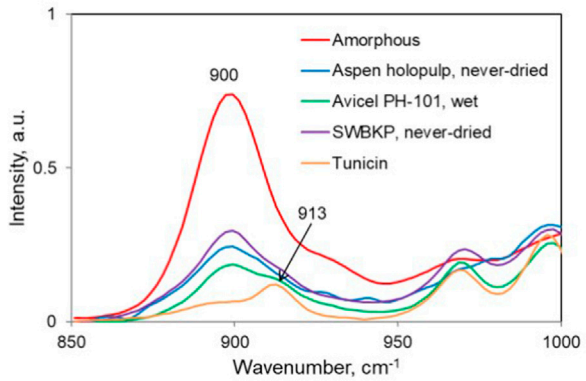

FIGURE 4 | 900-cm^{-1} region of the normalized Raman spectra of selected samples listed in **Table 3**. The crystalline contribution present at 913 cm^{-1} can also be seen for some samples.

compared in **Figure 4**. Based on the band intensities at 900 cm^{-1}, the rank of the samples with the least to most chain disorder is as follows: tunicin < wet Avicel PH-101 < never-dried 4% NaOH-treated aspen wood holocellulose < never-dried SWBKP < amorphous cellulose.

Considering the CCONDIS data, tunicin, highly crystalline cellulose, gave the lowest value (16.1%, **Table 3**), and it is likely that the non-zero value might be due to the contributions of the surface chains of the crystals. In the rest of the samples, the values were higher than tunicin. For instance, considering sample #5 (never-dried 4% NaOH-treated aspen wood holocellulose), it had a value of 33.1% (**Table 3**). However, on oven-drying, the chain disorder in the sample increased to 52.4%, an increase of 58%, suggesting that water removal played an important role in significantly increasing the CCONDIS. When the never-dried sample was treated with HCl to remove the remaining hemicellulose and amorphous cellulose from the sample, the CCONDIS value of the treated sample in the dry state (dried at 25°C) was still higher than the value in the wet state (45 vs. 33.1%, **Table 3**). This, once again, underscored the importance of water in reducing the CCONDIS because the removal of the less-ordered components from the sample should have resulted in the reduction of CCONDIS, which did not happen. One major difference between these two samples is the state in which they were analyzed—one sampled in the dry state whereas the other in the never-dried state. This order-inducing role of water is further seen when one considers the CCONDIS data for the SWBKP samples (#2–#4, **Table 3**). Of the three CCONDIS values reported for the pulp samples, the lowest was for the never-dried state (40.6%, **Table 3**). Once the pulp was freeze-dried, the value increased to 51.2% (#3, **Table 3**). However, on 5% NaOH treatment (at 170°C), the chain disorder of the dried pulp only slightly declined to 50.2% (#4, **Table 3**).

Next, wet Avicel PH-101 was compared with the sample where 10% xylan was added to it (#8 and #9, **Table 3**). The mixture sample was produced to mimic wood pulps, where in addition to cellulose, hemicelluloses are also present. It is found that presence of xylan increased the CCONDIS value only marginally (25.3–28.2%, **Table 3**), and 90% of the mixed-sample disorder originated from cellulose. This information is important for estimating CCONDIS in samples that additionally contain hemicelluloses. This is particularly relevant because wood hemicelluloses, xylan and glucomannan, both have Raman contributions at 900 cm^{-1} (Agarwal and Ralph, 1997).

Last, comparing the three pure crystalline celluloses (#8, #10, and #11, **Table 3**), the obtained data suggested that the chain disorder, from least to most, is in the order tunicin < Whatman CC31 < Avicel PH-101.

Glycosidic Linkage Orientation Disorder

In describing the aggregated state of cellulose, the last Raman parameter that has been found useful is the intensity ratio of two low-frequency bands located approximately at 350 and 380 cm^{-1} (**Eq. 4**, **Table 4**). Although, previously, based on the latter peak, a Raman CrI method (380-Raman) was developed (Agarwal et al., 2010), the ratio I_{350}/I_{380} in cellulose I materials provides a measure of the overall glycosidic linkage orientation disorder (GLOD) in a sample. In cellulose, this is brought about by the changes in the dihedral angles about the two bonds involved in the glycosidic linkage (Atalla and Dimick, 1975). It is important to note that between the two bands, whereas cellulose I

TABLE 4 | Glycosidic linkage orientation disorder.

Sample	Description	GLOD[a] (%)	References, for sample details
1	Amorphous cellulose (120 min ball-milled Whatman CC31)	100	Agarwal et al. (2010)
2	Wet amorphous cellulose (Whatman CC3)	32.3[b]	Agarwal et al. (2021a)
3	Freeze-dried softwood bleached kraft pulp (SWBKP)	11.0	Agarwal et al. (2021b)
4	10% NaOH-treated (at 170°C) SWBKP[b]	39.5[b]	Agarwal et al. (2021c)
5	4% NaOH-treated aspen wood holocellulose, freeze-dried	15.5	Agarwal et al. (2016)
6	4% NaOH-treated aspen wood holocellulose, oven-dried (110°C)	14.8	Agarwal et al. (2017)
7	4% NaOH- and 4 N HCl (100°C, 6 h)-treated aspen wood holocellulose	11.7	Agarwal et al. (2017)
8	Wet Avicel PH-101[c]	5.0	Agarwal et al. (2017)
9	Wet (Avicel PH-101 + 10% xylan)	4.9	Agarwal et al. (2017)
10	Whatman CC31 control	9.6	Agarwal et al. (2016)
11	Whatman CC31 (cellulose II), 100% crystalline[d]	86.2[b]	This work
12	Tunicin, 95.6% crystalline[e]	9.4	Agarwal et al. (2016)

[a]*GLOD was also estimated using bands that were shifted from 380 to 350 cm^{-1} positions. In case there was no peak, the intensity (**Eq. 4**) was still calculated at these wavenumbers.*
[b]*GLOD value is more complex due to the presence of cellulose II in the sample.*
[c]*Microcrystalline cellulose (MCC) obtained from softwood pulp.*
[d]*X-ray CrI method used as in Agarwal et al., 2021c.*
[e]*Segal-WAXS, crystallinity.*

contributes mostly at 380 cm^{-1}, cellulose II, cellulose III, and amorphous cellulose have principal contributions at ~ 350 cm^{-1} (Agarwal, 2014; Agarwal et al., 2021c). Therefore, in the presence of allomorphs cellulose II and cellulose III, the ratio's value is increased by these ordered crystalline forms and the GLOD information becomes difficult to interpret. In **Table 4**, GLOD data are listed for a variety of samples that also included high crystalline cellulose I and cellulose II materials. The Raman spectra in the selected region are shown in **Figure 5**. The GLOD data are reported for the first time here.

$$\text{Glycosidic linkage orientation disorder} = \frac{\left(\frac{I_{350}}{I_{380}}\right)sample*100}{\left(\frac{I_{350}}{I_{380}}\right)amorphous}. \quad (4)$$

Comparing the GLOD data for totally amorphous cellulose in dry and wet states (**Figure 5A**), although in the wet state, there is some cellulose II present, the one treated with water at 25°C showed more than 3 times reduction in the disorder (#1 and #2, **Table 4**). As was reported earlier (Agarwal et al., 2021a), this was due to significant reorganization of the amorphous cellulose into cellulose I and cellulose II type structures. Consequently, the Raman intensity at 353 cm^{-1} declined and increased at 377 cm^{-1}(**Figure 5A**). The next set of samples, #3 and #4, are SWBKP materials, one of which was treated with 10% NaOH at 170°C for 90 min (Agarwal et al., 2021c). As was reported in the cited reference, the alkali treatment partially converted pulp cellulose to cellulose II, which was revealed by its Raman spectrum due to the presence of a new cellulose band at 577 cm^{-1} (**Figure 5B**) (Agarwal et al., 2021c). This caused the estimated value of GLOD to increase since the 353 cm^{-1} intensity was higher, while the cellulose I contribution at 380 cm^{-1} declined (**Figure 5B**). As mentioned earlier, in the presence of cellulose II, the GLOD data are not reliable. Similar is the case with the pure cellulose II sample (#11, **Table 4**), where a very high value of GLOD was obtained due to this sample being a highly crystalline cellulose II material.

The next set of samples consisted of NaOH-treated aspen holopulp that was freeze-dried, oven-dried, and treated with HCl (#5, #6, and #7; **Table 4**). Whereas the GLOD data were similar between the freeze-died and oven-dried samples, indicating that they did not change significantly with regard to the GLOD in their aggregated structures, on acid hydrolysis at 100°C for 6 h, there was considerable decline in the GLOD value. The decline is caused by the removal of the amorphous cellulose domains in the holopulp, which led to an increase at 380 cm^{-1} as the sample became more crystalline (**Figure 5C**). Removal of amorphous cellulose by acid treatment is a widely recognized phenomenon and is used in the production of crystalline cellulose (Spiliopoulos et al., 2021). The next sample set contains pure Avicel PH-101 and 10% xylan-containing Avicel PH-101, and their spectra are shown in **Figure 5D**. Here, no changes were detected in 250- to 450-cm^{-1} region of the spectra, and this supported the similar GLOD values of the two samples (#8, #9; **Table 4**). In the normalized spectra, identical contributions at 350 and 380 cm^{-1} are expected from the two samples because xylan is known to have no significant bands at these band positions (Agarwal and Ralph, 1997).

Finally, the spectral features of two highly crystalline cellulose I samples—cotton MCC (Whatman CC31) and tunicin, along with 100% crystalline cellulose II (Whatman CC31) are shown in **Figure 5E**. As expected, the ratio values are similar between the two cellulose I samples (9.6 and 9.4; **Table 4**). In contrast, for cellulose II, the ratio is significantly higher (86.2; **Table 4**) due to the high intensity of the 355-cm^{-1} band in the Raman spectrum (**Figure 5E**). The origin of this intensity lies in the cellulose allomorph itself and not in amorphous cellulose because this sample was 100% crystalline.

Processability Parameter

In future, it may be possible to relate the processability of a material with one or more of the Raman parameters discussed here. For example, in case of enzymatic hydrolyzability of cotton MCC (Whatman CC31) and amorphous cellulose,

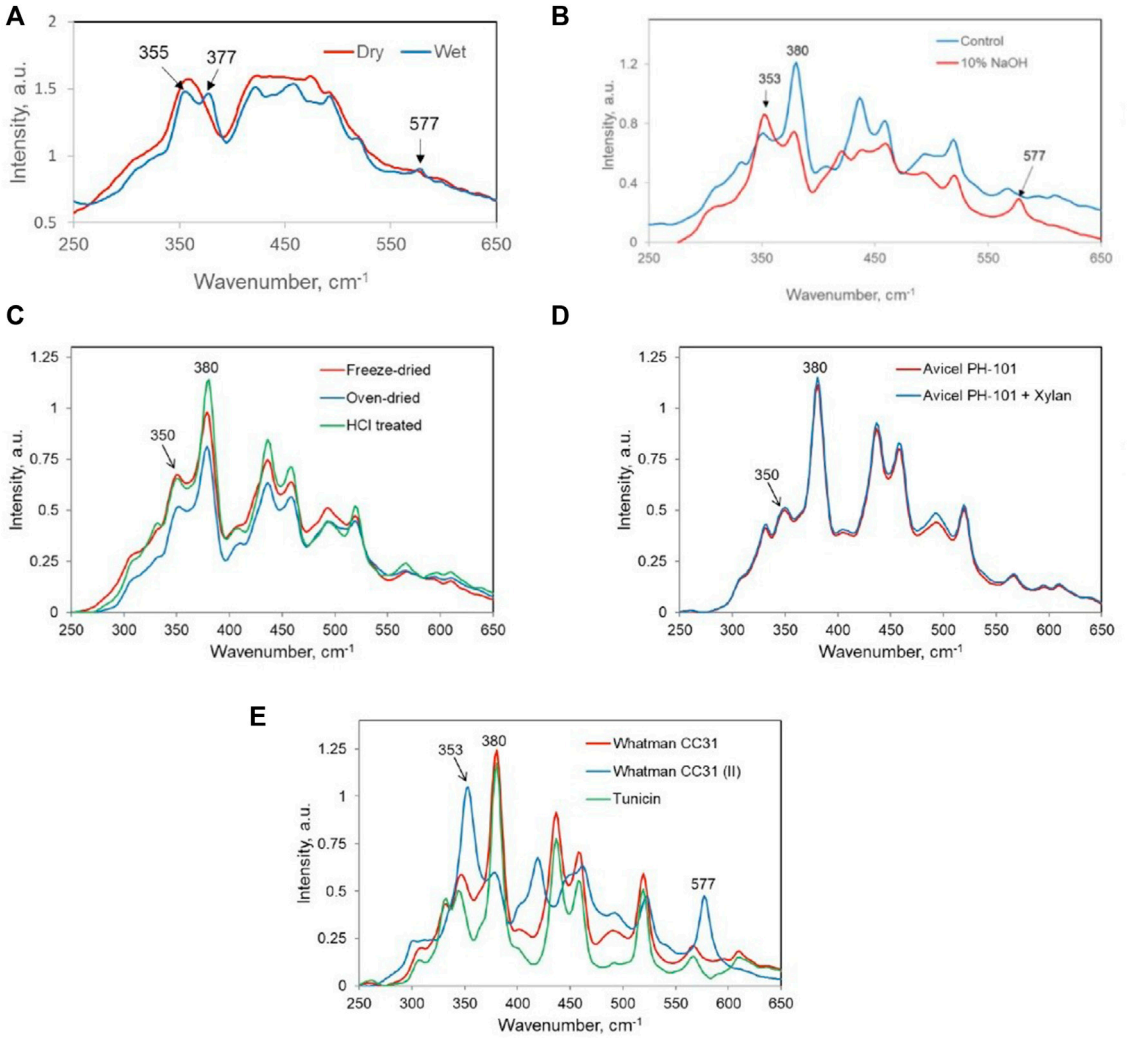

FIGURE 5 | Raman spectra of **(A)** dry amorphous and wet amorphous celluloses; **(B)** control and 10% NaOH-treated softwood bleached kraft pulp; **(C)** NaOH-treated aspen holopulp—freeze-dried, oven-dried, and HCl-treated (#5, #6, and #7, **Table 4**); **(D)** Avicel PH-101 and 10% xylan containing Avicel PH-101 (samples #8 and #9, **Table 4**); **(E)** Whatman CC31, Whatman CC31 (Cellulose II), and tunicin (#10–#12, respectively; **Table 4**).

TABLE 5 | Comparison of Raman parameters and enzymatic hydrolysis yields.

Parameter	Cotton MCC	Amorphous cellulose
gt/*tg* ratio	0.46	2.89
Accessibility to water	12.3%	100%
CCONDIS	27.5%	100%
GLOD	9.6	100%
Enzymatic hydrolysis yield after 72 h[a]	40%	90%

[a]*Agarwal et al., 2013a.*

these parameters and the hydrolysis yields of these samples (Agarwal et al., 2013a) are listed in **Table 5**. The amount of cellulose that can be saccharified from the MCC (40%, **Table 5**) was significantly lower than the amount obtained from amorphous cellulose (90%, **Table 5**). Based on these limited data and the sample-associated Raman parameters, it appears that to improve saccharification, the cellulose materials should be processed such that the values of some of their Raman parameters are similar to those observed for amorphous cellulose (**Table 5**), which was highly hydrolyzable. The manner in which this can be accomplished ought to be the objective of future research. Only such investigations would reveal which of the four parameters, listed in **Table 5** (*gt*/*tg* ratio, accessibility to water, CCONDIS, and GLOD), is actually important in the context of enzymatic hydrolysis.

CONCLUSION

As shown by the spectral analyses presented here, additional information on the aggregated state of cellulose can be

obtained by Raman spectroscopy. Beyond crystallinity, such supramolecular state-related parameters consist of the *gt*-to-*tg* ratio (CH_2OH conformation), accessibility to water, chain conformation disorder, and glycosidic linkage orientation disorder. As reported earlier, in case a sample consists of cellulose polymorphs other than cellulose I, they can also be detected and quantified (Agarwal, 2014; Agarwal et al., 2021c). Clearly, Raman spectroscopy is capable of playing an important role in the field of valorization of cellulose materials and therefore should be used more often in such endeavors.

AUTHOR CONTRIBUTIONS

UA, the sole author of the manuscript, obtained some of the data and wrote the entire manuscript.

ACKNOWLEDGMENTS

The author acknowledges the help received from Sally Ralph in carrying out various experiments, obtaining some of the Raman spectra, and making combined versions of **Figures 1**, **3**, **5**.

REFERENCES

Adar, F., Delhaye, M., and DaSilva, E. (2007). Evolution of Instrumentation for Detection of the Raman Effect as Driven by Available Technologies and by Developing Applications. *J. Chem. Educ.* 84, 50–60. doi:10.1021/ed084p50

Agarwal, U. P. (2014). 1064 Nm FT-Raman Spectroscopy for Investigations of Plant Cell walls and Other Biomass Materials. *Front. Plant Sci.* 5, 490. doi:10.3389/fpls.2014.00490

Agarwal, U. P. (2019). Analysis of Cellulose and Lignocellulose Materials by Raman Spectroscopy: A Review of the Current Status. *Molecules* 24, 1659. doi:10.3390/molecules24091659

Agarwal, U. P., Ralph, S. A., Baez, C., and Reiner, R. S. (2021a). Contributions of Crystalline and Noncrystalline Cellulose Can Occur in the Same Spectral Regions: Evidence Based on Raman and IR and its Implication for Crystallinity Measurements. *Biomacromolecules* 22, 1357–1373. doi:10.1021/acs.biomac.0c01389

Agarwal, U. P., Ralph, S. A., Baez, C., and Reiner, R. S. (2021c). Detection and Quantitation of Cellulose II by Raman Spectroscopy. *Cellulose* 28, 9069–9079. doi:10.1007/s10570-021-04124-x

Agarwal, U. P., Ralph, S. A., Baez, C., Reiner, R. S., and Verrill, S. P. (2017). Effect of Sample Moisture Content on XRD-Estimated Cellulose Crystallinity index and Crystallite Size. *Cellulose* 24, 1971–1984. doi:10.1007/s10570-017-1259-0

Agarwal, U. P., and Ralph, S. A. (1997). FT-Raman Spectroscopy of wood: Identifying Contributions of Lignin and Carbohydrate Polymers in the Spectrum of Black spruce (*Picea Mariana*). *Appl. Spectrosc.* 51, 1648–1655. doi:10.1366/0003702971939316

Agarwal, U. P., Ralph, S. A., Reiner, R. S., and Baez, C. (2018). New Cellulose Crystallinity Estimation Method that Differentiates between Organized and Crystalline Phases. *Carbohydr. Polym.* 190, 262–270. doi:10.1016/j.carbpol.2018.03.003

Agarwal, U. P., Ralph, S. A., Reiner, S. A., and Baez, C. (2016). Probing Crystallinity of Never-Dried Wood Cellulose With Raman Spectroscopy. *Cellulose* 23, 125–144.

Agarwal, U. P., Reiner, R. R., and Ralph, S. A. (2013b). Estimation of Cellulose Crystallinity of Lignocelluloses Using Near-IR FT-Raman Spectroscopy and Comparison of the Raman and Segal-WAXS Methods. *J. Agric. Food Chem.* 61 (1), 103–113. doi:10.1021/jf304465k

Agarwal, U. P., Reiner, R. S., Ralph, S. A., Catchmark, J., Chi, K., Foster, E. J., et al. (2021b). Characterization of the Supramolecular Structures of Cellulose Nanocrystals of Different Origins. *Cellulose* 28, 1369–1385. doi:10.1007/s10570-020-03590-z

Agarwal, U. P., Reiner, R. S., and Ralph, S. A. (2010). Cellulose I Crystallinity Determination Using FT-Raman Spectroscopy: Univariate and Multivariate Methods. *Cellulose* 17, 721–733. doi:10.1007/s10570-010-9420-z

Agarwal, U. P., Zhu, J. Y., and Ralph, S. A. (2013a). Enzymatic Hydrolysis of Loblolly pine: Effects of Cellulose Crystallinity and Delignification. *Holzforschung* 67, 371–377. doi:10.1515/hf-2012-0116

Aldaeus, F., Larsson, K., Srndovic, J. S., Kubat, M., Karlström, K., Peciulyte, A., et al. (2015). The Supramolecular Structure of Cellulose-Rich wood Pulps Can Be a Determinative Factor for Enzymatic Hydrolysability. *Cellulose* 22, 3991–4002. doi:10.1007/s10570-015-0766-0

Atalla, R. H., and Dimick, B. E. (1975). Raman-spectral Evidence for Differences between the Conformations of Cellulose I and Cellulose II. *Carbohydr. Res.* 39. **Cl–C3**. doi:10.1016/s0008-6215(00)82656-7

Baldwin, K. J., Batchelder, D. N., and Webster, S. (2002). "Raman Microscopy: Confocal and Scanning Near-Field," in *Handbook of Raman Spectroscopy*. Editors I. R. Lewis and H. G. Edwards (New York: Marcel Dekker), 145–190. Ch. 4.

Chundawat, S. P. S., Donohoe, B. S., da Costa Sousa, L., Elder, T., Agarwal, U. P., Lu, F., et al. (2011). Multi-scale Visualization and Characterization of Lignocellulosic Plant Cell wall Deconstruction during Thermochemical Pretreatment. *Energy Environ. Sci.* 4, 973–984. doi:10.1039/c0ee00574f

De Figueiredo, L. P., and Ferreira, F. F. (2014). The Rietveld Method as a Tool to Quantify the Amorphous Amount of Microcrystalline Cellulose. *J. Pharm. Sci.* 103, 1394–1399. doi:10.1002/jps.23909

Edwards, H. G. M., Farwell, D. W., and Webster, D. (1997). FT Raman Microscopy of Untreated Natural Plant Fibres. *Spectrochimica Acta A: Mol. Biomol. Spectrosc.* 53, 2383–2392. doi:10.1016/s1386-1425(97)00178-9

Fan, L. T., Lee, Y.-H., and Beardmore, D. H. (1980). Mechanism of the Enzymatic Hydrolysis of Cellulose: Effects of Major Structural Features of Cellulose on Enzymatic Hydrolysis. *Biotechnol. Bioeng.* 22, 177–199. doi:10.1002/bit.260220113

Foston, M., Hubbell, C. A., Samuel, R., Jung, S., Fan, H., Ding, S.-Y., et al. (2011). Chemical, Ultrastructural and Supramolecular Analysis of Tension wood in Populus Tremula X alba as a Model Substrate for Reduced Recalcitrance. *Energ. Environ. Sci.* 4, 4962–4971. doi:10.1039/c1ee02073k

Gao, J., Jebrane, M., Terziev, N., and Daniel, G. (2021). Enzymatic Hydrolysis of the Gelatinous Layer in Tension wood of Salix Varieties as a Measure of Accessible Cellulose for Biofuels. *Biotechnol. Biofuels* 14, 141. doi:10.1186/s13068-021-01983-1

Gierlinger, N., Goswami, L., Schmidt, M., Burgert, I., Coutand, C., Rogge, T., et al. (2008). *In Situ* FT-IR Microscopic Study on Enzymatic Treatment of poplar wood Cross-Sections. *Biomacromolecules* 9, 2194–2201. doi:10.1021/bm800300b

Himmel, M. E., and Picataggio, S. K. (2008). "Our challenge Is to Acquire Deeper Understanding of Biomass Recalcitrance and Conversion," in *Biomass Recalcitrance*. Editor M. E. Himmel (Oxford, United Kingdom: Blackwell Publishing Lt.), 1–6.

Huber, G. W., Iborra, S., and Corma, A. (2006). Synthesis of Transportation Fuels from Biomass: Chemistry, Catalysts, and Engineering. *Chem. Rev.* 106, 4044–4098. doi:10.1021/cr068360d

Ibbett, R., Gaddipati, S., Hill, S., and Tucker, G. (2013). Structural Reorganisation of Cellulose Fibrils in Hydrothermally Deconstructed Lignocellulosic Biomass and Relationships with Enzyme Digestibility. *Biotechnol. Biofuels* 6, 33. doi:10.1186/1754-6834-6-33

Jeoh, T., Ishizawa, C. I., Davis, M. F., Himmel, M. E., Adney, W. S., and Johnson, D. K. (2007). Cellulase Digestibility of Pretreated Biomass Is Limited by Cellulose Accessibility. *Biotechnol. Bioeng.* 98, 112–122. doi:10.1002/bit.21408

Johnson, D. K., and Elander, R. T. (2008). "Pretreatments for Enhanced Digestibility of Feedstocks," in *Biomass Recalcitrance*. Editor M. E. Himmel (Oxford, United Kingdom: Blackwell Publishing Lt.), 436–453.

Leu, S.-Y., and Zhu, J. Y. (2013). Substrate-related Factors Affecting Enzymatic Saccharification of Lignocelluloses: Our Recent Understanding. *Bioenerg. Res.* 6 (2), 405–415. doi:10.1007/s12155-012-9276-1

Ling, Z., Wang, T., Makarem, M., Santiago Cintrón, M., Cheng, H. N., Kang, X., et al. (2019). Effects of ball Milling on the Structure of Cotton Cellulose. *Cellulose* 26, 305–328. doi:10.1007/s10570-018-02230-x

Maddams, W. F. (1980). The Scope and Limitations of Curve Fitting. *Appl. Spectrosc.* 34, 245–267. doi:10.1366/0003702804730312

Mosier, N., Wyman, C., Dale, B., Elander, R., Lee, Y. Y., Holtzapple, M., et al. (2005). Features of Promising Technologies for Pretreatment of Lignocellulosic Biomass. *Bioresour. Tech.* 96, 673–686. doi:10.1016/j.biortech.2004.06.025

Ohmine, K., Ooshima, H., and Harano, Y. (1983). Kinetic Study on Enzymatic Hydrolysis of Cellulose by Cellulose fromTrichoderma Viride. *Biotechnol. Bioeng.* 25, 2041–2053. doi:10.1002/bit.260250813

Park, S., Baker, J. O., Himmel, M. E., Parilla, P. A., and Johnson, D. K. (2010). Cellulose Crystallinity index: Measurement Techniques and Their Impact on Interpreting Cellulase Performance. *Biotechnol. Biofuels* 3, 10. doi:10.1186/1754-6834-3-10

Park, S., Johnson, D. K., Ishizawa, C. I., Parilla, P. A., and Davis, M. F. (2009). Measuring the Crystallinity index of Cellulose by Solid State 13C Nuclear Magnetic Resonance. *Cellulose* 16, 641–647. doi:10.1007/s10570-009-9321-1

Parrott, E. P. J., and Zeitler, J. A. (2015). Terahertz Time-Domain and Low-Frequency Raman Spectroscopy of Organic Materials. *Appl. Spectrosc.* 69, 1–25. doi:10.1366/14-07707

Peciulyte, A., Karlström, K., Larsson, P. T., and Olsson, L. (2015). Impact of the Supramolecular Structure of Cellulose on the Efficiency of Enzymatic Hydrolysis. *Biotechnol. Biofuels* 8, 56. doi:10.1186/s13068-015-0236-9

Rollin, J. A., Zhu, Z., Sathitsuksanoh, N., and Zhang, Y.-H. P. (2010). Increasing Cellulose Accessibility Is More Important Than Removing Lignin: A Comparison of Cellulose Solvent-Based Lignocellulose Fractionation and Soaking in Aqueous Ammonia. *Biotechnol. Bioeng.* 108, 22–30. doi:10.1002/bit.22919

Schenzel, K., Fischer, S., and Brendler, E. (2005). New Method for Determining the Degree of Cellulose I Crystallinity by Means of FT Raman Spectroscopy. *Cellulose* 12, 1971–1924. doi:10.1007/s10570-004-3885-6

Spiliopoulos, P., Spirk, S., Pääkkönen, T., Viljanen, M., Svedström, K., Pitkänen, L., et al. (2021). Visualizing Degradation of Cellulose Nanofibers by Acid Hydrolysis. *Biomacromolecules* 22, 1399–1405. doi:10.1021/acs.biomac.0c01625

Vieira, F. S., and Pasquini, C. (2014). Determination of Cellulose Crystallinity by Terahertz-Time Domain Spectroscopy. *Anal. Chem.* 86, 3780–3786. doi:10.1021/ac4035746

Wang, H., Horikawa, Y., Tsuchikawa, S., and Inagaki, T. (2020). Terahertz Time-Domain Spectroscopy as a Novel Tool for Crystallographic Analysis in Cellulose. *Cellulose* 27, 9767–9777. doi:10.1007/s10570-020-03508-9

Wang, H., Tsuchikawa, S., and Inagaki, T. (2021). Terahertz Time-Domain Spectroscopy as a Novel Tool for Crystallographic Analysis in Cellulose: The Potentiality of Being a New Standard for Evaluating Crystallinity. *Cellulose* 28, 5293–5304. doi:10.1007/s10570-021-03902-x

Wickholm, K., Larsson, P. T., and Iversen, T. (1998). Assignment of Non-crystalline Forms in Cellulose I by CP/MAS 13C NMR Spectroscopy. *Carbohydr. Res.* 312, 123–129. doi:10.1016/s0008-6215(98)00236-5

Wiley, J. H., and Atalla, R. H. (1987). Band Assignments in the Raman Spectra of Celluloses. *Carbohydr. Res.* 160, 113–129. doi:10.1016/0008-6215(87)80306-3

Yu, Y., Wu, J., Ren, X., Lau, A., Rezaei, H., Takada, M., et al. (2022). Steam Explosion of Lignocellulosic Biomass for Multiple Advanced Bioenergy Processes: A Review. *Renew. Sustain. Energ. Rev.* 154, 111871. doi:10.1016/j.rser.2021.111871

Zhou, Z., Lei, F., Li, P., and Jiang, J. (2018). Lignocellulosic Biomass to Biofuels and Biochemicals: A Comprehensive Review with a Focus on Ethanol Organosolv Pretreatment Technology. *Biotechnol. Bioeng.* 115, 2683–2702. doi:10.1002/bit.26788

Zhu, J. Y., Pan, X. J., Wang, G. S., and Gleisner, R. (2009). Sulfite Pretreatment (SPORL) for Robust Enzymatic Saccharification of spruce and Red pine. *Bioresour. Tech.* 100, 2411–2418. doi:10.1016/j.biortech.2008.10.057

Conflict of Interest: The author declares that the research was conducted in the absence of any commercial or financial relationships that could be construed as a potential conflict of interest.

Publisher's Note: All claims expressed in this article are solely those of the authors and do not necessarily represent those of their affiliated organizations, or those of the publisher, the editors, and the reviewers. Any product that may be evaluated in this article, or claim that may be made by its manufacturer, is not guaranteed or endorsed by the publisher.

frontiers | Frontiers in Energy Research

BRIEF RESEARCH REPORT
published: 24 June 2022
doi: 10.3389/fenrg.2022.879257

The Flexible and Transparent Film Heaters Based on Regenerated Cellulose and Carbon Nanotubes

*Jiedong Cui[1], Pengbo Lu[1,2], Yinghui Li[1], Ke Xu[1], Yang Li[1], Haoyu Shen[1], Chaocheng Liu[1], Tianyi Zhang[2] and Detao Liu[1]**

[1]School of Light Industry and Engineering, South China University of Technology, Guangzhou, China, [2]Gree Intelligent Equipment Co., Ltd., Zhuhai, China

The flexible and transparent film heaters (FTFHs) with the advantages of mechanical flexibility, portability, and excellent electrothermal performance, are key to the next generation portable, wearable heaters and thermal protection systems. However, the present flexible and transparent substrates of FTFHs are fabricated by typical plastic PET films, which suffer from poor interfacial adhesion with the thermally conductive materials. In this work, the transparent regenerated cellulose fibers made of completely dissolved in NMMO solution followed by regeneration process is presented to disperse and support carbon nanotubes (CNTs) by a vacuum-dewatering process. In the presence of cellulose fibers, these CNTs have strong hydrogen bonding properties in the dehydration-deposition process and thus respond to tight intertwining structures in fibrous composites. The resulting regenerated cellulose fibers exhibit high optical transparency of 88% (@550 nm) and good mechanical properties (30 MPa). Interestingly, the FTFHs show a rapid heating response, high generation temperature, and resistance stability for up to 2 h. The FTFHs made with earth-abundant, cost-effective, and recyclable materials, have excellent potential in the areas of green flexible and transparent film heaters.

Keywords: flexible heaters, regenerated cellulose, NMMO, CNFS, transparency

OPEN ACCESS

Edited by:
Xiaojun Shen,
Dalian Institute of Chemical Physics, (CAS), China

Reviewed by:
Li Fengfeng,
Qilu University of Technology, China
Liangcai Peng,
Huazhong Agricultural University, China

****Correspondence:***
Detao Liu
dtliu@scut.edu.cn

Specialty section:
This article was submitted to Bioenergy and Biofuels, a section of the journal Frontiers in Energy Research

Received: *19 February 2022*
Accepted: *30 May 2022*
Published: *24 June 2022*

Citation:
Cui J, Lu P, Li Y, Xu K, Li Y, Shen H, Liu C, Zhang T and Liu D (2022) The Flexible and Transparent Film Heaters Based on Regenerated Cellulose and Carbon Nanotubes. Front. Energy Res. 10:879257. doi: 10.3389/fenrg.2022.879257

INTRODUCTION

Due to its attractive characteristics of portability, quick response, and flexibility, the flexible and transparent film heaters (FTFHs) are directing the development of the next generation of flexible heaters such as vehicle window defrosters, outdoor panel displays, and automobile mirrors (Madaria et al., 2011; Lee et al., 2016; Song et al., 2017; Lee et al., 2020b), and so on. Until now, the FTFHs are typically fabricated by sputtering, coating, or printing electrothermal materials such as ITO (De et al., 2009), graphene (Zhang Q. et al., 2017), conducting polymers (Kim et al., 2011) and AgNWs (Wang et al., 2018) onto the surface of flexible polyethylene terephthalate (PET) (Tokuno et al., 2011) or rigid glass substrates. However, research efforts over the past years have encountered numerous problems, such as non-biodegradability, fragility, and non-transparency with low electrothermal efficiency (Jang and Choi, 2021; Yu et al., 2021). More importantly, loading electrothermal materials onto the smooth-faced PET, glass, or metal substrates, renders the poor adhesion and easier debonding between them (Hutchinson and Suo, 1992; Yu et al., 2019). Compared to the typical substrates with mechanical brittleness, scarcity, and fragile property (Cotterell and Chen, 2004), the flexibly porous fiber substrates display outstanding binding force due to their abundant hydroxyl groups combined with electrothermal materials. Furthermore, with porosity present, this FTFHs

composite is usually opaque, and hence a general mechanism to decrease the contradiction between them remains intricate.

Nowadays, natural biopolymers have been utilized to substitute plastic-based film substrates. Cellulose, an inexhaustible biopolymer resource, has excellent biocompatibility, biodegradability, mechanical and thermal stabilities (De France et al., 2020; Ma et al., 2021). Cellulose is an ideal candidate material to replace PET film substrates due to the rich hydrogen groups between cellulose molecules that can promote fiber bonding and improve the mechanical strength of the films (Ji et al., 2021). However, regular films made of cellulose fibers have high surface roughness and porosity, the natural difference in refractive index between air and cellulose make a negative influence on the transparency of substrate materials and electrical properties of devices (Fang et al., 2014). Su et al. (Su et al., 2019) fabricated FTFHs using a solution-based pressured extrusion papermaking process that conducting polymer (PEDOT: PSS) enhanced silver nanowire (AgNW) networks adsorbed on the cellulose nanofibers (CNFs) film substrate. CNFs are outstanding materials to prepare transparent films because there are few void spaces inside the paper, and the refractive index of light is reduced (Isogai et al., 2011; Isogai, 2013). However, the preparation process of CNFs is complicated and has high energy consumption, time consumption, and high cost, limiting the large-scale production of flexible and transparent film substrates (Li et al., 2019). Therefore, it is of significance to look for novel alternative materials to prepare FTFHs with good electrical conductivity, excellent mechanical properties, flexibility, and environmental friendliness. Interestingly, direct dissolution of cellulose with cellulose solvents assisted by subsequent treatment is an efficient process to produce transparent films on a large scale and at a low cost. Recent studies have shown that ionic liquids are suitable solvents for cellulose, which can dissolve cellulose and then regenerate it in an aqueous solution or ethanol solution to prepare regenerated cellulose. And regenerated cellulose is also an excellent material to fabricate transparent film substrates. (Lu et al., 2017a) firstly reported an all-cellulose transparent film fabricated by a novel microwave-assisted ionic liquids technology, which shows high optical transparency of 82% (@550 nm) and high tensile stress (46.0 MPa). The most common solvents used in these processes mainly include NaOH/urea aqueous solutions (Kong et al., 2021), LiCl/DMAc (Gao et al., 2021), PF/DMSO (He and Wang, 2000), and N-methyl Morpholine, Nmethylmorpholine-N-oxide (NMMO) (Protz et al., 2021). Among them, NMMO has attracted significant attention because of its green, non-toxic, high recyclability (99%), and good solubility (Zhang Y. et al., 2017). In addition, Carbon nanotubes (CNTs) (Zhang et al., 2006; Cao and Rogers, 2009) have the advantages of outstanding thermal conductivity, excellent mechanical flexibility, and exceptional optical properties, which are regarded as the ideal candidates for replacing ITO. CNTs can also be cross-linked with cellulose by hydrogen bonding, which solves poor adhesion between conductive materials and the transparent substrates.

In this work, we fabricated FTFHs with high optical transparency and promising electrothermal properties by using regenerated cellulose to prepare film as flexible transparent substrates and CNTs as thermally conductive materials. This new method for preparing FTFHs had the following advantages: 1) The NMMO solution is non-toxic, recyclable and high-efficiency in dissolving cellulose; 2) Regenerated cellulose is an outstanding material for preparing flexible and transparent films that can substitute PET films for better bonding with thermal conductive materials; 3) The FTFHs made of regenerated cellulose and CNFs, exhibits high generation temperature (50.5°C), shorter response time (15 s) and long-term stability of resistance (2 h), shows a good case for designing FTFHs with high-performance and environmental friendliness in flexible heaters applications.

EXPERIMENTAL

Materials

Commercial eucalyptus dissolving pulp was used as the raw cellulose source material and was purchased from Guangzhou Chenhui Paper Co., Ltd. (China) and the average polymerization degree of eucalyptus dissolving pulp was 652. The carbon nanotubes (~50 μm) were purchased from Shanghai Lishuo Co., Ltd. (China); N-methyl -morpholine-N-oxide (NMMO) was purchased from Aladdin-Reagent Co., Ltd. (Shanghai China). All the reagents were used as received.

Preparation of Regenerated Cellulose

Firstly, the mass fraction of 50% NMMO solution purchased directly was diluted to obtain an aqueous NMMO solution with a mass fraction of 13%. Then 2 g cellulose fibers were added to the 100 ml 13% aqueous NMMO solution and stirred for 2 h at 90°C to obtain the dissolved cellulose. Add dissolved cellulose solution to deionized water and rotate it in a high-speed emulsifier at 5000 rpm/min to get the regenerated cellulose. The regenerated cellulose with a concentration of 0.5 wt%% was centrifuged at 4000 rpm/min for 10 min and the supernatant was smaller than regenerated cellulose and the turbid solution was larger than regenerated cellulose.

Dispersion of Carbon Nanotubes

The CNTs used in this study are multiwalled CNTs synthesized by chemical vapor deposition and the length of the CNTs is about 50 μm. First, 40 ml HNO_3 and 120 ml H_2SO_4 were added into the beaker to mix evenly, and 0.4 g CNTs were added to the mixed solution. After ultrasonic treatment for 2 h, CNTs were centrifuged at 4000 rpm/min for 20 min, and then the CNTs were washed to neutral with deionized water. Then a 0.5% CNT dispersion was prepared with deionized water.

Fabrication of Flexible and Transparent Film Heaters

The flexible transparent paper with a base density of 30 g/m^2 and an area of 28 cm^2 was prepared by suction filtration. Then, the dispersed CNTs solution was poured on the surface of the flexible transparent paper and continued to filter. After carbon nanotubes

were completely deposited on transparent paper, FTFHs were obtained by hot pressing at 110°C and 0.4 MPa for 5 min. For comparison, we also prepared transparent films using the smaller regenerated cellulose (supernatant of the solution)as raw material without CNTs, called Film-1 and using the larger regenerated (raw solution) cellulose as raw material without CNTs, called Film-2. The FTFHs with contents of CNTs were 0.1 g/m^2, 0.15 g/m^2 and 0.2 g/m^2 were called FTFH-0.1, FTFH-0.15, FTFH-0.2.

Characterizations

Scanning Electron Microscopy

The film morphologies were tested with scanning electron microscopy (SEM) with an accelerating voltage at 5–10 kV. A KajaaniFS300 Fiber Analyzer was used to quantitatively analyze the dimensions of the regenerated cellulose fibers and the original cellulose fibers in DI water (18.2 MΩ/cm).

Transmission Electron Microscopy

The samples were observed with transmission electron microscopy (TEM) using a JEM-2100 transmission electron microscope at an accelerator voltage of 200 kV. A droplet of the diluted slurry was dropped on the carbon-coated electron microscopy grid and then negatively stained with 1 wt% phosphotungstic acid solution to enhance image contrast. The dimensions of the DCCs were determined from the TEM images using the Image J TEM-image-processing software.

Transmittance

UV-Vis spectrometer with an integrating sphere (UV-9000 Shanghai Yuanyi Inc. China) was used to measure the total transmittance of the films in a wavelength range of 400–900 nm.

X-ray Diffraction

X-ray diffraction (XRD) patterns of the film samples were carried out on an X-ray diffractometer (D8 ADVANCE, Bruker Inc., Germany) with area detector operating at a voltage of 40 kV and a current of 40 mA using Cu Kα radiation (λ= 0.154 nm). The scanning scope of 2θ was from 4° to 50° at room temperature.

Thermogravimetric Analysis

Thermal stability and changes in degradation patterns associated with regenerated cellulose film and original cellulose were assessed with TGA (TA Instruments TGA Q500). Samples were tested under a flowing nitrogen atmosphere with sample 5–7 mg. Samples were heated from room temperature to 120°C at a rate of 10°C/min under a flowing nitrogen atmosphere, then held at 120°C for 20 min, and then heated to 600°C at a rate of 10°C/min.

Mechanical Strength

The mechanical strength of samples was measured using a universal tensile tester (Instron5565, Instron Instruments Inc. United States). Samples were cut into 5.0 mm × 25.0 mm. The resistances of the FTFHs were recorded by a multimeter (VC890D, China). Samples were cut into 25.0 mm × 25.0 mm. The samples were placed in a constant temperature and humidity chamber at (50 ± 1) % relative humidity (RH) and (23 ± 1)°C for 24 h to ensure the stabilization of their water content before characterization.

Temperatures and Heat Distributions

The temperatures and heat distributions of the FTFHs were measured using a thermal imager (DT-980, China). Samples were cut into 80.0 mm × 80.0 mm. The applied DC voltage was supplied by a power supply (HY3005ET, China). Two copper conductive tapes were pasted at the FTFHs to form a complete circuit system.

RESULTS AND DISCUSSION

Fabrication Process for the Flexible and Transparent Film Heaters

The schematic illustration of the procedure of FTFHs was shown in **Figure 1**. Ordinary paper made of cellulose is optically opaque, due to the void spaces in the fiber network and scattering of light at the interfacial area between the fibers, hindering their practical application as substrates in transparent film heaters. The transparent film made of regenerated cellulose reported in this work exhibited excellent optical transparency. The original cellulose dissolves in the mass fraction of 13% aqueous NMMO solution then regenerated in deionized water. NMMO is a tertiary aliphatic amine N-oxide hydrate with strong dipole N-O moiety. The oxygen groups form one or two hydrogen bonds with an anhydrous glucopyranose unit (AGU) of cellulose, which leads to the cleavage of intermolecular hydrogen bonds of cellulose chains and cellulose is dissolved. The dissolved cellulose was added to deionized water, and the N-O groups of NMMO form hydrogen bonds with the hydroxyl groups of water molecules (Bang et al., 1999; Zimmermann et al., 2016; Sayyed et al., 2019). The regenerated cellulose is obtained due to the released cellulose molecules rapidly regenerate by reforming new hydrogen-bond networks. CNTs were tightly deposited on the flexible transparent film by suction filtration. The oxidized CNTs have hydroxyl and carboxyl groups on the surface (Guo et al., 2018), which form hydrogen bonding with regenerated cellulose. The compatibility and interaction between the CNTs and regenerated cellulose enhanced the interfacial adhesion. Through the hot-pressing process, the bonding strength between carbon nanotubes and regenerated cellulose is greatly improved, and the porosity of the film is reduced, which led to the increase in the mechanical strength and transparency of the film.

The Structure of Samples

The differences of Original paper (made of raw cellulose, by paper making), Film-1, and FTFHs have distinctly been observed from the scanning electron microscope (SEM) images by scanning cross-sections and fracture surfaces in **Figure 2**. As shown in **Figures 2A,B**, the surface of the original paper is rough and porous with long fibers attached intricately. The voids between the cellulose are the main reason for the opacity of papers (Khakalo et al., 2017). After dissolution and regeneration, the film prepared by regenerated cellulose has a smooth surface without apparent pores (**Figures 2C,D**). Accompanied by the

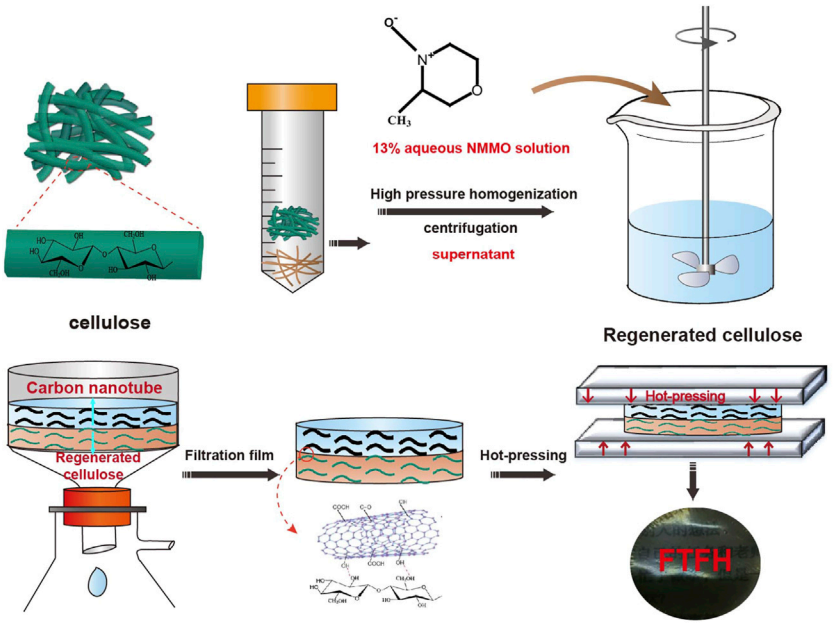

FIGURE 1 | Schematic illustration of the fabrication process for the FTFHs.

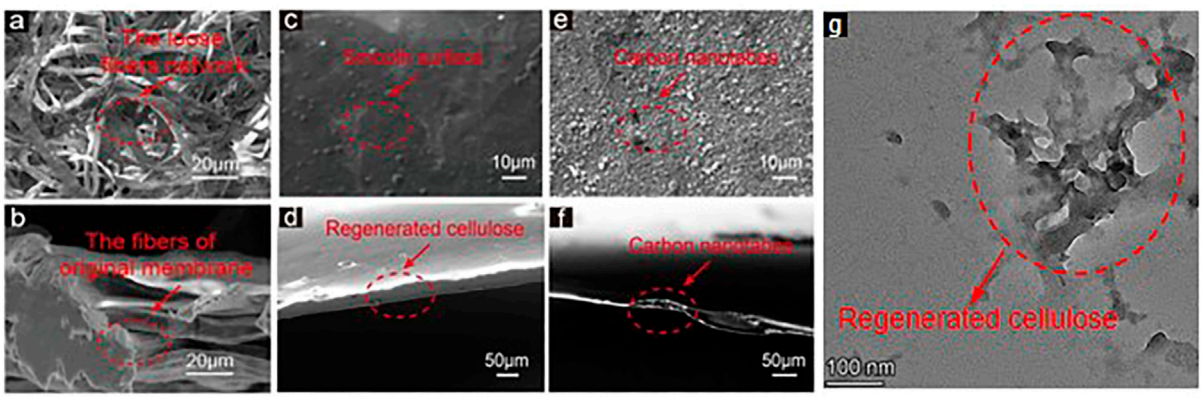

FIGURE 2 | SEM images of cross-sections: **(A)** Original paper; **(C)** Film-1; **(E)** FTFH; SEM images of the fracture surface: **(B)** Original paper; **(D)** Film-1; **(F)** FTFH; **(G)** TEM image of regenerated cellulose.

dissolution process, the hydrogen bond between the cellulose is destroyed and the cellulose is broken down into small sizes. The small size of cellulose is tightly intertwined due to hydrogen bonds during the filtration process, and the holes between the fibers are filled with smaller cellulose. CNTs are deposited onto the wet flexible transparent film to fabricate FTFHs. The surface of FTFHs in **Figure 2E** is significantly rougher than Film-1, due to the size of the CNTs is larger than the size of the underlying regenerated cellulose. The fracture surface of FTFHs in **Figure 2F** only shown the CNTs layer, and the cellulose fiber layer does not appear because it has not been sprayed with gold to prevent the effect of the metal gold coating on CNTs. As shown in **Figure 2G**, the length of regenerated cellulose is about 100–200 nm.

The dimension of cellulose fiber is an essential factor in affecting the transparency of the substrate. As shown in **Table 1**, the regenerated cellulose fibers have an average fiber length of 0.66 mm and an average fiber width of 11.45 μm, whereas original cellulose fibers have an average fiber length of 2.40 mm and an average fiber width of 25.82 μm. It is proved that the aqueous NMMO solvent can cleavage intermolecular hydrogen bonds of cellulose chains and reduce cellulose size, indicating that aqueous NMMO solvent is the excellent solvent system for cellulose. Regenerated cellulose fibers have a higher curl index (28.87%) but a lower kink index (9.63 L/m) compared to original pulp fibers, which is conducive to the formation of flexible transparent film. The fine content of the regenerated cellulose fibers (fiber length less than 200 mm, 66.98%) is much

TABLE 1 | Fiber dimension of regenerated cellulose and the original pulp fibers.

Samples	Length (mm)	Width (μm)	Curl index (%)	Kink index (L/m)	Cellulose fines (%)
Regenerated cellulose	0.66	11.45	28.87	9.36	66.98
Original cellulose	2.40	25.82	18.51	1334.82	8.33

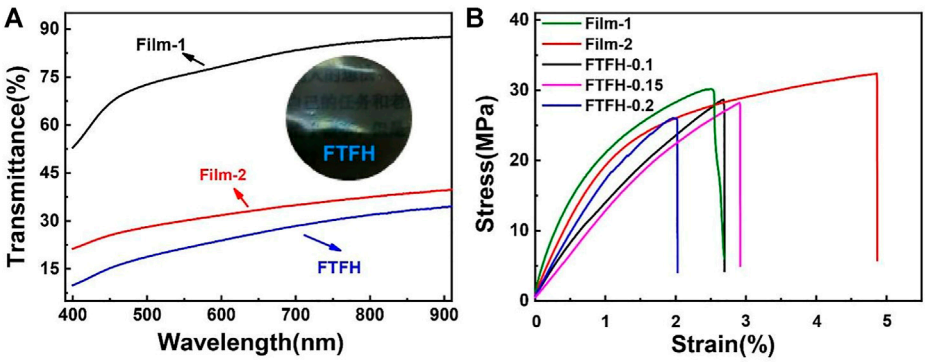

FIGURE 3 | (A) Optical transmittance plot for all Film-1, Film-2 and FTCT-0.15 in the range from 400–900 nm **(B)** Stress-strain curves of the Film-1, Film-2, FTFH-0.1, FTFH-0.15 and FTFH-0.2.

higher than that of original pulp fibers (8.33%). In the process of film formation, the rich hydroxyl among fines promotes the binding between the fibers, which reduces the void spaces of fines and improves the transparency of the film.

The Mechanical and Optical Performances of Samples

Transparency plays a crucial role for FTFHs, the transmittance of Film-1, Film-2, and FTFHs shown in **Figure 3A**. The Film-1 exhibits a high optical transmittance of 88% at the wavelength 550 nm, while the Film-2 is only 40%. The difference in refractive index between the air in pores and the cellulose fibers is a primary factor in reducing transparency. The transparency of Film-2 is significantly lower than film-1, due to the interleaving of the longer cellulose fibers leads to the formation of pores in the process of forming Film-2. As the content of CNTs increases, the optical transmittance decreases from 88 to 30%. The opaque CNTs are evenly deposited on the surface of the transparent fiber film, which seriously affects the transparency of the original film. Although FTFHs have a low level of transparency, we could recognize the back pattern of FTFHs.

Figure 3B shows the mechanical properties of Film-1, Film-2, and FTFHs. From **Figure 3B**, we concluded that the tensile strength of film 2 is 32 MPa, similar to that of Film-1 with 30 MPa. The abundant hydrogen groups in regenerated cellulose fiber enhance the contact strength between adjacent regenerated cellulose and improve the tensile strength of the substrate. With the increase of the content of CNTs, the tensile stress of FTFHs will gradually decrease. But, the tensile strength of FTFHs is only slightly lower than that of Film-1, because CNTs would bind with hydrogen bonds of regenerated cellulose fibers and weaken the adhesion between the fibers. The hydrogen bonding can make the CNTs tightly intertwined with the transparent substrate, which can effectively prevent the CNTs from falling off during the use of FTFHs. **Table 2** shows the summary of the mechanical properties of cellulose/CNT composite films and the manufacturing method is the key factor of the mechanical properties of cellulose/CNT composite films.

X-ray Diffraction Profiles of Original Paper and the Regenerated Cellulose

X-ray diffraction (XRD) patterns of the original cellulose and regenerated cellulose are compared in **Figure 4**. The XRD patterns of the original cellulose displayed two distinct characteristic peaks at $2\theta = 14.86$ and $2\theta = 22.75$, which corresponded to the (1–10) and (200) planes of the typical cellulose-I structure, respectively. After the cellulose was dissolved and regenerated, regenerated cellulose showed the typical cellulose II crystalline form, with diffraction peaks at $2\theta = 12.1$ and $2\theta = 21.97$. In the dissolution and regeneration process, cellulose I was transformed into cellulose II, and its crystal structure changed. According to the Segal formula, the crystallinity index (CrI) of original celluloses and regenerated celluloses are 73 and 53%, respectively. The reduced crystallinity demonstrates that the aqueous NMMO solvent enters into the crystallization zone of cellulose and the free hydroxyl groups of cellulose form intramolecular and intermolecular hydrogen bonds with solvent, causing the cellulose to dissolve gradually.

TABLE 2 | Summary of the mechanical properties of cellulose/CNT composite films.

Key materials	Stress (MPa)	Strain (%)	Manufacturing method	Refs.
Original cellulose/CNT	36	2.1	airbrush spraying	Callone et al. (2008)
Original cellulose/CNT	61.6	15.2	casting methond	Xie et al. (2020)
Original cellulose/CNT	180	12	dry–wet spinning	Liang et al. (2022)
Regenerated cellulose/CNT	32	3	Suction filtration	Our work

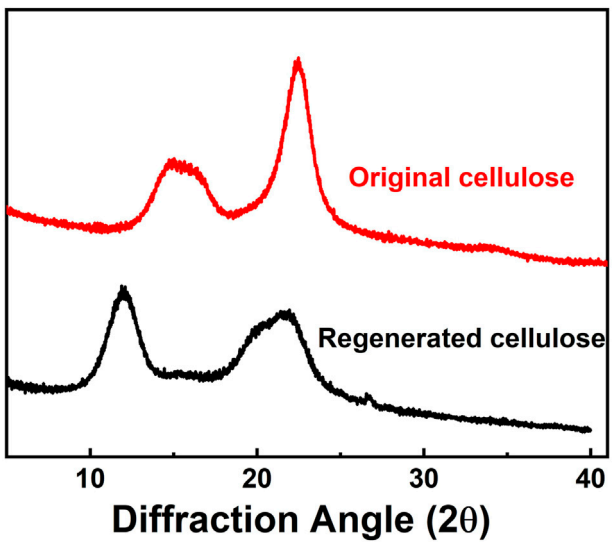

FIGURE 4 | X-ray diffraction profiles of original cellulose and the regenerated cellulose.

Thermal Stability of Original Cellulose and Regenerated Cellulose

The thermal decomposition behavior of original cellulose and regenerated cellulose was investigated by TGA. The results was shown in **Figure 5**. When the temperature rises above 400°C, the residual rate of regenerated cellulose is about 40%, which is about two times of the original cellulose. The glass transition temperature of the regenerated cellulose is 336°C, which is lower the glass transition temperature of original cellulose (361°C). The results of the TGA analysis showed that the thermal stability of the regenerated cellulose is better than original cellulose.

Electrical and Thermal Properties of the Flexible and Transparent Film Heaters

The infrared thermal images of FTFH-0.1, FTFH-0.15, FTFH-0.2 were taken to study their electrical and thermal properties (**Figures 6A–C**). The resistance and generated a temperature of the FTFH-0.1, FTFH-0.15, FTFH-0.2 were shown in **Figure 6D** and **Figure 6E**. All samples were driven at 20 V for 15 s. When the current passes through the FTFH-0.1, FTFH-0.15, FTFH-0.2, they can be rapidly heated from room temperature to 31.8°C, 39.9°C, and 50.5°C and remain stable. The resistance of the FTFH-0.1, FTFH-0.15, FTFH-0.2 is 3423 Ω, 2233 Ω, and 1593 Ω, respectively. The high generated temperature is a significant part of evaluating the performance of the self-heating heater device. As the CNTs' content increases, the resistance of FTFHs' decreases, and the generated temperature rise slowly. It is mainly attributed to the fact that the expansion of CNTs content increases the deposition thickness of CNTs on the flexible film, and the conductive network is formed and improved. However, as the content of CNTs continues to increase, the transparency of FTFHs will be severely affected. In our paper, the content of CNTs is only 0.2 g/m^2, and the generated temperature is as high as 50.5°C. This result demonstrates the feasibility of CNFs deposition on flexible and transparent regenerated cellulose film and FTFHs have broad application prospects in heat preservation heating and electronic devices.

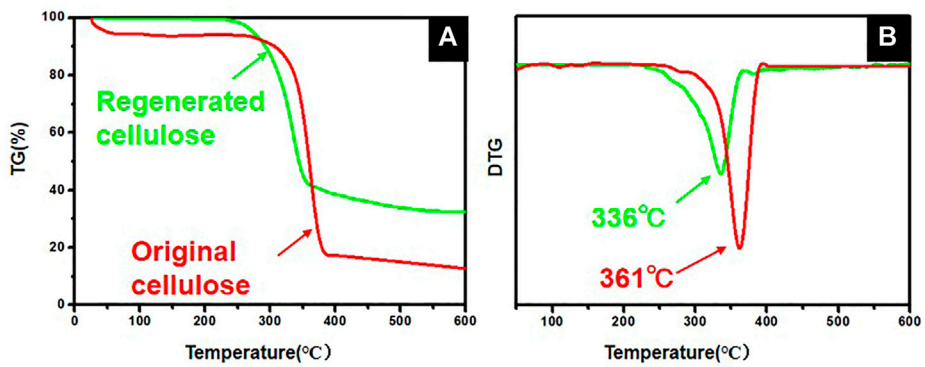

FIGURE 5 | TG and DTG curves of original cellulose and regenerated cellulose. the red lines stand for orginal cellulose, and green lines stand for regenerated cellulose in **Figure 5A,B**.

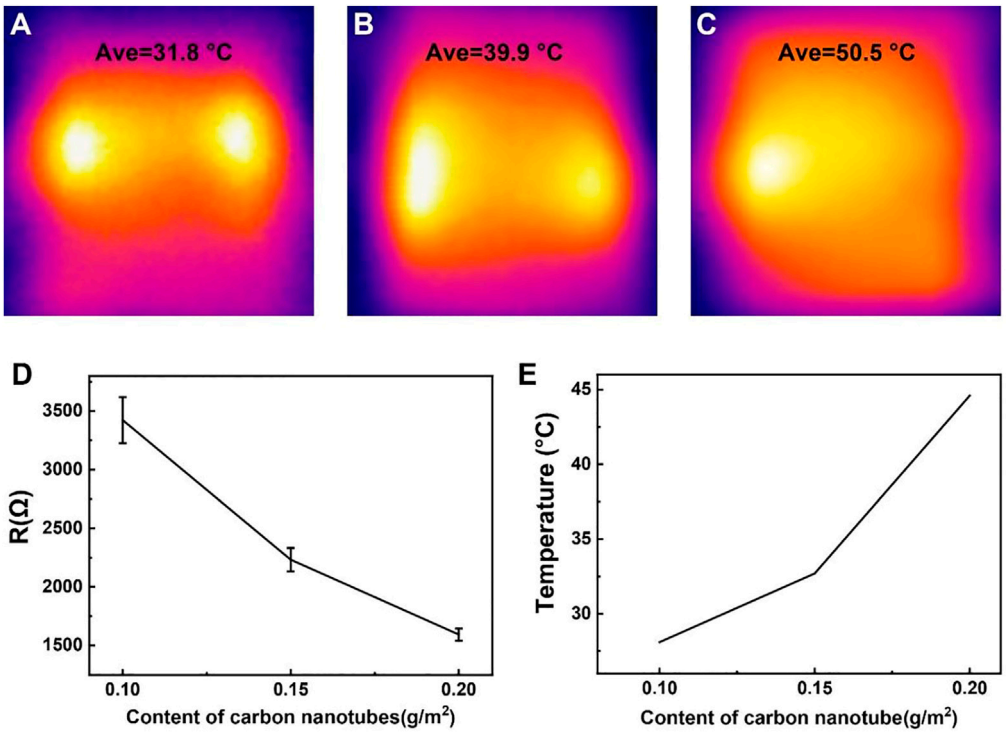

FIGURE 6 | The infrared thermal images: **(A)** FTFH-0.1, **(B)** FTFH-0.15, and **(C)** FTFH-0.2, **(D)** the resistance of FTFH with the content of carbon nanotube ranging from 0.1 g/m^2 to 0.2 g/m^2 **(E)** the generated temperature of the FTFH with the content of carbon nanotubes ranging from 0.1 g/m^2 to 0.2 g/m^2.

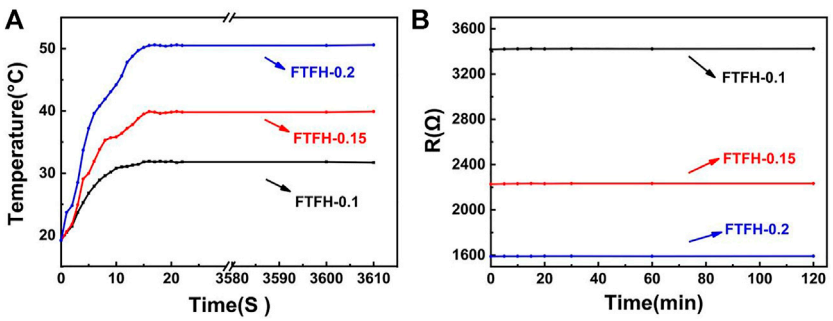

FIGURE 7 | (A) The generated temperature-responsetime of the FTFH with the various carbon nanotubes content. **(B)** The resistance-response time of the FTFH with various carbon nanotubes content.

TABLE 3 | Comparison with other film heaters as previously reported.

Deposition method	Voltage applied (V)	Temp (°C)	Materials	Transparency (%)	Refs.
Chemical techniques	20	90	Carbon fiber composite	70	Lu et al., 2017b
Sputtering	13	100	ITO/CU/ITO films	80	Lee et al., 2020a
PLD	12	140	GZO thin films	85	J Beckford, et al., 2021
Suction filtration	20	40	CNT	90	Our work

Figure 7 exhibits the thermal response time and resistance stability of the FTFHs. As shown in **Figure 7A**, the generated temperature of FTFHs increases with the increase of time, but after 15 s, the generated temperature remained unchanged. This result indicates that FTFHs have a quick thermal response time, and CNTs are an excellent electrothermal material for FTFHs. On

the other hand, the stability of resistance also plays a vital role in FTFHs. The change of the resistance of the FTFHs (**Figure 6B**) along the time was determined, which indicated that the resistance value remains stable and almost no change for about 2 hours. The stability of the resistance is the key to the safety of FTFHs commercial applications. Therefore, the properties of the FTFHs meet the requirement of a flexible and transparent film heater due to shorter response time, the long-term stability of the resistance, and higher generated temperature. **Table 3** exhibits some properties of different film heaters, the two main factors that mainly can affect properties of film heaters are deposition method and materials.

CONCLUSION

In summary, the FTFHs with high optical transmittance, excellent tensile strength, and good heat transfer performance were successfully prepared by simple vacuum filtration. We found that the aqueous NMMO solvent is an excellent solvent system for cellulose, and cellulose that is dissolved and regenerated with aqueous NMMO solution has a small size (0.66 mm in length and 11.45 μm in width). The obtained regenerated cellulose is used to produce flexible transparent film substrates with high optical transparency of 88% (@550 nm) and good mechanical properties of 30 MPa. FTFHs were prepared by depositing CNTs directly on the flexible transparent film, and the extensive hydrogen bonding between CNTs and the cellulose matrix gives FTFHs a high tensile strength of 28 MPa. Furthermore, the FTFHs exhibits higher generation temperatures (50.5°C), shorter response time (15 s), and long-term stability of resistance (2 h). This work demonstrates the broad application prospects of FTFHs in the next generation of green flexible and transparent film heaters.

DATA AVAILABILITY STATEMENT

The original contributions presented in the study are included in the article/supplementary material, further inquiries can be directed to the corresponding author.

AUTHOR CONTRIBUTIONS

Investigation, Visualization, Writing-Original draft preparation; PL: Investigation, Validation, JC and PL contributed this work equally, YL: Formal analysis, Writing-Original draft preparation; KX: Software, YL: Data curation, HS and ZT: Resources, CL: Methodology, DL: Conceptualization, Supervision, Project administration, Funding acquisition, Writing—Review and; Editing.

FUNDING

This work was kindly supported by Guangdong Basic and Applied Basic Research Foundation of Guangdong Province (No. 2020A1515011013; No. 2022A1515010910) and Science and Technology Planning Project of Guangdong Province (No. 2020A050515004) in China.

REFERENCES

Bang, Y. H., Lee, S., Park, J. B., and Cho, H. H. (1999). Effect of Coagulation Conditions on Fine Structure of Regenerated Cellulosic Films Made from cellulose/N-Methylmorpholine-N-oxide/H2O Systems. *J. Appl. Polym. Sci.* 73, 2681–2690. doi:10.1002/(sici)1097-4628(19990923)73:13<2681::aid-app16>3.0.co;2-z

Beckford, J., Behera, M. K., Yarbrough, K., Obasogie, B., Pradhan, S. K., and Bahoura, M. (2021). Gallium Doped Zinc Oxide Thin Films as Transparent Conducting Oxide for Thin-Film Heaters. *AIP Adv.* 11 (7), 075208. doi:10.1063/5.0016367

Callone, E., Fletcher, J. M., Carturan, G., and Raj, R. (2008). A Low-Cost Method for Producing High-Performance Nanocomposite Thin-Films Made from Silica and Cnts on Cellulose Substrates. *J. Mater Sci.* 43 (14), 4862–4869. doi:10.1007/s10853-008-2707-x

Cao, Q., and Rogers, J. A. (2009). Ultrathin Films of Single-Walled Carbon Nanotubes for Electronics and Sensors: A Review of Fundamental and Applied Aspects. *Adv. Mat.* 21, 29–53. doi:10.1002/adfm.20069006510.1002/adma.200801995

Cotterell, B., and Chen, Z. (2004). Buckling and Cracking of Thin Films on Compliant Substrates under Compression. *Int. J. Fract.* 104, 169–179. doi:10.1023/A:1007628800620

De France, K., Zeng, Z., Wu, T., and Nyström, G. (2020). Functional Materials from Nanocellulose: Utilizing Structure-Property Relationships in Bottom-Up Fabrication. *Adv. Mat.* 33, 2000657. doi:10.1002/adma.202000657

De, S., Higgins, T. M., Lyons, P. E., Doherty, E. M., Nirmalraj, P. N., Blau, W. J., et al. (2009). Silver Nanowire Networks as Flexible, Transparent, Conducting Films: Extremely High DC to Optical Conductivity Ratios. *ACS Nano* 3, 1767–1774. doi:10.1021/nn900348c

Fang, Z., Zhu, H., Bao, W., Preston, C., Liu, Z., Dai, J., et al. (2014). Highly Transparent Paper with Tunable Haze for Green Electronics. *Energy Environ. Sci.* 7, 3313–3319. doi:10.1039/c4ee02236j

Gao, X., Li, M., Zhang, H., Tang, X., and Chen, K. (2021). Fabrication of Regenerated Cellulose Films by DMAc Dissolution Using Parenchyma Cells via Low-Temperature Pulping from Yunnan-Endemic Bamboos. *Industrial Crops Prod.* 160, 113116. doi:10.1016/j.indcrop.2020.113116

Guo, B., Zhang, X., Cen, X., Chen, B., Wang, X., Song, M., et al. (2018). Enhanced Mechanical Properties of Aluminum Based Composites Reinforced by Chemically Oxidized Carbon Nanotubes. *Carbon* 139, 459–471. doi:10.1016/j.carbon.2018.07.026

He, C., and Wang, Q. (2000). The Rheological Property of Cellulose Solution in PF/DMSO. *J. China Text. Univ.* 17, 43–46. doi:10.19884/j.1672-5220.2000.03.010

Hutchinson, J. W., and Suo, Z. (1992). Mixed Mode Cracking in Layered materialsAdvances in Applied Mechanics. *Adv. Appl. Mech.* 29, 63–191. doi:10.1016/s0065-2156(08)70164-9

Isogai, A., Saito, T., and Fukuzumi, H. (2011). TEMPO-oxidized Cellulose Nanofibers. *Nanoscale* 3, 71–85. doi:10.1039/c0nr00583e

Isogai, A. (2013). Wood Nanocelluloses: Fundamentals and Applications as New Bio-Based Nanomaterials. *J. Wood Sci.* 59, 449–459. doi:10.1007/s10086-013-1365-z

Jang, J., and Choi, J.-W. (2021). Silver Alloy-Based Metal Matrix Composites: a Potential Material for Reliable Transparent Thin Film Heaters. *J. Mat. Chem. C* 9, 4670–4681. doi:10.1039/D1TC00132A

Ji, Q., Yu, X., Yagoub, A. E.-G. A., Chen, L., and Zhou, C. (2021). Efficient Cleavage of Strong Hydrogen Bonds in Sugarcane Bagasse by Ternary

Acidic Deep Eutectic Solvent and Ultrasonication to Facile Fabrication of Cellulose Nanofibers. *Cellulose* 28, 6159–6182. doi:10.1007/s10570-021-03876-w

Khakalo, A., Filpponen, I., and Rojas, O. J. (2017). Protein Adsorption Tailors the Surface Energies and Compatibility between Polylactide and Cellulose Nanofibrils. *Biomacromolecules* 18, 1426–1433. doi:10.1021/acs.biomac.7b00173

Kim, Y. H., Sachse, C., Machala, M. L., May, C., Müller-Meskamp, L., and Leo, K. (2011). Highly Conductive PEDOT:PSS Electrode with Optimized Solvent and Thermal Post-Treatment for ITO-free Organic Solar Cells. *Adv. Funct. Mat.* 21, 1076–1081. doi:10.1002/adfm.201002290

Kong, W., Yu, G., Xing, J., Zhang, H., Liu, M., and Shi, Y. (2021). Effect of the Dissolving Method on the Dissolution of Dissolving Pulp Cellulose Fibers with Different Dried-States in Different NaOH/Additives Aqueous Solutions. *J. Polym. Environ.* 29, 3909–3917. doi:10.1007/s10924-021-02149-8

Lee, E. Y., Han, K., Kim, D. H., Park, Y.-M., Kwon, H.-S., Yoon, K.-H., et al. (2020a). Exposure-weighted Scoring for Metabolic Syndrome and the Risk of Myocardial Infarction and Stroke: a Nationwide Population-Based Study. *Cardiovasc. Diabetol.* 19 (1), 153. doi:10.1186/s12933-020-01129-x

Lee, H., Kim, M., KimLee, I. H., and Lee, H. (2016). Flexible and Stretchable Optoelectronic Devices Using Silver Nanowires and Graphene. *Adv. Mat.* 28, 4541–4548. doi:10.1039/C4TC02448F10.1002/adma.201505559

Lee, S., Jang, J., ParkParkChung, T. Y. M. C. H., Park, Y. M., Park, J. S., Kim, Y.-K., et al. (2020b). Electrodeposited Silver Nanowire Transparent Conducting Electrodes for Thin-Film Solar Cells. *ACS Appl. Mat. Interfaces* 12, 6169–6175. doi:10.1021/acsami.9b17168

Li, Z., Liu, W., Guan, F., Li, G., Song, Z., Yu, D., et al. (2019). Using Cellulose Fibers to Fabricate Transparent Paper by Microfibrillation. *Carbohydr. Polym.* 214, 26–33. doi:10.1016/j.carbpol.2019.03.019

Liang, Q., Zhang, D., Wu, Y., Chen, S., Han, Z., Wang, B., et al. (2022). Self-Stretchable Fiber Liquid Sensors Made with Bacterial Cellulose/Carbon Nanotubes for Smart Diapers. *ACS Appl. Mat.* 18, 21319–21329. doi:10.1021/acsami.2c00960

Lu, P., Cheng, F., Ou, Y., Lin, M., Su, L., Chen, S., et al. (2017b). A Flexible and Transparent Thin Film Heater Based on a Carbon Fiber /heat-Resistant Cellulose Composite. *Compos. Sci. Technol.* 153, 1–6. doi:10.1016/j.compscitech.2017.09.033

Lu, P., Cheng, F., Ou, Y., Lin, M., Su, L., Chen, S., et al. (2017a). Rapid Fabrication of Transparent Film Directly from Wood Fibers with Microwave-Assisted Ionic Liquids Technology. *Carbohydr. Polym.* 174, 330–336. doi:10.1016/j.carbpol.2017.06.057

Ma, H., Yu, J., Liu, L., and Fan, Y. (2021). An Optimized Preparation of Nanofiber Hydrogels Derived from Natural Carbohydrate Polymers and Their Drug Release Capacity under Different pH Surroundings. *Carbohydr. Polym.* 265, 118008. doi:10.1016/j.carbpol.2021.118008

Madaria, A. R., Kumar, A., and Zhou, C. (2011). Large Scale, Highly Conductive and Patterned Transparent Films of Silver Nanowires on Arbitrary Substrates and Their Application in Touch Screens. *Nanotechnology* 22, 245201. doi:10.1088/0957-4484/22/24/245201

Protz, R., Lehmann, A., Ganster, J., and Fink, H.-P. (2021). Solubility and Spinnability of Cellulose-Lignin Blends in Aqueous NMMO. *Carbohydr. Polym.* 251, 117027. doi:10.1016/j.carbpol.2020.117027

Sayyed, A. J., Mohite, L. V., Deshmukh, N. A., and Pinjari, D. V. (2019). Structural Characterization of Cellulose Pulp in Aqueous NMMO Solution under the Process Conditions of Lyocell Slurry. *Carbohydr. Polym.* 206, 220–228. doi:10.1016/j.carbpol.2018.11.004

Song, C., Zhang, N., Lin, J., Guo, X., and Liu, X. (2017). Sb2O3/Ag/Sb2O3 Multilayer Transparent Conducting Films for Ultraviolet Organic Light-Emitting Diode. *Sci. Rep.* 7, 1–7. doi:10.1038/srep41250

Su, L., Ou, Y., Feng, X., Lin, M., Li, J., Liu, D., et al. (2019). Integrated Production of Cellulose Nanofibers and Sodium Carboxymethylcellulose through Controllable Eco-Carboxymethylation under Mild Conditions. *ACS Sustain. Chem. Eng.* 7, 3792–3800. doi:10.1021/acssuschemeng.8b04492

Tokuno, T., Nogi, M., Karakawa, M., Jiu, J., Nge, T. T., Aso, Y., et al. (2011). Fabrication of Silver Nanowire Transparent Electrodes at Room Temperature. *Nano Res.* 4, 1215–1222. doi:10.27200/d.cnki.gkmlu.2019.00191910.1007/s12274-011-0172-3

Wang, J., Jiu, J., Zhang, S., Sugahara, T., Nagao, S., Suganuma, K., et al. (2018). The Comprehensive Effects of Visible Light Irradiation on Silver Nanowire Transparent Electrode. *Nanotechnology* 29, 435701. doi:10.1088/1361-6528/aad619

Xie, Y., Xu, H., He, X., Hu, Y., Zhu, E., Gao, Y., et al. (2020). Flexible Electronic Skin Sensor Based on Regenerated Cellulose/carbon Nanotube Composite Films. *Cellulose* 27 (14), 10199–10211. doi:10.1007/s10570-020-03496-w

Yu, H., Fang, D., Dirican, M., Wang, R., Tian, Y., Chen, L., et al. (2019). Binding Conductive Ink Initiatively and Strongly: Transparent and Thermally Stable Cellulose Nanopaper as a Promising Substrate for Flexible Electronics. *ACS Appl. Mat. Interfaces* 11, 20281–20290. doi:10.1021/acsami.9b04596

Yu, S., Liu, X., Wu, M., Dong, H., Wang, X., and Li, L. (2021). All-Solution-Processed Molybdenum Oxide-Encapsulated Silver Nanowire Flexible Transparent Conductors with Improved Conductivity and Adhesion. *ACS Appl. Mat. Interfaces* 13, 14470–14478. doi:10.1021/acsami.0c22324

Zhang, D., Ryu, K., Liu, X., Polikarpov, E., Ly, J., Tompson, M. E., et al. (2006). Transparent, Conductive, and Flexible Carbon Nanotube Films and Their Application in Organic Light-Emitting Diodes. *Nano Lett.* 6, 1880–1886. doi:10.1021/nl0608543

Zhang, Q., Wang, A., Zhang, S., Li, N., Chen, S., Zhang, Y., et al. (2017a). Asymptomatic Polyvascular Disease and the Risks of Cardiovascular Events and All-Cause Death. *Atherosclerosis* 262, 1–7. doi:10.1016/j.atherosclerosis.2017.04.015

Zhang, Y., Tang, S., and Zhang, T. (2017b). Homogeneous Alkalization of Cellulose in N-Methylmorpholine-N-Oxide/water Solution. *Cellulose* 24, 1235–1245. doi:10.1007/s10570-017-1195-z

Zimmermann, R., Müller, Y., Freudenberg, U., Jehnichen, D., Potthast, A., Rosenau, T., et al. (2016). Oxidation and Structural Changes in NMMO-Regenerated Cellulose Films. *Cellulose* 23, 3535–3541. doi:10.1007/s10570-016-1084-x

Conflict of Interest: PL, TZ was employed by Gree Intelligent Equipment Co., Ltd.

The remaining authors declare that the research was conducted in the absence of any commercial or financial relationships that could be construed as a potential conflict of interest.

Publisher's Note: All claims expressed in this article are solely those of the authors and do not necessarily represent those of their affiliated organizations, or those of the publisher, the editors and the reviewers. Any product that may be evaluated in this article, or claim that may be made by its manufacturer, is not guaranteed or endorsed by the publisher.

Advantages of publishing in Frontiers

OPEN ACCESS
Articles are free to read for greatest visibility and readership

FAST PUBLICATION
Around 90 days from submission to decision

HIGH QUALITY PEER-REVIEW
Rigorous, collaborative, and constructive peer-review

TRANSPARENT PEER-REVIEW
Editors and reviewers acknowledged by name on published articles

Frontiers
Avenue du Tribunal-Fédéral 34
1005 Lausanne | Switzerland

Visit us: www.frontiersin.org
Contact us: frontiersin.org/about/contact

REPRODUCIBILITY OF RESEARCH
Support open data and methods to enhance research reproducibility

DIGITAL PUBLISHING
Articles designed for optimal readership across devices

FOLLOW US
@frontiersin

IMPACT METRICS
Advanced article metrics track visibility across digital media

EXTENSIVE PROMOTION
Marketing and promotion of impactful research

LOOP RESEARCH NETWORK
Our network increases your article's readership